Interpreting Radar Scattering: Circular-polarization Perspectives from Three Terrestrial Planets

Thesis by

Albert Frank Christian Haldemann

In Partial Fulfillment of the Requirements

for the Degree of

Doctor of Philosophy

California Institute of Technology

Pasadena, California

1997

(defended May 19th, 1997)

For Sue

Acknowledgements

My heartfelt thanks to Dewey Muhleman for mentoring me, for trusting me with huge amounts of complicated data, for cajoling me when that would do, and for admonishing me when that worked better. I enjoyed the association, and am proud to count myself among his academic offspring. I thank Bruce Murray for listening to my ideas about planetary exploration, career choices, and life decisions. Yuk Yung helped maintain my curiosity about terrestrial methane, and its biospheric genesis---the path not taken. Jim Westphal will, I hope, never stop telling stories, especially about airplanes! Ed Danielson is, I think, the "sleeper" in South Mudd. Thank you, Ed, for quietly suggesting Case for Mars and MVACS! The latter requires me to thank Dave Paige for broadening my horizons Mars-ward. I need to aknowledge Dewey again here for allowing me to get up to all these shenanigans. Of course, I would have accomplished infinitely less without the help of Kay, Irma and Tammy; many thanks to them.

There are JPL-denizens a-plenty who went well beyond the call of duty to aid me on my path. To Marty Slade I am indebted for the whole Pathfinder landing site selection experience. Ray Jurgens patiently explained delay-Doppler processing more than once...and probably will have to again. My Pathfinder participation would not have been possible without Matt Golombek's willingness, and for that I am eternally (martian and) grateful. For the SIR-C work, I want to especially thank Ellen O'Leary who always came up with the data. Among the many others who contributed are Steve Ostro, Tom Farr, and Oliver Chadwick.

My time at CIT would not have passed so pleasantly without my cohort of fellow students and friends. Brian Butler played a large role in my scientific development with the Venus work, and receives my special thanks. I profited too from the wisdom of my many office mates: Eric, Mark (G), Toshiko, Kim, Steve, Rob, and Yibo from whom many people heard that I wasn't here. Others, "down the hall" helped too: Stuart, Don, Adam, Ant'. And I don't expect to write a paper as easily again as at coffee breaks with Mark (Data). Beyond the feifdom of the first floor of South Mudd I found friends too. For their cheerfulness throughout, I thank Mark (Abby), Bob, Jean, Miriam and Dick, "Psycho" Pete and Caroline. Sharon, Deniz and Adriana made carpooling fun.

It goes without saying that I'm indebted to my three parents. They have always supported my professional ambitions, and I am forever lovingly grateful. My Toronto TFS friends are always a foundation I can rely on, and they made no exception when I came to California. Thank you for your visits Ballu, Jana, Wing-Yee and Paul. Other visitors of note were Pouffi and Flo...who should visit more often. I appreciated Ken's scientific encouragement on his visits.

There are many people at Caltech and elsewhere who helped to produce this thesis to some degree or other. None are as cherished as Sue. I am proud that I finish my tenure at Caltech not only with a Ph.D., but with a lifetime best friend, team-mate and partner. Loving thank-yous Sue, for your caring and support, for your teasing to keep me smart, for being there, being you, with a twinkly-eyed smile! What next? Xander has it right: "A-bert, what doin'?"

Abstract

Planetary radar astronomy has used circular polarization radar signals to probe the surfaces of many solar system targets. However the trend for terrestrial observations has been toward greater use of linearly polarized imaging radars. Fortunately the latest generation of imaging radars has been developped with a multi-polarization capability. This should allow a synergy of the two research communities to occur.

One of the unresolved debates on planetary radar astronomy is the nature of the scattering processes from cold planetary ices. This question recently received input from a terrestrial source: Greenland (Rignot et al. 1993). In this thesis a survey is made of high altitude sites to discover if the Greenland percolation zone scattering behavior is wide-spread on the Earth. The survey was carried out with the enormous, publicly available dataset from the 1994 missions of Shuttle Imaging Radar payload. This instrument (SIR-C) obtained full-polarization information with its linear-polarization system. These data allow reconstruction of circular polarizations for comparison to planetary results. The search proved fruitful. Hundreds of square kilometers in western Tibet's Kunlun Shan, and in the Central Andes at the latitude of Santiago display radar scattering behavior quite similar to that in Greenland where internal reflections of the radar waves within icy inclusions in the firn enhance scattering in the same sense of circular polarization.

A separate unresolved issue in the planetary radar astronomy is the question of the nature of the highlands of Venus that exhibit high radar reflectivity and low emissivity. These so-called anomalous radar behavior in these regions have alternately been ascribed to high-dielectric doping or low dielectric volume scatterinig. We present new dual circular-polarization radar maps of the western hemisphere of Venus. The results are from a 1993 experiment to image Venus with 3.5 cm radar. Maps of Venusian radar albedo were made for each of two days of observation in both OS (echo principally due to specular reflection) and SS (diffuse echo) channels. On both days, the sub-earth longitude was near 300E. The SS maps are dominated by a significant component of diffuse backscatter from the 285E longitude highlands: Beta, Phoebe, and Themis Regiones. Beta Regio includes previously observed radar-anomalous regions. The nature of these altitude-related electrical properties on Venus is one of the outstanding surface process questions that remain after the Magellan mission. Our experiment provides the first full-disk polarization ratio (μ_c) maps. The data show that different geology determines different radar scattering properties within Beta. Diffuse scattering is very important in Beta, and may be due to either surface or volume scattering. We find a strong correlation of the SS albedo σ_{SS} with altitude R_p (km) in Beta, $\sigma_{SS} \propto 0.3R_p$. Also, $\sigma_{OS} \propto 0.7R_p$. The onset of this relationship is at the R_p~6054 km planetary radius contour. The nature and morphology of the highland radar anomalies in Beta is consistent with a diffuse scattering mechanism. In Beta Regio we find $\mu_c > 0.5$ in general, with μ_c as high as 0.8 between Rhea and Theia

Montes, to the west of Devana Chasma. These values are compatible with measurements of blocky terrestrial lava flows if surface scattering dominates. If volume scattering is important, the high RCP cross-sections may indicate an important decrease in embedded scatterer size with altitude, which could be related to enhanced weathering.

Finally, the techniques of planetary radar astronomy were used in an applied sense. Results are presented of 3.5-cm delay-Doppler and Doppler-only (continuous wave or CW) radar experiments to assess three potential Mars Pathfinder landing sites: Ares Vallis, Tritonis Lacus, and northwest (NW) Isidis. The regional relief at all of the landing sites is appropriate for a Pathfinder landing sequence: east-west slopes do not exceed 3° at any of the sites. We find that Ares Vallis has a Hagfors rms slope of θ_{rms}=4.8°±1.1° as measured by delay-Doppler radar, and θ_{rms}=6.4°±0.6° measured by CW radar. These values are similar to, or less than the previous measurements of the Viking Lander 1 region (θ_{rms}=6°, Tyler *et al.* 1976, *Harmon* 1997). The Tritonis Lacus landing site is rougher with delay-Doppler, θ_{rms}=5.6°±0.6°, while the NW Isidis landing site is very smooth, both in a regional sense (slopes < 0.7°) and in a Hagfors rms slope sense: θ_{rms}=1.8°±0.2°. Reflectivities at all of the sites should be sufficient to allow the radar altimeter on Pathfinder to function properly.

Table of Contents

Acknowledgements iv

Abstract vi

Table of Contents ix

List of Figures xii

List of Tables xvi

Chapter 1 Introduction 1
- **1.1 Background** 1
- **1.2 Radar Scattering, Polarization, and *Jargon*** 3
  - *1.2.1 Scattering Behavior* 3
  - *1.2.2 Polarization Effects* 8
- **1.3 Radar Techniques** 12
  - *1.3.1 Delay-Doppler Radar* 13
  - *1.3.2 Goldstone-VLA* 16
  - *1.3.3 SAR* 17
- **1.4 Organization** 19
- **1.5 Themes** 22

Chapter 2 Mars Pathfinder Landing Site Assessment with Goldstone Delay-Doppler and CW Radar Experiments 23
- **2.1 Introduction** 23
- **2.2 Radar Experiments** 25
- **2.3 Scattering Properties of the Martian Surface** 32
- **2.4 Results: Regional Topography at the Landing Sites** 36
- **2.5 Results: Scattering Properties at the Landing Sites** 43
  - *2.5.1 Ares Vallis CW* 43
  - *2.5.2 Delay-Doppler* 44
- **2.6 Conclusion** 56

Chapter 3 The Western Hemisphere of Venus: 3.5 cm Dual Circular-Polarization Radar Images 58
- **3.1 Introduction** 58
- **3.2 Experiment** 60
- **3.3 Mapping Radar Cross-section** 63

3.4 **Regional Results** 72
3.5 **Beta Regio** 75
3.6 **Conclusions** 93

Chapter 4 Earth: Unique Radar Properties of High Altitude Ice Fields 96
4.1.1 Unique Radar Properties 96
4.1.2 Glaciers, Snow, and Ice 99
4.1.3 Ice Radar Properties 103
4.1.4 High Altitudes 110
4.2 **SIR-C** 112
4.2.1 Full Polarization SAR 112
4.2.2 Data selection 113
4.2.3 Data Processing 117
4.3 **Kunlun Shan** 118
4.3.1 Geography 118
4.3.2 SAR Images 122
4.3.3 Radar Cross-sections 122
4.3.4 Polarization Ratios 129
4.3.5 Scattering Behavior 134
4.3.6 Firn properties 138
4.3.7 Glaciologic Features 142
4.3.8 Fault Detection 147
4.4 **Central Andes** 150
4.4.1 Geography 150
4.4.2 Central Andes Glacial Phenomena 152
4.4.3 Radar Imaging 160
4.4.4 Scattering Behavior 165
4.5 **Conclusions** 176

Chapter 5 Summary 178
5.1 **Understanding Circular-polarization Radar** 178
5.1.1 Mars 178
5.1.2 Venus 180
5.1.3 Earth 180
5.1.4 What is "Normal" ? 184
5.1.5 What is "Unique" ? 185
5.1 **Applying Circular-polarization Radar: Outlook** 186
5.2.1 Snows of Venus 186
5.2.2 Snows of Earth 187
5.3 **Normal and Unique Radar Planetology** 188

Appendix A Venus Radar Glossary 189
A.1. Radar Terminology 189
A.2 Geologic Terminology 191

Appendix B Experimental Data Reduction and Processing . 193
B.1 Goldstone-VLA experiment 193
B.2 Initial Data Reduction 194
B.3 CLEAN Uncertainties 196

Appendix C Venus Atmospheric Correction and Radar Cross-Sections 197

Appendix D SIR-C High Altitude Full-polarization Data Takes 199

Appendix E Death Valley and SIR-C Circular-polarization Processing 200
E.1 Death Valley Data as Processing Check 200
E.2 Death Valley Polarization Ratios 209
E.3 Remarks on SIR-C Calibration 211

References 214

List of Figures

Figure 1.1 Plot of generic radar scattering behavior for quasi-coherent scattering off of a distribution of facets. 4
Figure 1.2 Cartoon of radar scattering behavior as a function of icidence angle θ_i, and as a function of increasing surface roughness. 5
Figure 1.3 Scattering mechanism relationships 11
Figure 1.4 Diagram of Doppler only, or CW-Doppler planetary radar response. After Simpson *et al.* 1992. 13
Figure 1.5 Diagram describing relationship of range rings and Doppler strips to planetary coordianates. 15
Figure 1.6 SAR range and doppler coordinate mapping onto terrain surface. After Elachi (1988), p.76. 18
Figure 2.1 CW spectrum and composite scattering model fit for the Ares Vallis landing site. 28
Figure 2.2 Viking composite image showing the Ares Vallis landing ellipse centered at 32.8°W, 19.5°N. The locations of the three delay-Doppler and one CW radar track through the region are shown.. 28
Figure 2.3 Diagram of geographic delay-Doppler frequency strip (N-S) and range ring coverage for a single range-gated spectra. 29
Figure 2.4 Example of a 20-s integration of delay-Doppler spectra. 29
Figure 2.5 Schematic plot of the geographic coverage of the delay-Doppler radar tracks, labeled in DOY. 36
Figure 2.6 The elevation results for each of the landing sites and regions of interest. 38
Figure 2.7 Excerpt from Rotto and Tanaka (1995) Geologic/geomorphologic map of the Chryse Planitia region of Mars framing the DOY 027, 029, and 030 delay-Doppler radar tracks near the Ares Vallis and the Maja Valles landing sites. 40
Figure 2.8 The rms slope (θ_{rms}) results for each of the landing sites and regions of interest.. 46
Figure 2.9 Reflectivity (ρ) results for each of the landing sites and regions of interest. 48
Figure 2.10 The θ_{rms} results for each of the landing sites and regions of interest, binned in 0.5° intervals and plotted as histograms. 51
Figure 2.11 The ρ results for each of the landing sites and regions of interest, binned in 1% intervals and plotted as histograms, as in Figure 2.9. . 52
Figure 3.1 A) Image of the SS echo from Venus on Mar. 4, B) Image of the Venus OS echo on the same day. 64
Figure 3.2 Orthographic reprojections of Magellan global altimetry on A) Feb. 28, and B) Mar. 4, with planetary radius grayscale in km. 65
Figure 3.3 A) Image of the SS echo from Venus on Feb. 28, B) Image of the Venus OS echo on the same day. 66

Figure 3.4 Mercator projection of Magellan altimetry between 65N and 65S for the hemisphere sampled on Mar. 4, 1993. 67
Figure 3.5 Mercator projection maps of radar results on Feb. 28th, 1993. A) σ_{SS}, B) σ_{OS},. C) μ_c 70
Figure 3.6 Mercator projection maps of radar results on Mar. 4th, 1993, A) σ_{SS}, B) σ_{OS}, and C) μ_c, ... 71
Figure 3.7 Mercator projection geologic sketch map of Beta Regio (based on Senske *et al.* 1991bc and 1992), with altimetry contours. 77
Figure 3.8 Mercator projection from sky coordinates of σ and σ in the region around Beta on Feb. 28. 79
Figure 3.9 Mercator projection from sky coordinates of σ and σ in the region around Beta on March 4. 80
Figure 3.10 Mercator projection from sky coordinates of μ_c in the region around Beta on A) Feb. 28, and B) March 4. 81
Figure 3.11 Scatterplots of data from the Beta Regio box (Fig.3. 4) on A) Feb. 28 and B) Mar. 4 showing correlations. 86
Figure 3.12 Scatterplots as in Fig.3.11, but restricted to the Rhea Mons box (Fig. 4) on A) Feb. 28, and B) Mar. 4. 87
Figure 3.13 Scatterplots as in Fig. 3.11, but for the Theia Mons box (Fig.3.4) on A) Feb. 28, and B) Mar. 4. 87
Figure 4.1 Schematic comparison of the typical backscattering dependance on incidence angle for a terrestrial planet with that of EGC. θ_i is the incidence angle at the radar equator. The plots represent results from Doppler-only (CW) radar observations. 97
Figure 4.2 Snow and ice zones in the accumulation zone of a glacier. After Figure 2.1 from Patterson (1994). 102
Figure 4.3 General behavior of a) σ°(RL), b) μ_c, and c) μ for AIRSAR measurements of the Greenland ice cap in the percolation zone as a function of incidence angle θ_i. After Rignot et al. (1993) Fig.2 . . . 109
Figure 4.4 Quad-pol SIR-C tracks over the Himalayas, Tibet, and Tien Shan. 114
Figure 4.5 Quad-pol SIR-C tracks over the northern Rocky Mts. 115
Figure 4.6 Quad-pol SIR-C tracks over the Andes and Patagonia. 115
Figure 4.7 Map of the distribution of glaciers in western China. 119
Figure 4.8 Landsat image mosaic of the Western Kunlun Shan. 120
Figure 4.9 SIR-C DT 1/58.10 scene pr12061 σ°(CRL). 124
Figure 4.10 Plots of average radar scattering behavior at different altitude on Zhongfeng Glaciers I and Ia. 125
Figure 4.11 Plots of average radar scattering behavior at different altitude on Chongce Glaciers I II and III. 126
Figure 4.12 Kunlun Mtn. scene from SIR-C DT 1/58.10 with linear polarization linear stretch. The black outlines on this Fig. show the locations of sampling sites for calculating scattering statistics. 128

Figure 4.13 Regional C-band circular polarization ratio behavior in DT 1/58.10 Kunlun Mtn. scene. Color assignments are: red for μ_c>1.0, green for 0.25<μ_c<0.7, and blue for μ_c<0.25. 130
Figure 4.14 Regional L-band circular polarization ratio behavior in DT 1/58.10 Kunlun Mtn. scene. Color assignment as in Fig. 4.13. 131
Figure 4.15 Regional C-band linear polarization ratio behavior in DT 1/58.10 Kunlun Mtn. scene. Red color indicates μ_c>0.35, while green shows 0.2<μ_c<0.35, and blue indicates μ_c<0.1. 132
Figure 4.16 Regional L-band linear polarization ratio behavior in DT 1/58.10 Kunlun Mtn. scene. Color assignment as in Fig. 4.15. 133
Figure 4.17 Circular polarization angular scattering behavior for forty-seven sites in DT 1/58.10 Kunlun Mt. scenes. 135
Figure 4.18 Linear polarization angular scattering behavior for the same sites as Fig. 4.17. 136
Figure 4.19 Chongce Icecap firn stratigraphic sections of the upper meters at several elevations. 139
Figure 4.20 Smooth snow surfaces on icecaps of the Western Kunlun . . 140
Figure 4.21 Toe of glacier at the head of Quan Shui gou stream, on the south slope and western tip of the Western Kunlun Shan. 146
Figure 4.22 μ_c (C-band) color and greyscale images of a portion of the DT 1/58.10 Western Kunlun scene. 148
Figure 4.23 Regional fault map for the Western Kunlun Shan region. The location of the SIR-C scene is outlined. 149
Figure 4.24 Sketch map of the distribution of glaciers in the Central Andes (After Lliboutry (1965). 153
Figure 4.25 Image mosaic of two Space Shuttle astronaut handheld photographs from March and April of 1994. 154
Figure 4.26 Firn surface in the Alps (Clariden) in July 1935. Picture from Streiff-Becker (1954). 157
Figure 4.27 Firn surface in the Alps (Bergell) on Aug. 1, 1935. Picture from Streiff-Becker (1954). 157
Figure 4.28 Snow penetentes. View is to the east. Picture from Lliboutry (1964). 158
Figure 4.29 View to the south of the same penitentes as Fig. 4.28. Picture from Lliboutry (1964). 158
Figure 4.30 Radar σ°(RL) image of DT 2/40.60 Tupungatito scene. Prominent geographic features are labeled. 162
Figure 4.31 Excerpt from handheld Shuttle astronaut photograph STS059-L15-048 from the April SRL-1 mission. 164
Figure 4.32 Tupungatito region C-band circular polarization ratios as observed by SRL-2 DT 2/40.60. Red color indicates μ_c>1, green 0.25<μ_c<0.7, and blue μ_c<0.25. 166
Figure 4.33 Tupungatito region L-band circular polarization ratios. Color assignments as in Fig. 4.32. 167

Figure 4.34 Tupungatito region C-band linear polarization ratios as observed by SRL-2 DT 2/40.60. Red color indicates μ_l>0.3, green 0.2<μ_l<0.3, and blue μ_l<0.1. 168
Figure 4.35 Tupungatito region L-band linear polarization ratios. Color assignments as in Fig. 4.32. 169
Figure 4.36 Distribution of statistical sampling regions for determination of enhanced μ_c scattering behavior. 172
Figure 4.37 Circular polarization angular scattering behavior for thirty-one sites in DT 2/40.60 Tupungatito volcaon scenes. 173
Figure 4.38 Linear polarization angular scattering behavior for the same sites as Fig. 4.37. 174
Figure E.1 SIR-C quad-pol image preparation and processing scheme . 202
Figure E.2 SIR-C RL polarization radar image of Stovepipe Wells (DT 1/120.30) L-band (scene pr12060). 205
Figure E.3 SIR-C RL polarization radar image of Stovepipe Wells (DT 1/120.30) C-band (scene pr12061). The yellow boxes represent sites examined by Weeks et al. (1996; 1997). 206
Figure E.4 Comparison of SIR-C σ° statistics from track 1/120.30 scenes with (grey) ranges of AIRSAR σ° values from Greeley and Blumberg (1995). 207
Figure E.5 Comparison of ER Mapper processed SIR-C CHH and LHH σ° statistics from Stovepipe Wells with published results of Weeks et al. (1997) 210

List of Tables

Table 1.1
Polarization designations* and synonyms 9
Table 2.1
Delay-Doppler and CW radar parameters 25
Table 2.2
Goldstone radar tracks for Pathfinder landing site assessment 27
Table 2.3
Mean scattering properties along the radar tracks 50
Table 3.1
Relevant observational parameters. 61
Table 3.2
Image quality parameters. 62
Table 3.3
Muhleman scattering model fits,
$\sigma_{OS} = \beta_{OS} \cos\theta_i / (\sin\theta_i + \alpha_{OS}\cos\theta_i)^3$ 69
Table 3.4
Average dual-polarization radar data for Themis Regio. 73
Table 3.5
Average dual-polarization radar data for Phoebe Regio. 75
Table 3.6
Analyses of Beta (Fig 3. 11), Theia (Fig. 3.12), and Rhea (Fig. 3.13) radar properties. Linear models are fit to the scatterplots 88
Table 4.1
SIR-C datatake selections for high altitude ices 116
Table 4.2
SIR-C Hotien East quad-pol scene processing parameters. 123
Table 4.3
Chongce Glacier crevasse radar properties 143
Table 4.4
Yulong Glacier III toe radar properties 145
Table 4.5
Yulong Glacier IV toe radar properties 145
Table 4.6
SIR-C Cerro Aconcagua quad-pol scene processing parameters. 161
Table 5.1
Hagfors roughness determinations for VL1 and Ares Vallis. 179
Table E.1
SIR-C Death Valley quad-pol data takes 202
Table E.2
SIR-C Death Valley quad-pol scene processing parameters 205
Table E.3
SIR-C calibration errors (Freeman et al. 1995) 213

Chapter 1

1 Introduction

1.1 Background

Radar by itself cannot really be used to infer surficial, or near-surface processes. Rather, if one can determine from the radar scattering with some degree of confidence the terrain's near-surface morphology, one can test hypotheses regarding surficial processes. The requisite interpretation of radar echoes from natural targets relies on, and is limited by, our understanding of how the incident electromagnetic (EM) waves interact with those targets. A vast body of knowledge has been, and is still being, built up to describe those interactions (*e.g.* Ulaby *et al.*, 1986). Often, a single radar experiment will not provide a unique determination of the nature of a target surface. For example, by analogy to the radar properties exhibited by the icy Galilean satellites of Jupiter, water ice is the favored explanation for Mercury's polar deposits (Butler, 1994, Butler *et al.*, 1993, Harmon *et al.*, 1994, Slade *et al.*, 1992). However, confirmation of this awaits future experiments. Radar itself can be brought to bear on such problems: several wavelengths can be used and the polarization behaviour of the backscattered radiation can be analyzed. As more parameters are examined, the characteristic radar behaviour of a given target surface is more precisely

determined. Still, it is safer to avoid discussion of the "radar signature "of a target surface, and to replace that term with the target's "radar response" (Van Zyl and Ulaby, 1990).

The exploration of planets with radar has proceeded in tandem with the radar examination of terrestrial surfaces. Reviews of the history of planetary radar astronomy include Piddington (1961), Smith and Carr (1964), and most recently Butrica (1996). They do not always agree. However, they clearly show that the development of planetary radar astronomy has been a full player in space age exploration of the planets. The beginning of planetary radar investigations is most often cited as occurring with the detection of the first radar echoes from the Moon by John Dewitt at the U.S. Army Signal Corps Evans Signal Laboratory on January 10th 1940¶. Technical mastery of planetary radar remote-sensing over the last half century has led to achievements from the determination of the astronomical unit (Muhleman, 1962) to the complete mapping of cloud-shrouded Venus (Saunders *et al.*, 1990) and the discovery of ice inside permanently shadowed craters at Mercury's poles.

Terrestrial radar remote-sensing had its beginning with the accelerated military development of radar during World War II. Early military applications of radar scattering by terrain (Ulaby *et al.*, 1986, v.1) were radar altimetry (1940, Japan) and terrain imaging (1946, MIT Lincoln Lab). Side-looking airborne radar

---

¶I'm more impressed by Hungarian Zoltan Bay's independant detection one month later with an novel integrating water electrolysis detector!

(SLAR) had produced many classified images[§] by the time the first radar echoes were being received from Venus in 1961 (Goldstein, 1962). All of these uses required an understanding of the behavior of radar scattering by terrain, which led to our modern uses that include environmental monitoring. Indeed, sequences of radar images can be used to investigate temporal effects. These changes can be due to either natural or anthropogenic processes (e.g. Ray, 1995). For example, the state of agricultural fields can be monitored during a growing season, since the scattering behavior of the terrain changes as the crops grow. Another example, involving the understanding of the radar response of ice and snow is the imaging of sea-ice on the Earth's polar seas with Synthetic Aperture Radar (SAR) satellites. This low Earth orbit monitoring has become an operational tool for high latitude navigation over the last half-decade.

1.2 Radar Scattering, Polarization, and *Jargon*

1.2.1 Scattering Behavior

Planetary radar astronomy and terrestrial radar remote sensing share a common physical basis which can be summarized by Fig. 1.1. The behavior of the scattered or reflected power is plotted as a function of the incidence angle of the illuminating radar radiation relative to the local vertical of the target surface. When the centimeter-length EM waves arrive at normal incidence toward the

---

[§]These 8.6 mm wavelength images made with the Westinghouse AN/APQ-97 SLAR were declassified in 1964, and the system was later used to image 0.5×10^6 km^2 ! (Ulaby *et al.*, 1986, v.1).

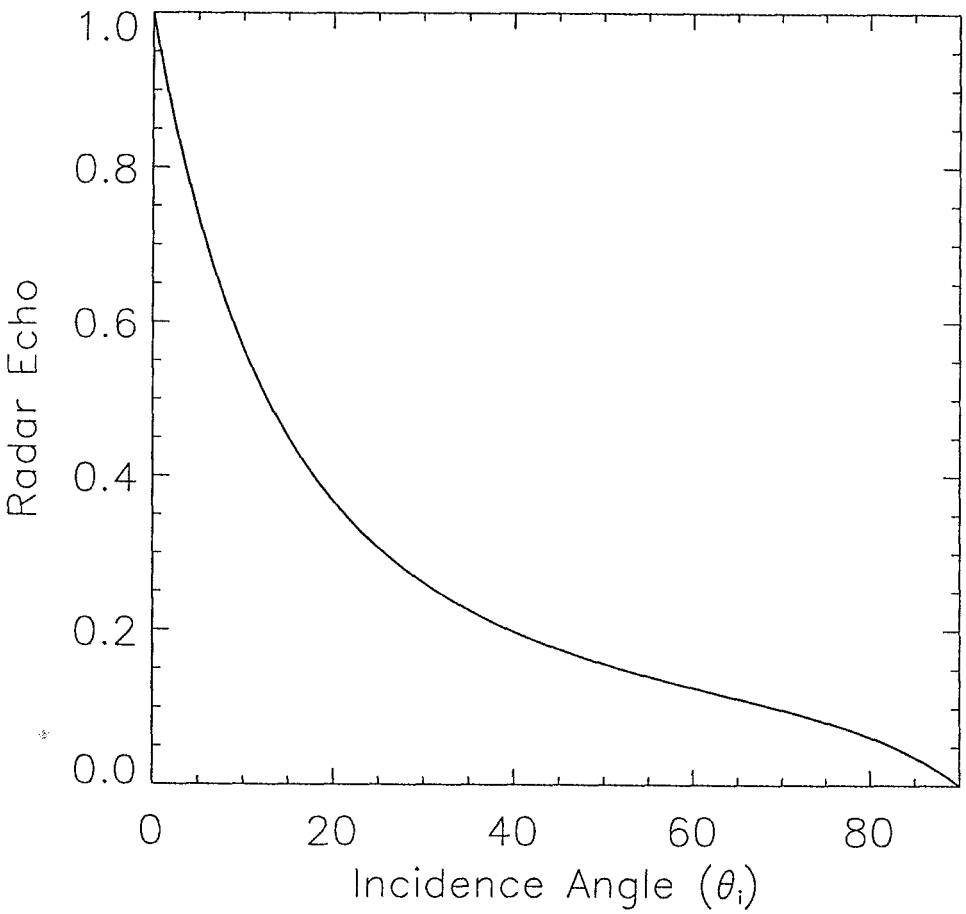

Figure 1.1 Plot of generic radar scattering behavior for quasi-coherent scattering off of a distribution of facets. The behavior of the (back-)scattered or reflected power is plotted as a function of the incidence angle, θ_i of the illuminating signal relative to the local vertical of the target surface. The sharp peak near normal incidence is due to semi-coherent reflections.

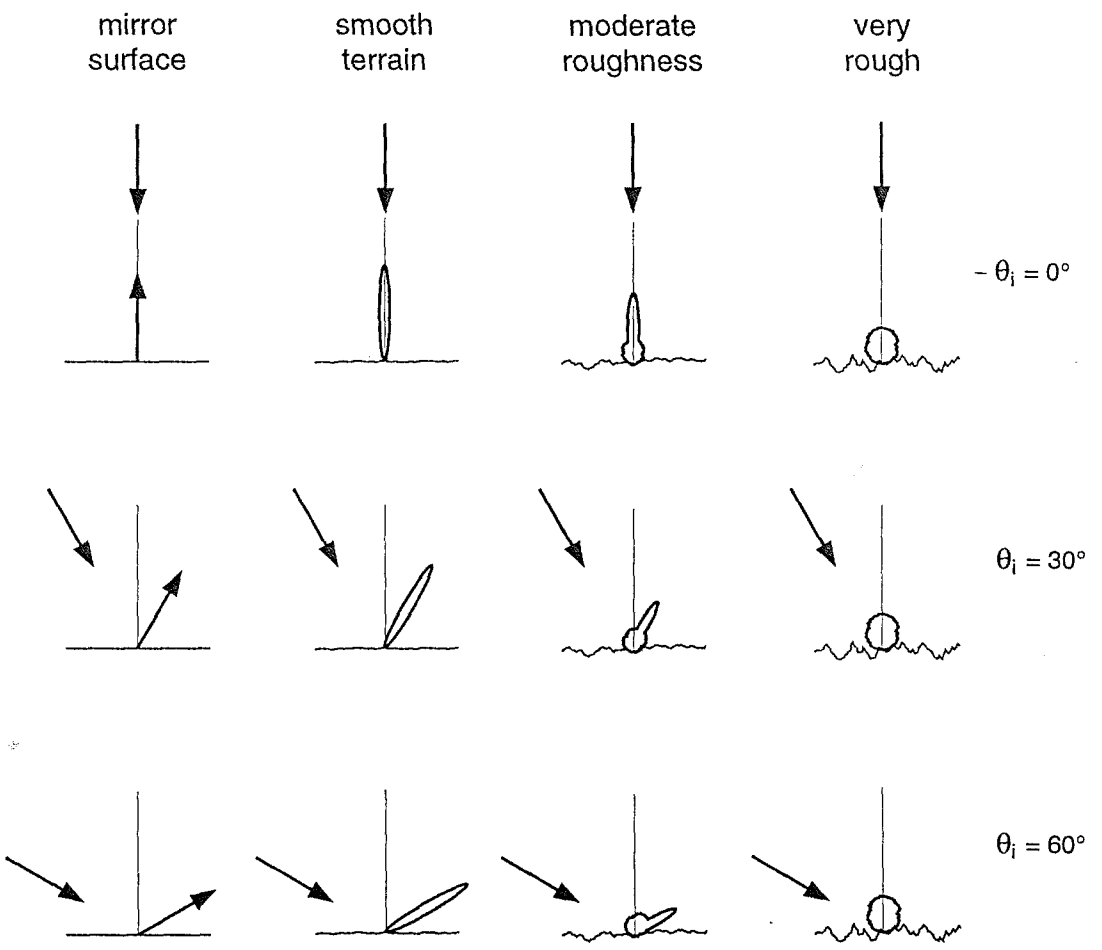

Figure 1.2 Cartoon of radar scattering behavior as a function of icidence angle θ_i, and as a function of increasing surface roughness. The schematic polar plots at the incidence points depict the angular distribution of the scattered radiation.

surface, the latter behaves for the most part like a poor mirror and reflects a good portion of the incident energy back toward the radar. As the incidence angle is increased, the amount of the signal returned toward the radar decreases precipitously out to around θ_i=30°, and then further declines more gently. Now, if the surface is mirror-like, why should any of the incident radiation be backscattered at all? The answer is addressed by Fig. 1.2. As shown in the first row of Fig. 1.2, as the surface becomes progressively rougher, more radiation is scattered in directions other than the nadir backscatter direction. Remote sensing radars looking at the Earth typically have a resolution pixel several meters on a side. Thus, the radar response is produced by tens of m^2 of terrain. If the terrain is perfectly flat, an entire pixel can behave as a mirror and reflect the radar energy in the specular direction according to the standard law of reflection. As gentle ripples and swales are added to an otherwise smooth surface, there will be some surface elements within the pixel that scatter slightly away from the specular direction. As the surface gets rougher there will be more surface elements angled further away from the pixel mean, and the scattering will become more isotropic. *Diffuse scattering* refers to any form of re-radiation that tends toward isotropic (last two columns in Fig. 1.2).

If the distribution of surface element tilts within a pixel is statistically well-behaved, an analytical scattering model can be written. All scattering models describe the behavior of the radar cross-section as a function of incidence angle (Figs. 1.1 and 1.2). The *backscatter cross-section*, σ^o, is defined as the ratio of

the energy detected at the receiver over what would have been received from an isotropic scatterer. In the case of an entire planet, if the planet's surface is relatively homogeneous, a single scattering model can describe the behavior or the cross-section over the whole disk (Cohen, 1959). All locations from the sub-Earth point out to the limb are viewed, and thus, the scattering behavior is sampled over all incidence angles. Common facet scattering models in planetary radar astronomy are the *Muhleman model* (1964) the *Hagfors model* (1964). Small scale roughness at larger incidence angles has been described by uniform-brightness models, Lambertian models (Evans and Hagfors, 1968), point scatterer models, and Bragg models (Elachi, 1987, Elachi, 1988, Ulaby, 1982).

Natural terrains are not usually made up of perfect conductors, so some of the radar energy will penetrate below the surface and experience volume scattering. In an environment without liquid water†, penetration depths are of the order 10λ (Campbell and Ulrichs, 1969). Liquid water is nearly ubiquitous on Earth, and so radar is used to infer soil water content. On Mars and on Venus especially, both much drier, radar probes the near-surface environment as well as the surface. While surface scattering behavior still lends itself to human intuition, volume scattering adds a huge amount of additional parameter space for interpreting terrain radar response. This is precisely the case with cold snow or ice which, unlike water are rather transparent.

---

†For water at 10 cm, the index of refraction is 9 and the absorption coefficient, α is approximately 1.5 cm^{-1} (Jackson, 1975).

1.2.2 Polarization Effects

Scattering models that rely on facet reflections do not fully describe the radar response of any surface other than a mirror. This is because specular or facet-like reflections have a precise polarization behavior. An incident *linearly polarized* EM wave will be reflected with the same linear polarization. A *circularly polarized* EM wave will be reflected with the opposite sense of circular polarization. The reflection mechanism in these cases can be understood as arising from the generation of currents by the incident EM wave, which re-radiate some or all of the energy as a coherent reflected wave. At an infinite half-space dielectric boundary, all of the currents can preserve the appropriate polarization behavior. Natural terrain's inhomogeneities however, will constrain the currents to directions not aligned with the incident wave's polarization, and will then re-radiate a portion of the energy with a component of orthogonal polarization.

"De-polarizing" behavior can be all the more important if the subsurface is also probed and *volume scattering* occurs. *Multiple scattering* is the case when more than one scattering event occurs before the radiation is returned in the backscatter direction. *Coherent backscatter* is a particular form of volume, multiple forward scattering in a transparent medium. Several examples below will serve to illustrate various polarization responses of these different scattering mechanisms, and the figures of merit that can distinguish among them.

First, polarization nomenclature needs to be reviewed. Table 1.1 attempts to summarize the various polarization designations. The task is complicated by

the fact that terrestrial radar remote sensing, for which the most *radar polarimetry* work has been carried out, uses phase-coherent linear polarizations (*horizontal H, vertical V,* with respect to the plane of incidence). Planetary radar astronomy on the other hand, due to ionospheric Faraday rotation, works with circular polarization (*R, right, L, left,* viewed in the direction of propagation). A common notation however is to refer to a backscattered signal with a pair of letters, *TR,* for

Table 1.1
Polarization designations* and synonyms

Radar Polarimetry Designation	Scattering mechanisms^	
	Diffuse, Volume, Multiple, Coherent	Specular
Cross-polarized	linear: HV, VH	circular: RL, LR (OS^{+}, OC^{++}, polarized$^{\sim}$, matched$^{\sim}$, expected)
Co-polarized	circular: RR, LL (SS^{+}, SC^{++}, depolarized$^{\sim}$, mismatched$^{\sim}$, unexpected)	linear: HH, VV

* The first letter designates the transmitted polarization, the second the received polarization. H is horizontal linear, V is vertical linear, R is right circular and L is left circular.

^ See text.

$^{+}$ Caltech and Goldstone-VLA designation for Opposite-Sense (OS) and Same-Sense (SS) of circular polarization.

$^{++}$ Arecibo and Goldstone asteroid radar designation for Opposite-sence Circular (OC) and Same-sense Circular (SC) polarization.

$^{\sim}$ These terms arise from the notion that the specular echo is to be expected and thus that the OS return is the appropriate polarization signature, while SS is the unexpected or mismatched polarization.

the transmitted polarization state, *T*, and the received polarization, *R*. Thus, the polarized backscatter cross-section is σ°_{TR}.

Polarization ratios, μ_{pol}, can be useful measures of the degree of non-specular scattering and are defined as follows.

$$\mu_c = \frac{RR}{RL} \quad , \quad \frac{LL}{LR} \tag{1}$$

is the *circular polarization ratio*, and

$$\mu_l = \frac{HV}{HH} \quad , \quad \frac{VH}{VV} \tag{2}$$

is the *linear polarization ratio*. These definitions are such that;

1. for pure reflection μ_c=0 (since RR and LL =0) and μ_l=0 (since HV or VH =0),
2. for volume scattering at normal incidence (Campbell *et al.*, 1993) from a half-space of randomly oriented dipoles, μ_c=1 and μ_l=⅓ (Long, 1965), and
3. for double-pure-reflection off a *dihedral* with one surface horizontal HV (or VH) = 0 and RL (or LR) =0, so μ_l=0 and μ_c=∞ (if the material is perfectly reflecting).

When μ_{pol} is considered in conjunction with the cross-section, different scattering behaviors can be distinguished. The following summary is after Rignot (1995). "Normal" radar behavior for terrain surfaces implies mostly surface scatter with moderate cross-section ($\sigma^{\circ} \leq 0.1$), $\mu_c << 1$ and $\mu_l << 1/3$. Earth's forests are the best understood volume scattering and multiple-scattering radar target. They

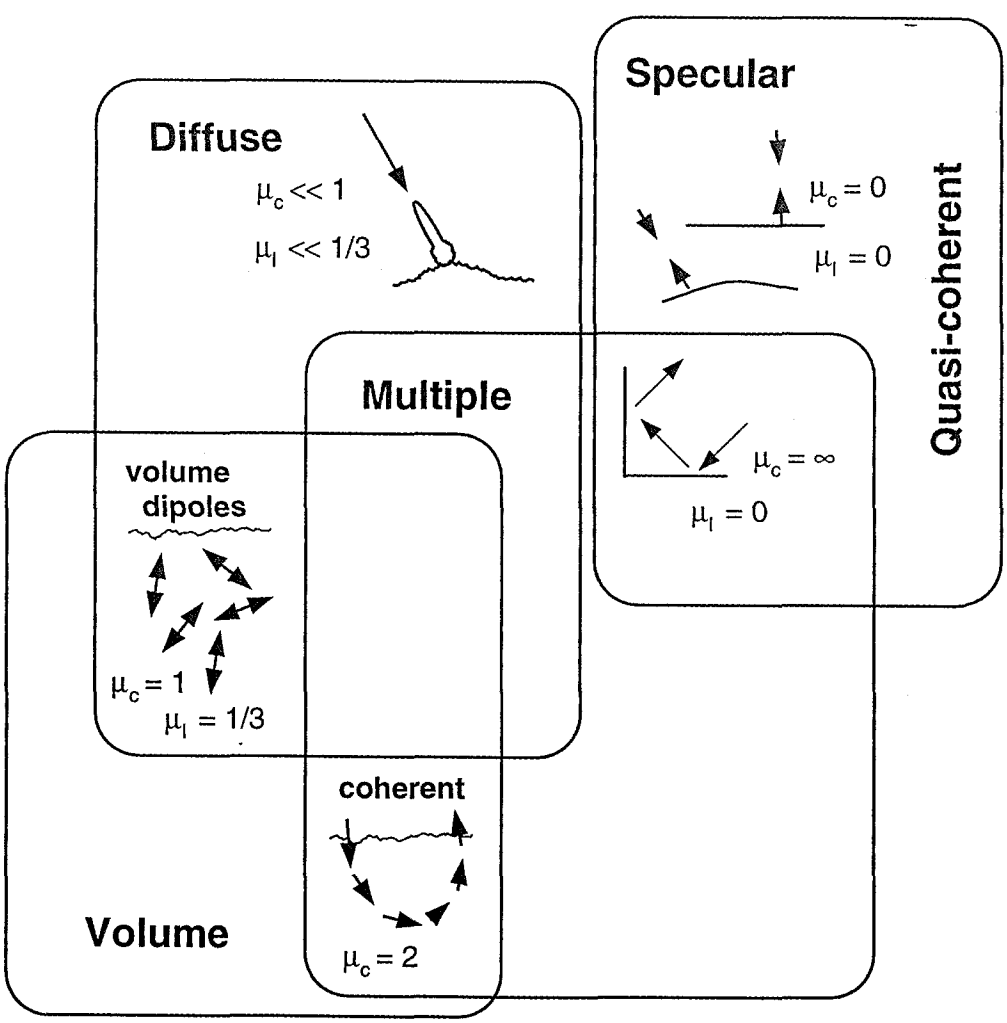

Figure 1.3 Scattering mechanism relationships.

typically have moderate cross-sections but often $\mu_c \approx 1$ and $\mu_l \approx 1/3$. For some forests with less deveolopped canopies and at larger λ, μ_c can exceed unity due to trunk-ground scattering. Rough lava flows on the other hand are generally found to have $\mu_c < 1$ (not $<<1$) and$_l$ $\mu < 1/3$ (not $<<1/3$), but also with moderate cross-sections. Very blocky cases are known with $\mu_c > 1$ and $\mu_l \sim 1/3$ suggesting double-bounce scattering from randomly oriented dihedrals (Campbell and Campbell, 1992, Rignot *et al.*, 1993). Startling polarization behavior is exhibited by ices. The icy Galilean satellites (Europa, Ganymede and Callisto, EGC) exhibit $\mu_c > 1$ with high cross-sections ($\sigma^o \sim 0.5 - 1.0$) (Goldstein and Morris, 1975). Curiously, for EGC $\mu_l > 1/3$. Terrestrial snow with embedded ice in Greenland exhibits similar σ°, μ_c, and μ_l values as EGC (Rignot *et al.*, 1993). These ice observations in particular will be discussed further in Chapter 4. This review is by no means exhaustive, but provides the flavor of the sattering behaviors that are observed in the present work. Figure 1.3 summarizes some of the scattering behaviors and their relationships to one another.

1.3 Radar Techniques

For this thesis, three separate radar remote sensing techniques are used to examine three very different surfaces on three terrestrial planets. The three techniques are delay-Doppler radar, bi-static continuous-wave interferometric imaging, and SAR. These techniques were applied to Mars, Venus and the Earth respectively.

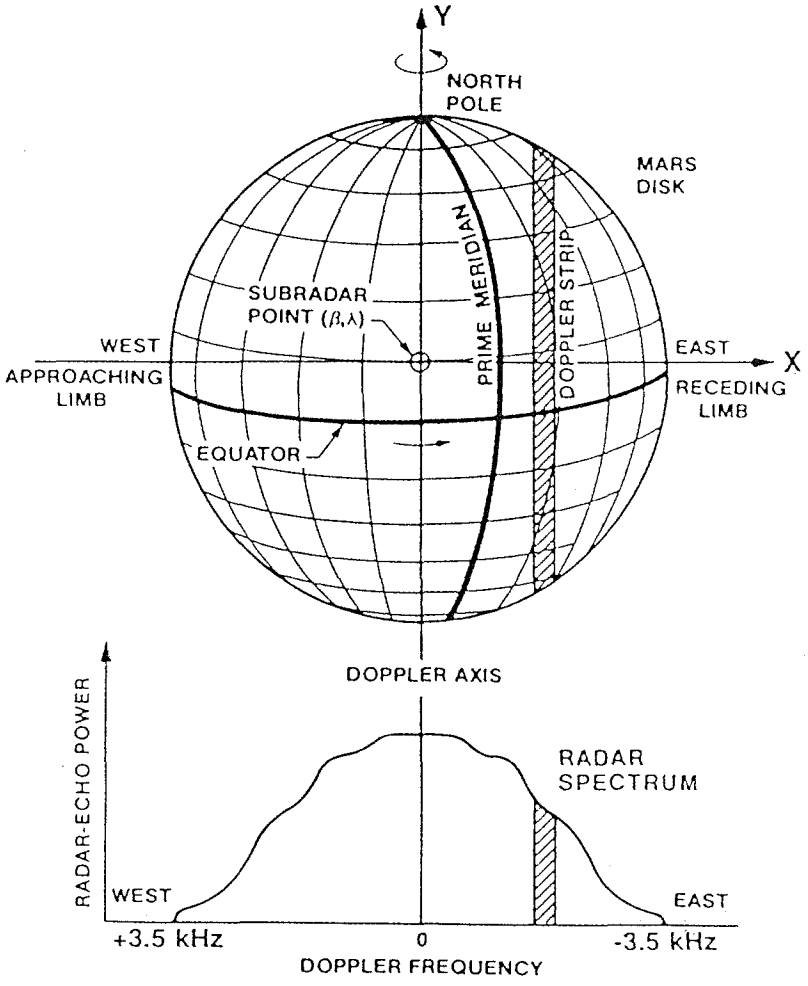

Figure 1.4 Diagram of Doppler only, or CW-Doppler planetary radar response. After Simpson *et al.* 1992.

1.3.1 Delay-Doppler Radar

The planetary echo of a monochromatic, continuous-wave (CW) radar signal from Earth will be Doppler-shifted by the relative motion of the Earth and the planet, and by the planet's rotation. The Doppler effect spreads out the echo signal over a bandwidth that is proportional to the apparent angular velocity of the

planetary disk. A given frequency interval within the bandwidth corresponds to a set of apparent velocities, which map into a strip on the planet's disk that is aligned with the planet's apparent rotation axis. This phenomenon is shown diagrammatically in Fig. 1.4. Thus the echo strength in a given Doppler-frequency interval corresponds to the signal backscattered by the surface in the Doppler-strip. This technique does not provide any ranging information, and goes by the name of Doppler-only or continuous-wave Doppler (CW-Doppler).

Combining CW-Doppler with timing information provides target range information. A spherical target such as a planet is closest to the radar where the line from the radar to the center of the sphere intersects the surface. Radiating outward from this sub-radar point will be rings consisting of all surface locations that are equidistant from the radar, and progressively further away from it. These are the range or delay rings or strips. The relationship that exists between these delay-Doppler coordiantes (time and frequency) and the surface coordinates of a planet is shown in Fig. 1.5. It should be noted that there is not a unique mapping of delay-Doppler coordinates to planetary coordinates. This is because two spots on the planet, north and south of the radar track, contribute to an echo with a given Doppler-frequency and time-delay. This north-south ambiguity is inherent to the delay-Doppler technique. More detailed treatments of CW-Doppler and delay-Doppler can be found in (Evans and Hagfors, 1968, Ostro, 1993).

The CW-Doppler technique is commonly applied when both OS and SS information is sought. The delay-Doppler technique lends itself less well to

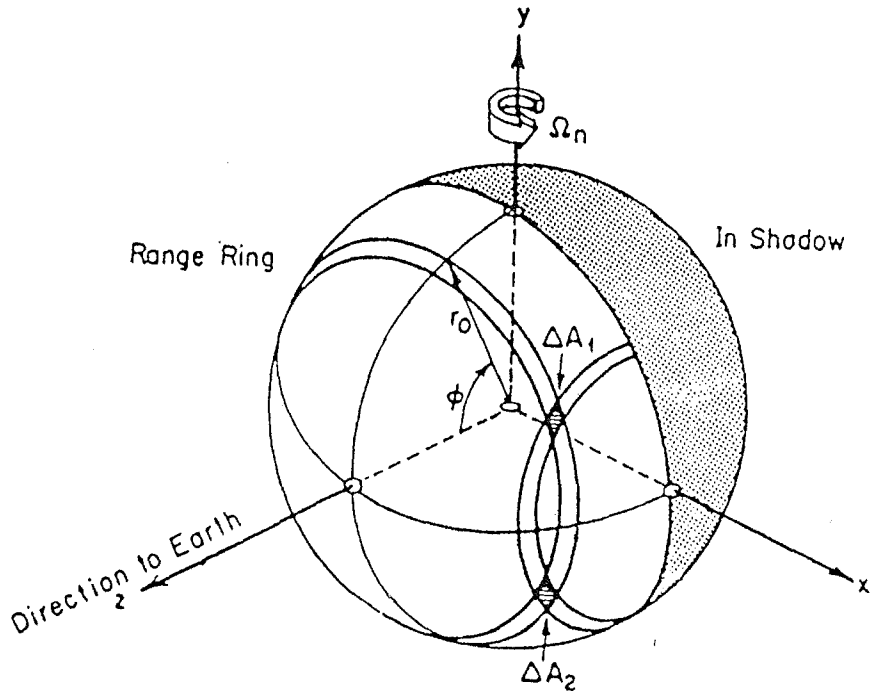

Figure 1.5 Diagram describing relationship of range rings and Doppler strips to planetary coordianates.

dual-polarization experiments. Since the SS echoes are so much weaker than the OS echoes, much spatial resolution would be lost in allowing sufficient integration to detect the SS signals.

The CW-Doppler and delay-Doppler techniques are the "classic" or workhorse tools of planetary radar astronomy. There are several installations that

have and can use these techniques. Current facilities are the 70-m Goldstone Solar System Radar antenna which is part of NASA's Deep Space Network operated by the Jet Propulsion Laboratory (JPL), and the soon-to-be re-activated Arecibo Observatory in Puerto Rico. Many examples of the results from these two facilities are listed in Ostro (1993) and in Butrica (1996).

1.3.2 Goldstone-VLA

This technique owes much to radio astronomy. The technique is distinct from most of radio astronomy however, in that an active form of remote sensing is carried out. The transmitter is a radar facility, and so perhaps for that reason we are comfortable designating it a radar technique. For an experiment, a CW radar signal transmitted from Goldstone illumintes the targetted planet. Then, the National Radio Astronomy Observatory's (NRAO) Very Large Array (VLA) radiotelescope is used to image the backscattered echo, making this a bi-static technique. The VLA has twenty-seven 25 m antennas, which, used as an interferometer, synthesize the small-angle beam ($\leq$ 1 arcsec) of a km-sized antenna. With interferometric imaging, a Goldstone-VLA experiment provides latitudinal information unlike CW-Doppler which is its closest analogue. The interferometric reconstruction of images from the radio sky brightness avoids the north-south ambiguity of delay-Doppler imaging. While the images obtained by Goldstone-VLA experiments are generally of lower resolution than can be obtained with delay-Doppler, the full disk of the planet can be unambiguously imaged at once, which is not the case for the more "classical" technique.

The VLA is also well-suited to calibrated measurements of both circular polarization or even of the complete Stokes matrix. This has proved invaluable for the technique: Goldstone-VLA experiments have provided some exciting results. Titan was detected with the technique (Muhleman *et al.*, 1990), refuting the idea of a global hydrocarbon ocean on that Saturnian moon (Lunine *et al.*, 1983). Titan's radar response resembled that of EGC, suggesting that it too has an icy surface. Mars was observed, and it's austral residual cap was also found to exhibit the unique radar response of planetery ices (Muhleman *et al.*, 1991). When the technique was turned on Mercury, as mentioned above, ice deposits were also discovered (Slade *et al.*, 1992). Of course, the technique can be used to look at non-ice surfaces too. On Mars, a continent-sized region gave no echo at all, and was dubbed "Stealth" (Muhleman *et al.*, 1991). The techniques was used to probe Venus too (Tryka and Muhleman, 1992). Though only the SS channel provided useful information in the 1990 experiment, unique polarization behavior was discovered in highland regions. The Venus experiment was repeated in 1993 with both OS and SS results and is reported on here (and Haldemann *et al.*, 1997b).

1.3.3 SAR

SAR is well described by its name: Synthetic Aperture Radar. In a conceptual manner like the VLA's radiotelescope, a SAR system behaves as if it has a much larger antenna than it really has. Like the VLA it does this by coherently adding seperate samples of the echo from a given location. Unlike the VLA, an airborne or orbiting SAR's multiple antennas are in fact the same

antenna, just used sequentially at different points along the flight track. Like the delay-Doppler technique, locations on the observed surface are located by their Doppler shift and ranging information. SAR processing takes the ranging and Doppler information, and makes images. SAR avoids the ambiguity of the delay-Doppler technique by illuminating and looking at only one side of the flight track (see Figure 1.6). Further details regarding SAR processing can be found in Elachi (1987, 1988).

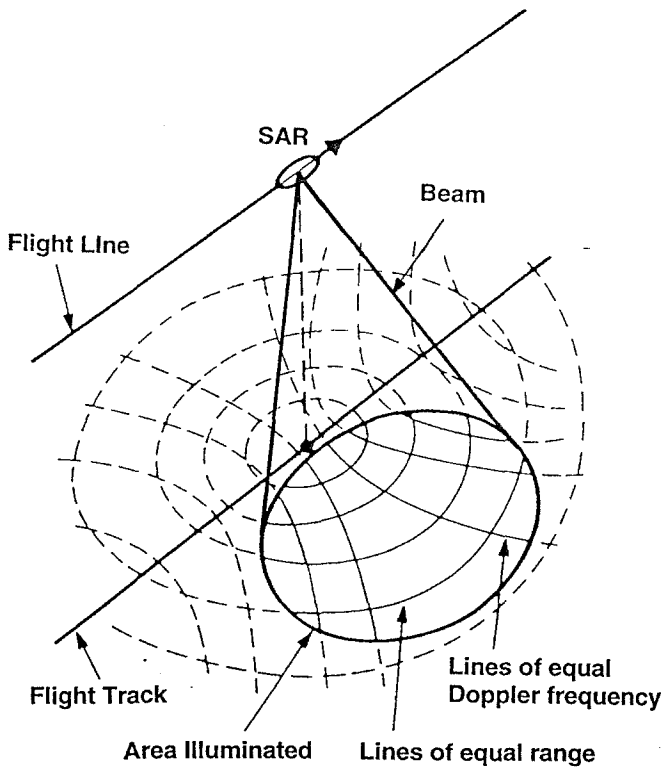

Figure 1.6 SAR range and doppler coordinate mapping onto terrain surface. Circles of equidistant range from the SAR platform intersect hyperbolas of equal Doppler shift caused by the motion of the platform. Ambiguity left and right of the flight track is avoided by illuminating and receiving from only one side of the track. After Elachi (1988), p.76.

SAR systems have been in development since the 1970's and several platforms are currently in orbit (ERS-1 and ERS-2 (Europe), JERS-1 (Japan), and Radarsat (Canada)). However all these platforms only make images with a single linear polarization transmitted and received. Full polarization SAR instruments have only been flown on aircraft (JPL's AIRSAR system), and recently on the Space Shuttle as the third Space Imaging Radar (SIR-C). It is these full polarization data that will be of the most interest to the planetar radar astronomy community. Full-pol data allow a reconstruction of the circular polarization response of terrain for comparison with OS and SS cross-sections measured for planetary targets.

1.4 Organization

This thesis is divided into thirds, one for each planet and the radar technique applied to study it. In each chapter a more detailed introduction reviews the nature of the particular questions that are addressed.

Chapter 2 covers the analysis of Martian delay-Doppler and Doppler-only (CW) radar tracks measured during the planet's 1995 opposition. The analysis was carried out in aid of the landing site selection process for Mars Pathfinder (Golombek, 1997). Dual circular-polarization was measured for the CW portion only, and was analyzed by David Mitchell. The author analyzed the delay-Doppler data which was recorded in only the SS channel. This chapter represents applied planetary science. The state of the art in "classical" planetary radar astronomy

predicts what surface roughness will be encountered by the Pathfinder lander and its rover Sojourner at a given site (see Fig. 1.2) Ares Vallis, Tritonis Lacus and Northwest Isidis sites were all found to be appropriate by this measure. The radar ranging provides regional topographic information that is also invaluable for the lander's arrival on Mars. Further, in the larger context of the choice of Ares Vallis as Pathfinder's prime landing site, many different remote sensing tools were brought to bear. The analysis of the radar results was more fruitful because it not only could be, but needed to be fit into the context of regional geomorphology and geology. Chapter 2 has been published as Haldemann et al. (1997a).

Chapter 3 reports the observation of Venus with the Goldstone-VLA technique during the 1993 inferior conjunction. At that time the sub-radar latitude on Venus was around 300°E. The dual circular-polarization information collected for the highlands at 285°E addresses the nature of altitude-related high-reflectivity/low-emissivity radar anomalies observed by single-polarization radars from Earth and on the Magellan spacecraft. The altitude behavior of the radar response is clearly observed, as is the regional variability. As it happens however, the added polarization information is still insufficient to determine whether surface- or volume- scattering is the dominant mechanism responsible for this unusual Venusian terrain. Thus, conclusions regarding the surficial processes remain indeterminate beyond the clear implication from the altitude-correlation that a temperature-related phase-change behavior is responsible. Chapter 3 comprises Haldemann et al. (1997b).

Chapter 4 presents the study of full-polarization SIR-C observations of high-elevation ice deposits on the Earth. Rignot et al. (1993) observed a unique radar response, similar to EGC, in the percolation facies of the Greenland ice sheet. The structures embedded in the ice that appear responsible for the volume scattering producing the characteristic response are due to liquid water from the previous season's melt. In search of other terrestrial analogue sites for planetary ices, and lacking full polarization radar data for Antarctic blue ice fields, candidate high altitude locations were selected. The search has proven fruitful, and unique ice radar behavior has been discovered. The nature of the snow and ice producing the features is discussed in Chapter 4. The observed radar properties are compared with existing observations and models, which prove inconclusive in determining the nature of the icy terrain. More useful are comparisons with visible datasets and ground truth from researchers familiar with the sites. It appears that distinct climates at the various locales are responsible for several morphologies that mimic the radar response of planetary ices. These may include the percolation facies like in Greenland, but additionally, crevasse zones and radiation-dominated evaporation structures appear to play a role.

Chapter 5 summarizes and concludes. Circular-polarization planetary radar astronomy is reviewed in the context of the results of this thesis. Directions for future investigation are presented and examined.

1.5 Themes

With three different planets, three different techniques and three different target terrain types, there are nonetheless common themes that run through this thesis. The overarching, specific theme of this thesis is the role of circular polarization for planetary radar experiments. Note circular polarization's strengths and limitations for infering the actual nature of a terrestrial planet surface in Chapters 3 and 4. In particular, the question of what kind of surfaces produce circular polarization ratio inversion was raised in this introduction, and will be re-examined for sites on Venus and the Earth.

The general topic of radar scattering by terrain introduced in Section 1.2 is the background refrain on which this thesis rests. Technical similarities among delay-Doppler, Goldstone-VLA and SAR, mentioned briefly in section 1.3, are a sub-theme. As another sub-theme, this thesis presents examples of the case for analyzing radar data in the context of other, separate data sets. Active radar remote-sensing techniques need not, and probably should not, be used in exclusion of visible, infra-red or other remote-sensing approaches.

Chapter 2

2 Mars Pathfinder Landing Site Assessment with Goldstone Delay-Doppler and CW Radar Experiments

2.1 Introduction

We present results of 3.5-cm wavelength delay-Doppler and Doppler-only (continuous wave or CW) radar experiments carried out during Mars' most recent opposition in 1995, when the planet was at a distance of 0.6 AU from Earth. These data are used to assess the various landing sites proposed for Pathfinder. The potential landing sites surveyed here are Ares Vallis (32.8°W, 19.5°N), Tritonis Lacus (252.0°W, 20°N), and Northwestern Isidis Planitia (275.3 W, 18.2°N). These are the sites that remained after other site selection criteria had been considered as discussed by Golombek et al. (1997). The (rejected) Maja Valles landing site (52.0°W, 18°N), crater Valverde (55.8 W, 20.3 N), and the Viking Lander 1 (VL1) region are also examined to provide context for our results. The landing site footprint has an approximate east-west extent of 200 km (Golombek et al., 1997).

Planetary radar astronomy is an important, if not crucial tool for assessing the potential Pathfinder landing sites. Several of the various engineering

constraints on landing site selection (Golombek et al., 1997) can be addressed by ground-based radar experiments. The altitude range constraint for a proper entry, descent and landing sequence can be assessed from the kilometer-resolution topographic profiles provided by delay-Doppler measurements. The minimum surface reflectivity for proper radar altimeter function is clearly accessible to radar experimentation. Airbag puncture or abrasion and rover trafficability limitations can be assessed for a given site based on delay-Doppler and CW radar studies because these techniques probe surface roughness at scales of the order of tens of radar wavelengths, which correspond well to the scales that will affect the lander.

A similar radar assessment was carried out during the Viking landing site selection. At that time, Goldstone CW results with modest signal-to-noise ratio (SNR) over the Ares region were in part responsible for its rejection as a Viking landing site (Masursky and Crabill, 1976; Tyler et al., 1976; Downs et al., 1978; Simpson et al., 1978a). Upgrades to the Goldstone radar system since 1976 improve the SNR by about an order of magnitude.

Delay-Doppler and CW radar techniques are well known and are described in detail in several review articles (e.g., Ostro, 1993; Simpson et al., 1992), so we do not provide a general discussion of them here. In particular, Downs et al. (1975) performed experiments using techniques very similar to ours. In this paper we first briefly describe the parameters of our radar experiments. Second, we review our understanding of, and our assumptions about the radar scattering behavior of the Martian surface. Third, we describe the topographic results in the

landing site regions obtained from the delay-Doppler data. In the fourth section we analyze the surface scattering properties inferred from both the delay-Doppler and the CW experiments and consider their implications for landing site selection.

2.2 Radar Experiments

Twenty radar tracks on Mars were measured during the 1995 opposition in aid of the Pathfinder project. Delay-Doppler and CW experimental parameters are summarized in Table1.1. Details of the seven radar tracks that probe landing sites, including map coverage of the tracks on the planet, are given in Table 2.1 Each radar track corresponds to a series of transmit-and-receive (T/R) cycles of about 10 min each.

Table 2.1
Delay-Doppler and CW radar parameters

	Delay-Doppler	CW
Wavelength λ, cm	3.5	3.5
Frequency		
Bins	128	280
Bandwidth, Hz	2645.5	27,324
Resolution, Hz	20.67	97.7
Ranging:		
Code elements	63	--
Baud, μs	6	--
Sampling, μs	3	--

Several CW tracks were obtained, but only the one track listed in Table 2 actually crossed a landing ellipse: Ares Vallis. For each T/R cycle within that track, a circularly polarized signal was transmitted toward Mars, and echoes were received simultaneously in both senses of circular polarization. The opposite sense echo from the T/R cycle over Ares Vallis is shown in Figure 1.1. The central portion of the opposite sense echo is dominated by a specular "spike," which arises from single backreflections from surface elements that are smooth at all scales within about an order of magnitude of the wavelength. The specular spike moves in longitude as Mars rotates. Weaker echoes in both senses of circular polarization are received from the entire hemisphere facing the radar. Such echoes can arise from a variety of mechanisms including multiple reflections and near-surface scattering from wavelength-scale structures. The CW data were recorded with a frequency resolution of 97.7 Hz, corresponding to 24 km (0.4°) longitude resolution at that track's subradar latitude. Data were averaged from the T/R cycle in which the subradar point passed over Ares Vallis, which introduces a smear of 2.4° of longitude. A specular plus diffuse scattering model is fit to the averaged CW data, as described in the next section. We define the "specular CW footprint" to be the full-width at half maximum (FWHM) of the specular spike which corresponds to twice the rms slope within the footprint. The rms slope within the specular CW footprint containing the Ares Vallis landing site is 6.4° (Figure 2.2).

Table 2.2
Goldstone radar tracks for Pathfinder landing site assessment

1995 Radar Tracks					Landing Sites			
Date	Day of Year, (DOY)	Latitude, °N	Longitude Range, °W	T/R Cycles	Name	Location	T/R Cycle Set	Longitude Range, °W
				Delay-Doppler tracks				
Jan. 27	027	19.96	332--82	17	Ares Vallis	32.8°W, 19.5°N	9--11	20.3--46.2
					VL1 Region	48°W, 23°N	12--14	37.1--63.0
					Maja Valles	52.0°W, 18.0°N		
					Crater Valverde	55.8°W, 20.3°N	13--15	45.6--68.8
Jan. 29	029	19.79	319--45	11	Ares		9--11	23.6--48.3
Jan. 30	030	19.69	316--48	14	Ares		12--14	20.1--46.0
Feb. 8	039	18.87	216--325	20	Tritonis Lacus	252.0°W, 20.0°N	6--8	239.6--264.5
					NW Isidis	275.3°W, 18.2°N	10--12	261.6--286.5
Mar. 11	070	16.84	268--337	10	NW Isidis		1--3	266.1--294.0
Mar. 18	077	16.83	208--311	16	NW Isidis		10--12	264.1--292.0
				CW track				
Apr. 17	107	18.7	317--43	10	Ares		9	30.9 -- 34.6

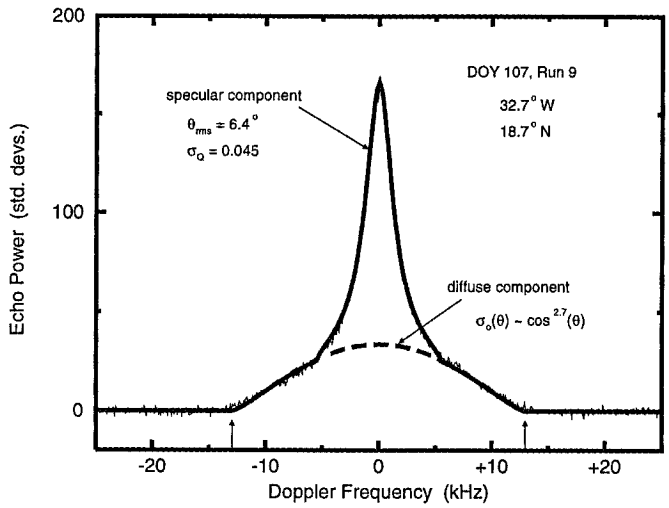

Figure 2.1 CW spectrum and composite scattering model fit for the Ares Vallis landing site. The specular "spike" sits atop the diffuse component. The units of the ordinate (radar cross section) are plotted in standard deviation units relative to the noise level. The limb-to-limb bandwidth of Mars (27 kHz as shown by the arrows) is covered by the diffuse portion of the echo, while the specular portion is only sensitive to a region near the subradar point.

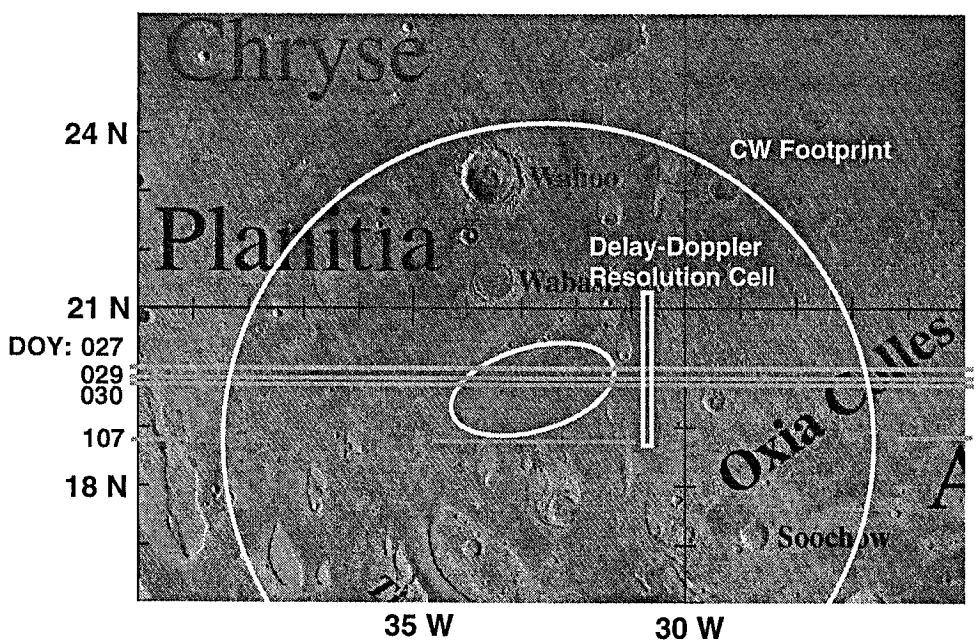

Figure 2.2 Viking composite image showing the Ares Vallis landing ellipse centered at 32.8°W, 19.5°N. The locations of the three delay-Doppler and one CW radar track through the region are shown. See Table 2 for radar track parameters. The 1 baud delay-Doppler resolution cell is shown and can be compared to the CW specular footprint, defined in the text.

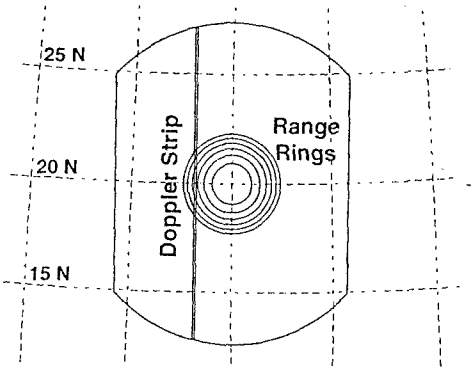

Figure 2.3 Diagram of geographic delay-Doppler frequency strip (N-S) and range ring coverage for a single set of range-gated spectra of a radar track at 20°N. The frequency and range parameters are those of Table 1. Only the first six range bins are depicted. The outermost envelope is the 63rd range ring, which is truncated in frequency by the 2.6-kHz Doppler bandwidth.

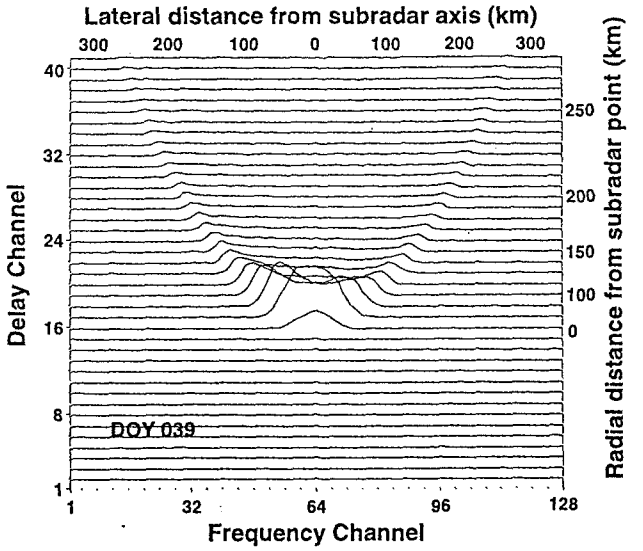

Figure 2.4 Example of a 20-s integration of delay-Doppler range-gated spectra. The 63 delay channels (not all of which are shown) are each a spectrum with 128 frequency channels. These spectra form an image from February 8, 1995 (DOY 039), over Isidis and show a very specular reflection within the first degree or so of the subradar point. Corresponding radial distance on Mars for the range rings, and lateral distance on Mars for the Doppler strips are shown for comparison.

The six delay-Doppler tracks used a repetitive binary phase code of 63 elements to modulate the 3.5-cm carrier wave. A code element's duration (baud) is 6 μs. This range code is periodic in 0.378 ms, and the planet is 22.6 ms deep, so the data are aliased approximately 60 times in range. However, the specular "spike" is largely confined to the first code length and is much stronger than the sum of the aliased power for all the regions we discuss here. Thus the alias power appears as an apparent noise source. This means we slightly underestimate our cross sections, but by no more than a few percent. The effective range resolution would normally be about 2/3 baud, but since we oversample in range by a factor of 2, we get a pixel range resolution of just one half baud, 3 μs (450 m). The ranging information from the delay-Doppler allows us to restrict our information to the nearest vicinity of the radar tracks. The delay-Doppler sampling bandwidth (BW) is the reciprocal of the period of the code, so BW=2.645 kHz. This frequency space was resolved into 128 frequency bins using a fast Fourier transform (FFT) giving a resolution of 20.7 Hz per bin, corresponding to a longitude resolution of 5.1 km (0.09°). This is a similar configuration to that used by Downs et al. (1975). The delay-Doppler BW corresponds to a total longitude extent of ±6°. The geographic coverage of a delay-Doppler sample at 20°N in both Doppler frequency and time delay (Table 1) is shown in Figure 2.3. An FFT of a full set (128) of complex range samples is produced, and the magnitude squared of the individual complex samples is formed to make a power spectrum about every 0.05 s. We add 103 power spectra together to produce a raw "image" every

4.98 s. In processing each track, we further add together four raw images, producing a full delay-Doppler image with a 19.93-s integration time, which corresponds to a 4.5 km (0.08°) longitude smearing due to Mars' rotation. Combined with the frequency resolution, the smearing produces a longitude resolution cell width of 9.6 km (0.17°). A typical image is shown in Figure 2.4.

Further data processing is carried out in preparation to fitting the summed data to a Hagfors scattering model. As Mars rotates, a point on the planet will sweep through the full Doppler BW. The data at all of the frequencies corresponding to a given longitude can be grouped together. This rebinning is crucial to our analysis, as it provides us with a sampling of radar cross section as a function of incidence angle for a fixed geographic location. Our fitting process is based on a least squares interpolation to a set of templates that assume a spherical planet and the resolving function of the radar. The templates are model power spectrum images produced for set values of the three parameters we wish to fit: range (R), reflectivity (ρ), and roughness (C). For ρ and C we assume a Hagfors scattering model. Our fitting algorithm is the following. First, for each image we make a rough fit of all parameters and then refine the fit of R to the first 10 baud or less. Second, we use this value of R to anchor a fit of ρ and C in the first baud of that longitude-specific image. This means that the scattering properties from the fit are those of a highly elongated rectangular pixel with longitude extent of 0.17° (9.6 km), and with latitude extent at most ±1.3° (±78 km) from the radar track. The true area which we are sensing does depend

somewhat on the scattering properties, with smoother surfaces producing echo power closer to the subradar track. The size of this pixel in comparison to the landing ellipse and the radar track extents is shown for the Ares site in Figure 2.2. We obtain statistical uncertainties on R, ρ, and C from the least squares fitting and report the three standard deviation uncertainties as our errors. In the case of R, fitting to single-longitude images reduces the uncertainty to less than 100 m. Data processing constraints limit us to processing only groups of three sequential T/R cycles at a time. The longitude coverage of the range-gated spectra allows us to interpolate scattering properties at longitudes not having nadir-illuminated data (gaps between transmit cycles). It should be noted at this point that a gain calibration error occurred on day of year (DOY) 027. It was discovered on DOY 029, and corrected at that time by switching receiver channels. We determined a multiplicative correction factor f by comparing the amplitudes in the two channels on DOY 029 (f=2.4±0.2), and applied it to the DOY 027 ρ fits. This introduced an additional source of uncertainty, which is included in the error bars.

2.3 Scattering Properties of the Martian Surface

We assume a Hagfors scattering model to obtain reflectivity and roughness estimates useful for landing site assessment. This requires both some explanation and some qualification. Briefly, the near-nadir, quasi-specular scattering properties of Mars are generally well fit by the Hagfors scattering model (Butler, 1994; Harmon and Ostro, 1985; Moore and Thompson, 1991; Simpson et al., 1992). This

is particularly true in the relatively smooth regions considered for Pathfinder landing sites.

The analytical form of the Hagfors model of quasi-specular differential radar cross section σ_o as a function of incidence angle θ is

$$\sigma_o(\theta) = \tfrac{1}{2}\,\rho\, C\,(\cos^4\theta + C\sin^2\theta)^{-3/2} \qquad (1)$$

where ρ is the reflectivity and $C=(\theta_{rms})^{-2}$ is the roughness parameter, related to an effective rms slope in radians, θ_{rms}. The Hagfors model assumes a gently undulating surface, and a Gaussian distribution of surface height deviations, where specular or mirror-like reflections provide the radar echo (Hagfors, 1964, 1966). We choose to use an exponential autocorrelation function in the Hagfors model because it is known to fit better than the Gaussian choice (Downs et al., 1975). The θ_{rms} is taken as a measure of slopes at all scales larger than 10 wavelengths but smaller than the footprint. Other scattering models based on Gaussian autocorrelation functions, or slightly different exponential autocorrelation functions exist (Muhleman, 1964) and are even in common use (Pettengill et al., 1991). We adopt the Hagfors model because our analysis is confined to the specular region of the radar echo, where the Hagfors model fits well for Mars, though Simpson et al. (1978b) caution against indiscriminate use. Furthermore, the Hagfors model was used for the Viking analyses (Masursky and Crabill, 1976; Tyler et al., 1976).

The Hagfors model assumes, as do all the other models, that the radar properties are homogeneous within the area probed and that the surface statistics are isotropic. McCollom and Jakosky (1993) show that the actual slope distributions for some regions of the Earth are not well described by the Hagfors model or other scattering models commonly used in planetary radar. Thus there is no guarantee that the θ_{rms} inferred here can be taken as absolute measures of the real slope distributions on Mars. Nevertheless, our results are still useful for comparative purposes.

Additionally, in choosing the Hagfors model, we are implicitly assuming that the radar echoes come from surface reflections, and therefore that all of the roughness probed by θ_{rms} is at the surface. However, if the radar is penetrating the surface, some of the contributing specular echo will be probing subsurface structure, and θ_{rms} would need to be considered as information of some form of "volume roughness." On Mars, which is dry and therefore has soil dielectric constants and conductivities much lower than the wet Earth, there is evidence from multiple wavelength studies that radar may be penetrating the surface up to tens of wavelengths (Harmon et al., 1992). For the purposes of landing site assessment it is appropriate to consider the worst case scenario for Pathfinder and Sojourner, i.e., that all roughness is at the surface. Thus we ignore the possibility of radar penetration into the soil.

The CW experiment probes regions beyond the specular spike and is thus analyzed with a composite model which combines the Hagfors model for the

specular spike with a "diffuse" scattering model with cosine dependence (Harmon and Ostro, 1985):

$$\sigma_o(\theta) = \tfrac{1}{2}\,\rho\, C\,(\cos^4\theta + C\sin^2\theta)^{-3/2} + A\cos^n\theta \qquad (2)$$

Here again, we choose this technique for reasons of comparison because we are primarily concerned with the specular region of the echo. The cosine term is empirical and is used because it provides a good match to the observed diffuse echo shape in many cases (e.g., Butler, 1994; Harmon and Ostro, 1985). Like ρ and C, the cosine exponent n is determined by a fit to the data. The physical process governing the diffuse echo is not understood, and so the relationship between n and wavelength-scale surface roughness is unclear. A better assessment of wavelength-scale roughness is given by the circular polarization ratio (Harmon et al., 1982)

$$\mu_c = \sigma_{SC}/\sigma_{OC} \qquad (3)$$

where σ_{OC} is the total radar cross section in the circular polarization opposite to transmitted sense (OC). The σ_{OC} is the integral of equation (2) over all θ and is made up of quasi-specular and diffuse components (Harmon et al., 1982):

$$\sigma_{OC} = \sigma_Q + \sigma_D \qquad (4)$$

In (3), σ_{SC} is the cross section in the same sense of circular (SC) polarization as transmitted. A rougher surface on Mars has μ_c closer to unity (Tharsis region (Harmon and Ostro, 1985)), while a more common value on Mars is 0.2.

2.4 Results: Regional Topography at the Landing Sites

The delay-Doppler data provide topographic information on the landing sites, independent of Hagfors fits. The locations of the delay-Doppler tracks listed in Table 2 relative to the various proposed landing sites, are shown in Figure 2.5.

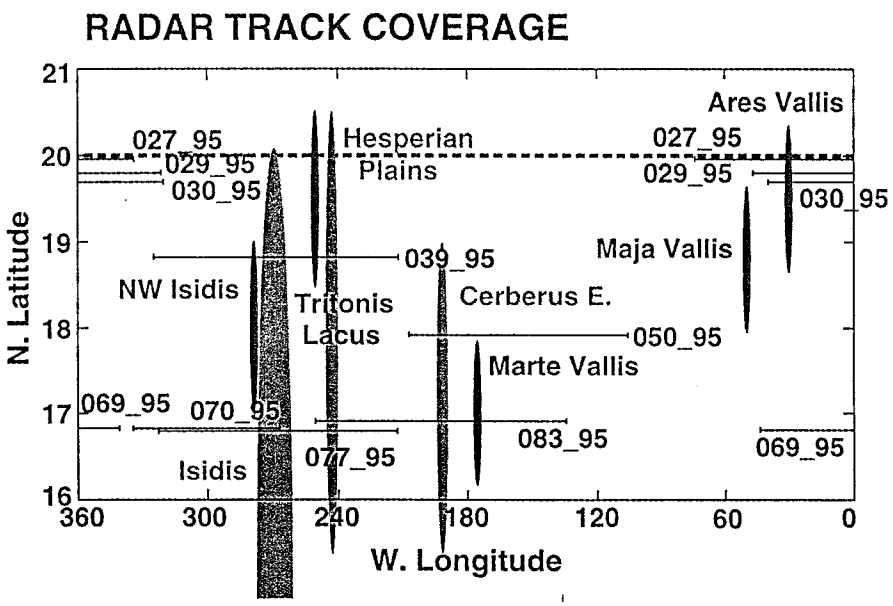

Figure 2.5 Schematic plot of the geographic coverage of the delay-Doppler radar tracks, labeled in DOY. Some additional tracks not considered in this paper are also shown. The dark grey ellipses are landing ellipses. Their shape and apparent directions are deformed by the longitude/latitude scale used. The light grey ellipses are nearby geographic regions shown for reference. The dashed line at 20°N indicates the insolation latitude limit for Pathfinder.

With the range information from the echo spectra, we can obtain elevation information referenced to our chosen ephemeris. We follow very closely the method of Goldspiel et al. (1993). To obtain elevation, the time residual range information, converted to distance, is added to the reference sphere of radius 3397.51 km used for data collection. The data were collected relative to the DE200 ephemeris; we convert the elevation to the recently released DE403 ephemeris for analysis. The basis for the interpretation is that the radar is sensitive to the highest, brightest location within the radar pixel.

Figure 2.6 shows elevation profiles that are obtained for the 15° of longitude around each site. The elevations are plotted in kilometers of planetary radius and are compared to the Mars digital topographic map (DTM) (U.S. Geological Survey (USGS), 1993), which was used for the initial elevation determinations of the landing sites. A second vertical axis of elevation relative to the 6-mbar level is provided, where the conversion is made relative to the areoid at the center longitude of each diagram. Smith and Zuber (1996) reanalyzed data used in the USGS DTM and point out that the DTM has an accuracy of only 1 to 3 km. Since our statistical uncertainty is much better than this, we present the DTMs for comparison only.

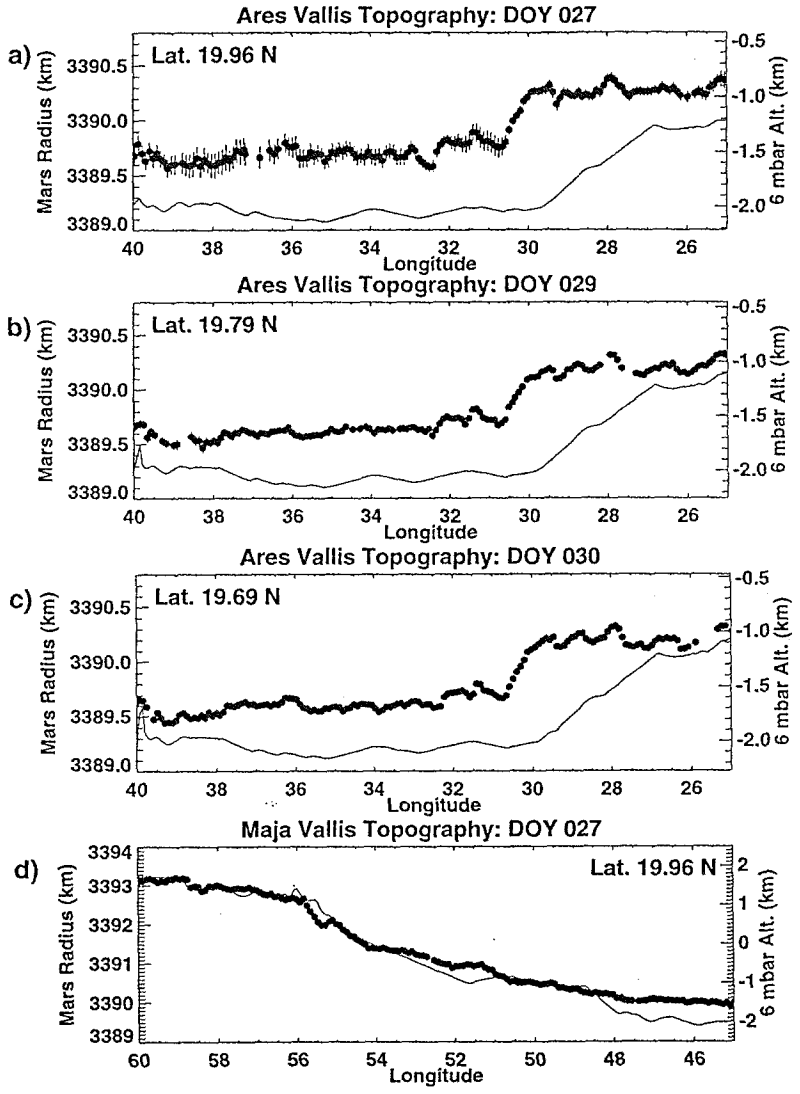

Figure 2.6 The elevation results for each of the landing sites and regions of interest. The elevations are plotted in kilometers of planetary radius on the left ordinate, and are compared to the Mars DTM (USGS, 1993). On the right ordinate the elevation relative to the 6-mbar datum is provided, where the conversion is made relative to the areoid evaluated at the center longitude of each diagram. (a) DOY 027, (b) 029, and (c) 030 radar tracks over Ares Vallis site. (d) DOY 027 track crossing VL1 region, north of Maja Valles site, and near Crater Valverde. (e) DOY 039 track over Tritonis Lacus site. (f) DOY 039, (g) 070, and (h) 077 tracks framing the NW Isidis site. Individual features are discussed in the text.

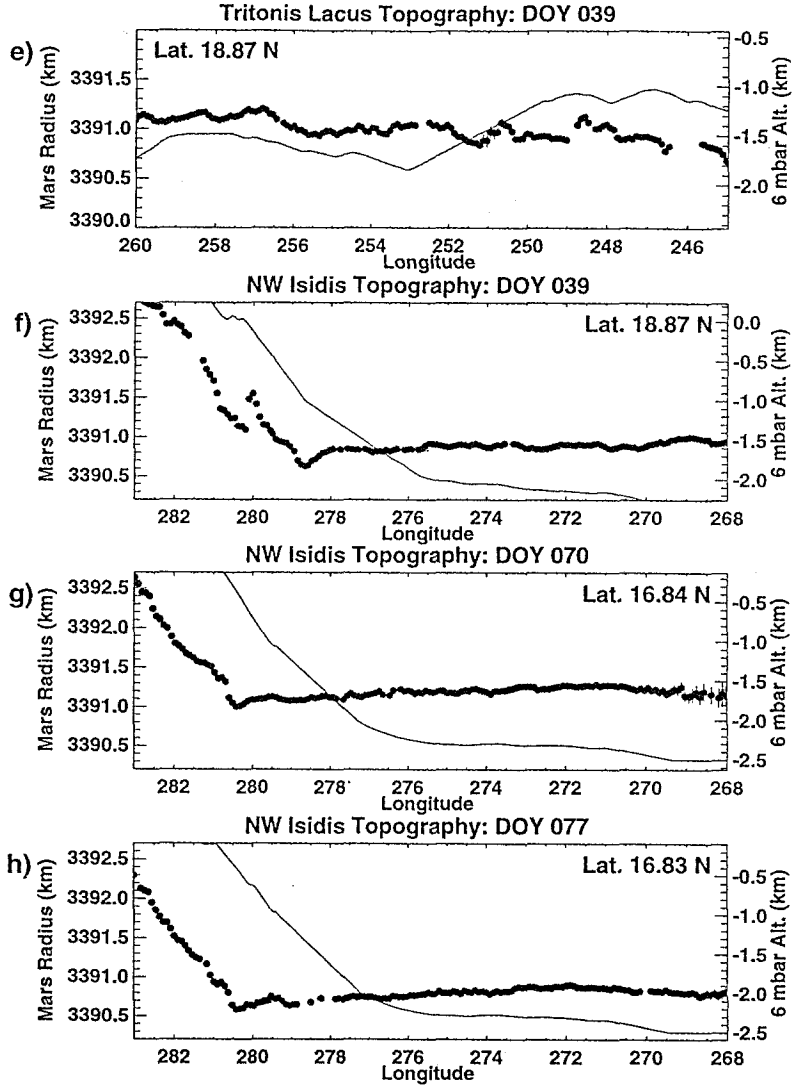

Figure 2.6 cont

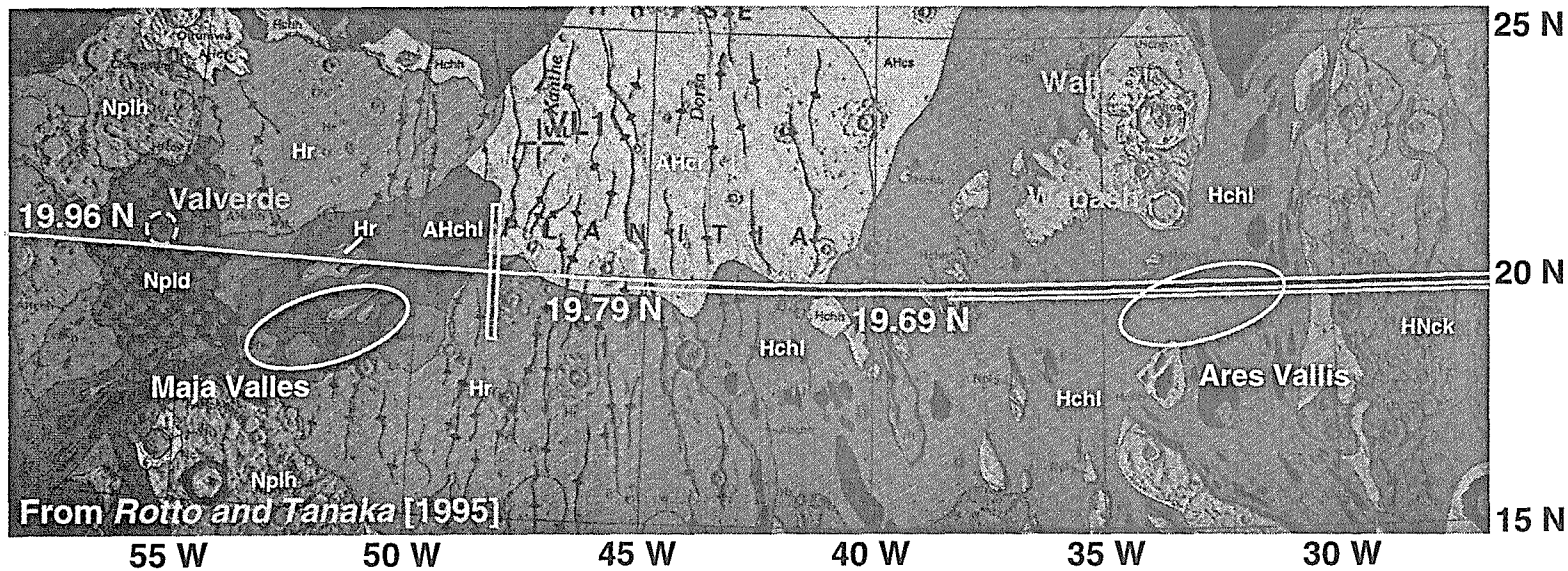

Figure 2.7

Excerpt from Rotto and Tanaka (1995) Geologic/geomorphologic map of the Chryse Planitia region of Mars framing the DOY 027, 029, and 030 delay-Doppler radar tracks near the Ares Vallis and the Maja Valles landing sites. Some of the map units of interest are Nplh, hilly unit (Noachian); Hr, younger ridged plains material (Hesperian); AHchl, younger lower channel floor (Amazonian-Hesperian); AHcr, subdued ridged unit. Other units are mentioned in the text. The delay-Doppler resolution cell is shown at 48°W.

Ares Vallis. Figures 2.6a, 2.6b, and 2.6c show the elevation results across the Ares Vallis landing site on DOY 027, 029, and 030, respectively. The three tracks are all within 0.3° (18 km) of latitude of one another, so we expect that all three should be very similar. Indeed they are and appear to track the same topographic profile from 25°W to 40°W. It is enlightening to consider these three profiles in conjunction with the regional geology, as shown in figure 2.7. The plateau from 25°W to 30°W follows the extent of the older knobby material unit (HNck) in the Rotto and Tanaka (1995) geologic map. The plateau is Oxia Colles (Figure 2.2) and has an additional topographic feature at 28°W interpreted as a wrinkle ridge in the geologic map. Moving west from the Oxia Colles scarp, the radar tracks move across the Hesperian channel units (Hchl), and all pick up the large streamlined islands within the channel, showing up to 200 m of relief. As the radar tracks pass across the landing ellipse at Ares Vallis, and west across more channel units into central Chryse, 200 m appears to be the maximum relief, and slopes appear small (<3°). In general, the elevation profile across the Ares site region makes sense in the geologic context.

Maja Valles region. The DOY 027 track crosses Chryse and climbs out of the basin on its western edge in 2 6d. This track passes 2.5° south of the VL1 site. The region of the track at VL1 longitudes (48°W) is fairly flat, with about 100 m of relief. The geologic context around the track in this region is shown in figure 2.7. The radar appears to pick up the ridged plains material (Hr) island in

the channel at 51.5°W, showing this feature with 300 m relief. This suggests that this track is not sensing the topography of the Maja Valles landing site, which lies south of the track. The profile also suggests that the Maja Valles channel has 1 km of relief from 50°W to 54°W, corresponding to a slope of 0.2°. Perhaps the most interesting feature on the DOY 027 track is Valverde Crater within Rotto and Tanaka's (1995) dissected unit (Npld). Valverde has 100-200 m ramparts and is about as deep. We will discuss this crater further in relation to its scattering properties. Along this part of the DOY 027 track the DTM profile is in better agreement with the elevation than in western Chryse, and the radar elevation profile is consistent with the geology.

Tritonis Lacus. The DOY 039 track passes south of the Tritonis Lacus landing site, tracing the elevation profile shown in Figure 2.6e. The landing site is on the border between a nobby plains material and a ridged plains material, as defined in the Greeley and Guest (1987) map. The track shows relief of up to 200 m in the region, but most of the topography is difficult to correlate with any features in the geology or photomosaics of the region. Two exceptions to this may be the topographic rises at 253°W and 257 W, which may correspond to compressional features noted by Greeley and Guest (1987). If the relief along this track is similar to that 1° of latitude further north, then the Tritonis Lacus site has relief similar to that at Ares Vallis.

NW Isidis. The tracks on DOY 039, 070, and 077 pass near the Isidis landing site, the first being north of the site, and the other two south of the site

(see Figure 2.5). The landing site itself lies in a region of the ridged member of the Vastitas Borealis formation, which is surrounded by smooth plains. The three tracks certainly show that the region is smooth on the kilometer to tens of kilometers scale: the total relief eastward of 279°W is less than 100 m in these plots, with regional slopes being <0.7°. However, the two southern tracks are not consistent. The DOY 077 trace is 400 m lower than on DOY 070. This is probably due to some intermittent measurement bias in the radar system, apparently of the order 1 baud, which we have not been able to correct. Goldspiel et al. (1993) observed similar discrepancies. This suggests that our overall elevation uncertainty for all tracks may still be 300-400 m, while our relative uncertainty along a track is represented by the small error bars in 2.6. This does not alter the fact that the landing site at Isidis appears extremely attractive from elevation considerations (Golombek et al., 1997).

2.5 Results: Scattering Properties at the Landing Sites

2.5.1 Ares Vallis CW

The CW results provide regional information for Ares. The OC CW spectrum for all the data at 32.7°W and 18.7°N, corresponding to the middle of the track shown in 2.2, is plotted in Figure 2.1. The best fit of the composite scattering law, equation (2), is shown as well. The largest scale information is from the diffuse component of the OC echo described by (2), and from the SC echo. The integrated diffuse component cross section is σ_D=0.055, and the diffuse

component cosine exponent in (2) is n=2.7. The result of the fit to the specular component is C=85±15 (θ_{rms}=6.4°±0.6°) and σ_Q=0.045. The total OC cross section is thus σ_{OC}=0.100. The total SC cross section for the same location is σ_{SC}=0.019, making μ_c=0.19. This is a reasonable result for the Martian hemisphere observed (Harmon and Ostro, 1985; Butler, 1994). The specular OC echo is probing the restricted region of the CW footprint shown in Figure 2.2. In general, it is expected that θ_{rms} will increase with decreasing wavelength. Thus our OC result is consistent with the CW results of Simpson et al. (1978a), who found θ_{rms}=5°±1° with 12.6-cm radar at 30°-35°W and 17°N. Our value of θ_{rms} represents a large portion of southern Chryse. With the delay-Doppler results, we can confine our analyses to the more immediate vicinity of the Ares landing site.

2.5.2 Delay-Doppler

We fit to images along the delay-Doppler radar tracks every 0.09° of longitude. The Hagfors C parameters from the fits are converted to θ_{rms}, and are shown in Figure 2.8 for the 15° of longitude around each of the sites of interest. The results are plotted with their 3σ fitting uncertainties. The ρ results are plotted versus longitude in Figure 2.9. We note that in the fitting process the range solutions are uncorrelated with the scattering results; however, as can be seen in Figures 2.8 and 2.9, ρ is strongly correlated with θ_{rms} for all the sites with the exception of NW Isidis. This effect is present in the data of Downs et al. (1975, 1978). It may represent an inability of the Hagfors model to adequately represent

the data, and/or it may be a consequence of our truncation of the measurements beyond 6° incidence angle for the model.

Since the purpose of this analysis is landing site assessment, we also carry out a statistical assessment of all the data associated with each site. The means and standard deviations of the data along each radar track and within ±0.9° (±50 km), ±1.8° (±100 km), and ±2.7 (±150 km) of the site center longitude are summarized in Table 3. For each of the four landing sites, we also examine the distribution of scattering parameters within ±1.8° of the site longitude. We combine all the results for a given landing site and plot histograms of θ_{rms} and ρ. This 3.6° along-track coverage corresponds approximately to the east-west extent of the landing ellipse (Golombek et al., 1997). The histograms for θ_{rms} are shown in Figure 2.10, and those for ρ are shown in Figure 2.11.

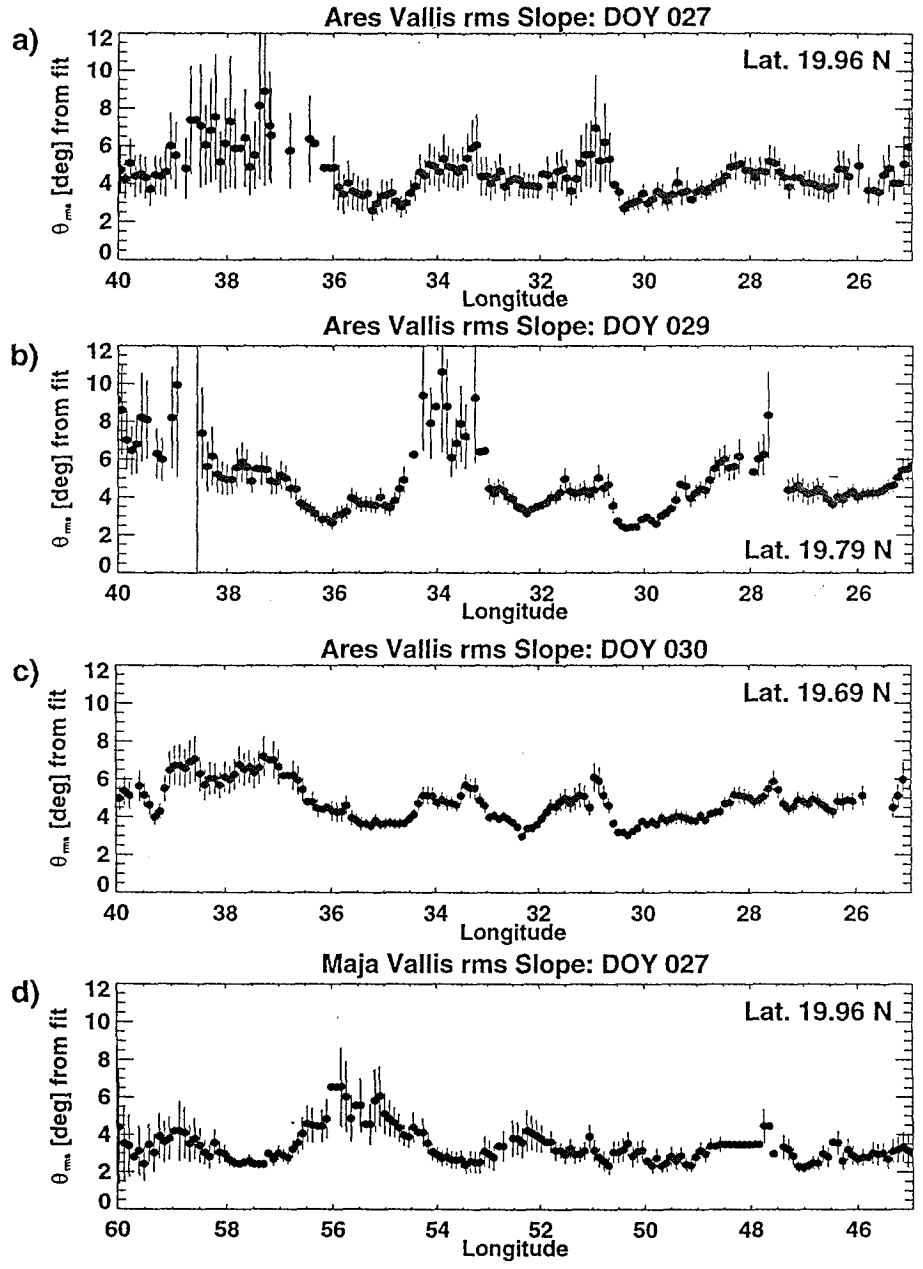

Figure 2.8 The rms slope (θ_{rms}) results for each of the landing sites and regions of interest. The individual plots are for the same radar tracks and locations as in Figure 2.6. Figure continued on next page.

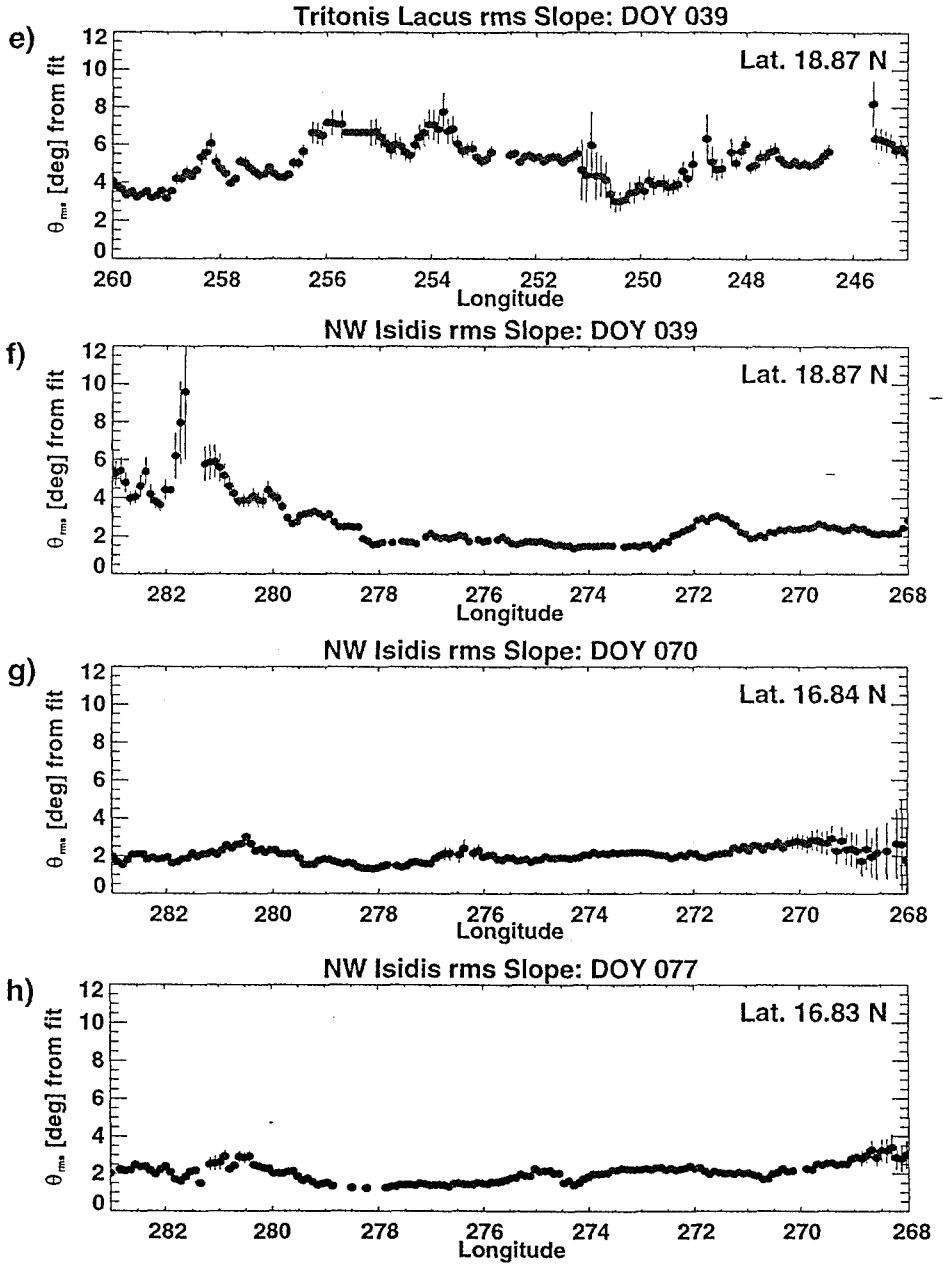

Figure 2.8 cont.

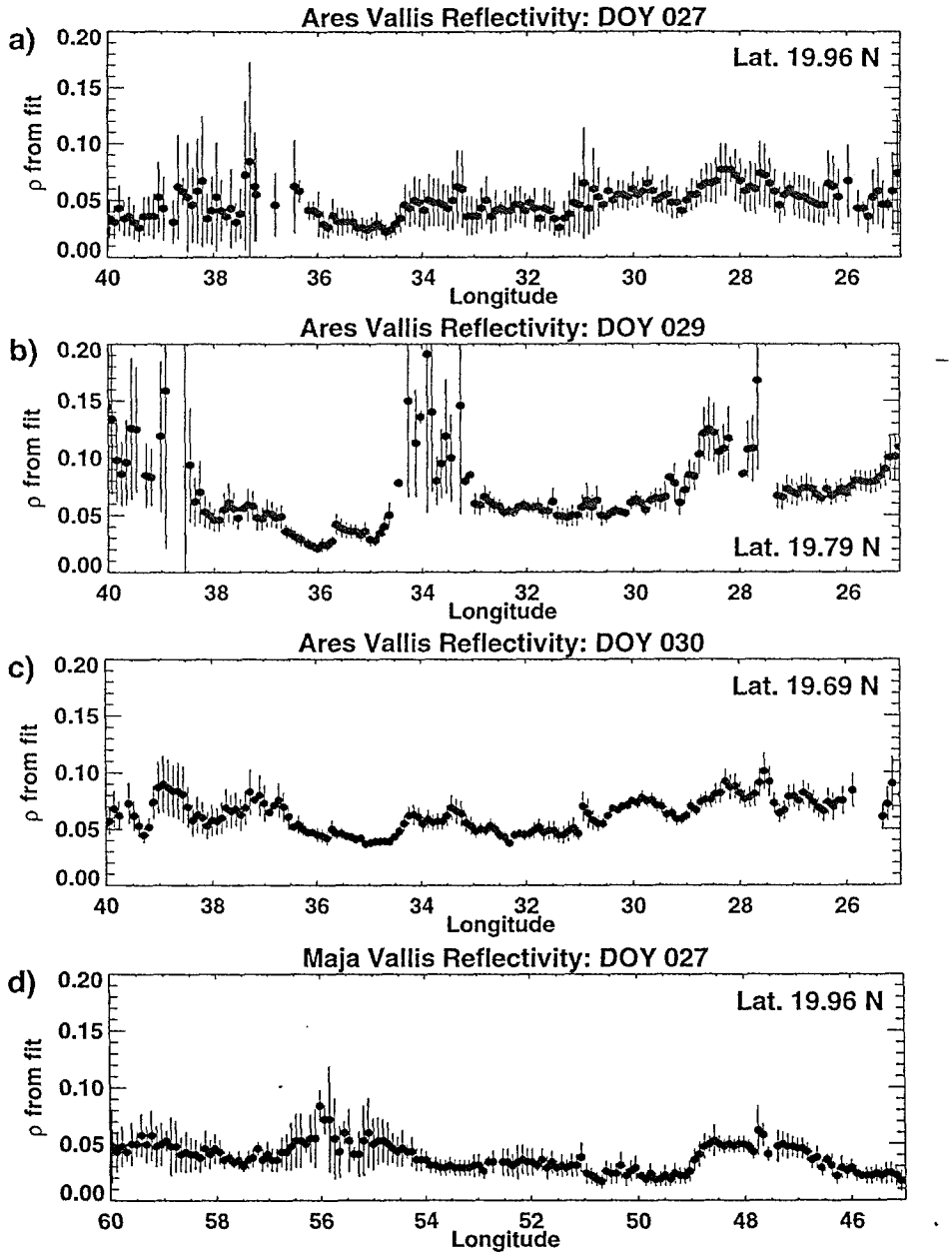

Figure 2.9 Reflectivity (ρ) results for each of the landing sites and regions of interest. The individual plots correspond to those in Figures 2.6 and 2.8. Figure continued on next page.

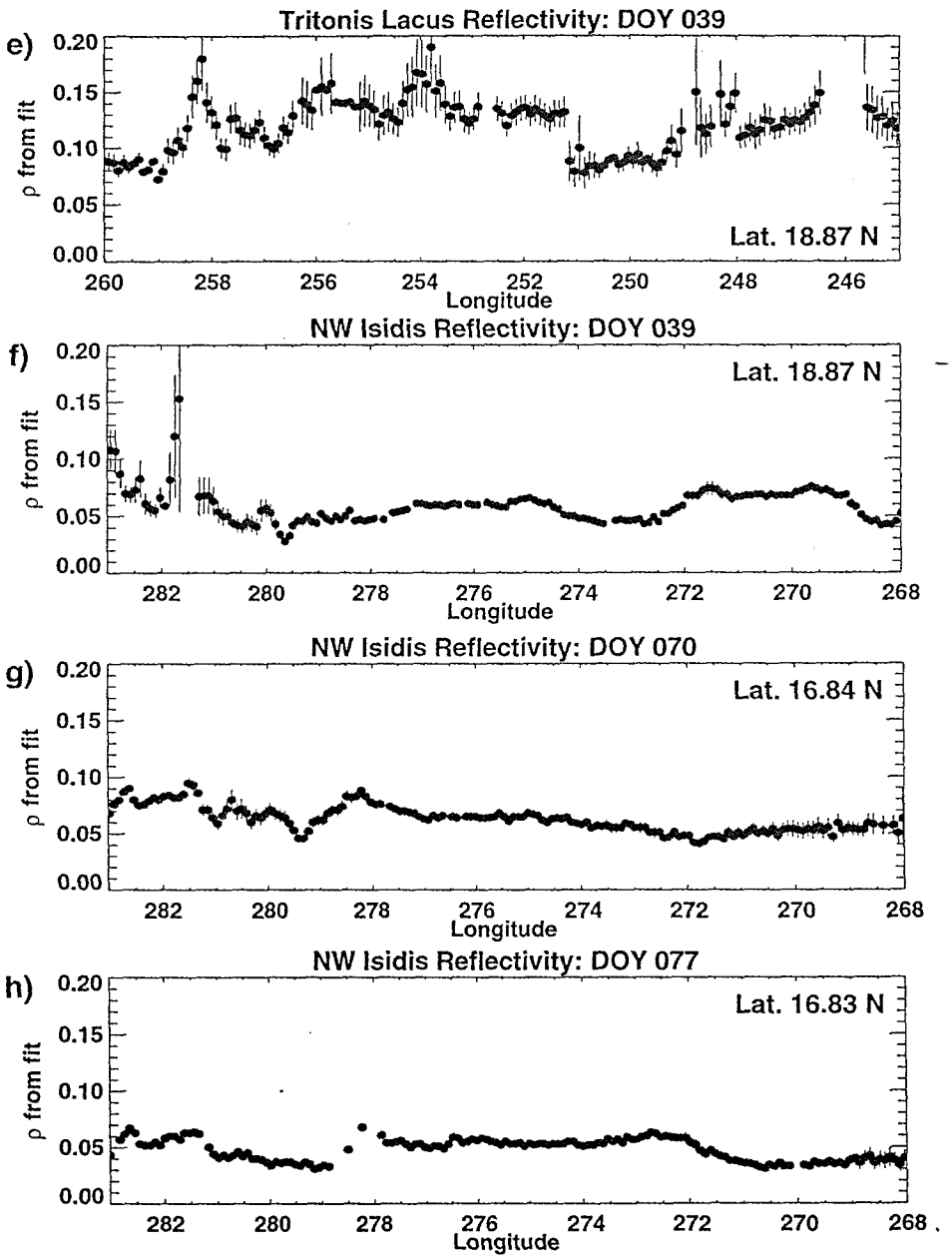

Figure 2.9 cont.

Table 2.3
Mean scattering properties along the radar tracks centered at the longitudes of the landing sites and regions of interest

1995 DOY	Track	Location		East-West Extent for Averaging					
	Latitude, °N	Name	Longitude, °W	±50 km (1.8° extent)		±100 km (3.6° extent)		±150 km (5.4° extent)	
				θ_{rms}, deg	ρ	θ_{rms}, deg	ρ	θ_{rms}, deg	ρ
027	19.96	Ares	32.8	4.5 ± 0.6	0.04 ± 0.01	4.5 ± 0.6	0.04 ± 0.01	4.3 ± 0.9	0.04 ± 0.01
		VL1	48.0	3.4 ± 0.5	0.05 ± 0.01	3.1 ± 0.6	0.04 ± 0.01	3.0 ± 0.5	0.03 ± 0.02
		Maja	52.0	3.5 ± 0.4	0.03 ± 0.01	3.2 ± 0.5	0.03 ± 0.01	3.2 ± 0.5	0.03 ± 0.01
		Valverde	55.5	5.5 ± 0.6	0.06 ± 0.01	4.5 ± 1.0	0.05 ± 0.01	3.9 ± 1.0	0.05 ± 0.01
029	19.79	Ares	32.8	5.2 ± 1.8	0.08 ± 0.02	5.5 ± 2.4	0.08 ± 0.03	5.1 ± 2.0	0.07 ± 0.03
030	19.69	Ares	32.8	4.3 ± 0.8	0.05 ± 0.01	4.5 ± 0.7	0.05 ± 0.01	4.3 ± 0.7	0.05 ± 0.01
039	18.87	Tritonis	252.0	5.3 ± 0.2	0.13 ± 0.01	5.6 ± 0.6	0.14 ± 0.01	5.8 ± 0.9	0.14 ± 0.02
		Isidis	275.0	1.7 ± 0.3	0.06 ± 0.01	1.7 ± 0.2	0.06 ± 0.01	1.7 ± 0.2	0.06 ± 0.01
070	16.84	Isidis	275.0	1.9 ± 0.1	0.06 ± 0.01	2.0 ± 0.2	0.06 ± 0.01	1.9 ± 0.2	0.06 ± 0.01
077	16.83	Isidis	275.0	1.8 ± 0.3	0.05 ± 0.01	1.8 ± 0.3	0.05 ± 0.01	1.8 ± 0.4	0.05 ± 0.01

The uncertainties are the standard deviations of the unweighted means. The 3.6° extent corresponds approximately to the E-W extent of the landing ellipse (Golombek et al. 1997).

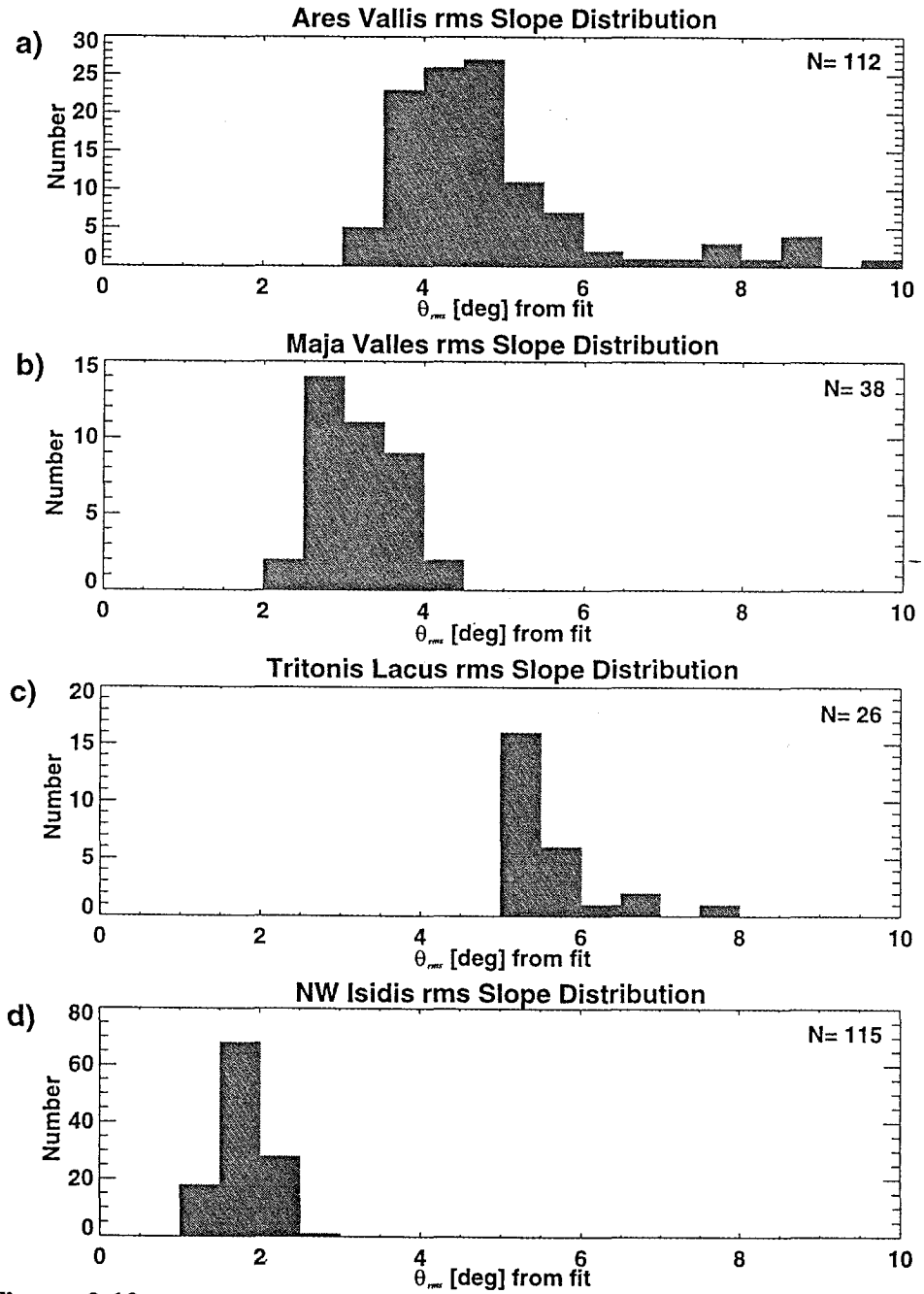

Figure 2.10

The θ_{rms} results for each of the landing sites and regions of interest, binned in 0.5° intervals and plotted as histograms. (a) All results (DOYs 027, 029 and 030) for the Ares Vallis landing site. (b) DOY 027 results along the radar track north of the Maja Valles landing ellipse, and within the Maja Valles Channel. (c) DOY 039 results along the radar track south of the Tritonis Lacus landing ellipses. (d) all results (DOY 039, 070, and 077) for the NW Isidis landing site. The means of these histograms are mentioned in the text.

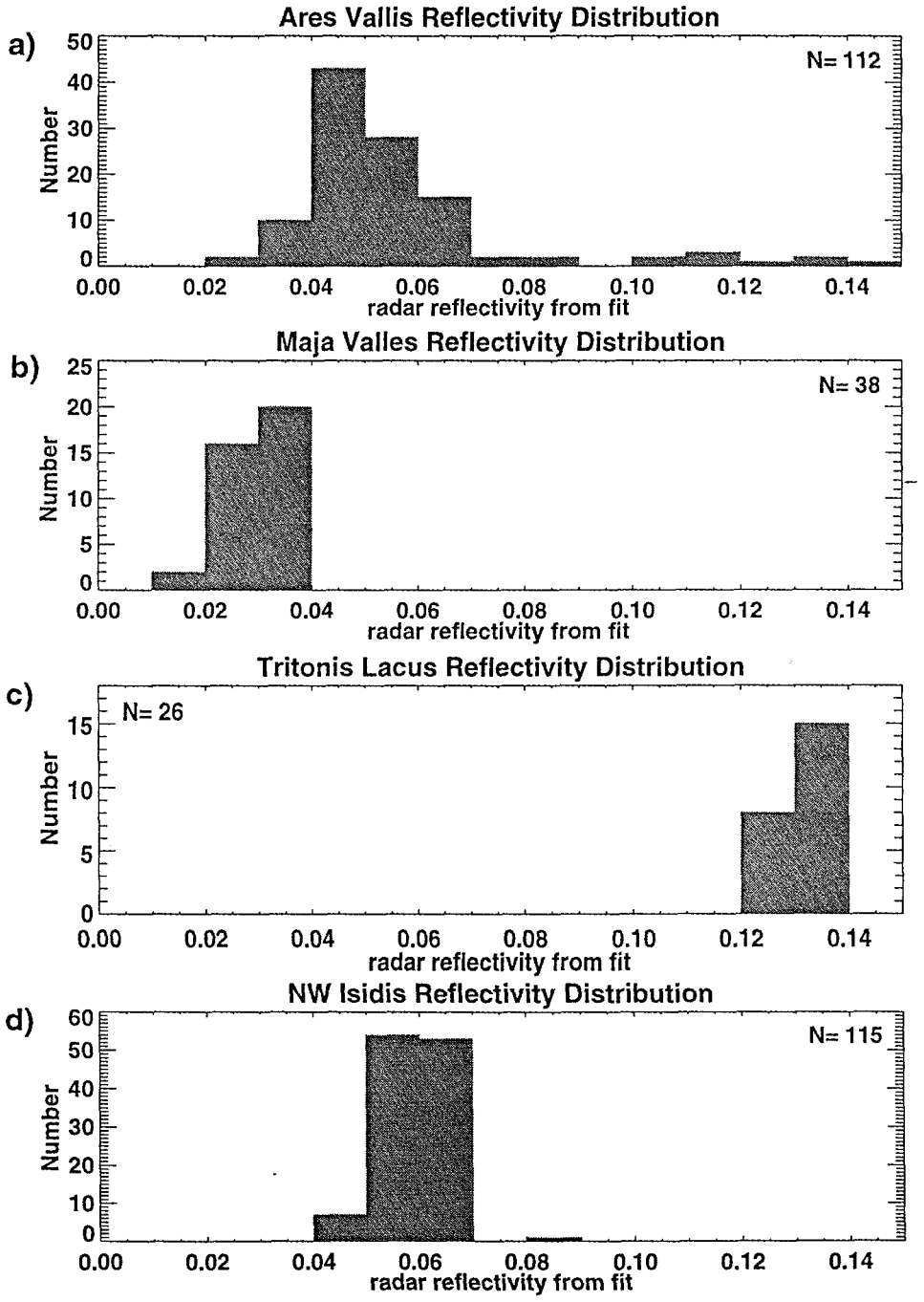

Figure 2.11 The ρ results for each of the landing sites and regions of interest, binned in 1% intervals and plotted as histograms, as in Figure 2.9.

Valverde crater. To aid interpretation of the numerical results, we have included the DOY 027 coverage of crater Valverde. Crater Valverde (35 km diameter) is a major part of Rotto and Tanaka's (1995) dissected unit comprising cratered material altered by ground-water sapping or runoff. The unit as a whole does appear rougher than the adjacent channel floor material and younger ridged plains material. However, when Valverde itself is fully within the delay-Doppler pixel, the scattering parameters are more extreme still. The rims of the crater, as determined by the ranging data (Figure 2.6d) have θ_{rms} =6° (Figure 7d), and ρ=0.06 (Figure 2.9d).

VL1. Another location that provides some comparative numbers is the region at 47.5°W, south of VL1. Here ρ=0.05 (Figure 2.9d), and θ_{rms}=4° (Figure 2.8d). We note that the θ_{rms} fits immediately around 48°W are fixed, and underestimate the roughness because a stable fit cannot be found for a higher value of θ_{rms}. The θ_{rms} and ρ enhancement at this longitude may be due to the crater at 48°W, south of the track on the Rotto and Tanaka (1995) map. More representative numbers may be those to the east, ρ=0.03 and θ_{rms}=3°, where the track crosses the subdued ridged unit (AHcr) in which VL1 is located. Our results can be compared with the 12.6-cm results of Tyler et al. (1976) and Simpson et al. (1978a), who reported θ_{rms}=6° at 23°N for the VL1 site region itself. Tyler et al. (1976) point out that roughness at 3.5 cm was observed to increase toward the north in Chryse, so our observations are in line with the earlier data.

Ares Vallis. The θ_{rms} values of the three delay-Doppler tracks over the Ares landing site on DOYs 027, 029, and 030 all show similar features. The DOY 029 fits were less successful, and the results are noisier. The ρ values on DOY 027 are still generally lower than the other two days, which perhaps indicates that we were not able to fully compensate a posteriori for the poor receiver channel. The average parameters for all the Ares Vallis tracks (Figures 2.10a, 2.11a) are θ_{rms} =4.8°±1.1° and ρ =0.06±0.02. These delay-Doppler results at Ares are just consistent within the uncertainties with our CW results, although θ_{rms} is much lower. This is not entirely surprising, since the CW footprint covers more streamlined islands, the large craters Wahoo and Wabash, which we expect are rougher than their surroundings, and goes farther north into rougher central Chryse. The high value tail on the Ares histograms is due to the poor fits on DOY 029. Also, the more extreme values of θ_{rms} and ρ included in the histogram are at the eastern and western edges of the Ares landing ellipse.

Our results reflect the many different features in the Ares Vallis region of southern Chryse. From 25°W to 31°W, θ_{rms} is around 4°. Between 27.5°W and 28.5°W θ_{rms} increases somewhat, as does ρ. This seems associated with the wrinkle ridge noted at this longitude in the topographic data, as well as in figure 2.7 The θ_{rms} has a clear minimum at 30.5°W in the channel, and rises abruptly to 5°-6° over the streamlined islands. The θ_{rms} is at 4° again at the center of the landing site, while ρ remains around 0.05. Both ρ and θ_{rms} rise again around 34°W, the longitude of Wabash crater whose south rim and ejecta probably lie

within our pixel. Still further west, after a dip in both ρ and θ_{rms} at the Tiu Vallis channel, the values rise again, associated perhaps with the scabby terrain to the west of the Ares site.

Maja Valles. The results for Maja Valles are shown in Figures 2.8d and 2.9d, and in histogram form in Figures 2.10b and 2.11b. The DOY 027 track passes north of the proposed landing site in Maja Valles. The average scattering parameters for the site, given in Table 2.3, are $\theta_{rms}=3.2°\pm0.5°$ and $\rho=0.03\pm0.01$. The θ_{rms} values in the Maja Valles channel bed are similar to or smoother than those in the Ares channel at 30.5°W. The ρ values are lower, indicating perhaps that the Maja channel has lower density soil, by virtue of more dust perhaps, than the channel east of the Ares landing ellipse. It does appear that the scattering parameters of channel units in Chryse are similar.

Tritonis Lacus and NW Isidis. The results at Tritonis Lacus have slightly higher θ_{rms} than those in Ares, while ρ values are much higher. At Isidis all three tracks show a rather flat surface with $\theta_{rms}\approx2°$, and ρ similar to that at Ares. The overall averages for Tritonis are $\theta_{rms}=5.6°\pm0.6°$ and $\rho=0.14\pm0.01$ (Figures2.10c, 2.11c), while for Isidis $\theta_{rms}=1.8°\pm0.2°$ and $\rho=0.06\pm0.01$ (Figures 2.10d, 2.11d). The reflectivities on the DOY 039 track at Isidis are consistent with the two tracks south of the Isidis site, so the elevated values of ρ at Tritonis are probably correct inasmuch as the Hagfors model can be applied there. The reflectivities at Tritonis may be suggesting that there is a more compact soil surface producing the higher

reflectivity or, alternately, that both Ares and Isidis have somewhat less dense soils or more dust, thereby reducing their reflectivities.

Our DOY 039 track matches the location of the 12.6-cm results of Simpson et al. (1978a), and for Tritonis, we reproduce their θ_{rms} results very closely. However, for Isidis our θ_{rms} values are much lower. There are some differences in our Isidis tracks. We would expect this for a separation of 2°, as between the DOY 039 track and the other two; however, slight differences are evident between DOYs 070 and 077, which are geographically close. This is despite the fact that all three tracks seem to show that the region itself is fairly homogeneous in its radar properties. We suggest that the reason for this discrepancy lies in the fact that the region is so specular that the echo is heavily weighted toward the region of our pixel directly around the radar track. If this is the case, then a change of only 500 m in longitude could mean that we detect slightly different features.

2.6 Conclusion

Our results, where we have multiple tracks, are reasonably reproducible, and are comparable to previous results. The present results have better resolution than previous data in the regions observed and provide important input for the selection of Pathfinder's landing site.

We find that Ares Vallis has a Hagfors rms slope of $\theta_{rms}=4.8°\pm1.1°$ as measured by delay-Doppler radar, and $\theta_{rms}=6.4°\pm0.6°$ measured by CW radar. The

Tritonis Lacus landing site is rougher with θ_{rms}=5.6°±0.6°, while for NW Isidis, θ_{rms}=1.8°±0.2°. The topographic relief at all three of the retained Pathfinder landing sites, Ares, Tritonis Lacus, and Isidis are reasonable for Pathfinder's landing sequence. Isidis is by far the flattest, both at a regional scale (E-W slopes < 0.7°) and at scales of the order of tens of radar wavelengths and would seem to have the least obstacles for an airbag landing. The Ares site is somewhat less rough in a Hagfors sense than the rim of crater Valverde and is rougher than the region south of VL1. The similarity of our θ_{rms} values for Ares with those measured previously for the Viking site may suggest that a landing at Ares could expect to encounter surface roughness with spatial scales similar to those at VL1, and this is apparently allowable by the Pathfinder landing parameters. The roughness results for Tritonis Lacus appear to be similar in magnitude to those at Ares. All three of the landing sites would seem to have sufficient reflectivity and, when combined with the *C* parameters, sufficient radar cross section for the Pathfinder radar altimeter to function properly.

Finally, it should be possible to refine the radar ranging analysis to provide Pathfinder with a more precise topography for the chosen landing site, allowing a timed landing sequence should Pathfinder's radar altimeter malfunction. This would work best for the Ares site, where the DOY 027 radar track falls within the landing ellipse and can be tied to the VL1 topography which is known very well.

Chapter 3

3 The Western Hemisphere of Venus : 3.5cm Dual Circular-Polarization Radar Images

3.1 Introduction

With the notable exception of the Venera landers, the surface of Venus has been probed exclusively at radio wavelengths, with both passive and active sensors. Such observations allow significant progress in understanding the geologic context of the Venusian surface. Various regional tectonic regimes are apparent in the results of both spaceborne (e.g. Saunders *et al.* 1991), and Earth-based (Campbell and Campbell 1992, Senske *et al.* 1991a, 1991b, 1991c) radar observations. One of the remaining controversies after the Magellan mission is the nature of low emissivity, high reflectivity radar features, most of which are at high elevations. Are they evidence of high dielectric constant materials (Pettengill *et al.* 1988, Pettengill *et al.* 1996, Shepard *et al.* 1994), perhaps products of *in situ* alteration (Greeley *et al.* 1992, Klose *et al.* 1992)? Are these radar features produced by extreme roughness of the surface? Or are they produced by scatterers embedded in soil (Tryka and Muhleman 1992)? Perhaps some combination of the preceding models is closer to the answer. Our new results from Earth-based observation of Venus near inferior conjunction in 1993 have important

implications for the observed radar anomalies: wavelength-scale morphology is significant and correlates with altitude. We analyse our new multiple-polarization radar data in the context of the regional geology of Beta Regio in particular. The Magellan radar only provides linear polarization information, so our analysis is complementary to Magellan analyses of Beta Regio.

Some of the most exciting recent results from planetary radar observations---ice deposits at Mercury's poles for example (Slade *et al.* 1992)---have come from experiments obtaining multiple-polarization data. Multiple-polarization planetary radar experiments can be carried out with the Arecibo and Goldstone monostatic radars and with the bistatic Goldstone-VLA system used in this work. The latter avoids the north-south ambiguity implicit in Arecibo's single dish delay-Doppler observations by using the Very Large Array (VLA) radiotelescope to construct images interferometrically. The images simultaneously map both the right-circular polarization (RCP) and the left-circular polarization (LCP) backscatter from an illuminating RCP signal. We synonymously use the terms "same sense circular-polarization" (SS) and "opposite sense circular-polarization" (OS) when referring to the RCP and LCP echo images respectively. The images obtained reflect

(1) the regional variation of slope,

(2) the regional variation of wavelength-scale structural properties or roughness, and

(3) the regional variation of material electrical properties.

While (1) and, to some extent (2), are related to regional geologic and tectonic settings, (3), and also (2), are influenced by small-scale processes such as

weathering. An analysis of dual-polarization radar properties in a context of regional geology should allow inferences about (3) and (2).

Analysis of dual circular-polarization Goldstone-VLA images of terrestrial planets has been carried out for Mars (Butler 1994, Muhleman *et al.* 1991), and Mercury (Butler *et al.* 1993, Slade *et al.* 1992), and was reviewed by Muhleman *et al.* (1995). Tryka and Muhleman (1992) presented results from a Venus Goldstone-VLA experiment. Only their RCP map was useful as the LCP channel was dynamic-range-limited. Beta Regio was the prime target of our experiment to image Venus on two days in 1993. This paper continues with (i) a general description of the experiment, of data calibration, of processing, and of noise levels, (ii) a summary of the atmospheric correction used to produce radar albedo maps, (iii) a discussion of the implications of the maps in the context of the regional geology, in particular as regards Beta Regio, addressing the altitude dependence of radar properties. A glossary of relevant radar and geologic terminology is given in Appendix A. More details regarding (i) and (ii) are provided in Appendices B and C respectively.

3.2 Experiment

We transmitted a continuous-wave 3.5 cm RCP beam from the 70 m Deep Space Network (DSN) antenna at Goldstone, California. We collected the backscatter at the National Radio Astronomy Observatory, VLA in New Mexico, observing Venus as if it were a bright, spectral line radio source. We processed the interferometer data to produce images of sky brightness, initially in sky

coordinates of right ascension and declination. We converted the images to maps of radar albedo which can be examined in planetary coordinates. An overview of our experimental method is given in Butler *et al.* (1993), and a complete examination of interferometric imaging is given by Clark (1989), Sramek and Schwab (1989 and Cornwell and Braun (1989).

The orbital and planetary parameters of our Venus experiments on February 28, and March 4, 1993 are given in Table 3.1. During our experiment Venus was near inferior conjunction. This is required for sufficient signal-to-noise ratio with the best spatial resolution over as much of the planet as possible. Experimental constraints discussed in Appendix B led to our synthesized Gaussian beam sizes ($FWHM_b$) of 0.94 arcsec on February 28, and 0.70 arcsec on March 4. These correspond to sub-Earth resolutions of 280 km and 200 km on the first and second days, respectively. The calibration and processing of the raw data is discussed in Appendix B. After further self-calibration using the OS specular echo,

Table 3.1

Relevant observational parameters. *D*, distance to Venus from Earth in AU; ϕ_o, sub-earth latitude on Venus; β_o, sub-earth longitude; and *PA*, position angle of the north pole of Venus, measured east on the celestial sphere.

Date	*D* (AU)	ϕ_o (deg.)	β_o (deg.)	*PA* (deg.)
Feb. 28, 1993	0.402	-6.6	295.3 E	22.5
Mar. 4, 1993	0.376	-7.3	302.5 E	22.4

Table 3.2

Image quality parameters. t_{obs}, cumulative time for good radar visibilities. P_t transmitted power; $FWHM_b$, the full-width half-maximum diameter of the synthesized beam; pix. size is just the pixel size chosen for the FFT deconvolution and CLEANing; N_{OS}, the noise flux (measured off Venus) in the final OS 512^2 images; and N_{SS}, the noise flux in the final SS images. N_{OS} was strongly affected by the specular spike.

Date	t_{obs}	P_t (kW)	$FWHM_b$ (arcsec.)	pix. size (arcsec.)	N_{OS} (mJy/beam)	N_{SS} (mJy/beam)
02/28/93	1 hr. 24 min.	447	0.94	0.2	73.4	13.6
03/04/93	5 hr. 14 min.	410	0.70	0.2	78.3	5.9

the antenna response was deconvolved using the CLEAN algorithm to produce images. The image quality parameters discussed in Appendix B are given in Table 3.2. Figures 3. 1 and 3.2 show the images we obtain. Fig. 3.1A is the image of the SS echo on Feb. 28, and Fig. 3.1B is the simultaneous image of the OS echo. The better resolution on Mar. 4 is apparent in Figs.3. 2A and B which are the images of SS and OS echoes respectively, on that day. Snow in New Mexico on Feb. 28 doubled the noise level in the SS channel and images. The snow cut short our observing run degrading synthesized beam resolution. Projections of Magellan global altimetry to the observed hemisphere of Venus for Feb. 28 and Mar. 4, are shown in Figs. 3.3A and B. They are used to identify the features in the images. Fig. 3.4 is a mercator projection map, equivalent to those portions of Fig. 3.3B between 65N and 65S. It provides a longitude-latitude reference for the radar maps that follow.

3.3 Mapping Radar Cross-section

Notably in Figs.3.1 and 3.2, the limb of Venus cannot be seen. This is due to the atmospheric attenuation of our 3.5 cm radar signal: the two-way optical depth at the sub-radar point is of the order three! Thus, we never see the Maxwell region, and Alpha Regio is barely visible in only the Mar.4 SS echo image (Fig. 2A) at the 4 o'clock position.

We corrected for the attenuation (see Appendix 3) to make maps of 3.5 cm surface radar cross-sections. Pixel values less than $3N_{OS}$ or $3N_{SS}$ were ignored. The images were ratioed pixel by pixel to make maps of polarization ratio, $\mu_c = P_R(\mathrm{SS})/P_R(\mathrm{OS})$, where P_R is the actual flux density received per pixel in Jy/beam. As the atmospheric correction is the same in both polarizations, maps of μ_c were made prior to atmospheric correction. The atmospheric correction was applied to the noise-blanked, polarized images to produce corrected noise-blanked images of the expected flux density on the sky, F_R (units Jy/beam). F_R is related to P_R by the atmospheric correction factor in any pixel, $\alpha(x,y)$; $F_R = \alpha(x,y)P_R$. Now, F_R is also given by the radar equation

$$F_R = \frac{P_t A_t \Omega_b}{4\pi \lambda^2 D^2 \Delta f} \sigma(\theta_i) \qquad 3.1$$

(Butler *et al.* 1993), where P_t is the transmitted power, $_tA$ is the effective transmitter area, Ω_b is the effective resolution solid angle, D is the distance to

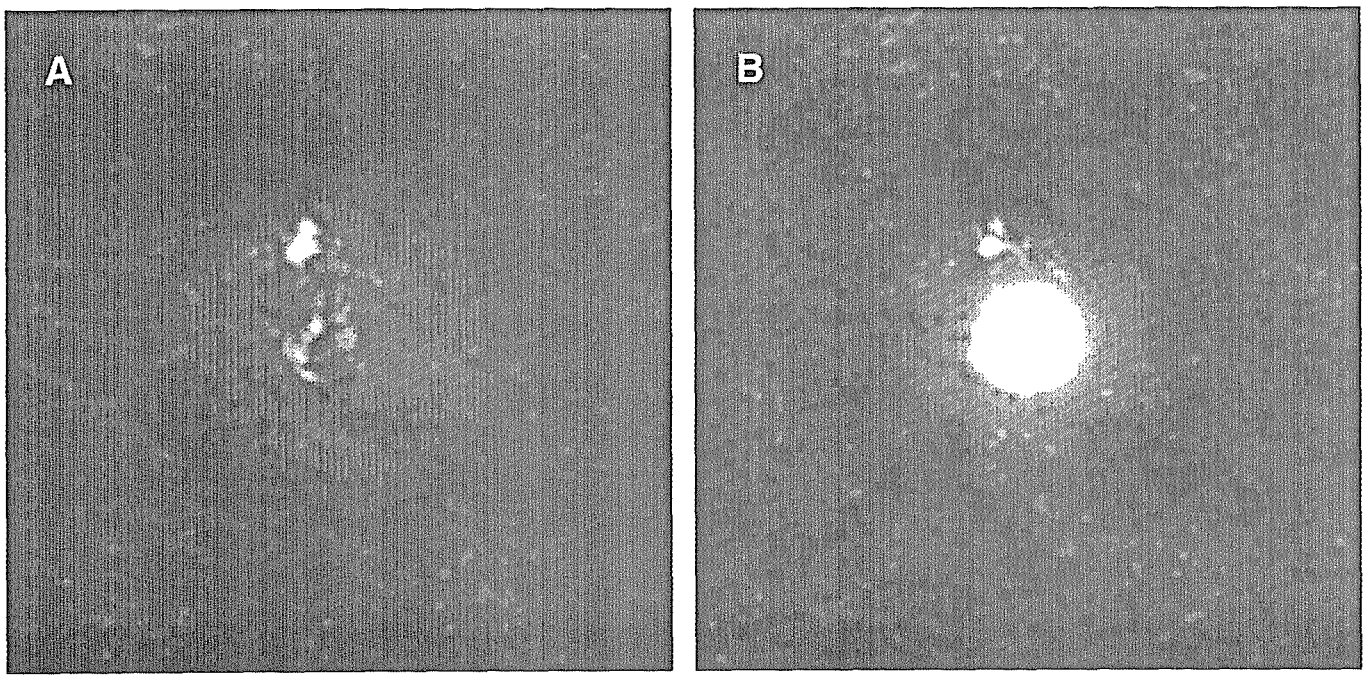

Figure 3.1 A) Image of the SS echo from Venus on Mar. 4, B) Image of the Venus OS echo on the same day. The resolution is equivalent to the synthesized gaussian beam of FWHM 0.70 arcsec diameter. The noise level in A) in particular is very good and Beta Regio appears clearly in the upper left of each image. See Fig. 3 for identification of other features.

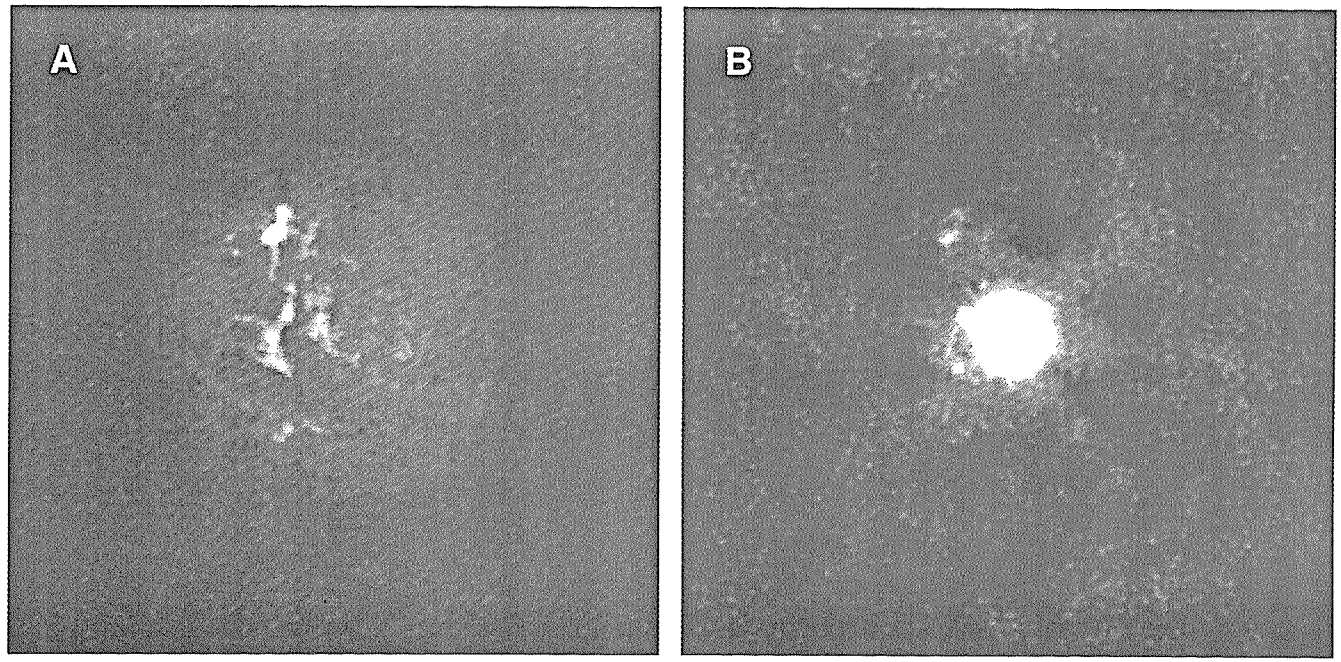

Figure 3.2 Orthographic reprojections of Magellan global altimetry on A) Feb. 28, and B) Mar. 4, with planetary radius grayscale in km. The scale in both of these images is the same as Fig. 1 and 2 (0.2 arcsec per pixel). The apparent disk diameters are 41.5 arcsec in A) and 44.2 arcsec in B). Features discussed in the text are labeled. The circles to the lower right of each image show the sizes of the synthesized beam on each day: 0.94 arcsec on Feb. 28, and 0.7 arcsec on Mar. 4.

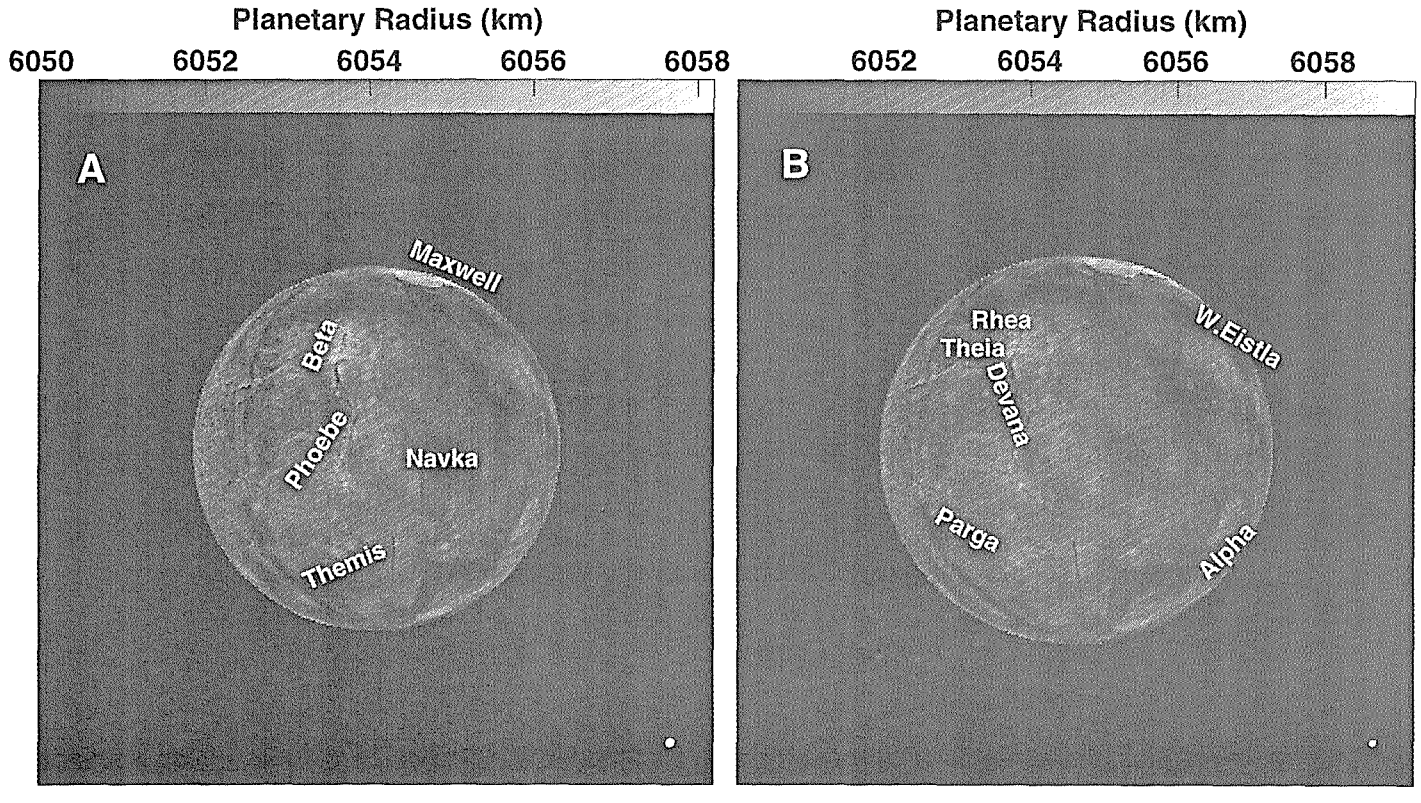

Figure 3.3 A) Image of the SS echo from Venus on Feb. 28, B) Image of the Venus OS echo on the same day. The resolution is equivalent to the synthesized gaussian beam of FWHM 0.94 arcsec diameter. Beta Regio is the bi-modal feature in the upper portion of all images, left of the center-line. See Fig. 3 for identification of other features.

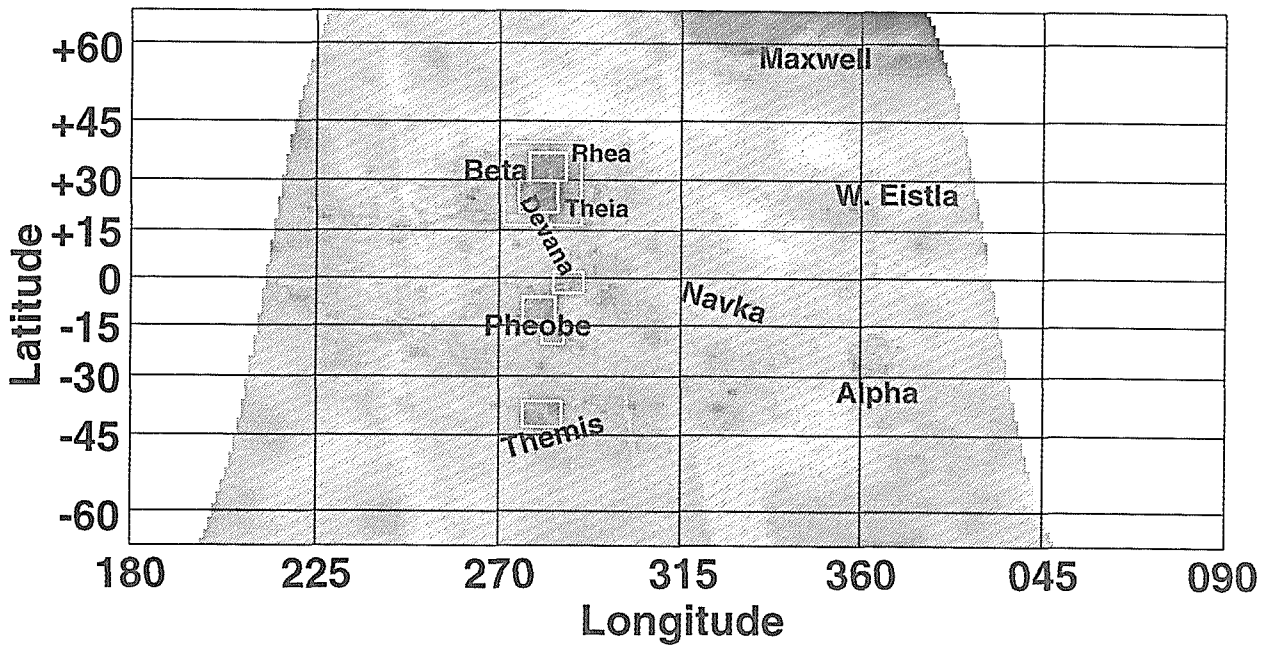

Figure 3.4 Mercator projection of Magellan altimetry between 65N and 65S for the hemisphere sampled on Mar. 4, 1993. Geographic features are labelled for reference with features in the radar maps of Figs. 5 and 6. The boxes around features correspond to the approximate locations in the sky-coordinate maps used to calculate regional averages in Tables V, VI and VII, which were chosen based on altimetry contours (see text).

Venus, Δf is the effective reception bandwidth, and $\sigma(\theta_i)$ is the radar cross section as a function of incidence angle (units cross section per unit area, dimensionless). With the known values of our experimental set-up, Eq. (1) can be re-written as

$$F_R = \kappa\sigma(\theta_i) \qquad 3.2$$

On Feb. 28, κ=58.15 Jy/beam, and on March 4, κ=36.97 Jy/beam. The difference is caused primarily by Ω_b on Feb. 28 being about twice that on Mar. 4 (see $FWHM_b$ in Table 3.2). With this we produce maps of both SS and OS apparent radar cross sections, σ_{SS} and σ_{OS}, respectively. These radar cross sections are inherently normalized, and as such can be considered radar albedos, equivalent to surface reflectivities which include effects of Fresnel surface reflectivity and radar backscatter phase function. Figs. 5 and 6 are our final contour maps of σ_{SS}, σ_{OS} and μ_c for each of the two days of observation. The uncertainties affecting these maps are presented in Appendices B and C.

The specular spike dominates the σ_{OS} maps as expected, with radar cross sections per unit area near the sub-earth point as high as 15 on March 4. This means the region to the east of Phoebe Regio is smooth on a wavelength scale (3.5 cm) with gentle slopes on a scale of many wavelengths. This is consistent with previous Venus observations (Campbell and Burns 1980) and observations of terrestrial planets in general. It is also consistent with Venera 13 images (Weitz and Basilevsky 1993) showing a flat surface of mostly layered bedrock; the

landing site is very close to our sub-Earth point on March 4. The OS spikes were analyzed by least squares fitting of the Muhleman model ,

$$\sigma_{OS} = \beta_{OS}\cos\theta_i / (\sin\theta_i + \alpha_{OS}\cos\theta_i)^3 \qquad 3.3$$

Model parameters α_{OS} and β_{OS} (shown in Table 3.3) agree with previous measurements. The reflective regions of Beta and Phoebe Regiones were excluded from the fits as their scattering laws are clearly very different from the planetary average, as can be seen in Figs. 5 and 6.

Table 3.3

Muhleman scattering model fits, $\sigma_{OS} = \beta_{OS}\cos\theta_i / (\sin\theta_i + \alpha_{OS}\cos\theta_i)^3$. The results are compared with previous measurements, albeit at different wavelengths (λ).

Date	λ (cm)	α_{OS}	β_{OS}
Feb. 28, 1993	3.5	0.18	0.08
Mar. 4, 1993	3.5	0.10	0.03
Pettengill *et al.* (1988)	17	0.133	0.032
Muhleman (1964)	12	0.12	N/A

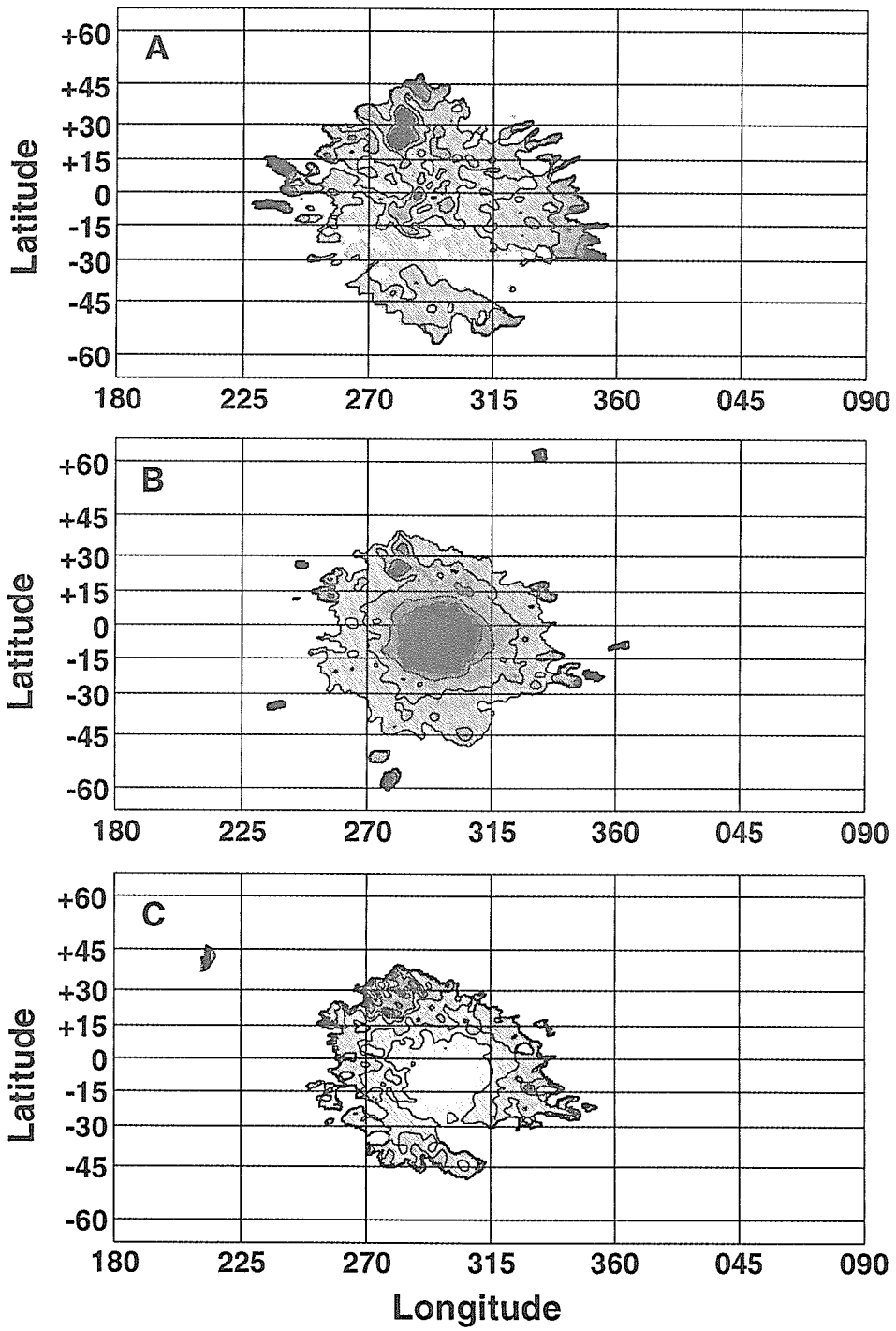

Figure 3.5 Mercator projection maps of radar results on Feb. 28th, 1993. A) σ_{SS}, with contours 0.025, 0.05, 0.10, 0.15, 0.20; the maximum σ_{SS} in the map is 0.42. B) σ_{OS}, with contours 0.10, 0.25, 0.50, 0.75; max. σ_{OS}=8.2. C) μ_c, with contours 0.05, 0.1, 0.2, 0.3, 0.5, 0.7.

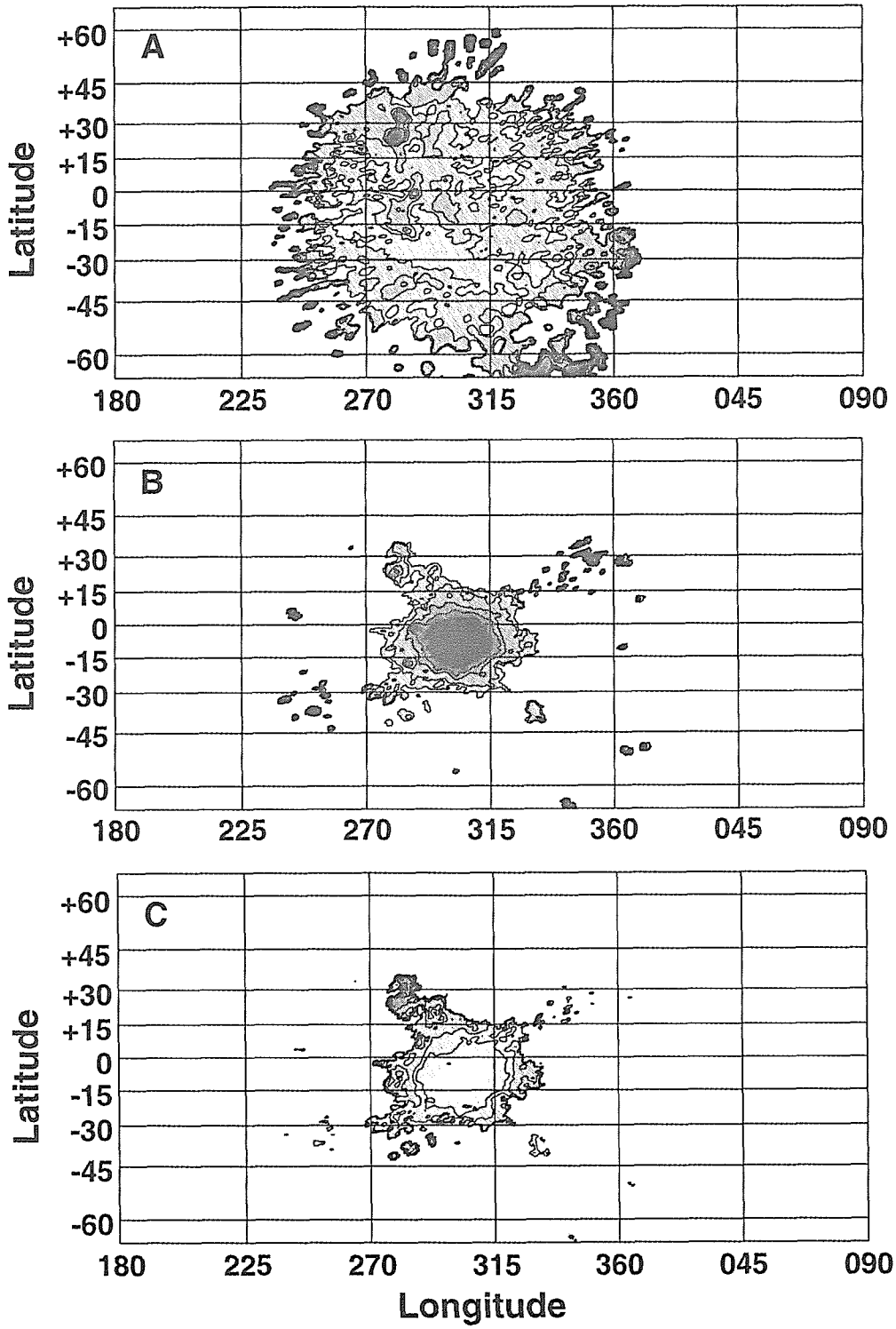

Figure 3.6 Mercator projection maps of radar results on Mar. 4th, 1993, A) σ_{SS}, B) σ_{OS}, and C) μ_c, with all contours as in Fig. 5. Max. σ_{SS}=4.8. and max. σ_{OS}=15.5.

3.4 Regional Results

The σ_{SS} maps (Fig. 5A and 6A) are dominated by Beta Regio and the 285E longitude highlands. Beta Regio is examined in the following section. Themis and Phoebe Regiones, which in some ways are geologically analogous to Beta, are discussed here. Their radar properties serve as a starting point for our discussion of scattering mechanism in Beta. It should be noted here, and kept in mind throughout our discussion, that our real resolution is the synthesized beam. In the images each pixel is an average over a beam spot centered at the pixel location. In the mercator maps the σ and μ_c at any location represents an average value over an area equal to the projected beam, or about 300 km FWHM diameter at Beta. Thus, it is likely that we smooth-over any small regions, say < 50 km, with unique properties.

The radar data for Themis are summarized in Table IV. Themis pixels are defined as those with altitudes > 6052.75 km (planetary radius), boxed in Fig. 4. Themis is a volcanic highland associated with the NW-trending chain of coronae of Parga Chasma. This NW-trending structure is apparent in the σ_{SS} maps (from 315E, 35S to 270E, 15S). Along Parga Chasma the low SS albedo values between Themis and Phoebe in Fig. 6A in particular indicate that these lower areas are smoother than the adjacent highlands. The volcanic structure of Themis produces a weak, but significant SS echo, implying moderate wavelength-scale roughness either at the surface or in the subsurface. Campbell and Campbell (1992) distinguish terrestrial pahoehoe lavas (smoother) from a'a lavas (rougher) with $\mu_c(\theta)$. A'a lavas have μ_c>0.2 at 10° to >0.4 at 60°, while pahoehoe lavas have

smaller μ_c's. This lava-type boundary for their 24 cm wavelength would be at higher μ_c in our 3.5 cm case. Themis' μ_c suggests pahoehoe-like roughness.

Table 3.4

Average dual-polarization radar data for Themis Regio. The area of the averages is a box defined on the sky map corresponding approximately to the R_p > 6052.75 km contour. The approximate geographic location is shown by a box in Fig. 4. The 0.2" sky-pixels are resampled to beam resolution, and only non-zero pixels are included in these averages. The uncertainties of the averages are the rms standard deviations among the pixels, and do not include the inherent uncertainties in the data discussed in the text.

Date	θ_i (deg.)	σ_{OS} (n)	σ_{SS} (n)	μ_c (n)
Feb. 28, 1993	37.4	0.19±0.06	0.03±0.01	0.16±0.05
Mar. 4, 1993	38.9	0.14±0.07	0.06±0.02	0.30±0.10

The scattering mechanism for such terrestrial lava flow morphologies is thought to be surface scattering, where increased μ_c comes from enhanced dielectric constants enhancing higher order reflections (Campbell *et al.* 1993). However, increased μ_c may be due to increased σ_{SS} caused by volume scattering from common basalt embedded in a low loss material (Tryka and Muhleman 1992). Such a material---a dry soil is suggested---would probably also have increased σ_{OS} values as quasi-specular reflection would occur at the surface but also at embedded scatterers. The second mechanism can also display low emissivity. Deciding which of these scattering behaviors is more appropriate has implications for the morphology of Themis. A dry soil layer on this volcanic

edifice would imply some weathering rate for Venus, while surface scattering from a barer rock surface would imply either slower weathering or a more recently formed surface. A choice for one mechanism or the other cannot be made solely with these data.

Phoebe Regio is more extended than Themis. Table V presents average values for northern, middle and southern parts of Phoebe, marked by boxes in Fig. 4. The regions are above the 6053 km planetary radius contour. Considering Phoebe's proximity to the sub-Earth point on both days, and given that σ_{OS} decreases with increasing θ_i while μ_c increases with θ_i, the values in Table V are, as for Themis, indicative of moderate wavelength-scale surface roughness, similar to that of terrestrial pahoehoe lavas if surface scattering dominates. The geologic context of Phoebe has been described by Senske *et al.* (1991a) based on Arecibo OS radar images. They note that Phoebe and Beta are related, in that both are "characterized by extension, rifting, ... and volcanism." The linear elongation of Phoebe follows Devana Chasma. Our north Phoebe spot is apparently a volcanic feature at the point where the Devana rift system seems to pass through an eastward-trending transfer zone after running south from Beta. The middle Phoebe spot falls on Devana's arcuate extension southward toward another volcanic construct correlated with our south spot. The comparative value of the Phoebe radar results to those in Beta Regio will be explored in the next section.

Table 3.5
Average dual-polarization radar data for Phoebe Regio. The three Phoebe sub-regions correspond to R_p > 6053 km, approximately shown by the boxes in Fig. 3.4. Uncertainties are as discussed for Table 3.4.

Date	Phoebe sub-region	θ_i (deg.)	σ_{OS}	σ_{SS}	μ_c
Feb. 28, 1993	North	9.5	2.06±1.15	0.07±0.03	0.03±0.01
	Middle	14.7	0.75±0.20	0.06±0.02	0.08±0.03
	South	15.2	0.99±0.42	0.05±0.02	0.05±0.02
Mar. 4, 1993	North	16.2	0.84±0.42	0.08±0.06	0.10±0.03
	Middle	21.0	0.33±0.11	0.08±0.02	0.24±0.06
	South	20.2	0.46±0.18	0.06±0.03	0.14±0.05

Other Venusian features are apparent in our data. The σ_{OS} feature at 335E, 37S in Fig.3.6B is significant. It appears related to the volcanoes Hathor and Innini Montes. Interestingly, it has higher σ_{OS} and lower σ_{SS} than Themis, suggesting smoother wavelength-scale morphology.

3.5 Beta Regio

Beta Regio is a rifted highland. Figure 3.7 is a regional geologic sketch map for Beta Regio in Mercator projection with Magellan altimetry based on a geological interpretation of Arecibo OS data by Senske *et al.* (1991b, 1991c). On the regional scale appropriate for our synthesized beam resolution , their mapping is consistent in most respects with more detailed Magellan results (*e.g.* C2-MIDR 30N284). Beta is dominated by the Theia Mons volcanic edifice at 280E, 24N, from which Devana Chasma's three arms radiate. A SSE arm points toward

Phoebe Regio, a SW arm points toward Atla Regio and a wider northern arm splitting Beta's topographic dome connects Theia to Beta's second topographic high at Rhea Mons (282E, 32N) on the western side of the Chasma. Rhea's original interpretation as a volcano (Campbell *et al.* 1984, Senske *et al.* 1991b, 1991c, Stofan *et al.* 1989) was reassessed with the Magellan data (Senske *et al.* 1992, Solomon *et al.* 1992). It appears more closely related to the tesserae in northern Beta. The map follows the more recent geological interpretation in most respects but maintains Senske *et al.*'s (1991b, 1991c) distinction of the banded terrain north of Rhea. That unit might also be called tessera. The association of the E-W trending lineaments at 25N north-east of Theia, with Hecate Chasma to the west was interpreted by Senske *et al.* (1992) to indicate an older phase of rifting prior to the formation of Devana. A time-sequence for Beta would start with the tesserae and perhaps the E-W lineaments expressing preexisting N-S extension, followed by deformation due to uplift forming Devana Chasma coeval with the emplacement of Theia Mons' volcanic edifice (Senske *et al.* 1992, Solomon *et al.* 1992).

While the geologic history describes the regional relationships which may dominate the radar maps, another element in the surface properties story is the modification and/or weathering which may occur. Processes which modify the

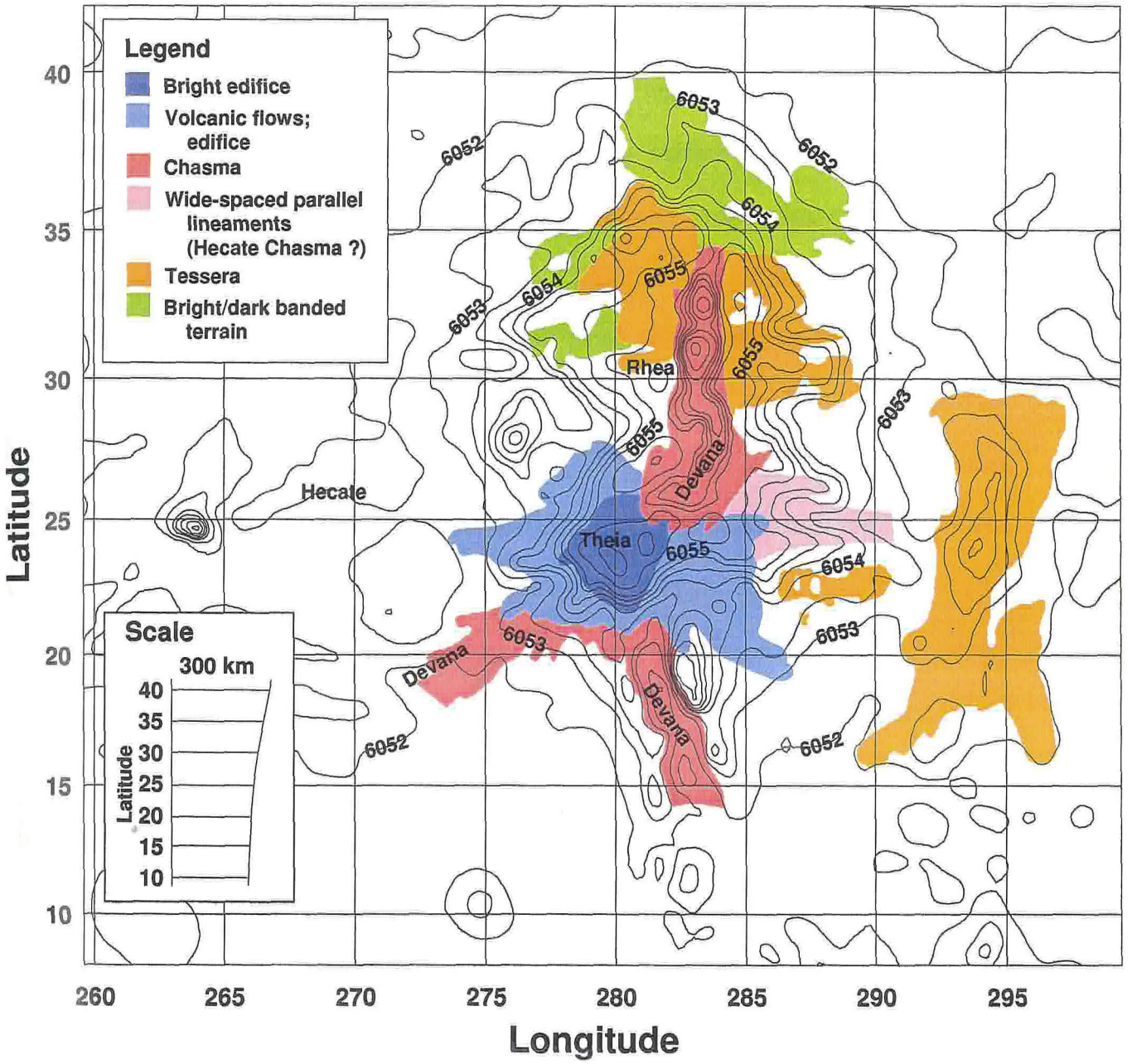

Figure 3.7 Mercator projection geologic sketch map of Beta Regio (based on Senske *et al.* 1991bc and 1992), with altimetry contours. The geologic units are given in the legend. The altimetry contours are, in km of planetary radius, 6051, 6052, 6053, 6053.5, 6054, 6054.25, 6054.5, 6054.75, 6055, 6055.5, and 6056.

small-scale radar properties over time can take place coevally with the formation of a unit or proceed later, depending on the nature of the process. On Earth, variability of radar properties within a geologic unit is common and depends most often on water content and differences in surface morphology caused by weathering, again most often related to the Earth's hydrological cycle. In Venus' hot, dry surface environment some other alteration mechanism, if such exists, must be responsible. Several mechanisms have been proposed from mechanical weathering due to wind (Arvidson *et al.* 1992, Greeley *et al.* 1992), to chemical weathering due to sulfides (Klose *et al.* 1992), chlorides or chalcogenides (Brackett *et al.* 1995). Chemical weathering may be acting in at least two ways. First, volatile minerals may be condensing out of the atmosphere in the cooler environment of high elevations, coating rocks and perhaps raising their apparent dielectric constant (Pettengill *et al.* 1996). Second, the same condensation process may act to break up the rock forming a rough pebbly surface or even soils. In the former case, surface scattering would probably dominate, while in the latter, some significant contribution from volume scattering would be expected. Another alternative is that no weathering occurs, and any changes to small scale morphology are due to regional tectonic evolution and any mass movement it provokes. The latter could conceivably also produce rubbly, reworked surfaces. Given the soundness of the regional geological interpretation in Beta, our data should indicate to what extent each alternative can explain the wavelength-scale morphology there. It should be remembered that all Venusian geology is radar-based.

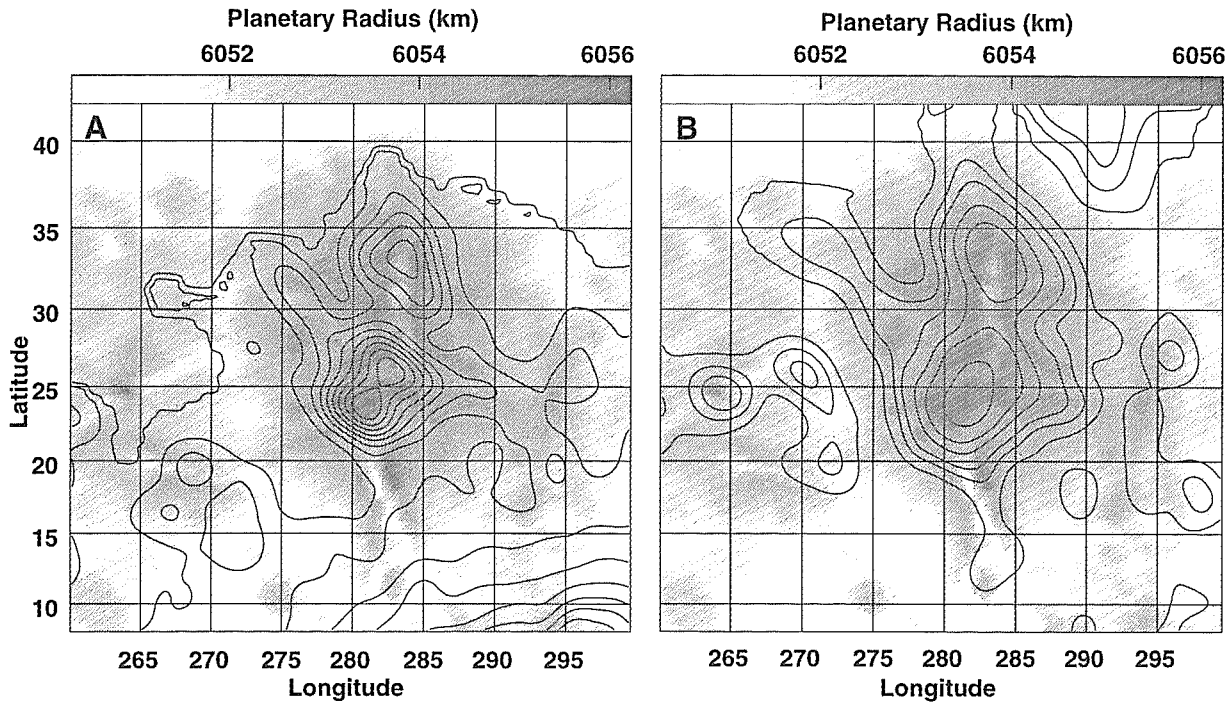

Figure 3.8 Mercator projection from sky coordinates of σ_{os} and σ_{ss} in the region around Beta on Feb. 28. A) σ_{OS}, with contours in increments of 0.1 from σ_{OS}=0.1 to 0.9 . B) σ_{SS} with contours σ_{SS}=0.050, 0.075, 0.10, 0.15, 0.2, and 0.3 . Reflectivity contours are overlain on a grayscale of topography, also reprojected from the sky coordinate topography image.

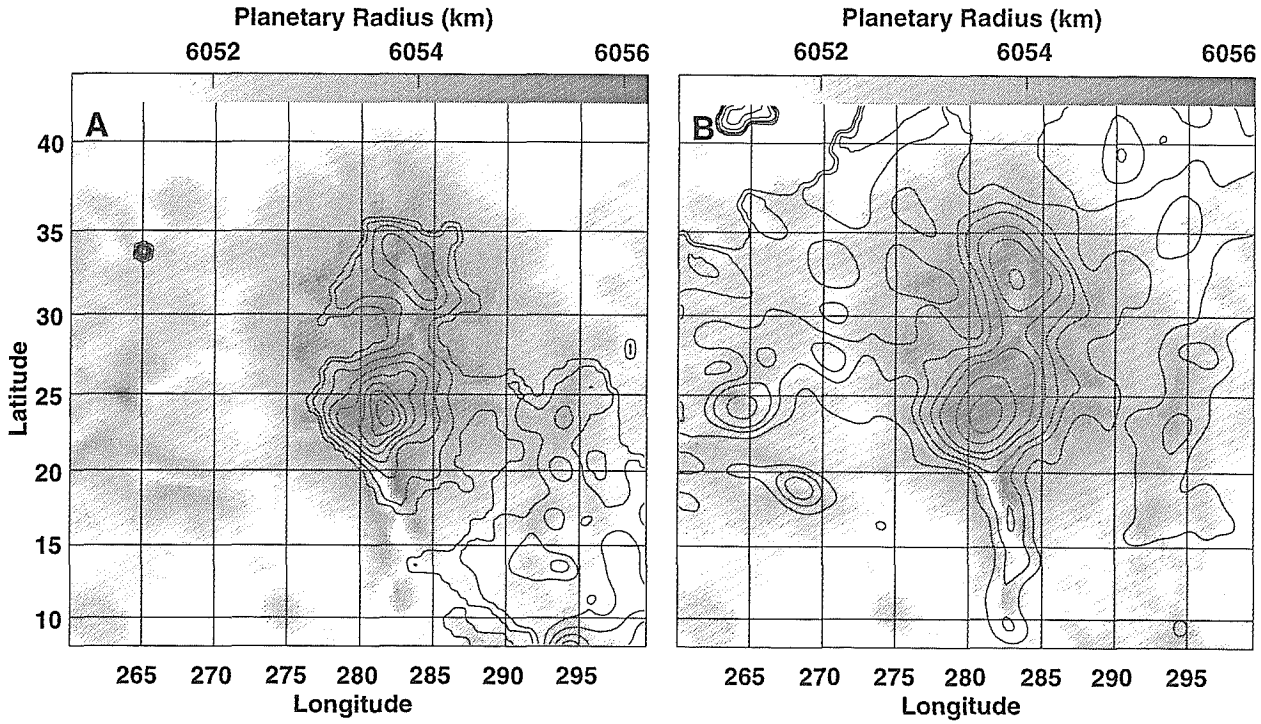

Figure 3.9 Mercator projection from sky coordinates of σ_{os} and σ_{ss} in the region around Beta on March 4. A) σ_{OS}, with contours in increments of 0.1 from σ_{OS}=0.1 to 0.9 . B) σ_{SS} with contours σ_{SS}=0.050, 0.075, 0.10, 0.15, 0.2, 0.3 and 0.4. Background topography grayscale like Fig. 9.

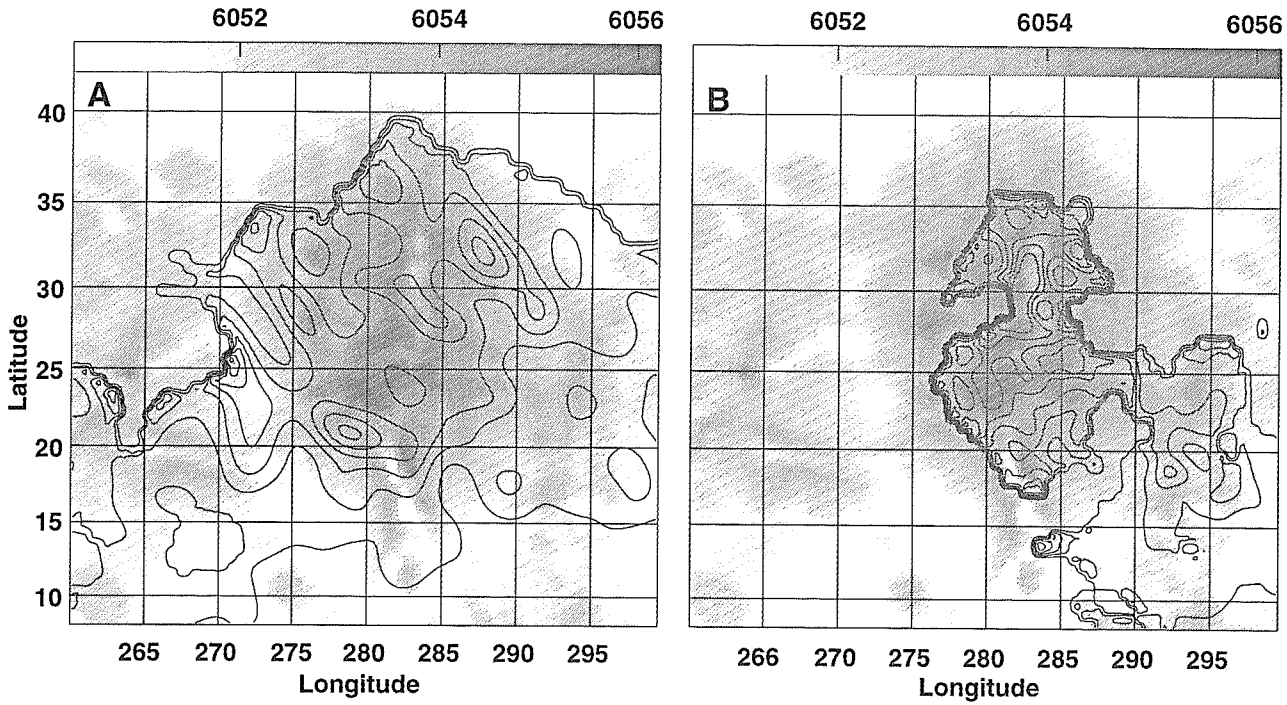

Figure 3.10 Mercator projection from sky coordinates of μ in the region around Beta on A) Feb. 28, and B) March 4, with contours in increments of 0.1 from μ_c=0.1 . Max. contours are A) μ_c=0.6, and B) μ_c=0.8 . Background topography grayscale like Fig. 9.

Figures 3.8 and 3.9 show cross-sections in the region around Beta on Feb. 28 and March 4 respectively. The contours of σ_{OS} and σ_{SS} are overlain on a grayscale of topography. Figures 3.10A and B similarly show μ_c results. The two days' Beta Regio maps are consistent, keeping in mind that a cross-section, σ_{OS} or σ_{SS}, on March 4 represents a beam-averaging over only half the area that it does on Feb. 28. Beta Regio was viewed at slightly lower incidence angles on the first day ($23^\circ<\theta_i<50^\circ$) and more along the N-S axis of Devana Chasma than on the second day ($26^\circ<\theta_i<53^\circ$). Both cross-sections, though σ_{OS} in particular, exhibit some enhancement on radar facing slopes. The OS albedo maxima are σ_{OS}=0.9 on Feb. 28 and σ_{OS}=0.8 on March 4. On both days the maximum contours cover the region of Theia's volcanic edifice. The SS albedo is also maximum over Theia Mons on both days, reaching σ_{SS}=0.3 on Feb. 28, and σ_{SS}=0.4 on March 4. The eastward lineaments north of Theia at 287E, 31N exhibit σ_{OS} enhancement in Figs. 3.8A and 9A. Also in Fig. 3.9A, with its better resolution, σ_{OS}=0.3 points toward the opening of Devana Chasma's southern arm (282E, 20N), and σ_{OS}=0.5 points toward the northern arm (283E, 26N). In general though, the specular albedo seems to correlate less well with the rift units than does σ_{SS}. On both days the σ_{SS}=0.05 contour follows Devana Chasma to the south. These albedos indicate a component of diffuse backscatter at a level above, though not markedly so, that of the surrounding plains; the rifts are rougher than the plains. The degree of cross-section enhancement for the rifts is however much smaller than that associated with Theia and Rhea Montes.

Over Rhea the σ_{OS}=0.4 contours correlate well with the outlines of tesserae in Fig. 7. Similarly, the Feb. 28 σ_{SS}=0.2 contour and the March 4 σ_{SS} =0.3 contour are well correlated with Rhea's tessera. The tessera region at 295E shows up almost exclusively in the σ_{SS} maps at a similar level of enhancement of diffuse backscatter as the rifts with σ_{SS}~0.05. This makes these eastern tesserae much less reflective than those surrounding Rhea. The two tessera units have similar geologic contexts, origins, and display structural similarity in Magellan images, yet they have different radar properties. Conversely, Theia and Rhea Montes are capped by different geologies but have similarly elevated σ_{OS} and σ_{SS} values. Thus, the high reflectivities are not uniquely dependent on geological unit.

Theia's σ_{OS} values are similar in magnitude to those for Phoebe on March 4, where the incidence angles were 10° smaller. However, the σ_{SS} values at Theia Mons are significantly greater than those observed over Phoebe's north and south spot volcanic edifices. This would suggest that the volcanic surface of Theia Mons is significantly rougher than its southern cousins in related tectonic environments. Of course, Theia Mons is much greater in extent and two kiliometers higher than Phoebe's two volcanoes. Pettengill *et al.* (1992) note that the extent of the Phoebe low emissivity anomalies is only one tenth that of Theia Mons. This confirms the observation of Tryka and Muhleman (1992), that σ_{SS}, like Magellan σ_{HH} , anticorrelates with emissivity.

The μ_C maps of Fig. 3.10 show the regional variation of the relative importance of the same-sense echo to the opposite-sense echo. In general on the two days μ_C > 0.5 over much of Beta. The maxima in Fig. 3.10A with μ_C=0.6

occur on the southwest flank of Theia and on the tessera to the east of Rhea. In this map, a cloverleaf-shaped μ_c=0.4 contour covers Beta. The trend is similar on March 4 (Fig. 10B), with $\mu_c > 0.8$ along the western radar-facing flank of Devana Chasma at the latitude of Rhea and southward. These values are compatible with the properties of blocky terrestrial lava flows if surface scattering dominates. Such a high μ_c near Rhea suggests that the rifted older tessera are associated with significant roughness at ~3.5cm scales. Note again that our μ_c maxima may be lower limits given our large pixel areas.

To pursue a regional geologic explanation for high σ_{os} and σ_{ss} on the Montes in Beta Regio, we examine the important and previously observed correlation of radar properties with altitude (Ford and Pettengill 1983, Garvin *et al.* 1985, Head *et al.* 1985, Klose *et al.* 1992, Pettengill *et al.* 1988, 1991, 1982, 1996, Tyler *et al.* 1991). Figure3.11 shows the correlation of σ_{os}, σ_{ss}, and μ_c with beam-averaged planetary radius R_p over Beta. Also shown are the correlations between the two cross-sections. These scatterplots are made by pixel-to-pixel comparison of beam-sized pixels. The region sampled is shown approximately in Fig.3.4. The average behavior of σ_{os} and σ_{ss} vs. R_p in Beta is distinctly bimodal. At low and intermediate altitudes from the datum at 6051 km to around 6054 km the cross-sections in both polarizations remain fairly constant and low. The values in this region are typically σ_{os}~0.2 and σ_{ss}~0.08. The reflectivity behavior above 6054 km shows an abrupt rise in reflectivity with altitude: σ_{os} increases with a slope of 0.7 km^{-1} in both our days' data, while σ_{ss} increases as 0.3 km^{-1}. The Pearson linear correlation coefficients, r, listed in Table VI are consistent with

linear trends. The results of straight line fits to the N non-zero data points with R_p > 6054 km are also given in Table VI, and plotted in Fig 3.11. The χ^2 fitting routine of Press *et al.* (1992 p.666) accounts for uncertainties in both coordinates. Uncertainties in σ and μ_c are described in Appendix C. The uncertainty in R_p is the standard deviation of the beam-weighted average within the $FWHM_b$ pixel. Our observed increases in cross-section with altitude are sharper than the increase found by Garvin *et al.* (1985) for Beta Regio 17 cm normal-incidence reflectivity, which they attributed to young, unweathered lavas. Furthermore, our correlation of σ_{OS} with σ_{SS} defines an average polarization ratio for Beta on each day: μ_c=0.39 on Feb. 28, and μ_c=0.55 on Mar. 4. We note that the fit on Mar. 4 has the highest ratio, χ^2/(N-2)=2.7. This apparent poor fit is due to the scatter of the lower cross-section data. The correlation however, r=0.9, is significant. Overall then, the Beta Regio data define a region of cross-section increasing with altitude in both polarizations, and also of σ_{OS} increasing more steeply than σ_{SS} with altitude.

The correlations of σ with R_p need to be decoupled from effects of resolution, geologic unit, and viewing angle. Beta Regio's σ_{SS} at a given point was generally higher on Mar. 4. The better resolution on that day explains this: the areas with high σ_{SS} do not fill the beam ($FWHM_b$-pixel). In scatterplots restricted to regions surrounding Rhea (Fig. 3.12) and Theia (Fig. 3.13) the properties of the two Montes appear distinct. This shows the consistency of the data between days. It also offers evidence that the distinct geology of each Mons is the first

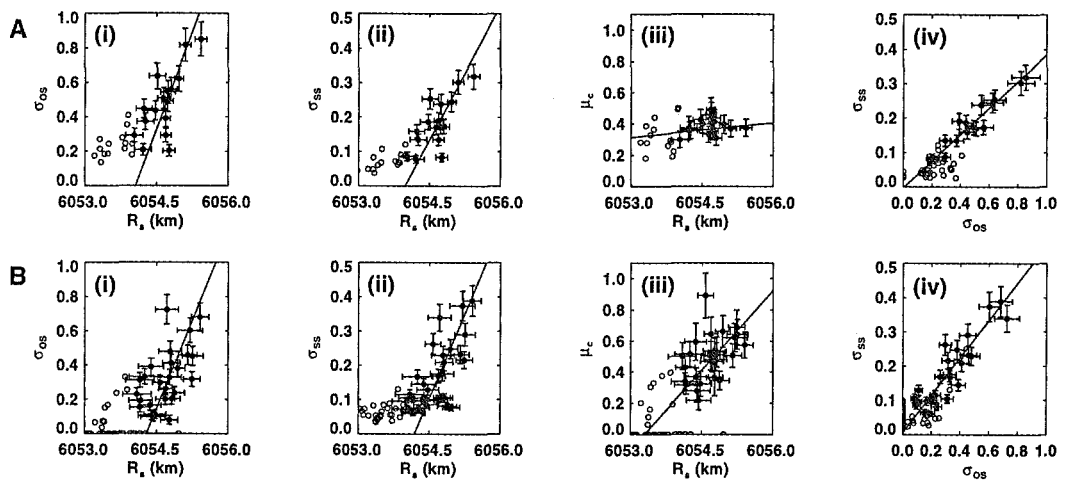

Figure 3.11 Scatterplots of data from the Beta Regio box (Fig.3. 4) on A) Feb. 28 and B) Mar. 4 showing correlations between (i) σ_{OS} in a $FWHM_b$-sized pixel vs. beam-averaged altimetry, R_p, for the pixel, (ii) σ_{SS} vs. R_p, (iii) μ_c vs. R_p, and (iv) σ_{SS} vs. σ_{OS}. The uncertainties in R_p are the standard deviations of the beam-weighted averages. The uncertainties in σ (both pol.) include 10% from CLEANing, about 6% from the atmospheric correction at the incidence angles over Beta, and a minor contribution from the background noise N_{pol}. The linearity of the relations is discussed in the text with values given in Table VI. Open circles are points not considered for the fitting either because they were zero or below the assumed "snow-line," R_p=6054km.

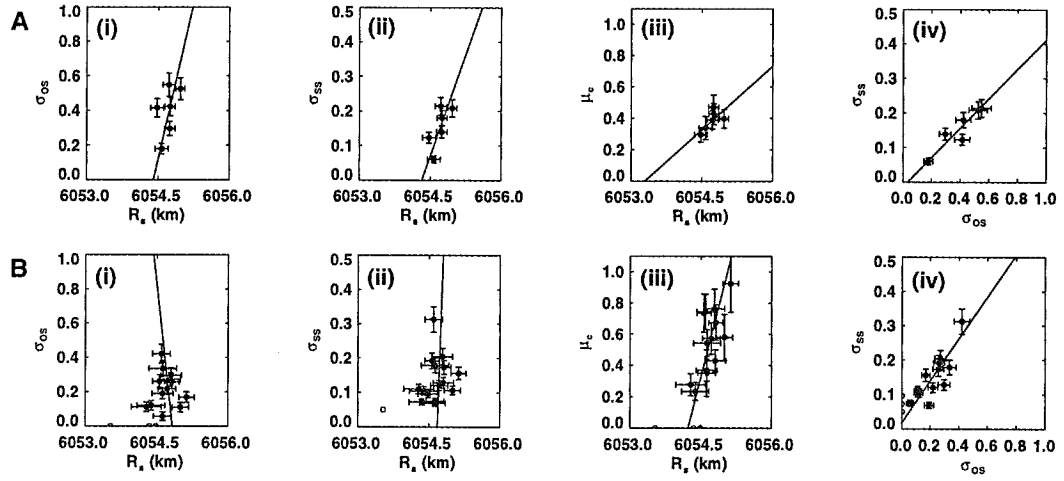

Figure 3.12 Scatterplots as in Fig.3.11, but restricted to the Rhea Mons box (Fig. 4) on A) Feb. 28, and B) Mar. 4.

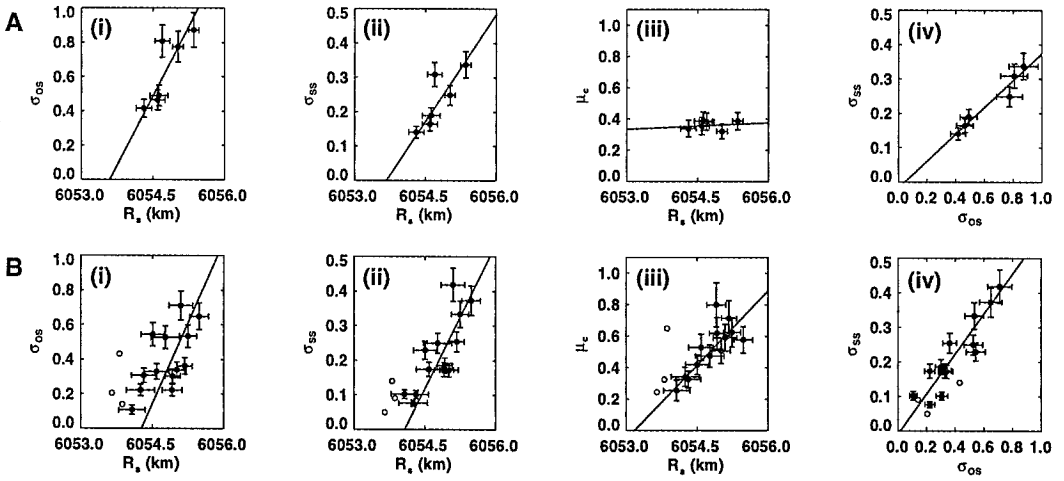

Figure 3.13 Scatterplots as in Fig. 3.11, but for the Theia Mons box (Fig.3.4) on A) Feb. 28, and B) Mar. 4.

Table 3.6

Analyses of Beta (Fig 3. 11), Theia (Fig. 3.12), and Rhea (Fig. 3.13) radar properties. Linear models are fit to the scatterplots of cross-section σ (both pol.) and polarization ratio μ_c vs. planetary radius R_p and of diffuse cross-section σ_{SS} vs. specular cross-section σ_{OS} The values are compared pixel-by-pixel for beam-FWHM-sized pixels in boxes defined on the sky map. The approximate geographic locations of the boxes are shown in Fig.3.4. The incidence angle θ_i coverage of the boxes is given. The linear model fit parameters are: N, the number of pixels used for the fitting; r, the Pearson linear correlation coefficient; b, the slope of the best fit line, y=a+bx, with uncertainties on both x and y; χ^2, the chi-squared value of the fit; and q, the probability that the observed chi-squared exceeds the value χ^2 by chance even for a correct model.

Date:	Feb. 28, 1993 (A)					Mar. 4, 1993 (B)				
Linear fit parameters	N	r	b	χ^2	q	N	r	b	χ^2	q
Beta			$23.5 < \theta_i < 49.5$					$26.3 < \theta_i < 53.1$		
(i) σ_{OS} vs. R_p	16	0.72	0.75 ± 0.12	35	0.0013	26	0.57	0.69 ± 0.14	42	0.011
(ii) σ_{SS} vs. R_p	16	0.75	0.26 ± 0.04	31	0.0049	32	0.72	0.33 ± 0.05	49	0.017
(iii) μ_c vs. R_p	16	0.21	0.03 ± 0.04	10	0.76	26	0.46	0.34 ± 0.08	33	0.095
(iv) σ_{SS} vs. σ_{OS}	16	0.95	0.39 ± 0.04	8.5	0.86	26	0.90	0.55 ± 0.05	65	0.00001
Rhea			$36.1 < \theta_i < 41.2$					$38.4 < \theta_i < 48.4$		
(i) σ_{OS} vs. R_p	6	0.49	1.22 ± 0.62	6.8	0.15	13	0.06	-2.5 ± 3.5	14	0.22
(ii) σ_{SS} vs. R_p	6	0.71	0.39 ± 0.17	4.2	0.38	15	0.21	4.1 ± 14.0	18	0.16
(iii) μ_c vs. R_p	6	0.67	0.27 ± 0.18	1.9	0.75	13	0.67	1.20 ± 0.51	7.8	0.73
(iv) σ_{SS} vs. σ_{OS}	6	0.93	0.43 ± 0.08	3.6	0.46	13	0.83	0.61 ± 0.10	25	0.0090
Theia			$30.8 < \theta_i < 35.9$					$32.5 < \theta_i < 41.9$		
(i) σ_{OS} vs. R_p	6	0.84	0.54 ± 0.14	4.3	0.37	13	0.64	0.62 ± 0.18	23	0.021
(ii) σ_{SS} vs. R_p	6	0.82	0.21 ± 0.05	5.4	0.25	13	0.81	0.28 ± 0.07	13	0.31
(iii) μ_c vs. R_p	6	0.22	0.01 ± 0.07	1.4	0.84	13	0.79	0.32 ± 0.08	6.8	0.81
(iv) σ_{SS} vs. σ_{OS}	6	0.97	0.39 ± 0.09	1.0	0.91	13	0.91	0.58 ± 0.05	27	0.0054

order control of radar properties. Preliminary analysis of these data (Haldemann *et al.* 1994) based on the association of the highest μ_c contour with the Devana Chasma rift south of Rhea led to a similar conclusion. Campbell and Campbell (1995) came independently to the same conclusion based on recently calibrated dual polarization Arecibo data. The correlation of cross-section in both polarizations with altitude is better for Theia than for Rhea. On Theia, both σ_{OS} and σ_{SS} appear to rise monotonically above 6054 km. On Rhea, σ's do rise above 6054 km, but the trend is less clear. Of the two tessera units, Rhea is more than 1 km higher in elevation. Its cross-sections exceed those on the 295 E tesserae, as do its μ_c's (0.50 for Rhea, 0.20 for 295 E). We observed both at similar incidence angles. Thus, while both regions are similar tesserae, the enhanced μ_c on Rhea must be due to the altitude difference.

The scatterplot behavior must arise from the actual radar scattering mechanism. The very good linear correlation between σ_{OS} and σ_{SS} over both Montes on both days indicates that the scattering mechanism must allow both cross-sections to rise in concert. This strongly implies diffuse scattering which is polarization independent. Diffuse scattering is associated with wavelength-scale roughness and multiple scattering which can occur at a reflecting interface or within a low-loss medium. To address whether this diffuse scattering is surface- or volume-driven, we examine the implications of each option in the context of our results.

Contemplating an end-member rough surface-scattering model is useful. Consider a field of planes intersecting at right angles (Muhleman, personal communication, 1993), resembling the silhouette of a variable sawtooth. The reflectivity of one such "corner reflector" is such that σ_{OS} is minimum for an incidence angle relative to one face of the corner reflector ϕ=45°, while σ_{SS} reaches a maximum. The polarization ratio μ_C can exceed unity at ϕ=45° for a dielectric constant ϵ>1.5, and reaches μ_C=5 for ϕ=45° and ϵ=8. This corner-reflector model is akin in a simplistic way to coherent backscatter (Hapke 1990) insofar as reverse wavepaths exist and could add coherently. A field of randomly oriented corner reflectors viewed from normal incidence, θ_i=0°, would have random ϕ, but could nevertheless reach μ_C~1.9 for ϵ=8. A case more appropriate to the data might be a surface with many horizontal and vertical surfaces, suggestive of columnar fracturing or jointing, such that μ_C would be maximum at θ_i=ϕ=45°. A terrestrial analogue is the blocky SP flow in Arizona (Campbell *et al.* 1993). Indeed μ_C is the most variable parameter between our observation days, and the data show $\mu_C(\theta_i \sim 40°) > \mu_C(\theta_i \sim 30°)$ for the same geologic units, implying some angular effect on the diffuse scattering component. The question then is, are there more "corner reflectors" with altitude, or are the surfaces just more reflective? Both suggestions imply alteration with altitude. The quotation marks around corner reflectors are meant to suggest that any angular or blocky roughness would suit such a surface scattering model.

Volume scattering still needs to be considered. The highest pixel-averaged polarization ratio, μ_C~0.8, does not correlate with a maximum of σ_{SS}, and is on a slope facing the radar. This is puzzling. It suggests that enhanced diffuse scattering is decoupled from specular reflection, supporting volume scattering or even coherent backscatter effects. Pioneer Venus results (17 cm) suggest that rms slopes in Beta Regio are moderately high but $\leq 5^\circ$ (Head *et al.* 1985, Pettengill *et al.* 1980), less than for Aphrodite Terra, Maxwell Montes or Alpha Regio. Tyler *et al.* (1992) find 6° with Magellan at 12 cm. These rms values were determined by fitting the Hagfors model to altimetry data, an application that may be beyond the assumptions of the model. A smooth surface with volume scattering could produce backscatter data which would appear to fit the Hagfors model and yield meaningless parameters. To get an enhanced σ_{SS} from a smooth surface requires volume scattering from beneath the surface. If chemical weathering is enhanced in Venusian highlands by appropriate thermodynamics, then the highlands would be the most likely places to find significant accumulation of soil. Going uphill on Theia and Rhea Montes σ_{SS} rises from 0.1 to about 0.4. Application of Tryka and Muhleman's (1992) model of basalt scatterers embedded in a low-loss soil suggests that the single-scattering albedo of the medium increases from 0.50 to 0.95. In their model this corresponds to a decrease in the radius of the scattering particles from >1m to ~5 cm. This is consistent with greater weathering at altitude.

Volume scattering may not be inconsistent with a rough surface. The Hagfors model (Hagfors 1964, Hagfors 1966) assumes a nearly smooth surface on long length-scales. A truly rough surface would appear to be effectively smoothed by this assumption. McCollum and Jakosky (1993) note that "the derived rms slope can best be used as a qualitative guide to the physical interpretation of actual surface properties." The penetration depth of λ=3.5 cm radar in a dry basalt is of the order 10 wavelengths (Campbell and Ulrichs 1969). Thus a good deal of rock volume determines the observed cross-sections, whether or not the surface is rough, unless the dielectric constant is very high. Terrestrial evidence argues against volume scattering on a bare lava surface (Campbell 1994) for λ<70 cm, but all rock deposits on Earth are affected by water. The lack of liquid water on Venus will enhance the portion of volume scattering on all surfaces.

3.6 Conclusions

Distinct geologies, meaning tectonic origins of the different parts of Beta Regio, significantly influence the radar scattering properties of the surface. Theia and Rhea Montes have similarly elevated σ_{OS} and σ_{SS} when compared to the rest of the imaged surface of Venus. In particular however, cross-sections over Theia Mons are greater than those over Rhea Mons, and the behavior of cross-sections with increasing elevation is distinct on both Montes. Diffuse radar cross-sections, σ_{SS}, for rifted areas in Beta are slightly elevated above the disk averages.

Polarization ratios, μ_c, for the more northern Rhea are greater or equal to those in Theia.

The very good linear correlation between increasing σ_{SS} and increasing σ_{OS} over all of Beta Regio as well as on each Mons implies significant diffuse scattering in this highland. Cross-section enhancement of both polarizations on radar-facing slopes is apparent, and an angular influence on the degree of diffuse backscatter is suggested. The onset of cross-section enhancement in the data at around 6054 km in both polarizations confirms previously observed elevation-related effects. We find σ_{OS} increasing at 0.7 km^{-1}, while σ_{SS} increases at 0.3 km^{-1}. The implication is that diffuse surface scattering is the mechanism, although diffuse volume scattering cannot be ruled out in the Venus environment. Further evidence comparing similar tessera units at different altitudes suggests that the altitude enhancement is superposed on the radar properties of the underlying rock. The altitude correlation makes a thermodynamic, chemical explanation compelling. Physical volcanism explanations such as a critical eruption style dependence on elevation might account for Theia Mons' radar properties, but would not explain Rhea. It is possible that two very distinct radar scattering mechanisms are in play on the two Montes, but the properties of the 295E tessera also need to be accounted for. The data at the resolution of this experiment are most consistent with the conclusion that an altitude-related geochemical alteration process affects radar properties in Beta Regio, but the data are unfortunately insufficient to distinguish between surface and volume scattering. This question certainly requires

further modeling of appropriate scattering scenarios. Whole disk images at different incidence angles over Beta would be beneficial to further analysis and modeling. Improved resolution would help of course, though the relatively constant location of the sub-Earth point on Venus near inferior conjunctions hampers better resolution if angular coverag of Beta is desired. There is also a great need for laboratory and ground-truth measurements. The geological structures and morphologies are really far too complex to ever be explained with theoretical arguments. Finally, it would be a boon if S-band receivers were installed at the VLA; we could then see through the Venus atmosphere and improve overall disk coverage and SNR by almost an order of magnitude.

Chapter 4

4 Earth: Unique Radar Properties of High Altitude Ice Fields

4.1 Introduction

4.1.1 Unique Radar Properties

The unique radar behavior of cold planetary ices was first observed on Ganymede by Goldstein and Morris (Goldstein and Morris, 1975). Later observations have confirmed similar behavior for all the icy Galilean satellites, Europa, Ganymede, and Callisto (EGC). Reviews of all the EGC observations are in Ostro (Ostro, 1982) and Ostro et al. (Ostro, 1992). The behavior consists of a high radar backscatter cross-section as compared to terrestrial planets. The enhancement is significant at all incidence angles, and in particular, SS>OS, or μ_c>1. The angular dependence of the backscatter is also different from the general behavior of terrestrial planets. Figure 4.1 schematically summarizes the differences. The significant cross-section enhancement as well as the μ_C behavior act as a signature of cold icy surfaces, and in addition to EGC, have been observed on Titan (Muhleman *et al.*, 1990) and at Mars' residual austral ice cap (Muhleman *et al.*, 1991). Slade, Butler and Muhleman's (1992) discovery of polar

ice deposits on Mercury was an elegant outcome to 20 years of observations of the unique properties of cold planetary ices by planetary radar astronomers. The unique radar signature of ice is made more compelling by localization of the deposits in permanently shadowed craters (Harmon and Slade, 1992) where thermal models (Butler, 1994, Butler *et al.*, 1993, Paige *et al.*, 1992) indicate that

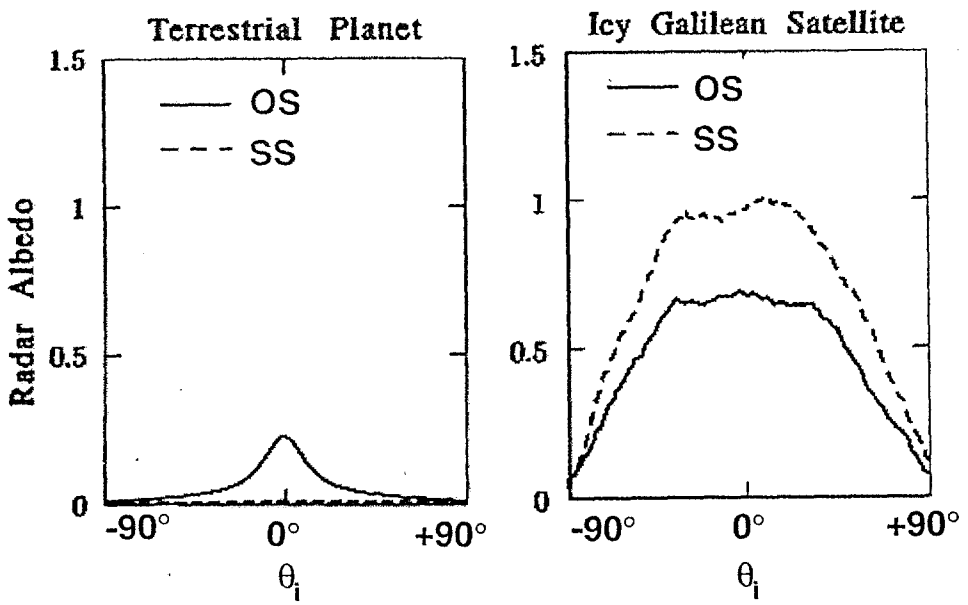

Figure 4.1 Schematic comparison of the typical backscattering dependance on incidence angle for a terrestrial planet with that of EGC. θ_i is the incidence angle at the radar equator. The plots represent results from Doppler-only (CW) radar observations.

ice would be stable.

As Figure 4.1 shows, the "standard" scattering model descriptions of terrestrial planets[‡] do not fit EGC. This becomes all the more interesting given theu other examples of unique radar-scattering planetary ice deposits. The key to all these observations appears to be the ice. Cold ice is highly transparent to radar wavelengths, and thus some form of volume scattering behavior is suggested. At least five different models have been put forward to explain EGC radar behavior. First, Double-bounces from hemispherical craters at the surface were suggested by Ostro and Pettengill (Ostro and Pettengill, 1978). This was refuted as requiring a surface refractive index too high for that of ice. Second, Goldstein and Green (Goldstein and Green, 1980) suggested that random cracks and voids in the near-surface might produce the unique signature through volume scattering at angles greater than the Brewster angle. Ostro (Ostro, 1982) pointed out an error that made the polarization inversion in this model inconsistent with high cross-sections. Various additional assumptions (other volume scatterers in addition to the voids) can somewhat salvage the cracks model. In the third model, Hagfors et al. (Hagfors, 1985) attempt to model the behavior with large refractive index inhomogeneities in the ice, but can not calculate actual cross-sections. Coherent volume backscattering off silicate particles was proposed as a fourth model by Hapke (Hapke, 1990) and Hapke and Blewitt (Hapke and Blewitt, 1991). This model involves volume scattering, but the radar cross-section is enhanced by a

---

[‡]Those without vegetation in any case.

factor of two in the backscatter direction due to the constructive interference summing of time-reversed ray-paths. The Goldstein and Green (Goldstein and Green, 1980) cracks model would also exhibit this behavior, and they seem not to have considered it. This suggests that it may still be possible to retain high cross-sections at the same time as $\mu_c>1$ in a model where the volume scatterers are cracks. The fifth model is the buried crater radar glory model proposed by Eshleman (1986) and developed further by Gurrola (1995). The general applicability of this last model is not clear, particularly in light of recent results from the Galileo spacecraft.

The story of unique radar scattering by ice was complicated somewhat by the discovery that a significant portion of Greenland also displays the EGC signature (Rignot *et al.*, 1993). It turns out that on Earth the behavior can be traced to the action of liquid water within firn, as will be detailed below. It seems unlikely however that liquid water is involved in producing the scattering structures on EGC or other planetary bodies. The purpose of the present study is to extend the search for ices on Earth with EGC-like radar signatures, to perhaps gain further insight into the nature of the extraterrestrial deposits. If we are to look for unique radar behavior of ice on the Earth, a review of the forms that ice takes in the terrestrial environment is in order.

4.1.2 Glaciers, Snow, and Ice

In the form of glaciers, ice is a rock whose sedimentation, diagenesis and eventual metamorphic deformation occur over timescales that a geologist can

observe (Sharp, 1988, p.4). As part of the Earth's hydrosphere, the cryosphere is being both supplied and eroded. The erosion takes place by melting, though it can happen after ice has been transported from a colder to a warmer locale as a glacier. The supply occurs as snow. Fallen snow takes on a character fundamentally different from falling snow flakes. Lliboutry (1965 p.199) points out that this explains why both the Greeks and the Eskimo have different words for each (fallen = χον and ganik, falling = νιφοζ and aput). The Eskimo of course have many more words to describe the great variety of snow and ice morphologies as the one is molded into the other (Lopez, 1980). Cold snow metamorphoses by sintering, which can occur at temperatures well below freezing. The metamorphosis is essentially an evolution from low density snow (0.10 g cm^{-3}) through packed snow (≥0.30 g cm^{-3}) to "firn" (≥ 0.55 g cm^{-3}, Sharp, 1960). Officially, firn is snow that is at least a year old and has survived one melting period. Ice is eventually formed when all interstitial voids are closed off (0.80-0.85 g cm^{-3}). Meltwater makes wet firn denser (≥0.7 g cm^{-3}) and accelerates the metamorphosis.

The progression from snow to ice corresponds to the progression of snow zones that exist on glaciers. In broad terms, glaciers are divided into an accumulation zone and an ablation zone by the equilibrium line. There is net gain of mass over the year above the equilibrium line, and net loss below. Following Benson (1962) and Patterson (1994), the accumulation zone is divided from the head of the glacier toward the equilibrium line into the dry-snow zone, the

percolation zone, the wet-snow zone, and the superimposed-ice zone. Figure 4.2 diagrams the different zones and their relative positions on a glacier. Few glaciers exhibit the whole sequence (Paterson, 1994).

No melting takes place in the dry-snow zone, even in summer. In the percolation zone some melting occurs, and the water percolates down into the snow where it may encounter a hydrologic discontinuity and spread out before it refreezes. In refreezing, ice layers or lenses form, and the vertical percolation channels refreeze as ice pipes or glands. Due to latent heat release from freezing, deeper layers of the snow get warmed and eventually raised to the melting point. In general, the lower the elevation, the greater the amount of melting that occurs in summer. Proceeding down-glacier, the wet-snow line is eventually reached where the whole year's snow reaches melting temperature in the wet-snow zone (also "saturation facies"). In this zone, some meltwater will percolate into previous years' deeper layers. The zone where so much meltwater is produced that a continuous mass of ice is formed on refreezing is the superimposed-ice zone. The boundary between the wet-snow zone and the superimposed-ice zone constitutes the snow line, firn line, firn edge or annual snow line. The superimposed-ice zone still has net annual accumulation of mass, and thus lies above the equilibrium line. The seasonal nature of the accumulation and melting metamorphosis leads to layering of the characteristic structures of each zone.

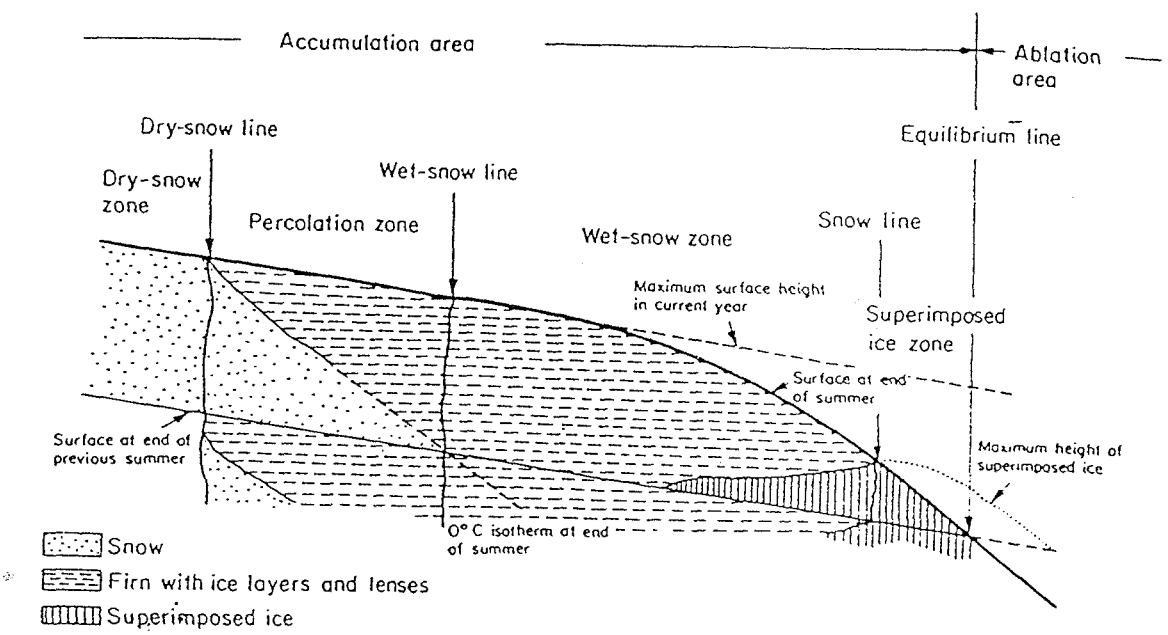

Figure 4.2 Snow and ice zones in the accumulation zone of a glacier. After Figure 2.1 from Patterson (1994).

4.1.3 Ice Radar Properties

The radar remote sensing of terrestrial ice and snow is highly dependent on water content (Ulaby, 1982). While we would rather avoid water in an attempt to find terrestrial ice analogue sites for EGC and other planetary ices, we must at least be aware of the effects of water on what we observe. From the preceding subsection it is clear that liquid water plays an important role in ice cap and glacier surficial processes. Still, there are significant periods when conditions are such that all the water is frozen, and what remain are snow, firn and ice structures.

Pure cold ice, as mentioned previously is very transparent to radio waves. A thick, featureless ice cap might thus simply absorb a good deal of the incident radiation. Yoshino (1967) calculated for shortwave-radio wavelengths that a vertical incidence reflection coefficient of about 0.1 was in part responsible for the difficulty in receiving transmissions across the Antarctic continent.

Later studies included grazing incidence backscatter measurements for snow and pack ice at 10 GHz (3 cm) by Hoekstra and Spanogle (Hoekstra and Spanogle, 1972). They report the earliest multiple-polarization measurements of snow and ice known to the author. At θ_i=89° Hoekstra and Spanogle (1972) observe $\mu_1 \sim 10^{-2}$ with σ°(HH) ~ 10^{-5}, and they report σ°(RR) ~ 10^{-6}. They also clearly observed a decrease of σ° by one order of magnitude when the ambient temperature rose from -4°C to 0°C.

Snow is essentially a mixture of pure ice with a dielectric constant of 3.2, and air with a dielectric constant of 1.0. Thus, as water with its high dielectric

constant forms within warming snow, the snow becomes more specularly reflecting. Indeed, Stiles and Ulaby (1980) observe snow emissivity at 10.7 GHz to increase from 0.78 for dry snow to 0.96 for snow with 3.3% volumetric water content ($\%v_m$). For a similar increase in wetness, and at $\theta=50^\circ$, they report σ°(HH) decreasing from -9 dB (0.13) to -17 dB (0.02) while μ_l increases from -4 dB (0.40) to -2 dB (0.63). A similar study by Mätzler et al. (1982) finds the σ°(HH) of wet snow to lie between 0.03 (dry) and 0.004 (wet) at $\theta_i=50^\circ$ and 10.4 GHz, while σ°(HV) remains < 0.001. The discrepancy between these two studies illustrates some of the difficulty in interpreting snow and ice radar information. Nevertheless, the large contrasts between wet and dry snow have made both active and passive microwave remote sensing fruitful tools in snow hydrology.

The elevated μ_l values reported by Stiles and Ulaby (1980) reinforce the importance of understanding the volume scattering contribution from a snow pack or ice. Ulaby (1982) points out that for completely dry snow a representative penetration depth (power e-folding length) of 4 GHz (7.5 cm) radar is up to 30 m, while for 10 GHz (3 cm), 4 m is typical. These penetration depths fall off drastically as did the σ° 's, to 25 cm and 4.5 cm respectively at $3\%v_m$. Ulaby's (1982) plot depends on theoretical assumptions about the dielectric constant of snow. Mätzler et al. (1984) developed a field sensor for measuring snow dielectric properties in situ, discovering certain inconsistencies. To better understand this behavior, Mätzler and Wegmüller (1987) studied the dielectric properties, and in particular the absorptivity, of ice. They observe that the minimum in the imaginary

index of refraction occurs at around 1 cm wavelength, and decreases with decreasing temperature. Mätzler (1996) has applied the earlier work to understand the dielectric behavior of dry snow, determining that the relative permittivity of dry snow is a function of snow density only. Still, tying the theory to remotely sensed measurements is far from straightforward. A further possible complication arises from the terrain backscatter from beneath snow cover, if the snow is not too thick (in the terms just presented). Ulaby et al. (Ulaby *et al.*, 1984) observed that a dry snow layer merely attenuates the cross-section of the underlying terrain. Still, dry snow greater than about 60 cm depth masks the underlying terrain, while 30 cm or less wet snow achieves the same effect.

The combined dielectric properties of both water and ice make the interpretation of radar scattering from a mixed-phase water target both complicated and fascinating. The task is rendered more challenging by mixing rocks into the ice as on a glacier surface, or by re-freeze structures in firn. Hall and Ormsby (1983) compared the value of SAR to Landsat multispectral visible data for Alaskan glaciology. The joint use of visible and radar data proved fruitful, though SAR's only advantage was in the identification of roughened crevasse regions.

Rott and Mätzler (1987) point out that the all-weather capabilities of SAR outweigh interpretation advantages of visible systems. Further, they point out that for mountainous regions, look angles of 40° to 50° alleviate layover difficulties, as experienced by Hall and Ormsby (1983). Still, in mountainous regions, Rott and Mätzler (1987) suggest that SAR is better suited to mapping snow-cover than to

detailed mapping of glaciers due to the topographic complications. They further point out that while SAR can discriminate between snow and bare ice on glaciers, it is not as straightforward as with visible images. They also point out that SAR can penetrate dry snow and probe firn structures, and also determine the location of wet and dry snow zones in the accumulation zone.

Fily et al. (1995) follow Rott and Mätzler's (1987) suggestion of examining snow-cover in mountainous regions with SAR. Beause Fily et al.'s (1995) SAR was airborne, their images required significant geometric corrections, which are not as important for a spaceborne instrument. Fily et al. (1995) determined that SAR was not sensitive to a thin layer of dry snow, but detected variations in underlying soil moisture and evidence of regional faults, consistent with Ulaby et al. (1984). They concluded that comparison between snow-free and snow-covered scenes would be most useful, but require careful calibration of the SAR.

Shi and Dozier (1997) examined the use of SAR to map snow cover in mountainous areas. One of their techniques requires a digital elevation model, but a second does not. They discriminate wet snow from bare surfaces and dry snow from short vegetation. The significant contribution of Shi and Dozier (1997) is the use of multiple polarization SAR data in developing their classification model. However, the application of their classification tree for snow-cover mapping required extensive field mapping, and was finally only 77% as accurate as classification with Landsat Thematic Mapper (TM) data.

The accuracy of SAR image interpretation of snow and ice is sufficient and appropriate when mapping areas much larger than a single catchment basin, or when the field information simply does not exist. Bindschadler and Vornberger (1992) used 23.5 cm L-band single polarization Seasat SAR in conjunction with Landsat TM images to examine the Greenland ice sheet. They detected the snow line in the October SAR imagery, and also noted that high backscatter from bare ice regions corresponded to crevasse zones, though the crevasses were unresolved in the SAR images. Penetration of the L-band signal into the ice seems to have blurred features in the images. Water above the snow line reduced backscatter, and Bindschadler and Vornberger (1992) note that this "permits the use of backscatter variations as a proxy indicator of surface topography in snow-covered regions experiencing melt." The Seasat observations (Bindschadler *et al.*, 1987, Bindschadler and Vornberger, 1992) spurred SAR observations of Greenland by demonstrating that the different snow zones could be distinguished, and monitored. Fahnenstock and Bindschadler (1993) proposed an ice sheet margin monitoring program with the European Space Agency ERS-1 SAR.

The layered nature of firn leads to layer models often being proposed to explain radar returns from snow pack, glaciers and ice caps. Long and Drinkwater (1994) present ice zone mapping with 6-km resolution Seasat 2-cm scatterometer data. While of much lower spatial resolution than SAR, the scatterometer data cover a wide range of θ_i over much of Greenland. Long and Drinkwater (1994) are thus able to propose 2- and 3-layer models and simulations to explain the

radar behavior of the Greenland ice cap. The models aid in classifying and mapping the different snow zones.

Jezek et al. (1993) analyzed the first multi-frequency and polarimetric SAR study of the Greenland ice sheet[¶¶]. Their data were collected in late August at P-, L-, and C-bands by the Jet Propulsion Laboratory (JPL) airborne SAR (AIRSAR). The 5.7 cm C-band wavelength is found to be the most sensitive to delineating boundaries of snow zones based on changing snow wetness. Jezek et al. (1993) produce a combined surface and volume scattering model that reproduces the C-band behavior in particular, but without substantiation of the model parameters such as grain size. In general dark areas are wet and exhibit surface scattering while bright areas are dry and volume-scattering is dominant. P-band (68 cm) behavior is proposed to be due to volume scattering from ice pipes and lenses, but no corroborative model is offered.

AIRSAR observations of Greenland were repeated in 1991. On that occasion, circular polarizations were also synthesized from the data and Rignot et al. (1993) discovered that the percolation zone exhibits EGC-like radar properties,

---

[¶¶]Another significant multifrequency polarimetric study of ice other than the Greenland work is Drinkwater et al.'s (1991) observation of Beaufort, Bearing and Chukchi Seas sea ice. While the evolution and variety of sea ice goes beyond the discussion here, their analysis can be of general comparative value. For rough surface scattering of C-band from thick first year ice at θ_i=39°, polarization ratios of μ_l=0.03 and μ_c=0.25 can be read from Drinkwater et al.'s (1991) polarization response plots. For Bragg scattering at C-band from thin first year ice at θ_i=48°, μ_l=0.1 and μ_c=0.75. Much effort has gone into the modeling of rough-surface scattering as it applies to sea-ice (e.g. Fung and Eom 1982, Bredow et al. 1989, Drinkwater 1989, Livingstone and Drinkwater 1991)

in particular at 5.6 and 24 cm. The general behavior of the Rignot et al. (1993) measurements as a function of θ_i are plotted in Figure 4.3.

A direct comparison of Fig. 4.3 with Fig. 4.1 shows that in fact the details of the Greenland radar properties are quite different from those of EGC. Rignot et al. (1993) point this out firmly. Whereas the percolation zone properties, averaged over θ_i might be similar to the disk-averaged EGC properties, the 24 cm Greenland σ° is much lower than the 5.6 cm σ°, and 68 cm P-band does not present the EGC signature at all. EGC radar properties on the other hand are

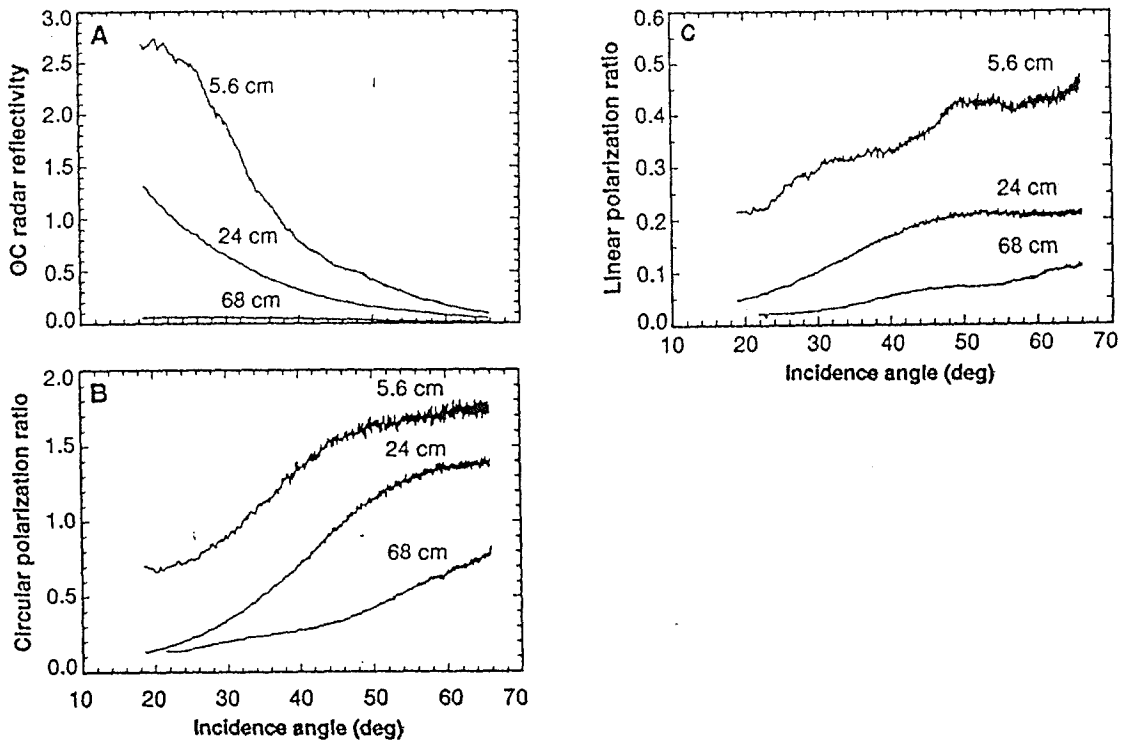

Figure 4.3 General behavior of a) σ°(RL), b) μ_c, and c) μ_l for AIRSAR measurements of the Greenland ice cap in the percolation zone as a function of incidence angle θ_i. After Rignot et al. (1993) Fig.2

apparently maintained from 3.5 cm out as far as 70 cm. Furthermore, while for EGC, μ_c exceeds unity over the whole disk, and therefore all incidence angles, the percolation zone only exhibits the behavior at $\theta_i \geq 30°$. Various lines of evidence including emissivity models of ice inclusions (Zwally, 1977), and surface-based radar observations (Jezek *et al.*, 1994) define the smoking gun responsible for the percolation zone radar behavior. It is in fact the refrozen ice inclusions in the firn that are responsible. Rignot (1995) developed a fairly successful scattering model for the ice pipes and lenses that traces the large radar reflectivities and polarization ratios to internal reflections within the icy inclusions. In the final analysis however, while the Greenland result is exciting, and provides an important analogy for EGC, it is not a complete analogy, as it does not address the EGC behavior at small incidence angle.

4.1.4 High Altitudes

The initial intent in looking for high altitude ice sites was to seek locations where liquid water might not affect the ice structure, to find other, different, and perhaps better analogues for the behavior of cold ices on airless bodies. The highest mountains on Earth do rise up to heights, above about 5500 m, where the ambient pressure is less than half that at sea level. The temperature lapse-rate in the troposphere is around 6°/km (Holton, 1992). Starting from a mean sea-level surface air temperature of 20°C, -4°C is reached at elevations above 4000 m. An annual mean surface air temperature of 20°C or colder is found at latitudes north and south of about 30° (Peixoto and Oort, 1992).

Benson (1962) carried out similar extrapolations to define the mean annual temperatures on Greenland that correspond to the borders between the various snow zones. The dry-snow line always lies above (in elevation) a mean annual isotherm, $\overline{T}$=-25°C, while the snow line lies approximately at $\overline{T}$=-10°C (Benson, 1962). Benson (1962) points out however, that the important temperature for mapping zone boundaries is not the air temperature so much as the ice temperature, and specifically the depth of the melting isotherm, which depends very much on the temperature history during the melting season. Thus, while dry snow conditions at 30°N may be unlikely based on $\overline{T}$=-25°C because there are no 8000 m peaks, local effects of microclimates and sun-shadowing could produce locally favorable conditions.

Patterson (1994) relates the heat-budget behavior of the accumulation zone of the Greenland Ice Sheet. He notes that the snow albedo and surface temperature, with long-wave emission and evaporation conspire to reduce the rate of warming of the snow. Applying this to locales that remain shadowed or partially shadowed during spring, we might hope to observe Greenland EGC-like radar behavior on mountain ice caps and glaciers. If they can be observed when the firn is cold (<-5°C), Greenland-like radar behavior may be observed, or perhaps some other features will appear.

4.2 SIR-C

4.2.1 Full Polarization SAR

Two Space Radar Lab missions of the Space Shuttle Endeavor flew in April and October of 1994 (SRL-1 and SRL-2 respectively). They carried the Shuttle Imaging Radar / X-band Synthetic Aperture Radar (SIR-C/X-SAR) instrument payload. The SIR-C instrument gathers linear polarization information in HH, HV, VV and VH polarization combinations for both C-band (5.7 cm) and L-band (24.0 cm) wavelengths (Stofan *et al.*, 1995). SIR-C can record all four polarization combinations simultaneously to acquire full polarization information, dubbed "quad-pol" mode, officially labeled mode-16. The X-SAR instrument measures X-band (3 cm) VV only. SIR-C data is freely available while X-SAR data must be purchased, and so, since it provides no polarization information, X-SAR data was not acquired for this study.

SIR-C full polarization information is distributed as a compressed form of the Stokes matrix, or Stokes scattering operator[§§] Decompression produces the 4x4 symmetric real scattering operator matrix for each measured pixel. From the Stokes scattering operator data, the radar polarization response of any pixel, or group of pixels can be synthesized. In this manner, the signal backscattered from the terrain recorded in the four fixed linear combinations, allows any particular backscatter polarization to be reconstructed. Applying this technique, data from

---

[§§]This text follows the scattering nomenclature and definitions of Van Zyl (1990).

SIR-C mode-16 tracks can be used to synthesize both C-band and L-band OS and SS circular-polarization σ° 's for terrestrial terrain.

4.2.2 Data selection

To examine the circular polarization properties of terrestrial sites, only full polarization SIR-C data provides widespread global coverage. However, while AIRSAR has been used in Greenland (Jezek *et al.*, 1993, Rignot *et al.*, 1993) and Alaska, SIR-C coverage is limited to +/-57° latitude. Since polar regions are excluded, high elevations are sought to examine ice radar properties. On SRL-1, 207 quad-pol tracks or data-takes (DT's) were planned, while for SRL-2, the number was 211. The high-altitude criterion reduces this set to 19 SRL-1 quad-pol DT's and 27 SRL-2 quad-pol DT's. The list of these 46 tracks with high elevation coverage is presented in Appendix D. Figures 4.4, 4.5, and 4.6 show the geographic locations of the high altitude tracks.

Some of the tracks in Fig. 4.4 to 4.6 sample areas where SIR-C data has been analyzed to investigate snow and ice properties. Shi and Dozier's (1997) work mentioned earlier used SIR-C quad-pol data. Although they did not specifically address the circular polarization behavior of their site, they did use an optimization of polarization parameter selection (Van Zyl *et al.*, 1990) to enhance the contrast between dry snow and short vegetation. Forster et al. (1996) used SIR-C data to examine the South Patagonian Icefield (SPI). They successfully classified the various ice and snow zones based on linear polarization data only in conjunction with extrapolated data from a weather station some 100 km away

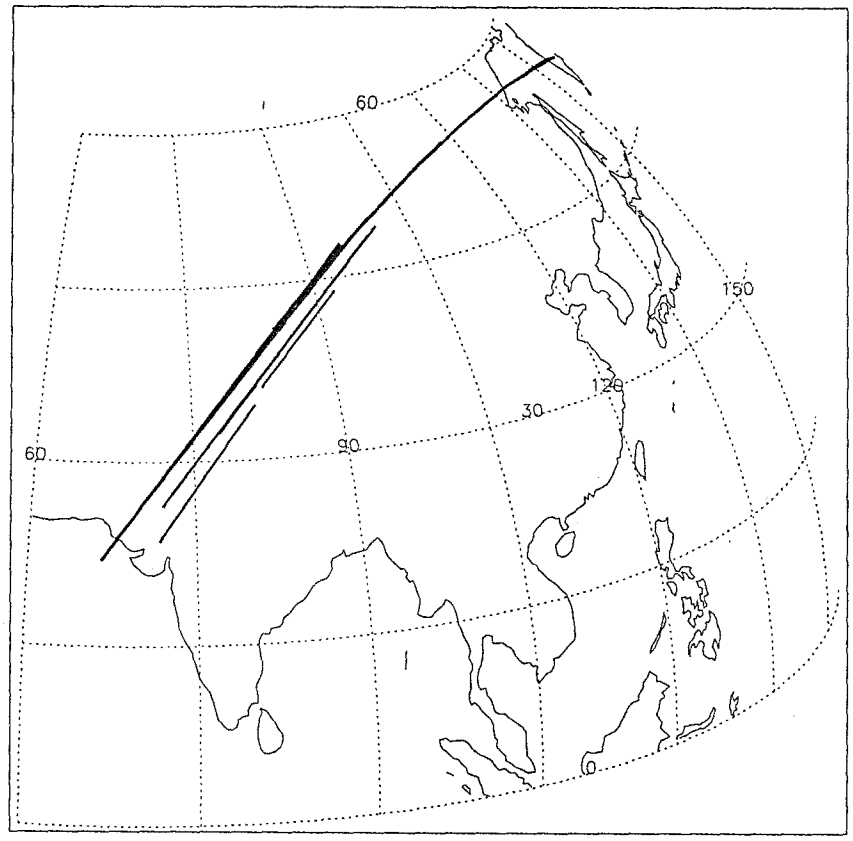

Figure 4.4 Quad-pol SIR-C tracks over the Himalayas, Tibet, and Tien Shan.

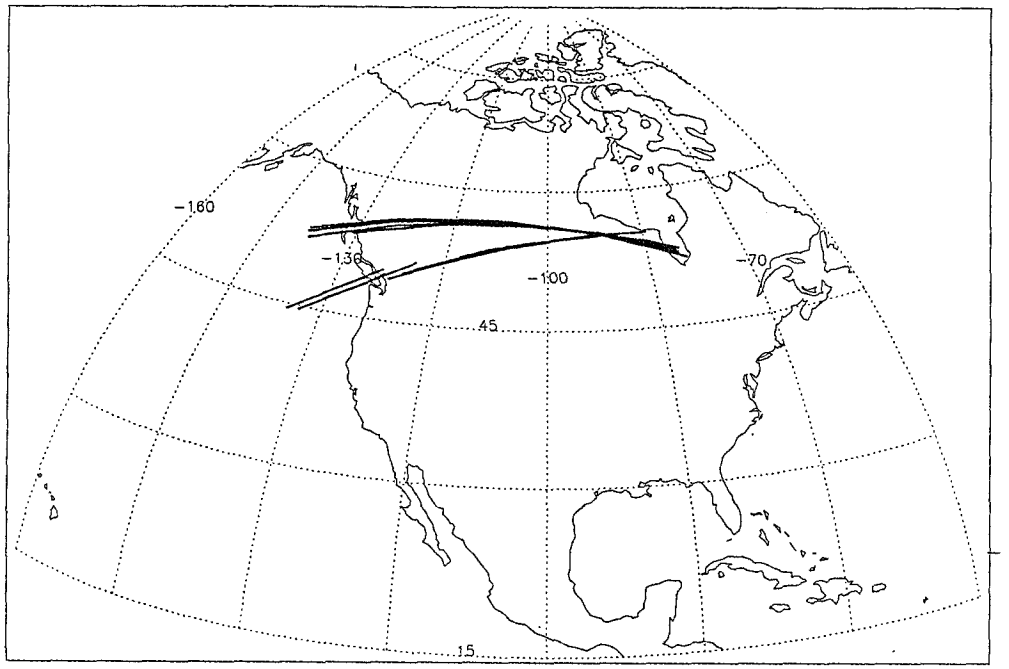

Figure 4.5 Quad-pol SIR-C tracks over the northern Rocky Mts.

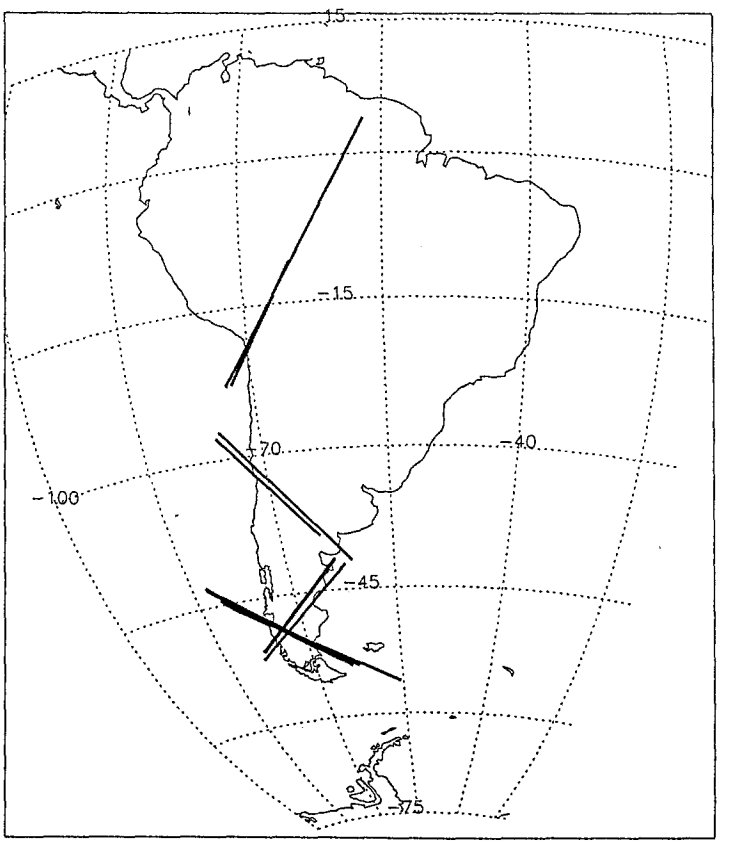

Figure 4.6 Quad-pol SIR-C tracks over the Andes and Patagonia.

from the imaged locations. The present study is similar to Forster et al.'s (1996) approach, although the intention is to examine ice circular-polarization properties specifically, and higher elevation sites in particular. Also, the SPI is not strictly speaking "high-altitude," reaching elevations of only 2.5 km. It's location at higher latitude suggested its inclusion in Appendix D and Fig. 4.6.

Certainly, only small portions of the DT's depicted in Figures 4.4 to 4.6 actually cross over terrain near or above 4000 m. Individual SIR-C scene images were ordered only after many radar track locations had been plotted on Defense Mapping Agency (DMA) 1:1,000,000 scale Operational Navigation Charts (ONC) or 1:500,000 scale Tactical Pilotage Charts (TPC) to determine likelihood of glaciers or ice cap data. In the end, two sites were retained.

Table 4.1
SIR-C datatake selections for high altitude ices

DT	Name	Orbit direction*	Illumi-nation**	θ_i
SRL1:				
58.10	Hotien East, China	A	S	29.00°
SRL2:				
40.60	Cerro Aconcagua, Argentina	D	S	34.60°

* A, ascending orbit; D, descending orbit
** S, illumination toward south; N, illumination toward north.

The two locations are scenes from SRL-1 DT 58.10 (Kunlun Mts., Tibet), and SRL-2 DT 40.60 (Central Andes Mts.). The track parameters for the sites are summarized in Table 4.1. The selection of these sites was determined mostly by convenience, and therefore involves some indeterminate randomness. For example, it proved impossible to obtain either the ONC's or TPC's for Western Canada in a timely fashion. Therefore, all Rocky Mountain SIR-C DT's were ignored, even though it might later have been easier to obtain high resolution terrain and glaciological information for these regions. In fairness, the lower elevations of the Rockies was also a factor in dismissing those tracks at an early stage of the study.

4.2.3 Data Processing

The Stokes scattering operator data decompression for the selected scenes, was carried out with a JPL-supplied software package. Image processing and analysis were performed with the ER Mapper commercial software package. More details of the data preparation are given in Appendix E along with results from processing of a test scene. A quad-pol scene of Death Valley, California, was processed in addition to the two chosen high altitude scenes. The Death Valley data, prepared and analyzed in the same manner as the Andes and Tibet data, are compared to previously published results (Greeley and Blumberg, 1995, Weeks *et al.*, 1997, Weeks *et al.*, 1996). The comparison indicates that the image preparation and processing methods are sound.

Image processing and data manipulation are carried out on σ° 's. Uncertainties on the σ° 's arise from SIR-C calibration uncertainties. These values

have been published (Freeman *et al.*, 1995), and are presented in Appendix E. In general it is assumed that within a scene σ° 's have 30% uncertainty (~ 1 dB). This uncertainty will be implicit in what follows. Error bars reported on σ° statistics and scattering laws will be based on root-mean-square standard deviations of the population of σ° 's considered.

4.3 Kunlun Shan

4.3.1 Geography

SIR-C DT 1/58.10 called Hotien East lies over western Tibet[††] and the Tarim basin. Figure 4.7 after Shih et al. (1980) maps the distribution of glaciers in the region. The mountain range called Kunlun Shan lies around 35°N and stretches from 75°E to approximately 95°E, forming the border between the Tibetan plateau and the Tarim basin in western China (Zuhui, 1990). The western portion of the Kunlun Shan (W of 80°30'E) is reported as having 3180 glaciers covering an area of 4331 km^2 (Li and Cheng, 1980, Shih and al., 1980). Many of the valley glaciers in the region are 20-30 km long (Li and Li, 1991). Figure 4.8 shows the main glacier area of the western Kunlun Shan. The location of the scene selected for study is plotted on Fig. 4.8. It should be noted that the glaciers of the Tibetan plateau are the source of the Yellow, Yangtze, Ganges and Indus

[††]The Tibetan plateau is known as the Qinghai-Xizang plateau in Chinese, but the common western usage is followed here.

rivers, and thus are of great climatological interest to a significant portion of humanity!

Recent joint Chinese-Japanese glaciologic expeditions have studied the glaciers north of Gozha Co. (Watanabe and Zheng, 1987). These glaciers on the south slope of the western Kunlun Shan drain into Gozha Co, and Aksayqin Co 100 km to the west. Zhang and Jiao (1987) give a detailed report of precipitation

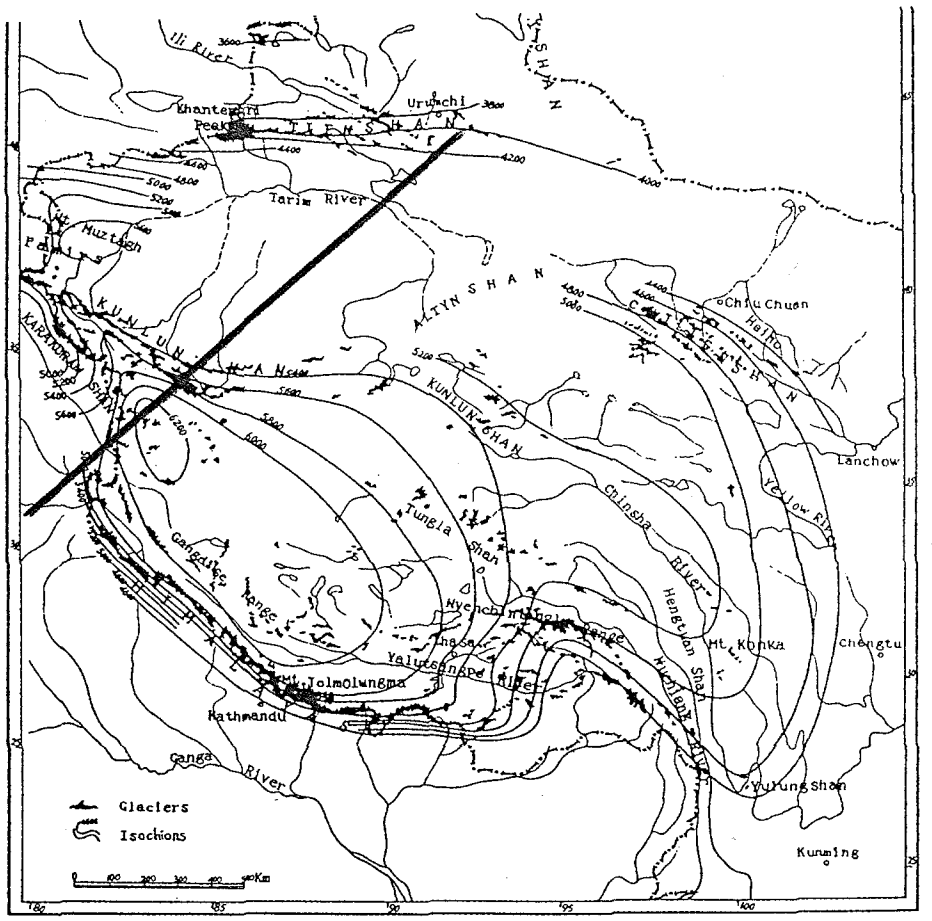

Figure 4.7 Map of the distribution of glaciers in western China. SIR-C DT 1/58.10 is plotted on the map, crossing the Kunlun Shan on the western Tibetan plateau, and then dropping into the Tarim basin. Regional snow line elevation is also shown on the map. After Shih et al. (1980).

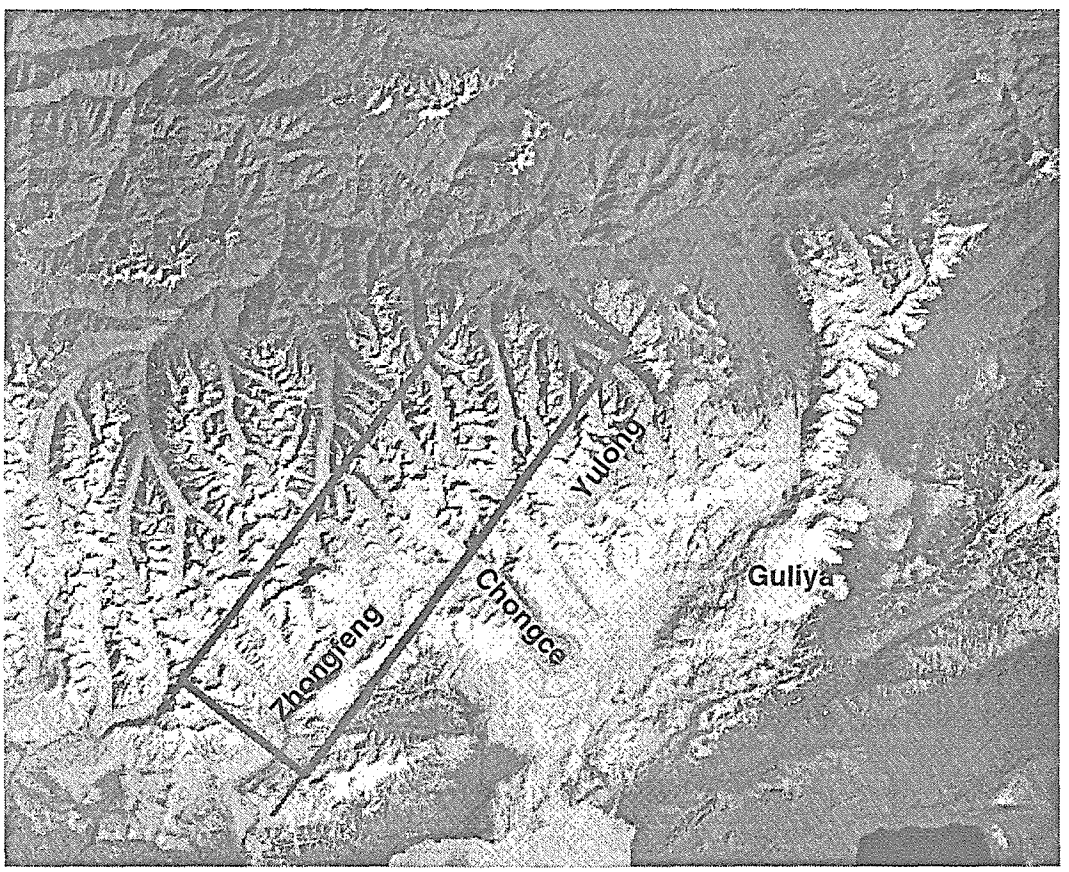

Figure 4.8 Landsat image mosaic of the Western Kunlun Shan. Image from around 1980 (T. Farr personal communication). Geographic locations are labeled. Sub-glaciers are numbered in roman numerals for each glacier drainage basin proceeding clockwise from the left-most glacier as seen going up the main channel.

patterns and drainages for the region. Zheng (1987) outlines the glacial paleogeography of the region and provides 1:200,000 scale topgraphic maps of the Zhongfeng Glacier and Chongce Glacier and Icecap drainage areas. More detailed 1:50,000 scale topographic maps of the Chongce Icecap were produced (Chen *et al.*, 1989), in aid of ice coring studies caried out there (Nakawo *et al.*, 1989). The ice core analyses (Han *et al.*, 1989) and the ice formation studies (Ageta *et al.*, 1989, Xie and Zhang, 1989) carried out by these expeditions provide some measure of ground truth for the radar measurements.

The north slope of the western Kunlun Shan unfortunately does not appear to have been as intensively studied as the south. There, information is limited to 1:200,000 scale Russian topographic maps made from airphotos dating from 1969 to 1973. These maps should be used with caution as Shih et al. (1980) point out that after retreating from the mid-1950's to the late 1960's, glaciers in the western Kunlun Shan were observed to be advancing in the late 1970's. Furthermore, the Russian maps disagree with the more recent Chinese topography by up to 200 m on the slouth slope. The Chinese contours are generally 80 m higher than the Russian contours, so assuming the relative contouring on the Russian maps is valid, we can extrapolate north slope elevations from the Chines contours on the south slope.

Additional Kunlun Shan glaciological information of a comparative nature is available from studies of the Guliya Icecap 30 km to the west of the Chongce Icecap (Thompson, 1996, Thompson *et al.*, 1995).

4.3.2 SAR Images

The image parameters for the L- and C-band scenes selected from DT 1/58.10 are listed in Table 4.2. A processed σ°(CRL) image is shown in Figure 4.9. Glacier names are labelled in Fig. 4.9, and the topographic contours from the Chinese maps have been drawn over the glaciers of the south slope drainages. The most prominent characteristic of the image is the increasing cross-section with altitude. The data appears to be of good quality. In particular for this mountainous region, there does not appear to be much layover or shadowing

The images for all the polarizations were examined. All the images display increasing σ° with altitude moving up the glaciers. While the different polarizations all increase with altitude, to interpret the radar scattering mechanisms and thereby infer ice properties we are interested in their relative behaviour of the different σ° 's.

4.3.3 Radar Cross-sections

A first assessment of the altitude behavior of the various different polarizations was performed by examining scattering behavior moving up the glaciers. Statistics were collected for wide regions (>1 km^2) at every 1000 m interval, and are plotted for the Zhongfeng Glacier in Fig. 4.10, and for Chongce Glacier in Fig. 4.11. Incidence angle variation was not considered for these plots, but will be investigated below.

Table 4.2

SIR-C Hotien East quad-pol scene processing parameters.

DT:		1/58.10	
Name:		Hotien East (Map 1), China	
Track angle:		40.69°	
Image center:		35.438°N, 80.966°E	
Time:	GMT	1994/102:23:36:19.7	
	Local*	05:06:19.7, April 13th, 1994	
Scenes:	L-band (24.0 cm)	pr14912	
	C-band (5.66 cm)	pr14913	
θ_i:	near range	29.042°	
	image center	31.161°	
	far range	33.083°	
Shuttle roll angle:		25.959°	
Near slant range:		245.4561 km	
Scales:		range	azimuth
	Slant range scene:	10.254 km	49.996 km
	Slant range pixels:	1539	9599
	Slant range pixel size:	6.662 m	5.208 m
	Ground range scene:	19.816 km	49.996 km
	Ground range pixel size:	12.876 m	5.208 m
	Multilook multiplier	2	5
	Multilook pixels:	769	1919
	Multilook pixel size:	25.75 m	26.04 m

*Local time reported here is not Chinese time zone, but Indian time zone, which is closer to the true local time in the western Kunlun Shan.

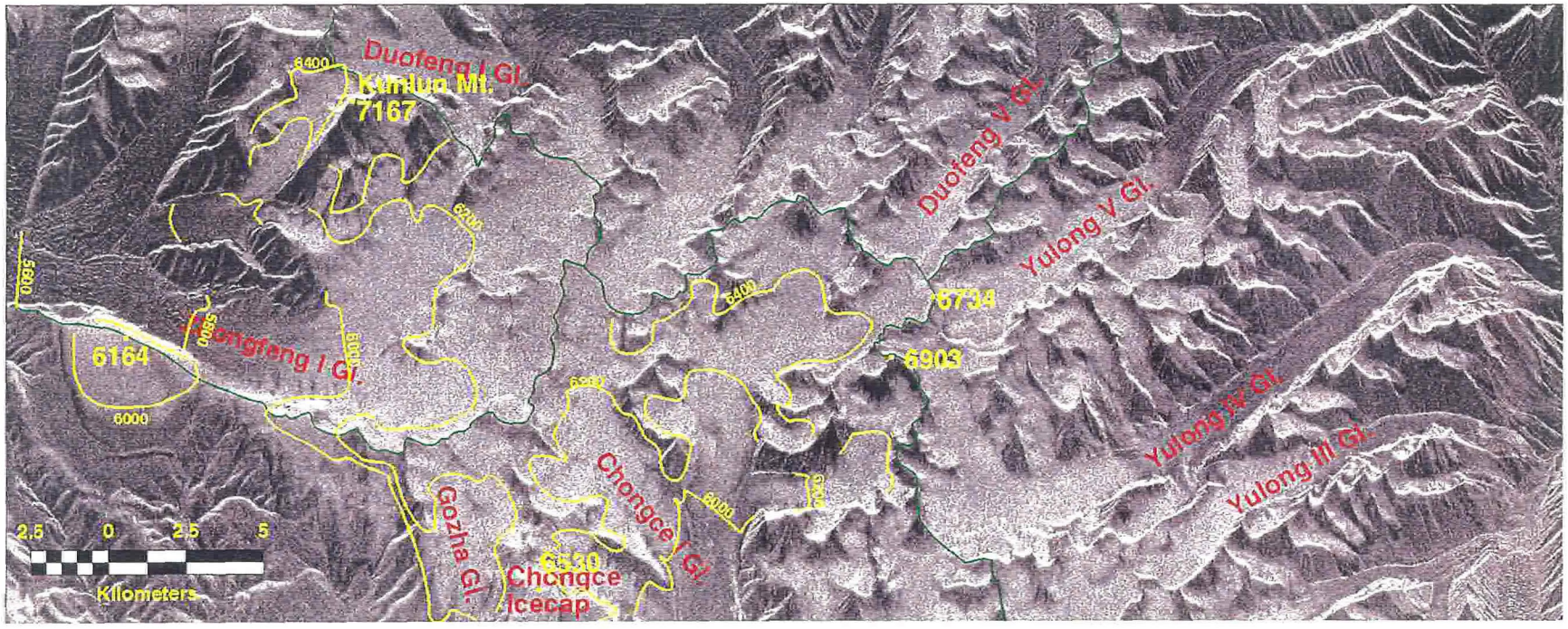

Figure 4.9 SIR-C DT 1/58.10 scene pr12061 σ°(CRL). Glacier drainages are separated by the green line. The yellow topographic contours are from the Chinese maps for the western Kunlun south slope.

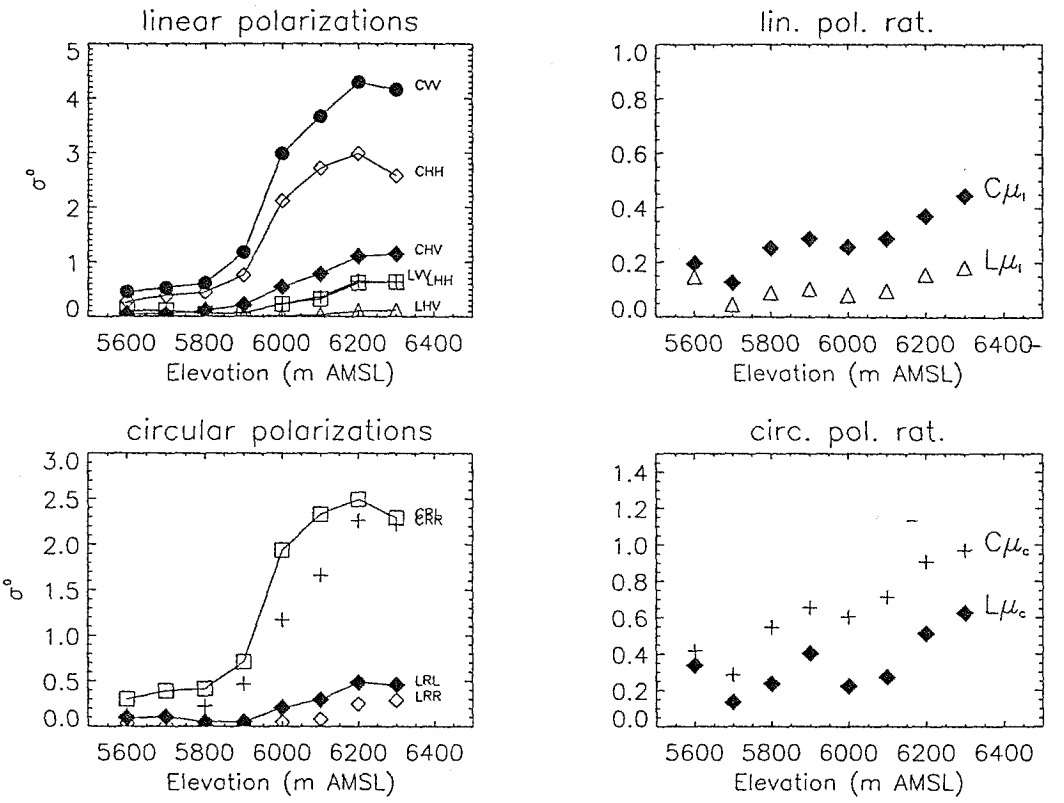

Figure 4.10 Plots of average radar scattering behavior at different altitude on Zhongfeng Glaciers I and Ia. Statistics sampling regions are plotted on Fig. 4.12.

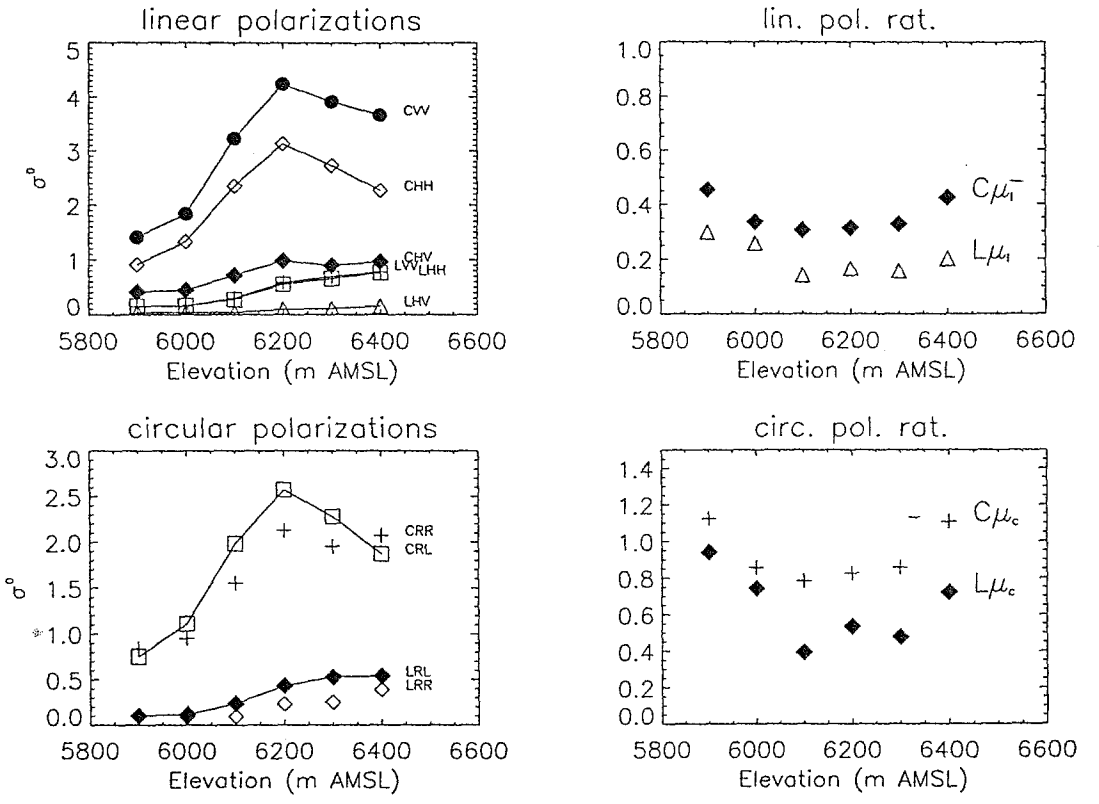

Figure 4.11 Plots of average radar scattering behavior at different altitude on Chongce Glaciers I II and III. Statistics sampling regions are plotted on Fig. 4.12.

The C-band σ°(RL) values reach levels at 6200 m that are perhaps 2 or 3 times the average values observed by Rignot et al. (1993) over Greenland at similar incidence angle ($\theta_i \sim 30^{\circ}$). The highest L-band σ°(RL) values on the other hand are quite close to the level Rignot et al (1993) reports. These maximum σ° levels in circular polarization occur in concert with maxima in the linear polarizations. The maximum linear cross-sections in both L- and C-bands are an order of magnitude larger than what Forster et al. (1996) found on the SPI in either fall (April) or summer (October) for their brightest scattering snow zone. The cross-polarized linear channel σ° 's are around 10% (-10 dB) of the co-polarized σ° 's, which is consistent with Stiles and Ulaby's (1980) observation for dry snow.

A direct comparison with Forster et al. (1996) is made in Fig. 4.12. The σ° 's of CHH, LHH and LHV are converted to dB and assigned to red, green and blue respectively, as described in the Fig. 4.12 caption. The image is predominantly orange where it shows any color at all. In these orange regions CHH is dominating over LHH while LHV is insignificant. The colorless white regions have elevated σ° 's in all three bands, at least within the limits of the chosen linear stretches. The orange regions can be ascribed to Forster et al.'s (1996) zone A: dry-snow with C-band volume scattering. At the time of Forster et al.'s "orangest" image (Forster *et al.*, 1996, Plate 2), the SPI had been below freezing temperature for several days in late winter (Oct. in the southern

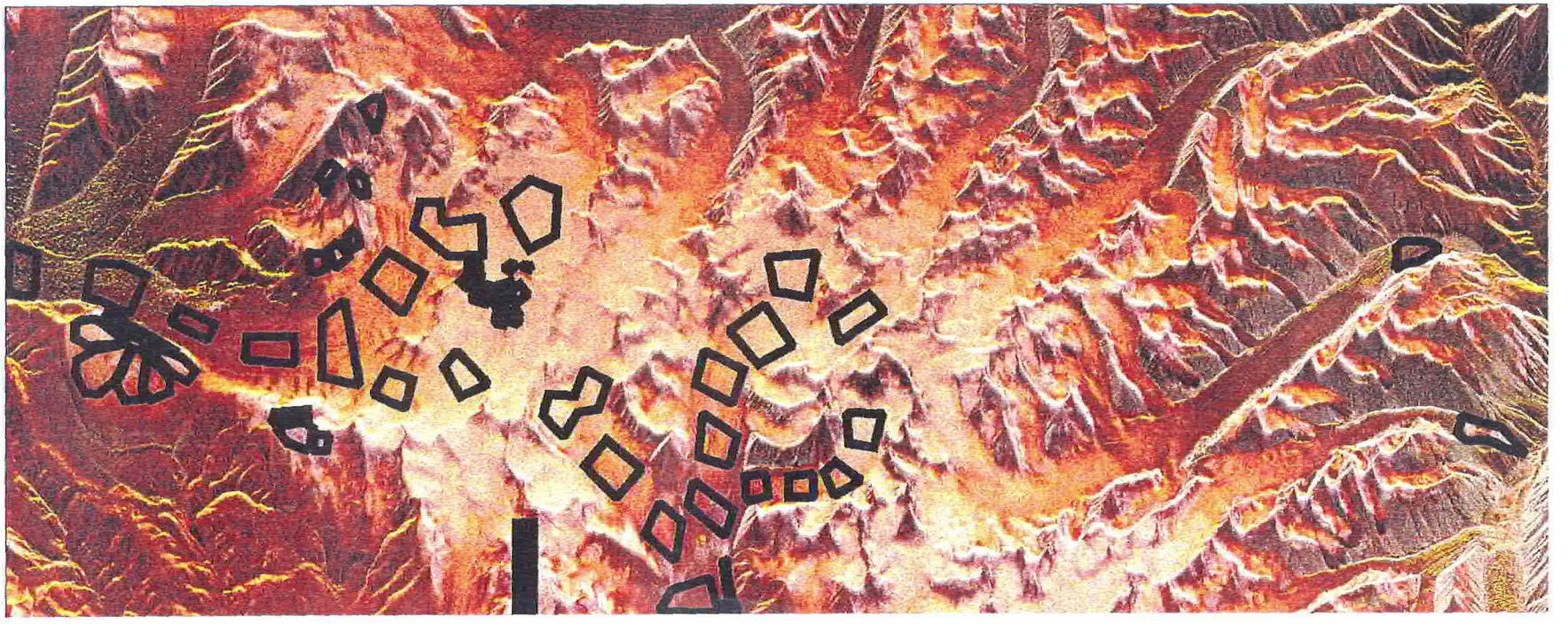

Figure 4.12 Kunlun Mtn. scene from SIR-C DT 1/58.10 with linear polarization linear stretch (255 value) color assignment to: red (C-band σ°(HH) from -35 to 5dB), green (L-band σ°(HH) from -35 to 5dB), and blue (L-band σ°(HV) from -45 to -5dB). Color assignment Follows Forster et al.'s (1996) study of the South Patagonian Icefield. The polarization choices were based in their case on the three least correlated channels. The black outlines on this Fig. show the locations of sampling sites for calculating scattering statistics.

hemisphere), which is a similar condition to the Kunlun Mtn. region considered here. However, it should be noted that DT 1/58.10 was taken early in the morning when the firn would be colder, and so we might expect that the near-surface conditions, dominating C-band in particular may have been particularly favorable to volume scattering.

4.3.4 Polarization Ratios

The μ_l behavior at C-band in Fig.4.10 seems to indicate volume scattering μ_l>1/3, while the ratio is somewhat subdued at L-band on both glaciers. The μ_c behavior is similar at the higher elevations on both glaciers arriving at μ_c=1 above 6200 m. The μ_c behavior on the lower reaches of the Chongce glacier appears unique from that exhibited by Zhongfeng, or indeed other glaciers in Fig. 4.9. This will be examined in more detail later.

The ratio CVV/CHH also serves as an indicator of surface vs. volume scattering (Forster *et al.*, 1996). CVV/CHH near unity, as it is below 6000 m on both glaciers, is consistent with volume scattering from spherical snow grains. The CVV/CHH ratio increases to around 1.3 at the top of the ice fields. A value as high as 1.6 might indicate surface scattering.

The regional behavior of the polarization ratios is plotted in Figs. 4.13 to 4.17. The first two plots show μ_c. Red color indicates μ_c>1, while green shows 0.25<μ_c<0.7, and blue indicates$_c$ μ <0.25. The color-coding on the linear polarization plots in Figs. 4.15 and 4.16 are red for μ_l>0.35, green for 0.2<μ_l<0.35, and blue for μ_l<0.1. The ratios are calculated at each pixel based on median 5x5

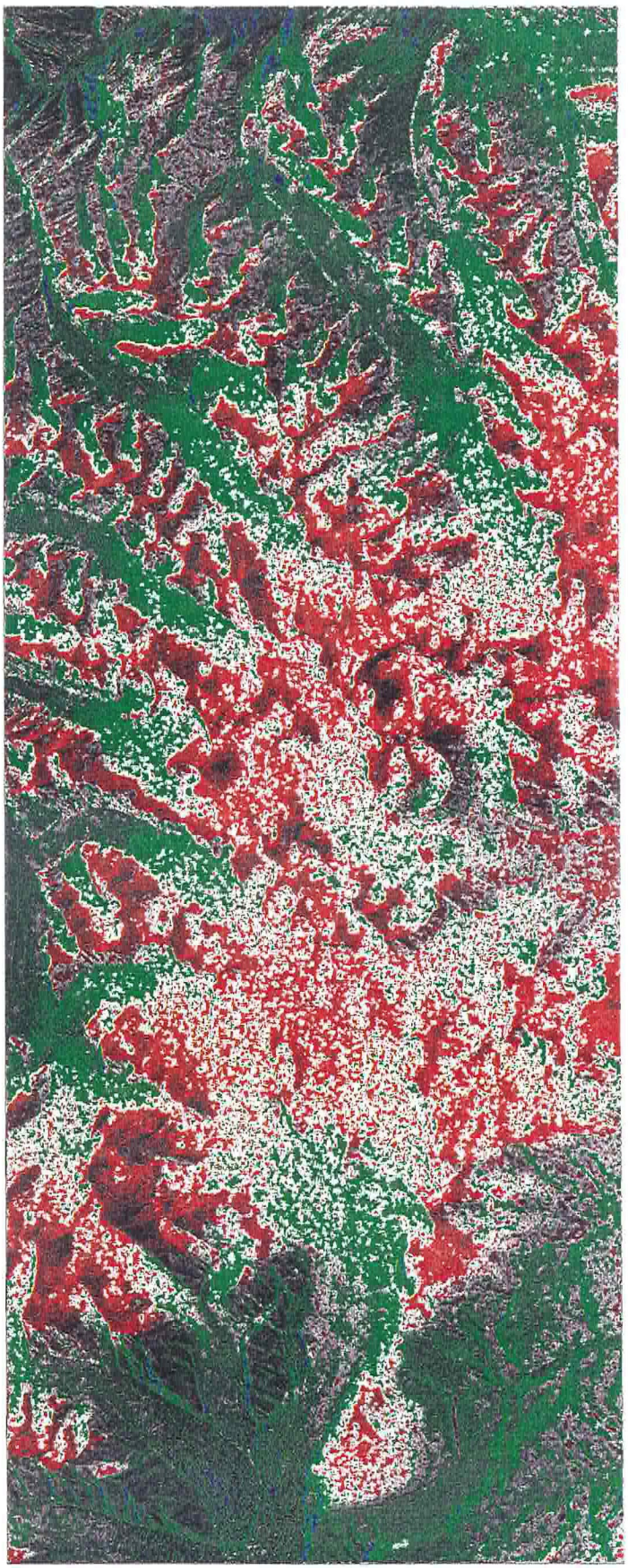

Figure 4.13 Regional C-band circular polarization ratio behavior in DT 1/58.10 Kunlun Mtn. scene. Color assignments are: red for $\mu_c > 1.0$, green for $0.25 < \mu_c < 0.7$, and blue for $\mu_c < 0.25$.

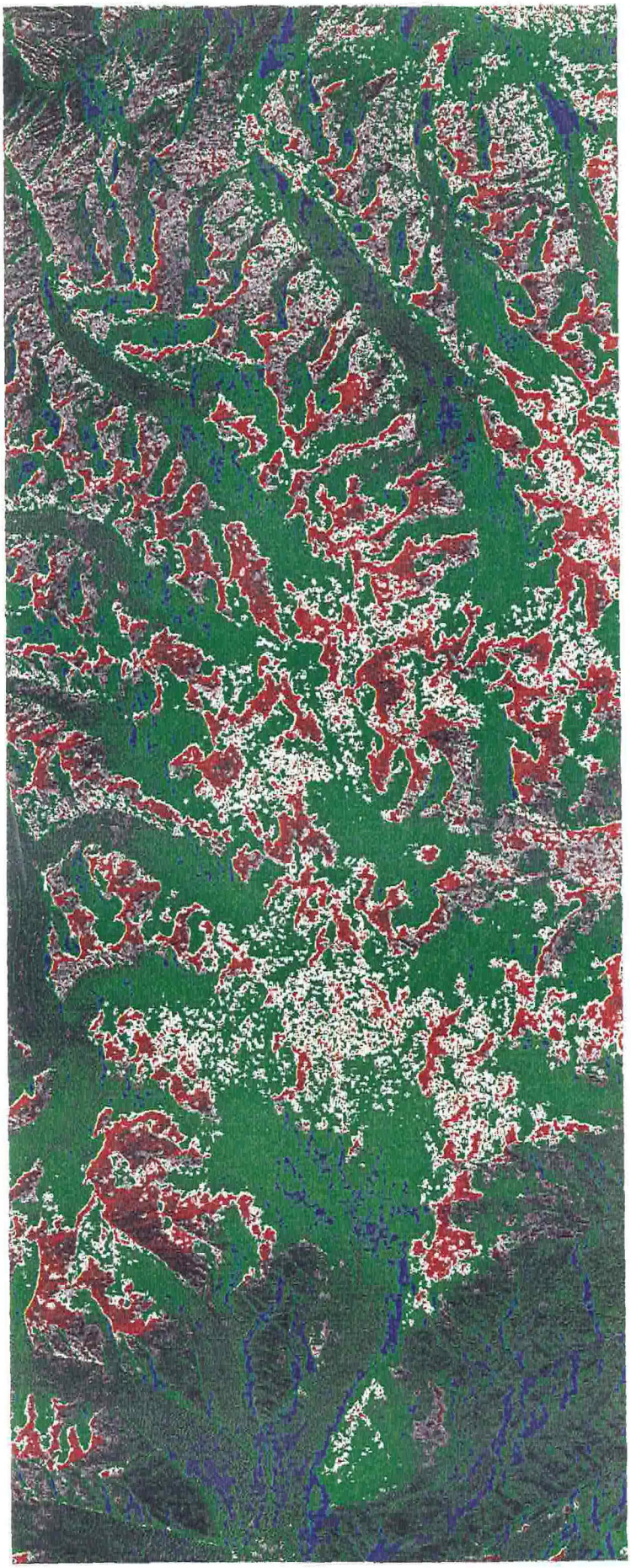

Figure 4.14 Regional L-band circular polarization ratio behavior in DT 1/58.10 Kunlun Mtn. scene. Color assignment as in Fig. 4.13.

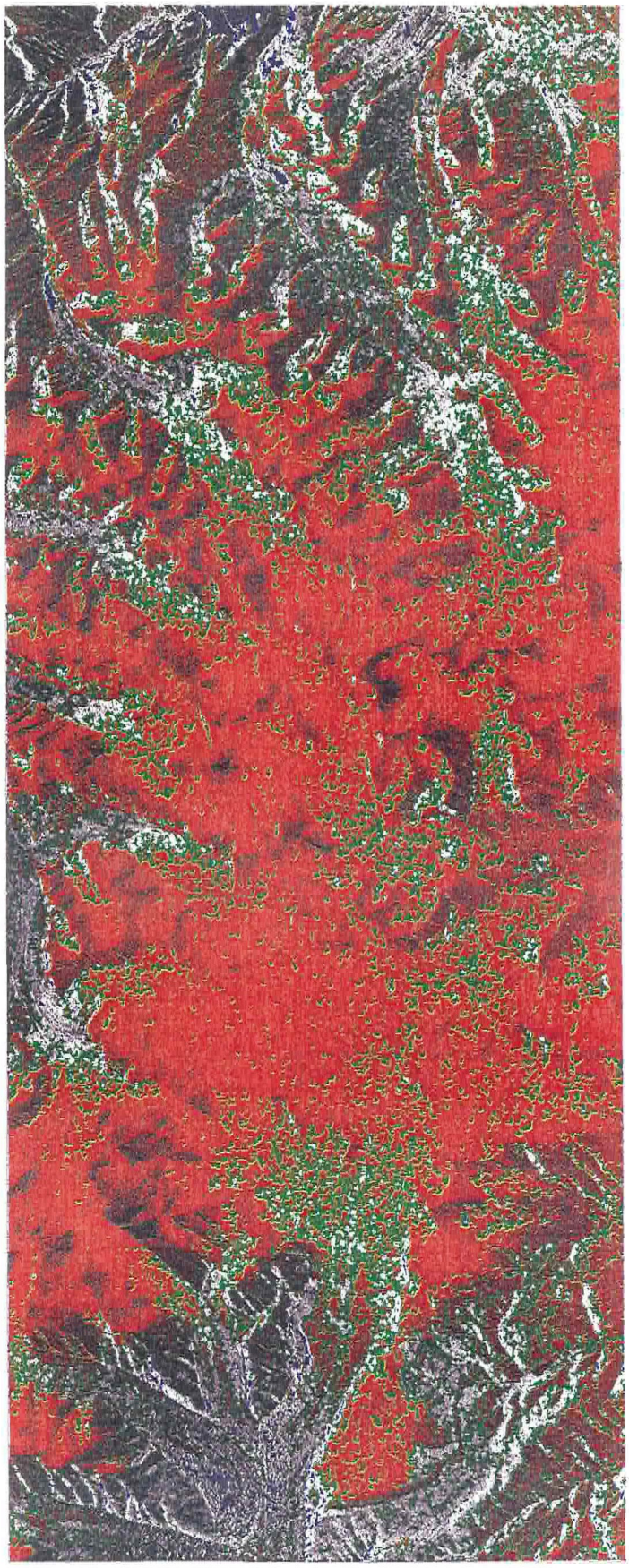

Figure 4.15 Regional C-band linear polarization ratio behavior in DT 1/58.10 Kunlun Mtn. scene. Red color indicates $\mu_c > 0.35$, while green shows $0.2 < \mu_c < 0.35$, and blue indicates $\mu_c < 0.1$.

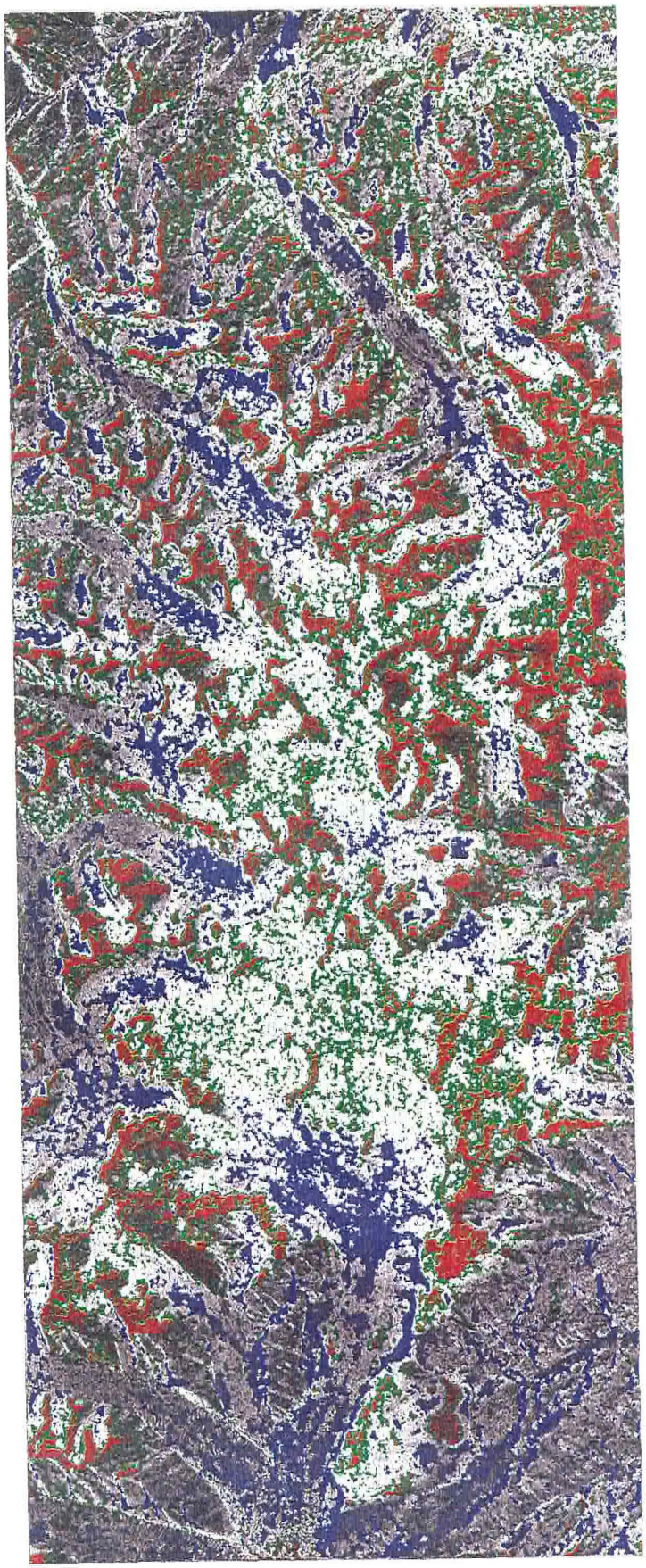

Figure 4.16 Regional L-band linear polarization ratio behavior in DT 1/58.10 Kunlun Mtn. scene. Color assignment as in Fig. 4.15.

filtered values of the σ° 's. The striking feature in all these polarization ratio figures is that the highest mountain slopes are red. In particular the highest feature in the scene, Kunlun Mt. displays the most obvious μ_c inversion feature.

4.3.5 Scattering Behavior

Forty-seven locations were chosen where slope reconstruction appeared feasible from the Chinese topographic maps (Zheng, 1987). The locations of these sites are also shown in Fig.4.C.3. Twenty sites were traced in radar range direction over the summit of the Chongce Icecap. A further twelve sample the radar data in the central portions of the Zhongfeng I Glacier's upper accumulation area. Six sites are located on the slopes around Kunlun Mt. west of Zhongfeng I. Another nine on the ice caps east of Zhongfeng I that are above 6000 m and exhibit high polarization ratios in Figs.4.13 to 4.14. The local groupings can be summarized as: Chongce Icecap, Upper Zhongfeng, Kunlun slopes, Zhongfeng East ridge ices. The sites were chosen primarily in regions where μ_c was greater than unity.

Averages are produced for all the σ° values in the different polarization channels at each site. The sites range from 80 pixels for the Chongce Icecap boxes to several thousand pixels on the Zhongfeng East ridge.

Each of the local groupings of sites were plotted together. The angular scattering behaviors were so similar for all of the locales that they could be plotted as one. The result is shown in Figs.4.17 and 4.18. From Figs. 4.13 and 4.14, $\mu_c>1$ behavior begins at around the 6000 m level. Thus, the selected sites are spread over elevations from 6000 m up to 6500 m. The overall similarity of

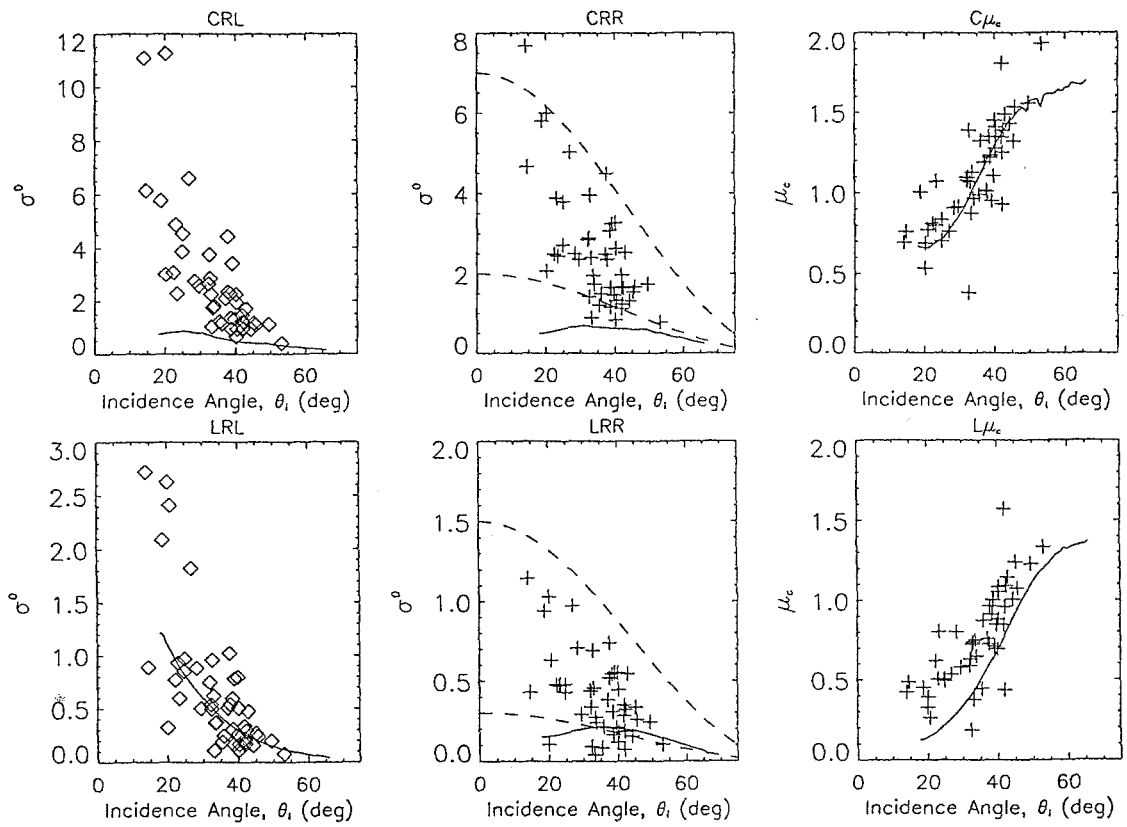

Figure 4.17 Circular polarization angular scattering behavior for forty-seven sites in DT 1/58.10 Kunlun Mt. scenes. The solid lines in the σ°(RL) and μ_c plots are the average behavior observed in Greenland by Rignot et al. (1993). The solid line in the σ°(RR) plot is derived from the other two lines. The dashed lines in the σ°(RR) plot represent $A\cos^2(\theta_i)$ scattering behavior for A-values that bracket the data.

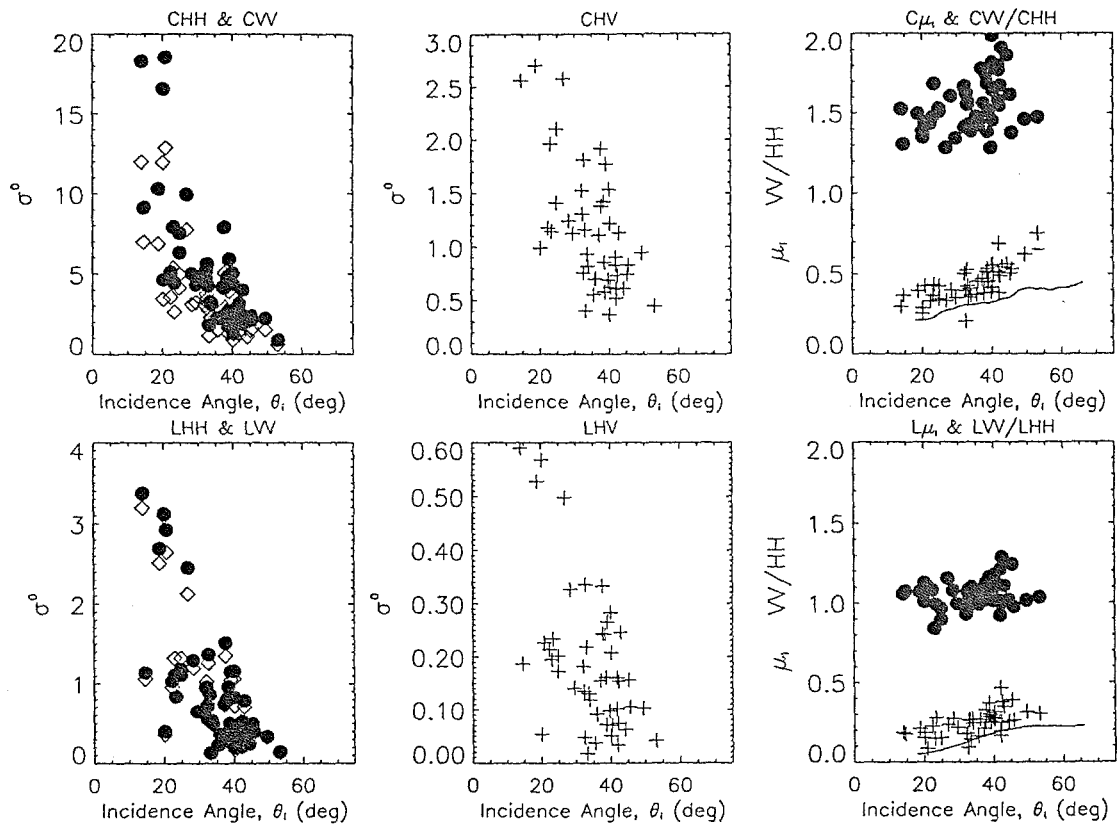

Figure 4.18 Linear polarization angular scattering behavior for the same sites as Fig. 4.17. Here the solid line in the μ_l plots is the average μ_l behavior that Rignot et al. (1993) observed.

scattering behavior suggests that the behavior of $\mu_c>1$ sites is not very altitude-dependent above 6000 m.

A significant observation from Figs. 4.17 and 4.18 is that the circular polarization and linear-polarization behaviors are directly correlated. For example the distribution of L-band σ°(RL) points has a pattern very similar to that of the L-band σ°(HH) and σ°(VV). This does not appear to be a processing artifact. This behavior indicates that all the $\mu_c>1$ locales are uniformly bright in all polarization channels. The μ_c measure of polarization, and at C-band in particular, appears to offer the most contrast as a function of θ_i. An application of this behavior is discussed below.

The polarization ratio and RL reflectivity behaviors that Rignot et al. (1993) observed are plotted on the appropriate graphs in Figs. 4.17 and 4.18 from the original data (Rignot, personal communication). It seems that while the σ°(RL) values observed here are significantly higher than the Greenland results, the μ_c and μ_l behaviors appear identical with Rignot et al.'s (1993) observations. This strong similarity implies a similar scattering mechanism, at least for those portions of the Western Kunlun ice fields that exhibit $\mu_c>1$. The linear cross-sections here are also significantly higher than Rott and Mätzler's (1987) pure dry snow observations, corroborating the idea that icy iclusions are involved.

The disappointment then in Figs. 4.17 and 4.18, if there is such, is that the scattering behavior does not match EGC. The μ_c inversion disappears at small incidence angles even while σ° 's increase. Some explanation for this may be

contained in the VV/HH ratio. The elevated C-band VV/HH ratio would suggest an important component of surface scattering, while the L-band behavior is consistent with volume scattering. The suggestion is then that at smaller incidence angles surface scattering dominates over the volume component and erases the μ_c inversion.

4.3.6 Firn properties

The strong suggestion that the scattering from the ice fields in the Kunlun Mt. SIR-C scenes is due to the presence of a percolation zone in the region is corroborated by field evidence. Han et al. (1989), Xie and Zhang (1989), and Ageta et al. (1989) all present firn stratigraphic sections for the Chongce Icecap. The profiles for the uppermost layers are reproduced in Fig. 4.19. The sections all indicate icy inclusions, ice crusts, depth hoar or superimposed ice in the upper 2 meters. The actual snow surface is otherwise unremarkable, as shown in Fig. 4.20 from Nakawo et al. (1989). The similarity of the radar behavior over the whole scene suggests that this firn structure is widespread in the Western Kunlun. Indeed, work on the Guliya Icecap (Thompson, 1996, Thompson *et al.*, 1995), located 30 km east of the Chongce Icecap has revealed similar structures (Thompson personal communication).

The observed buried ice structures suggest a further consideration for the scattering behavior. If the structures are primarily ice layers as the snow sections in Fig 4.20 suggest, then the decrease in μ_c at smaller incidence angles can be explained. Rignot (1995) modelled the Greenland results with populations of ice

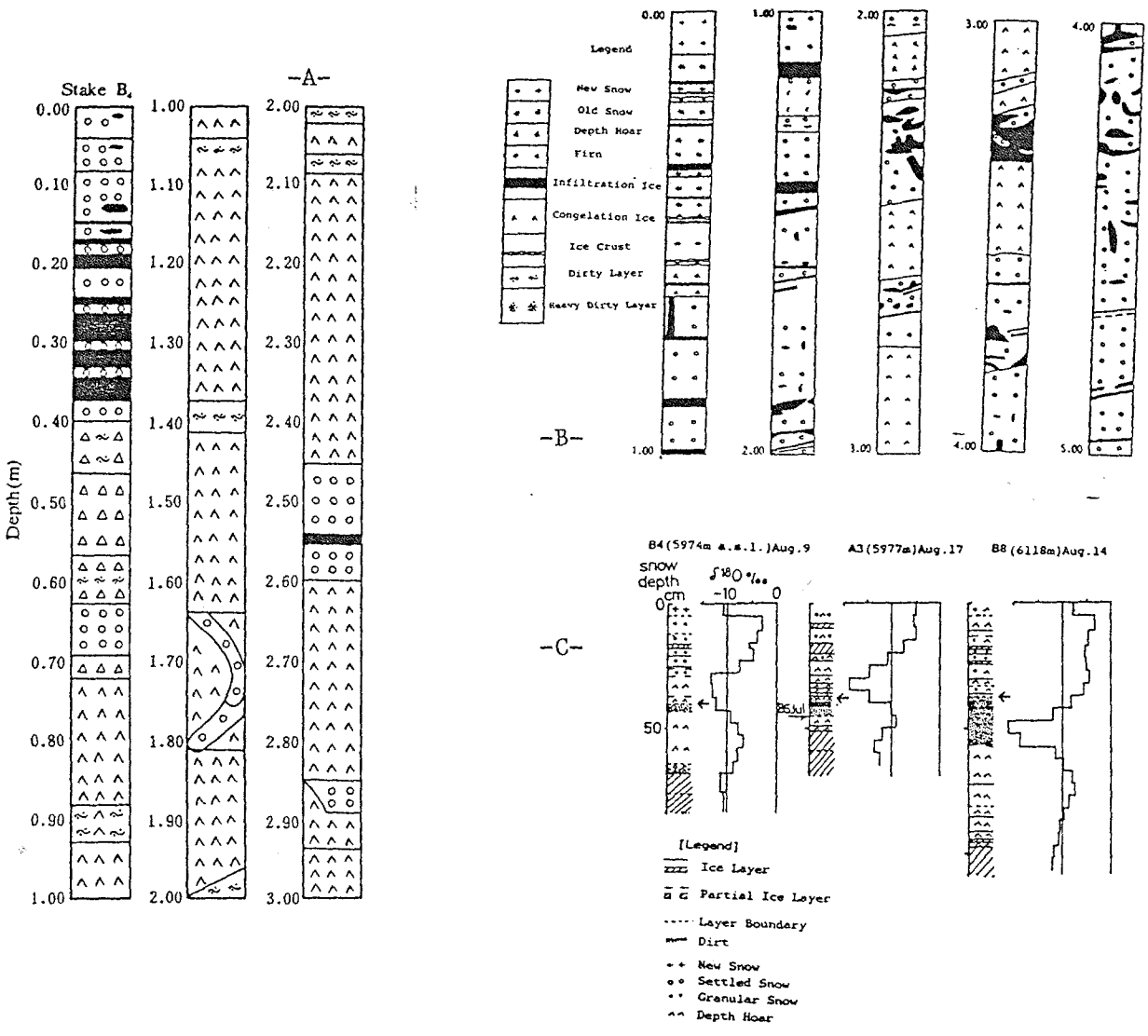

Figure 4.19 Chongce Icecap firn stratigraphic sections of the upper meters at several elevations. a) 5974 m from Xie and Zhang (1989), b) 6300 m from Han *et al.* (1989), c) 5970 - 6120 m, from Ageta *et al.* (1989). The different legends for each separate reproduction are shown as well. Note the occurrence of ice layers in the top 2 m of firn, and the description of depth hoar at b).

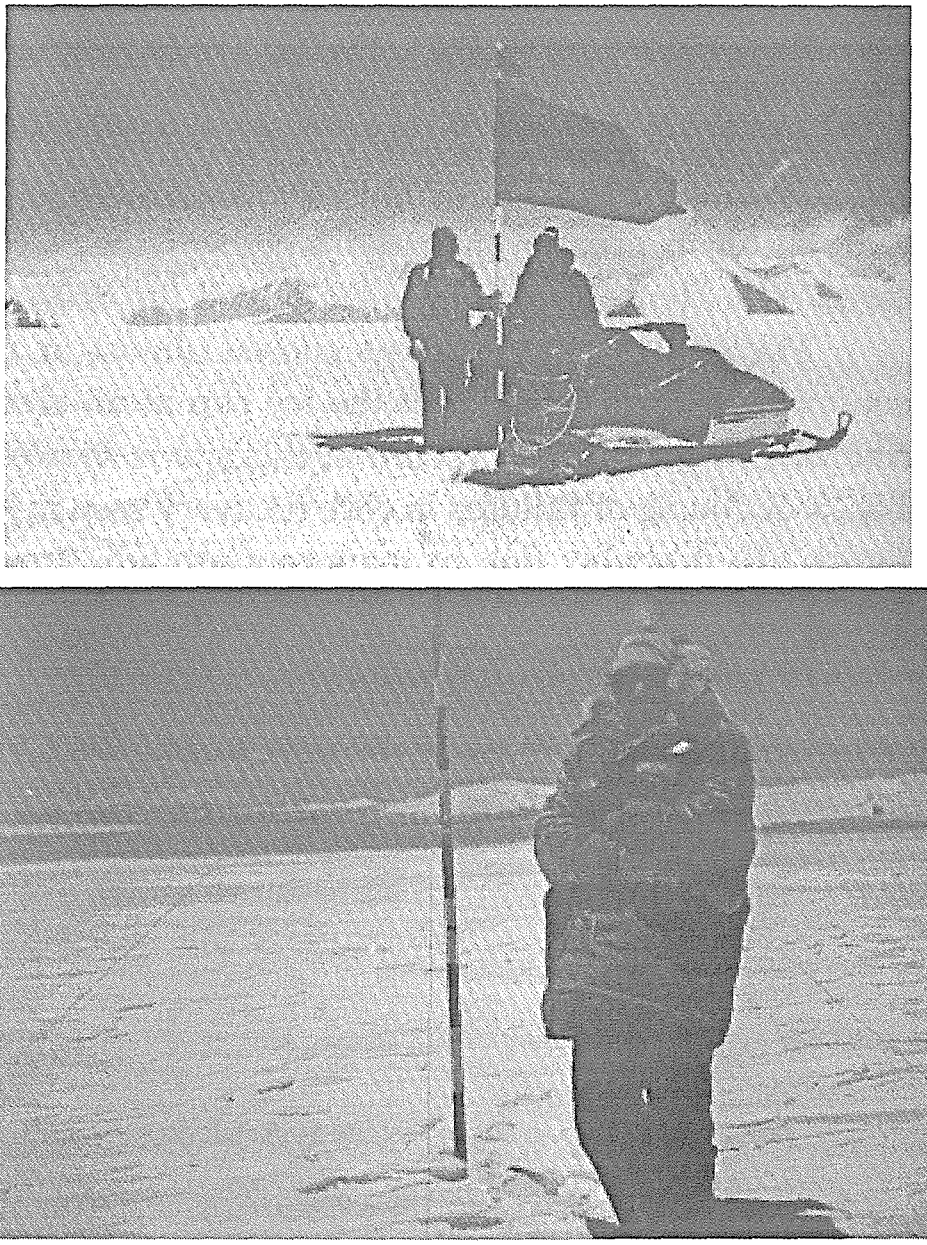

Figure 4.20 Smooth snow surfaces on icecaps of the Western Kunlun a) Snow surface at the highest site on the Chongce Icecap (Nakawo et al 1989). View probably to the north. b) Snow surface at the summit of Guliya icecap, 30 km east of Chongce Icecap at 7000 m (slide from L. Thompson).

cylinders. Ice layers can then be thought of as composed of these cylinders lying approximately horizontal. At small incidence angles, the deviations of the cylinders from horizontal become less apparent to the incoming radar waves, and μ_c is less affected. In this fashion the decrease in μ is probing a fundamental quality of the evolution of the firn: ice inclusions in the firn produced from meltwater are aligned by gravity and by the sedimentary snow-layering of the firn.

The DT 1/58.10 obervations were carried out in April when the firn surfaces in the region are still below freezing, and may even remain that way throughout the day. The average temperature at an automatic weather station in April, 1988 at 5260 m elevation north of Gozha Co was -8.4°C (Ohata and Kang, 1990). The maximum daily temperatures at the same station were at or below freezing in mid-April. Assuming only the free atmosphere lapse rate for the region which was 0.65°C/100m (Ohata *et al.*, 1989), April temperatures at 6000 m are well below freezing throughout the day. Ohata et al. (1989) point out that the observed surface lapse rate was greater than the free atmosphere rate as one moved onto the ice-covered regions due to the cooling effect of the latter.

The Tibetan plateau is subject to monsoonal precipitation. The Western Kunlun is an arid region, since the monsoonal flow is restricted by other intervening mountains. 70%-80% of the precipitation falls from May to September (Zhang *et al.*, 1989), with annual mean values around 30 cm on the top of the Chongce Icecap. The monsoon months of July and August also correspond to the

warmest temperatures in the Western Kunlun when snow wetting penetrates up to 25 cm at an elevation of 6100m (Takahashi *et al.*, 1989).

Thus, the April C-band radar measurements are likely probing to scatterers refrozen from the previous year's melting. The L-band σ° 's on the other hand may be integrating over several years worth of scatterers. The difference in the ratio of L/C co-polarized σ° 's to that obtained for Greenland may indicate differences in the scatterer populations. With field measurements of buried ice size and shape statistics these differences might lead to a measure of the extent and amounts of the previous season's melting. This kind of quantification of radar scattering would make SAR polarimetry imaging more useful than imaging alone as a tool for glaciologists monitoring climatic effects on ice sheets (e.g. Long and Drinkwater, 1994).

4.3.7 Glaciologic Features

The radar scattering results presented so far can be compared to the glaciological information for the Western Kunlun glaciers. The transitions to highest σ° 's plotted in Figs. 4.10 and 4.11 can be associated with the level of the snow line on the two glaciers. The snow line on Zhongfeng Gl. would be around 5950 m, while on Chongce Gl. it appears to be around 6100 m. These transitions do in fact correspond to the published snow line levels. Zhang and Jiao (1987) report the snow line at 5965 m for Zhongfeng, and at 6120 m for Chongce. The difference in snow line levels for these two neighbouring glaciers arises apparently

from their different orientations relative to the westerly and south-westerly arrival of monsoonal precipitation (Zhang and Jiao, 1987).

That a transition can be observed despite the very cold mid-April temperatures can be explained. Melting below the snow line would result in a fairly homogeneous ice mass (c.f. Fig 4.2). Homogeneous cold ice will backscatter less than the firn zone with icy inclusions that is present above the snow line. This technique of snow line detection from SAR single-polarization imagery was suggested by Bindschadler and Vornberger (1992), and is easily applied provided topographic information exists for the SAR scene.

Bindschadler and Vornberger (1992) also pointed out the use of SAR for detecting crevassed regions within the bare-ice (ablation) zone. The most likely candidate for a crevassed region in our images is the site on the northern edge of Chongce Glacier. The average properties of this radar-bright region are reported Table 4.3. The determination that this area is a crevasse zone is based on

Table 4.3
Chongce Glacier crevasse radar properties

	σ°(RL)	μ_C	σ°(HH)	μ_L	σ°(VV) / σ°(HH)
C-band	2.7±2.0	1.5±1.5	3.9±3.0	0.5±0.6	1.4±1.4
(range)	(0.2 to 15.3)		(0.3 to 18.1)		
L-band	0.8±0.6	0.7±0.6	1.4±1.1	0.4±0.4	1.0±1.0
(range)	(0.1 to 5.9)		(0.1 to 9.8)		

$\theta_i \simeq \theta_i + \alpha = 32.6^\circ + 2.3^\circ \approx 35^\circ$

cartographic information from Zheng (1987). The reported strike direction of the crevasses is perpendicular to the glacier flow and thus to the SAR range direction.

Since the location is below the snow line, and since the rest of the glaciers in the scene appear dark in the ablation zone, we can suppose that no significant snow layer covers the crevasses. Yet, both the circular and linear σ° 's are comparable to those observed on the Chongce Icecap for instance. Additionally, despite a low mean, L-band μ_c does exceed unity over much of this region, as can be seen in Fig. 4.14. In fact, the μ_c and μ_l values for both SIR-C wavelengths are on the high side of the scatter shown in Figs. 4.17 and 4.18.

If the scattering can be ascribed to the crevasses, this suggests that some form of Goldstein and Green's (1980) crack model for EGC may apply. However the limitations of their simple model still apply, and the high cross-sections could not be reproduced. Furthermore, we might expect to see other similarly bright regions associated with crevasses on other glaciers in the scene, and this appears not to be the case. This may be due to a preferred orientation of the crevasses on Chongce. More information would clearly be needed to address this question in detail. The notion that multiple-bounce scattering and internal reflections are occuring in a crevassed region remains intuitively appealing.

Further ambiguous radar behavior is demonstrated at the toes of glaciers. For example we might expect that the tips of Yulong III and IV both show similar radar behavior. They both appear oriented in a similar way to the radar, and their environments are also very similar. Yet, the toe of Yulong III has double the

cross-section of the toe of Yulong IV, and also has a more enhanced circular polarization inversion. The average radar properties are listed in Tables 4.4 and 4.5. The answer may in fact be that the structures at the toe are in fact not identical. The glacier toes are sites of intense melting, and also perhaps of debris accumulation. While the bare-ice toes were probably frozen in the April SIR-C scenes, melting ice can produce some unique structures, as evidence by Fig. 4.21, showing the toe of a south-slope glacier 50 km west of Kunlun Mt. The particular glacier shown at the end of the melt season in Fig 4.21 would in the author's

Table 4.4
Yulong Glacier III toe radar properties

	σ°(RL)	μ_C	σ°(HH)	μ_L	σ°(VV)/σ°(HH)
C-band	1.14	1.05	1.44	0.40	1.42
L-band	0.36	0.95	0.52	0.32	1.09

Table 4.5
Yulong Glacier IV toe radar properties

	σ°(RL)	μ_C	σ°(HH)	μ_L	σ°(VV)/σ°(HH)
C-band	0.56	0.74	0.64	0.30	1.45
L-band	0.17	0.68	0.23	0.23	0.94

opinion behave more like Yulong IV if entirely frozen. Its surface appears smooth and no fracturing of the toe is apparent. A more broken glacier toe, coupled with re-frozen ice structures may be a better candidate for Yulong III's behavior. This idea suggests that re-frozen melt structures in the crevasse zone may be responsible, in conjunction with multiple reflections at ice-air interfaces, for the radar behavior of the Chongce crevasse radar properties.

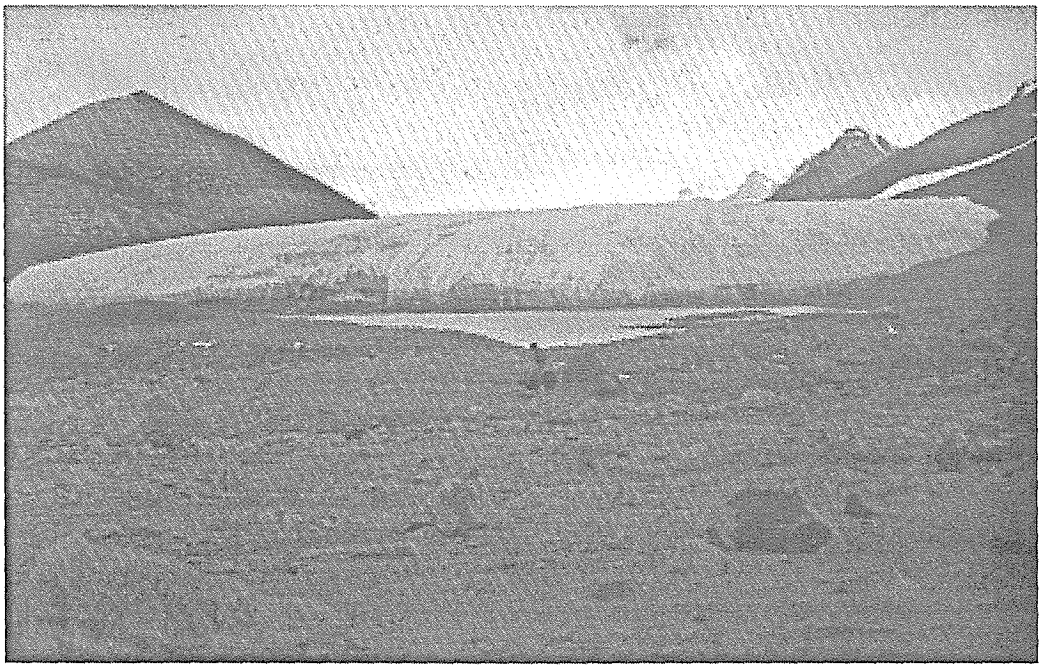

Figure 4.21 Toe of glacier at the head of Quan Shui gou stream, on the south slope and western tip of the Western Kunlun Shan. The elevation is around 5500m, and the picture was taken in mid-October. Photo by T.Farr.

4.3.8 Fault Detection

There is a linear feature, sub-parallel to the image azimuth direction that traces ENE from the 6100 m elevation level of the main channel of the Chongce glacier. The feature appears best in C-band circular polarization ratio images like Fig.4.13. We propose that this feature corresponds to a fault of the Altyn Tagh fault zone, specifically parallel to the southern arm where the Altyn Tagh splits before meeting the Karakorum fault (Avouac and Peltzer, 1993, Peltzer *et al.*, 1989). A magnified image of the proposed fault is shown in Fig.4.22, and a schematic of the regional faulting with the location of the new fault is shown in Fig 4.23.

The linear feature is most prominent at the base of the slope on the west side of Chongce III Glacier. It does not appear to be an artefact of the radar image given that it is not parallel to the azimuth direction. The main argument in favour of this feature being a fault is that it appears to continue north-eastward, across the upper reaches of Chongce III, across the catchment divide and further diagonally across the upper reaches of Yulong IV Glacier. We postulate that the feature is made visible precisely because it is modifying the surface topography of ice to some extent. It appears best in C-band μ_c because, as we have seen, this polarization measure has the greatest dependence on indidence angle. The actual mechanism translating what may only be a modest sub-glacial feature to something detectable at the surface may involve very local variations in snow and ice facies development due to minor surface slope variations. An actual

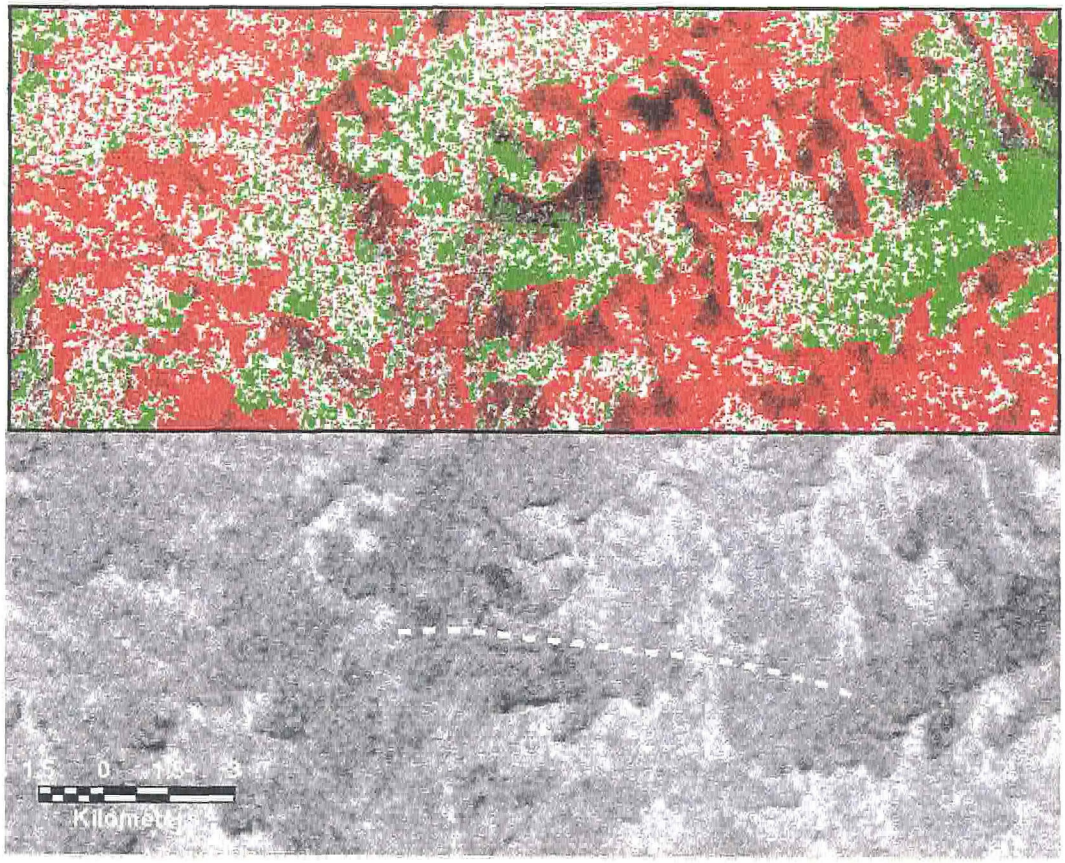

Figure 4.22 μ_c (C-band) color and greyscale images of a portion of the DT 1/58.10 Western Kunlun scene. This circular polarization ratio offers the best contrast as a function of incidence angle, and so we detect features in the glacier morphology better. Note the linear feature in the center of the figure. This can be followed across several glaciers and valleys, and so is proposed as being a fault. The location of this sub-scene is outlined in Fig. 4.13.

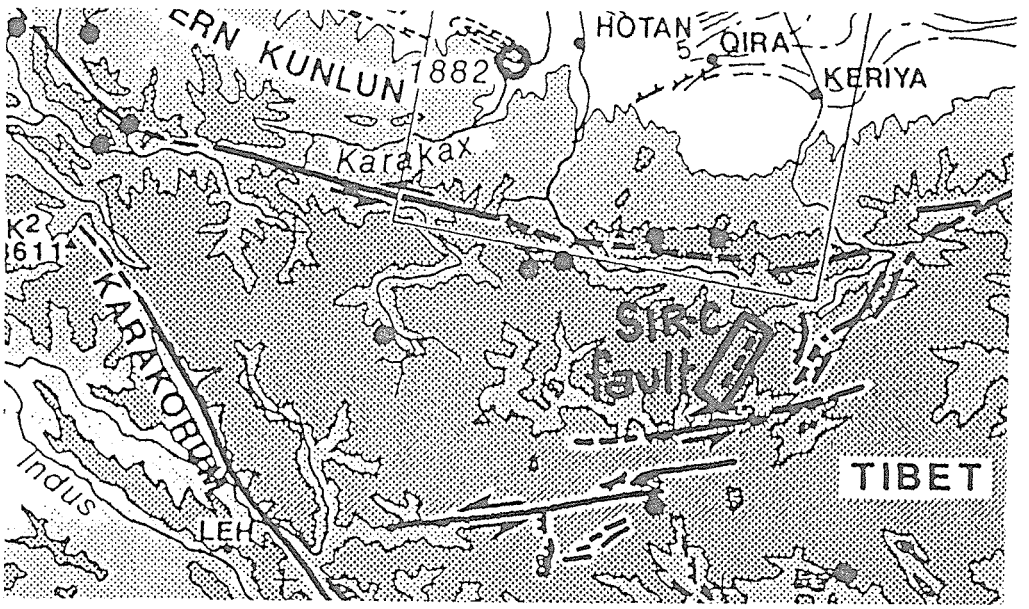

Figure 4.23 Regional fault map for the Western Kunlun Shan region. The location of the SIR-C scene is outlined. The fault identified in Figure 4.24 is sketched in. After Avouac and Pelzer 1993.

determination of whether the feature is a fault or not would require field work. However, the fact that it is remotely detectable in an erosive glacial environment suggests that the fault may have been active in the recent past.

This possible detection of a structural feature in an ice-covered environment has implications for geologic mapping in similar envronments. We suggest that a careful analysis of the spatial variation of snow radar properties on the surface can reveal buried features. A careful selection of polarization channel allows contrast enhancement (Van Zyl *et al.*, 1990). While polarization response contrast enhancement was applied to differentiate snow cover from vegetation by Shi and Dozier (1997), it should also prove very useful in mapping sub-surface features on ice fields of moderate thickness (tens of m?).

4.4 Central Andes

4.4.1 Geography

SIR-C DT 2/40.60 is named Cerro Aconcagua after the highest peak (6960 m) in the Americas that lies some 50 km to the north of the track. While not as high as the Tibetan plateau mountains, the Central Andes (Los Andes de Santiago), are still some of the highest mountains on Earth. South of Aconcagua, at the latitude of Santiago (33°20'S) on the Chilean-Argentinian border, is Cerro Tupungato (6570 m). Tupungato, is the northernmost active volcano in Chile's southern volcanic zone (Gerth, 1955, Zeil, 1964). Its smaller neighbour,

Tupungatito (5278 m) has been active during this century[‡‡]. Tupungato was first climbed by a european in 1897. Fitzgerald along with Vines and the Swiss mountaineer Zurbriggen successfully climbed both Aconcagua and its southern neighbour in a single season (Reichert, 1910). While the passage of a century has seen the former mountain become a tourist destination, the latter apparently remains somewhat remote.

The high elevations of the Central Andes were more glaciated in the past than they are today. The valleys draining the Rio Mapocho and Rio Maipo past Santiago record past glacial processes (Bruggen, 1934). The modern snow line however is around 4500 m at latitude 33°S (Clapperton, 1983). Some 30% of the terrain in the Central Andes lies above this level (Lliboutry, 1965, p.445), and some 50% of that is glaciated. Lliboutry (1956) has studied the modern glaciers of the region extensively. Figure 4.24 shows Lliboutry's (Lliboutry, 1965 p.497) sketch of the distribution of glaciers in the Central Andes.

The track of DT 2/40.60 is plotted on Fig. 4.24. The scene over Tupungatito that will be studied here is outlined. The extent of glaciers in this decade can be assessed from the mosaic of Shuttle handheld phographs shown in Fig. 4.25. The location of the radar scene is also shown in Fig. 4.25, and the image is aligned and scaled in a similar fashion to Fig. 4.24. Fig. 4.25 makes clear that an important surface area in the Tupungato region is covered. Lliboutry

---

[‡‡]Zeil (1964) reports eruptions in 1901, 1907, 1925, 1958, and 1960. It seems likely that more recent eruptions have occured but references are lacking.

(1965) estimated that 120 km^2 were covered by glaciers in the Tunuyan valley south of Tupungato.

The poor level of information available on the Tupungato region as recently as the 1950's is reported by Lliboutry (1965). Further proof exists in the form of inaccurate 1:100,000 Argentine topographic maps of the region. The Cerro Tupungato sheet (Argent., 1946) in particular is based on surveys from 1927, 1943, 1944, and 1945, and was published in 1946. It has apparently not been revised. Glacial retreat combined with eruptive volcanism in the last 50 years will certainly have affected the landscape. Chilean topographic information currently available is rather better, and has been relied on here (IGM, 1985, IGM, 1994). Still the Chilean sheet for Tupungato, while published in 1994, is based on a photogrammetric survey from 1955 and a terrain classification from 1965. The general slopes and features appear sound when compared with handheld shuttle photographs (see also Fig. 4.31).

4.4.2 Central Andes Glacial Phenomena

The climate in the Central Andes region is condusive to two distinct and somewhat peculiar glaciologic phenomena, rock glaciers and penetentes.

Rock glaciers, while not purely a glaciologic phenomenon, are often attributed to glacial processes (Vitek and Giardino, 1987). In the Central Andes rock glaciers are in fact often a glacial phenomenon. The rock glacier morphology can be either as a debris-covered glacier or a fluid rock mass. In the Central

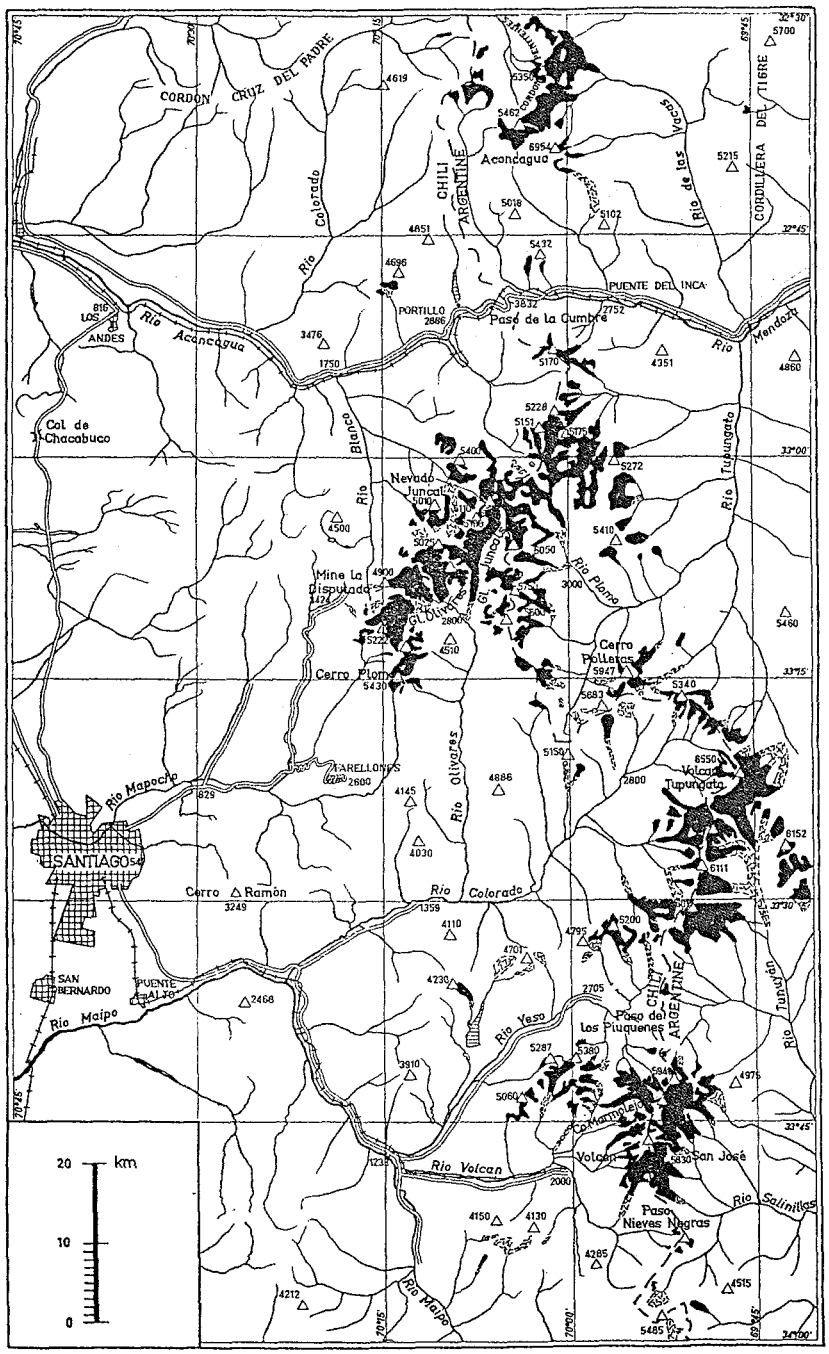

Figure 4.24 Sketch map of the distribution of glaciers in the Central Andes (After Lliboutry (1965). Filled zones are exposed ice, while stipled zones represent debris-covered glaciers or rock glaciers. The path of SIR-C track DT 2/40.60 is traced across the map. The location of the Tupungatito scene studied in this section is outlined.

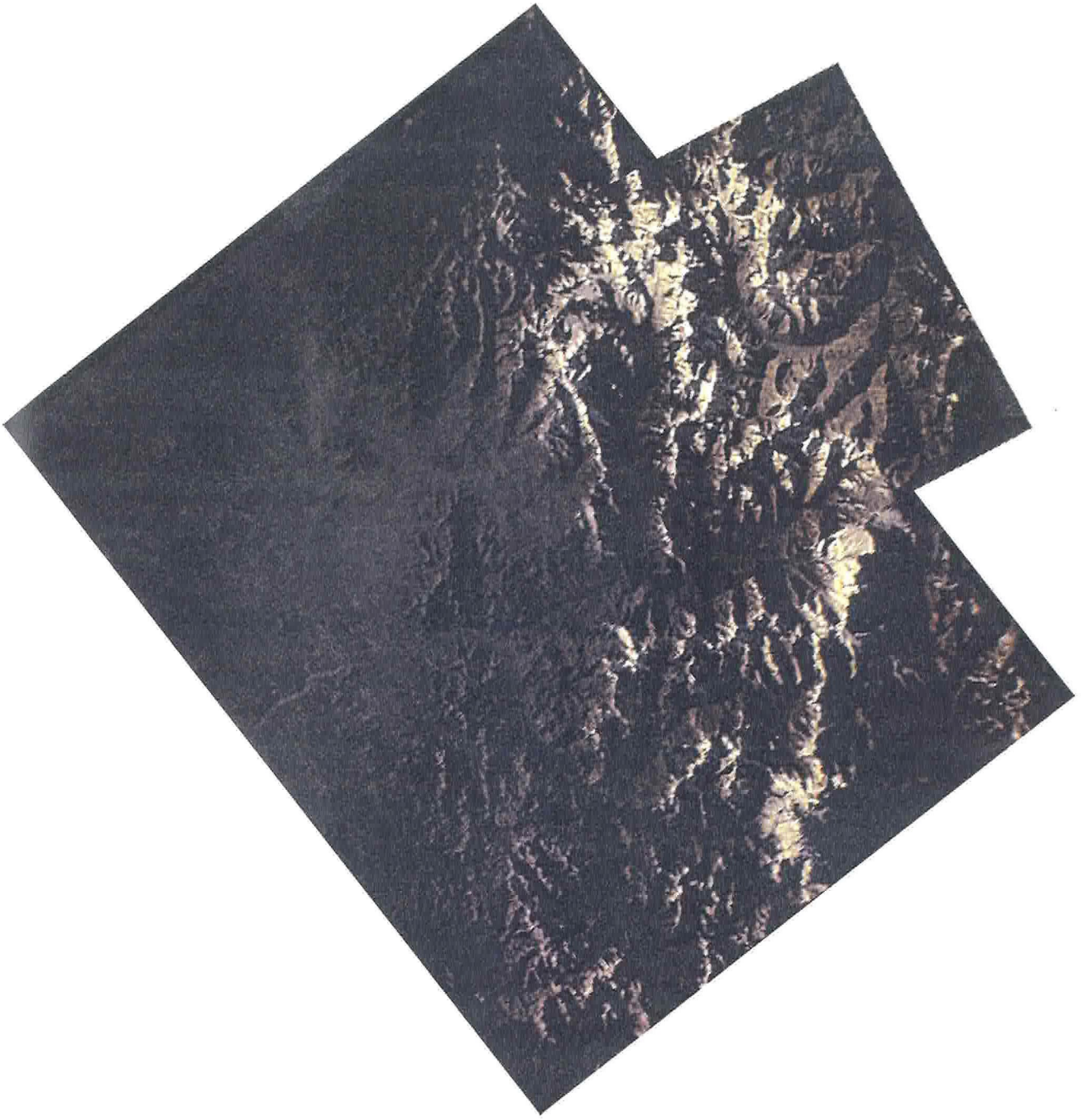

Figure 4.25 Image mosaic of two Space Shuttle astronaut handheld photographs from March and April of 1994 (STS059-L23-127 and STS062-153-186). The aligment and scale of the mosaic is similar to the regional map in Fig. 4.23. The radar scene that is analyzed here is outlined in the figure. Tupungato volcano is located at the southern corner where the two images overlay.

Andes debris-covered glaciers exist, where the "debris responds as an active layer over the glacier ice which behaves as permafrost" (Corte, 1987). The permafrost-like behavior is related to the altitude limits of permanent and seasonal freezing. In general, the depth of thawing at high elevations is around 20 cm at 4500 m, and at 60 cm or more at 4000 m.

The western side of the Central Andes receives precipitation from the Pacific. The same air masses, once dried bring less moisture to the Argentinian side of the watershed. At the foot of the moutains on the Chilean side 30 cm of precipitation per annum is normal (Lliboutry, 1965), while the eastern side receive perhaps 20 cm (Corte, 1980). The summit regions rececive 1 m or more. Lliboutry (1965) reports average conditions for the Juncal glacier system to the north-west of Tupungato. At 4400 m, where the equilibrium line is found, average annual temperature is -4.8°C, average summer temperature is -1°C, and all of the 125 cm of precipiation falls as snow. The main period of snow-fall (winter) runs from May to October. Typicial average temperatures at the end of winter at 4000 m are around -5°C. Lliboutry (1954) reports an average spring-time diurnal thermal cycle around 4000 m at the Paso de la Cumbre south of Aconcagua. The minimum of -5°C occurs at 7 am, and the maximum of 2°C around 2 pm on a sunny day (-4°C cloudy day). Freezing temperature returns by 7 pm.

For radar remote sensing we might expect to identify rock glaciers as features in the landscape that resemble glaciers morphologically, yet do not display the radar behavior of either cold firn, ice, or wet ice surfaces. That is to

say that the surfaces scatter by surface, quasi-coherent interactions with no signature of volume scattering expected. Yet, the surfaces should not be so smooth or absorbing as to be dark. Some measure of roughness would might exhibit Bragg-like scattering behavior.

Penetentes are snow morphologies formed in a radiation-dominated environment. They can be quite unusual and spectacular in well-developped form as evidenced by Figs. 4.26 to 4.29. Penitents were first observed by Charles Darwin in 1835 at 4000 m at the Paso de los Piuquenes (Lliboutry, 1965). Darwin ascribed their formation to the wind. They are understood to form in a radiation-dominated environment on a snow or ice surface. As Lliboutry (1954) points out, "during a sunny day at the end of winter or in spring the surface of the snow in central Chile generally does not melt as it does in the Alps; it sublimes instead." This can occur if the dew point is below 0°C. The paradoxical situation is reached where dry air with low dew point reduces ablation (Lliboutry, 1954). However, very local effects can change the situation. The interaction between radiation and ablation will reinforce one another inside a depresssion, deepening the latter. The sensitivity of this formation mechanism to the sun is evidenced by the alignment of fully developped penetentes in the east-west direction.

An important point about penetentes, that Lliboutry (1954) asserts is that the snow blades remain cold with frozen surfaces, while the snow or ground between the blades is wet or even slushy. This fact is confirmation of the thermal

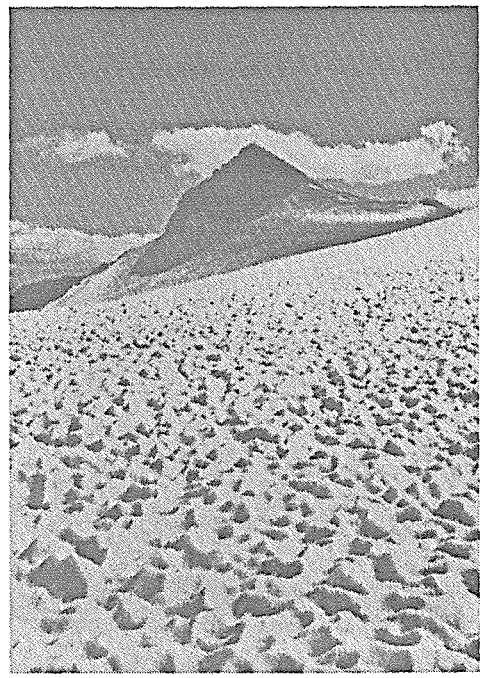

Figure 4.26 Firn surface in the Alps (Clariden) in July 1935. Picture from Streiff-Becker (1954). Note the general alignment of the troughs perpendicular to solar incidence.

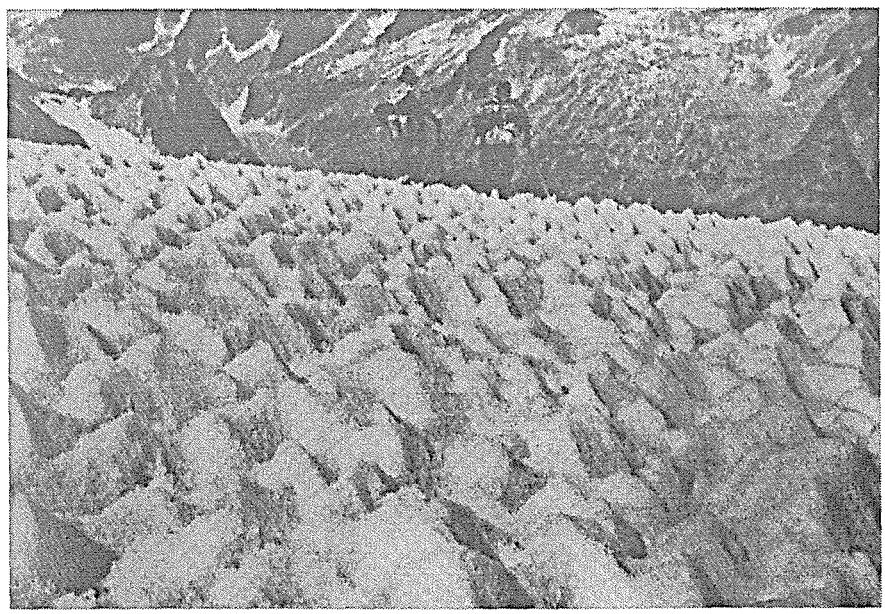

Figure 4.27 Firn surface in the Alps (Bergell) on Aug. 1, 1935. Picture from Streiff-Becker (1954).

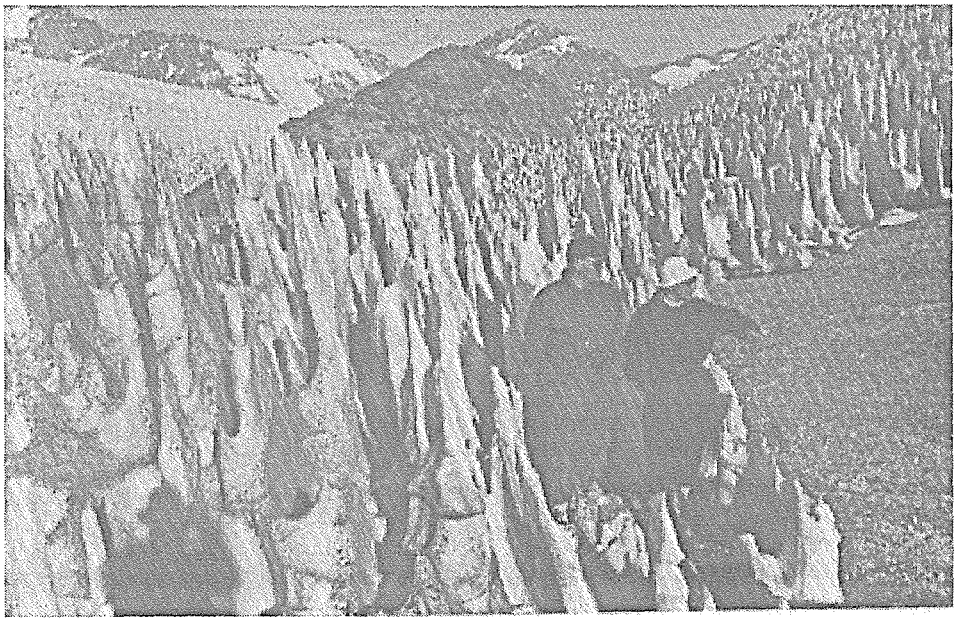

Figure 4.28 Snow penetentes. View is to the east, around 4600 m in the Juncal region (33°10'S). Note the thin profiles of the penetente blades, and their alignment minimizing shadowing. Picture from Lliboutry (1964).

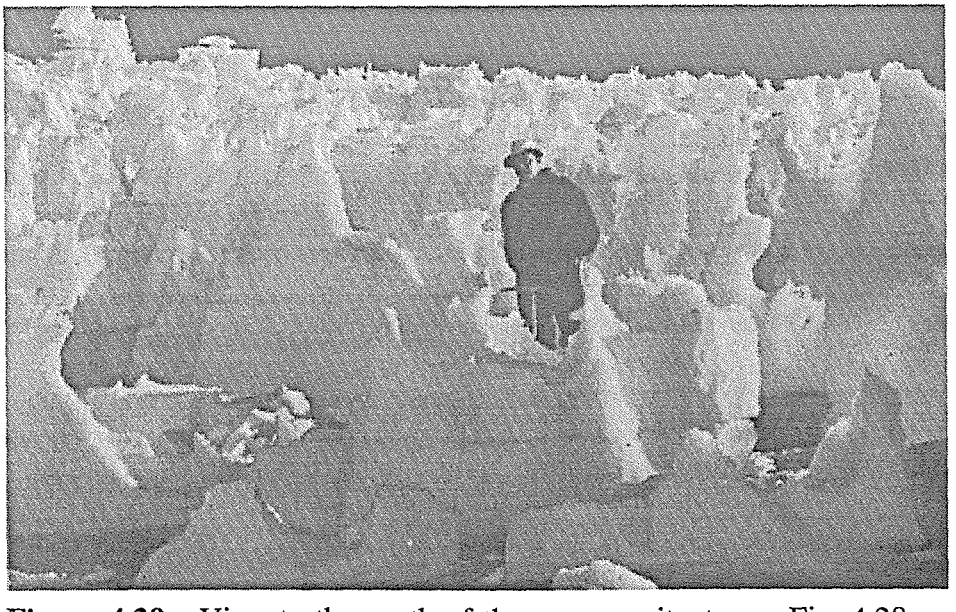

Figure 4.29 View to the south of the same penitentes as Fig. 4.28. Picture from Lliboutry (1964).

micro-environment that drives penetente formation. Radiation modelling of spherical penetentes has been carried out by Svitek (1992).

Of course, penetentes begin life as a snow surface, and develop progressively. In the Central Andes Lliboutry (1954) lists penitentes of 2 cm forming at the beginning of June at 2650 m, of 8 cm forming at the beginning of September at 2900 m, and of 12 cm forming at 2700 m in mid-October. By the beginning of November, he notes that penetentes of 3-15 cm for "everywhere above La Disputada" in the Juncal region from 3400 to 4000 m. By the end of summer at most elevations however, the temperatures have risen high enough that the whole snow pack melts, and the penetentes disappear. However, when penetentes form in snow on a glacier, and if conditionsa are favourable, such as at higher altitudes, the troughs will continue to burrow down into the ice, with water running away in the troughs. Then with the next season's snow, the troughs fill and the process repeats, leaving a very irregulat ice surface buried beneath the snow.

The radar signature of penetentes seems difficult to predict. Perhaps snow penetentes with re-frozen troughs (at night?) or percolation features, might scatter in a similar manner to the percolation facies. Certainly the existence of buried ice penetentes below a cold snow layer could cause significant volume scattering at the penetente-ice-blade/snow interfaces. In some sense these might behave a "vertical layers" of ice within the snow-pack in contrast to percolation facies horizontal features.

4.4.3 Radar Imaging

The image parameters for the DT 2/40.60 L- and C-band radar scenes over Tupungatito are listed in Table 4.6. We note that the image was acquired in the late afternoon, local time, when some amount of cooling of a snow surface would have occured. Furthermore, handheld shuttle photographs of the Central Andes (STS068-163-038), while not showing the Tupungatito region directly because of clouds, do show that the valleys were snow-covered down to 3500 m. An image of σ°(CRL) is shown in Figure 4.30. Prominent geographic features are labeled. Tupungato volcano itself is just off the top of the image.

The Tupungatito volcano cones are apparent under the terminal o's of the "Tupungatito Volcano" label. The bright feature in the center of the image is the Tupungatito icefield. Two glaciers, Tupuntatito I and II flow down from the glacier on the Chilean side. On the Argentinian side, a debris-covered glacier flows down from Tupungato, Tupungatito and Cerro Alto into the Rio Tunuyan. A well-developed morainal feature can be seen at the top of the Rio Colorado valley.

What is not immediately apparent in Fig. 4.30 is that the Tupugatito scene data were somewhat noisy. Some pixels appear to have been corrupted. They would appear with cross-sections of up to 10^{30}! The affected pixels were different in the different polarization and frequency channels. The distribution of affected

Table 4.6

SIR-C Cerro Aconcagua quad-pol scene processing parameters.

DT:		2/40.60	
Name:		Cerro Aconcagua	
Track angle:		142.82°	
Image center:		33.407°S, 69.737°W	
Time:	GMT	1994/275:21:51:49.9	
	Local*	17:51:49.9, October 2nd, 1994	
Scenes:	L-band (24.0 cm)	pr43677	
	C-band (5.66 cm)	pr43678	
θ_i:	near range	32.848°	
	image center	34.674°	
	far range	36.271°	
Shuttle roll angle:		25.987°	
Near slant range:		262.9919 km	
Scales:		range	azimuth
	Slant range scene:	10.707 km	49.999 km
	Slant range pixels:	1607	10251
	Slant range pixel size:	6.662 m	4.878 m
	Ground range scene:	18.820 km	49.999 km
	Ground range pixel size:	11.711 m	4.878 m
	Multilook multiplier	3	7
	Multilook pixels:	535	1464
	Multilook pixel size:	35.13 m	34.14 m

* Chilean time zone, UTC - 4h.

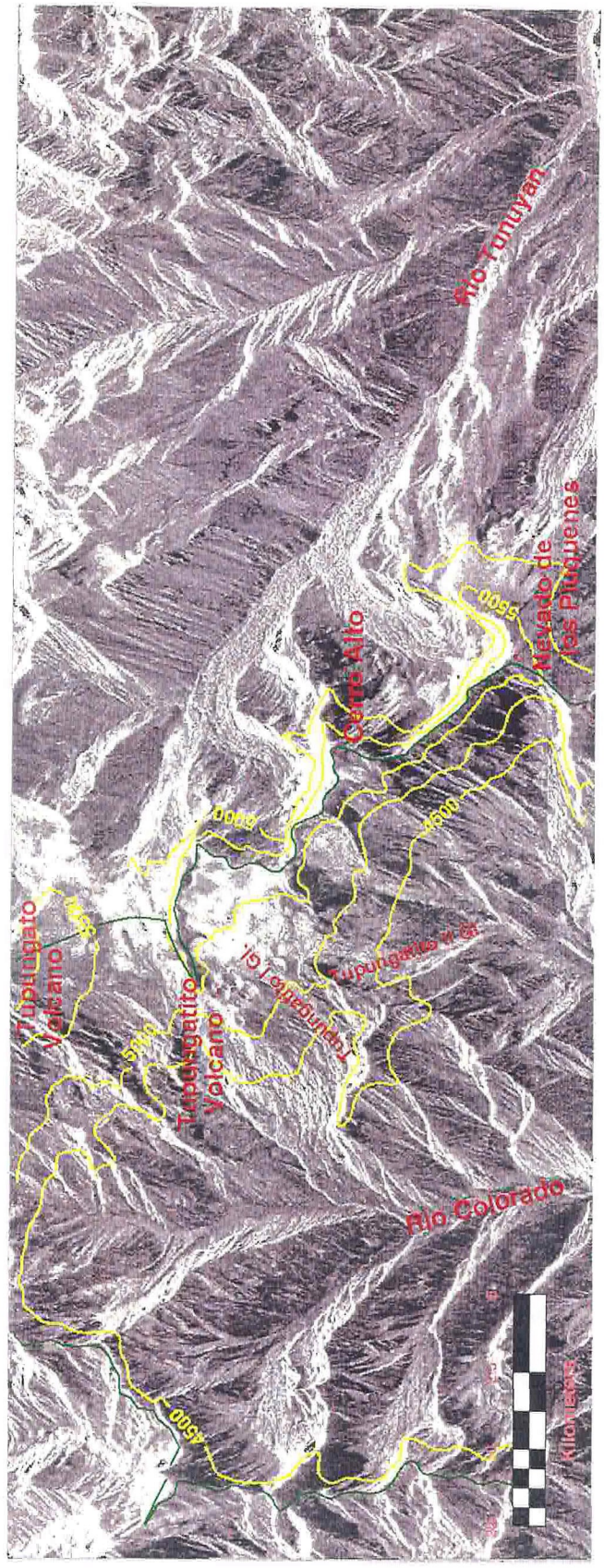

Figure 4.30 Radar σ (RL) image© of DT 2/40.60 Tupungatito scene. Prominent geographic features are labeled. The drainage divide, which is also the international border in this region is showin in green. The valley flowing toward the viewer is in Chile. Topographic contours above 4500 m have be drawn in yellow from Chilean 1:50,000 section topographic maps "E" 61, and "E" 69. Radar illumination is from the top, and SIR-C flight direction is to the right in the image.

pixels over the scene was apparently random. Thus we applied a low-pass step-filter, keeping only pixels with $\sigma^{\circ}<1000$. The nulled pixels do not affect pixel statistics, but will affect spatial filtering.

The interpretation of the radar image is simplified with the use of a Shuttle handheld photograph taken during SRL-1. The April view of the Tupungatito region scene is shown in Fig. 4.31. The Tupungatito icefield is in the middle of the image, slightly left of center. The Nevado de los Piuquenes icefield is toward the bottom of Fig. 4.31, slighty right of center.

A comparison of the radar image in Fig 4.30 with Fig. 4.9 of the Western Kunlun shows that there is no gradation in glacier properties with altitude: there are no glaciers long enough. The debris-free glaciers Tupungatito I, and II, and the debris-free glacer from Tupungato into the Rio Tunuyan valley are only moderately radar-bright in Fig. 4.30, and show no indication of snow-line or elevation related radar properties. The elevation of the terrain is insufficient, given the steepness of the slopes, for long glaciers. While the peaks are above 5000 m, the valley floors only 5 km away in the Rio Colorado valley for example are below 3500 m. This far below the reported snow line it is not surprising that we can not observe a variation of glacier zones. An examination of Fig. 4.31 and comparison with the topographic contours on Fig. 4.30 confirms a lower limit of permanent ice at around 3500 m, and the snow line must lie somewhere above this.

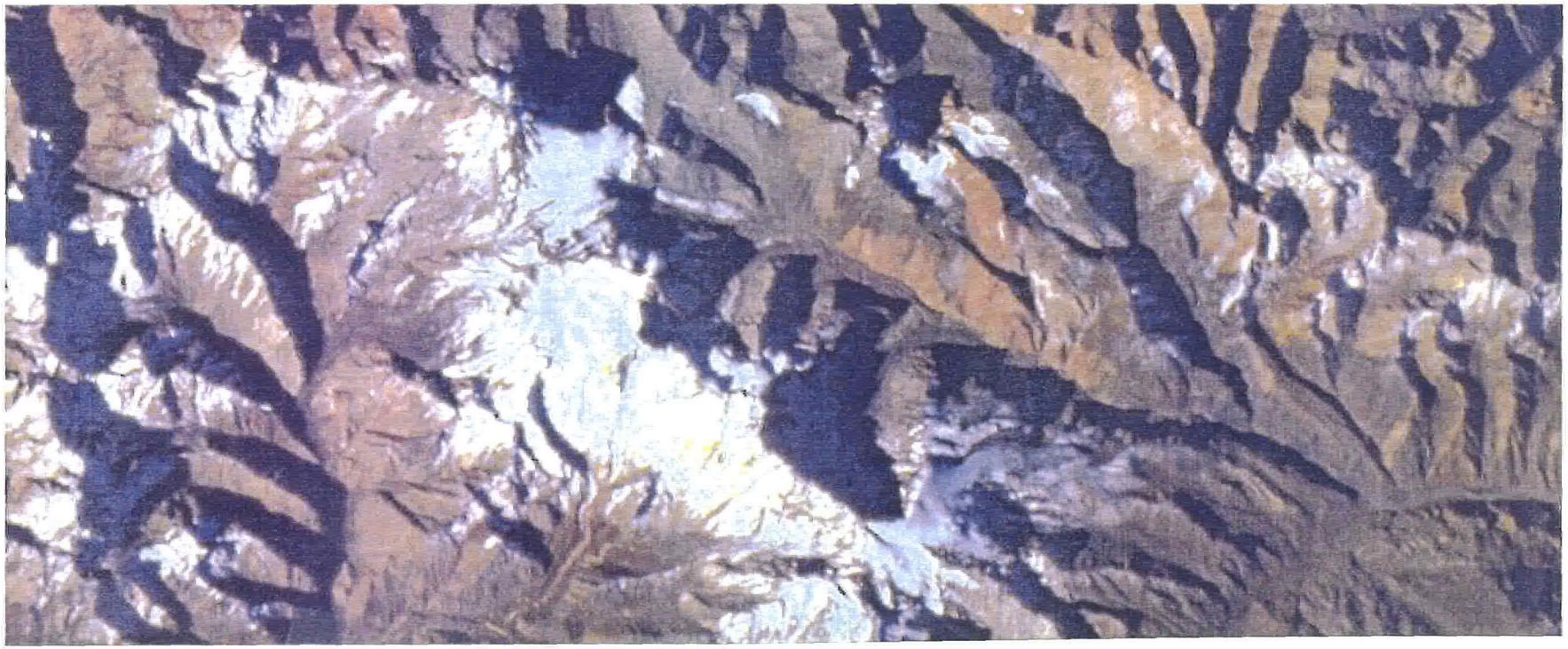

Figure 4.31 Excerpt from handheld Shuttle astronaut photograph STS059-L15-048 from the April SRL-1 mission. The view toward the north-east from an orbit that is parallel to the October SRL-2 orbit, views the scene with a perspective that mimics somewhat the ground range deformation of the south-west illuminating radar image.

4.4.4 Scattering Behavior

Polarization ratio maps for the DT 2/40.60 scene are shown in Figs. 4.32 to 4.35. The μ_c maps are shown first, in both C-band (Fig 4.32) and L-band (Fig 4.33), followed by the μ_l maps with C-band (Fig 4.34) and then L-band (Fig 4.34). The color-coding in the μ_c plots has red for $\mu_c>1.0$, green for $0.25<\mu_c<0.7$, and blue for $\mu_c<0.25$. The ratios are calculated at each pixel as they were for the Western Kunlun scene after median 5x5 filtering the σ° 's. The square colorless spots within the red fields arise from the effect of the nulled pixels on the 5x5 filter, but do not affect pixel statistics. The color-coding for the μ_l plots is red for $\mu_c>0.3$, green for $0.1<\mu_l<0.2$, and blue for $\mu_l<0.1$.

Both C-band polarization ratios are enhanced ($\mu_c>1$, $\mu_l\geq 1/3$) predominantly at those locations that had permanent ice at the end of the previous summer, as shown in Fig. 4.31. However, as we have mentioned, during the SRL-2 mission when DT 2/40.60 was acquired on October 2nd, all regions above about 3500 m were still snow-covered. Clouds in the Tupungatito region on October 2nd would suggest that the high-altitude temperatures were below freezing when the image was obtained. The suggestion would be that the scattering is again due to icy scatterers within the cold frozen firn. If the 1994 snowfall was typical (1m for the winter) we might still expect the C-band response to be due to the previous season's firn. As Ulaby (1982) points out, in dry, cold snow 4 GHz radar can penetrate tens of meters. For the most part in the polarization ratio maps the corrspondence of $\mu_c>1$ with $\mu_l>1/3$ suggests that volume scattering is occurring.

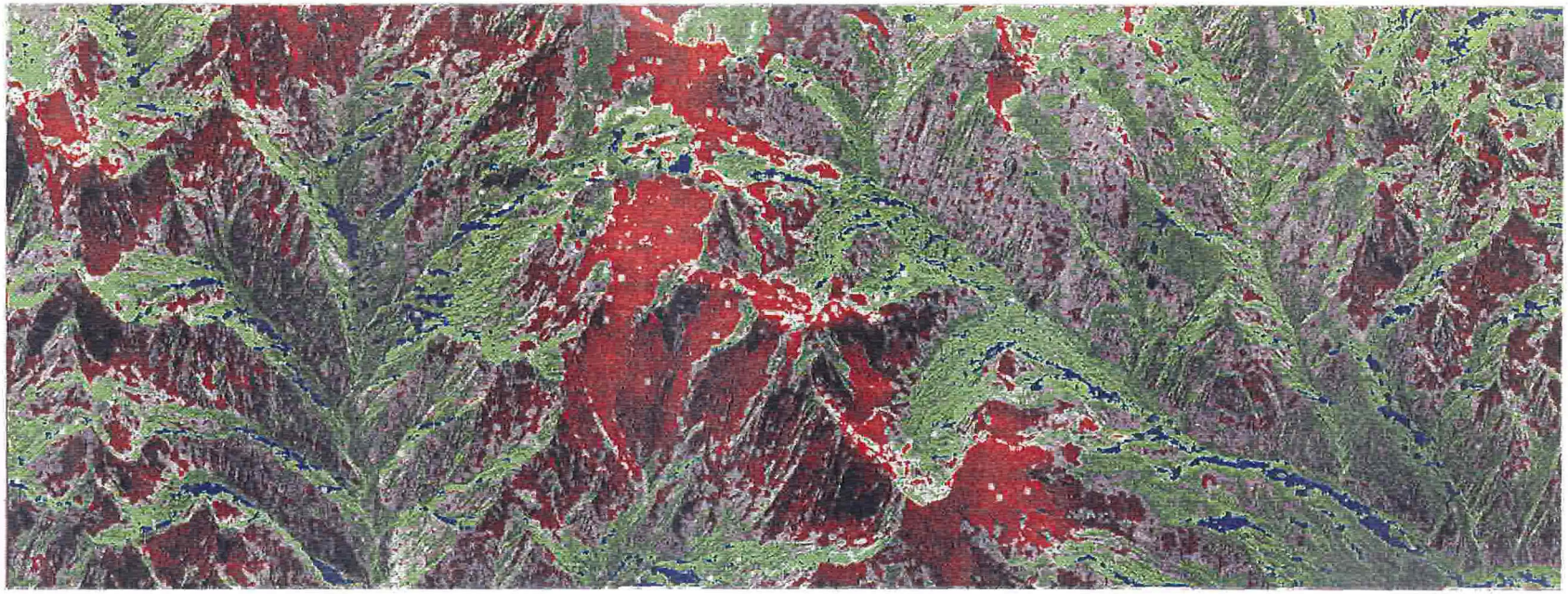

Figure 4.32 Tupungatito region C-band circular polarization ratios as observed by SRL-2 DT 2/40.60. Red color indicates $\mu_c>1$, green $0.25<\mu_c<0.7$, and blue $\mu_c<0.25$. The regions with permanent ice at the end of summer as shown in Fig. 4.31 are those that primarily display $\mu_c>1$ in the SRL-2 spring scenes here. See text for ratioing procedure.

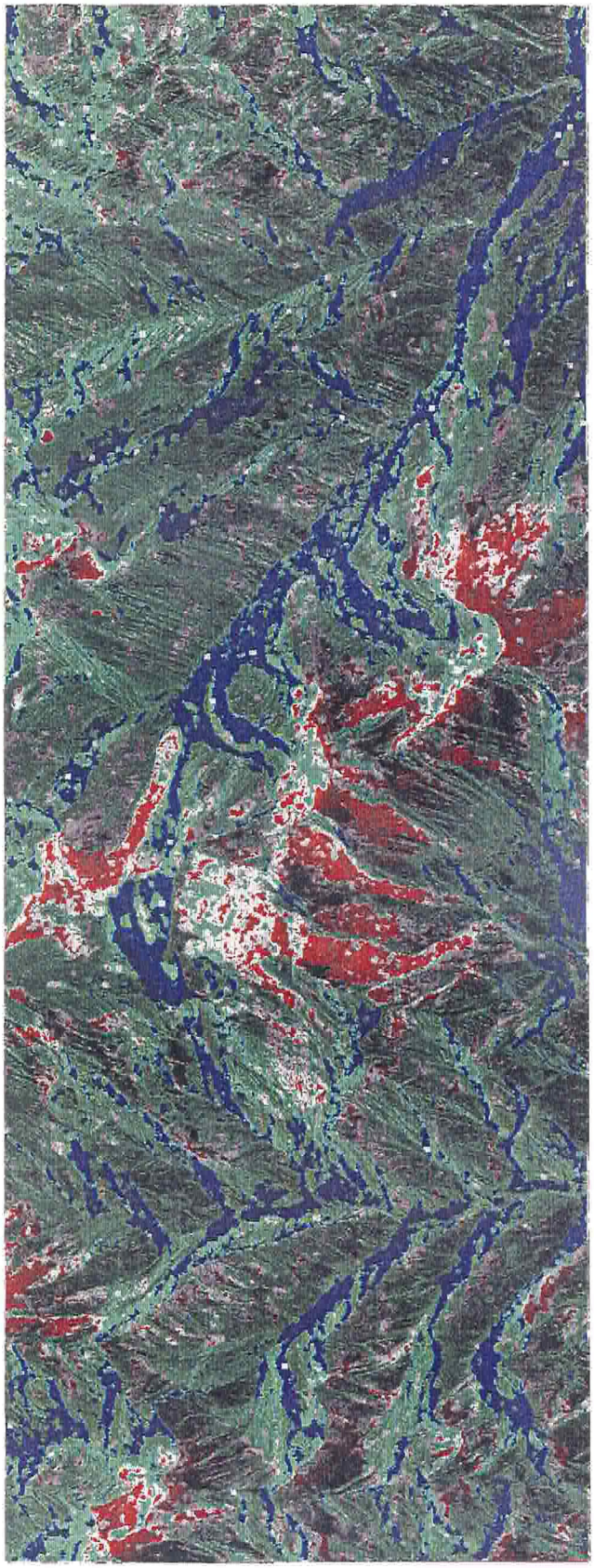

Figure 4.33 Tupungatito region L-band circular polarization ratios. Color assignments as in Fig. 4.32. Note that the upper reaches of the Tupungatito icefield display μ_c<0.7 at L-band, while much of the rest of the permanent ice regions have μ_c>1 where C-band μ_c is also greater than unity.

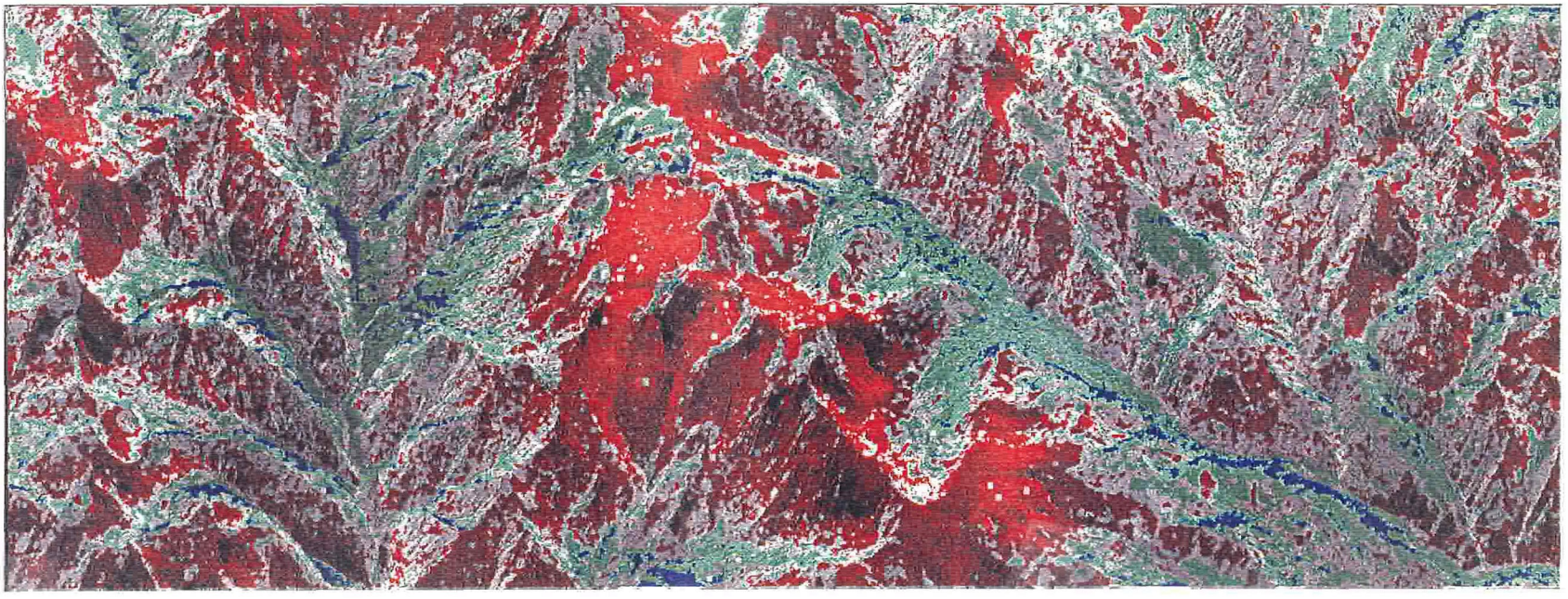

Figure 4.34 Tupungatito region C-band linear polarization ratios as observed by SRL-2 DT 2/40.60. Red color indicates μ_l>0.3, green 0.2<μ_l<0.3, and blue μ_l<0.1. Like for μ_c(C), most of the locations with enhanced μ_l (i.e. >0.3) are the same locations as have permanent ice in Fig. 4.31.

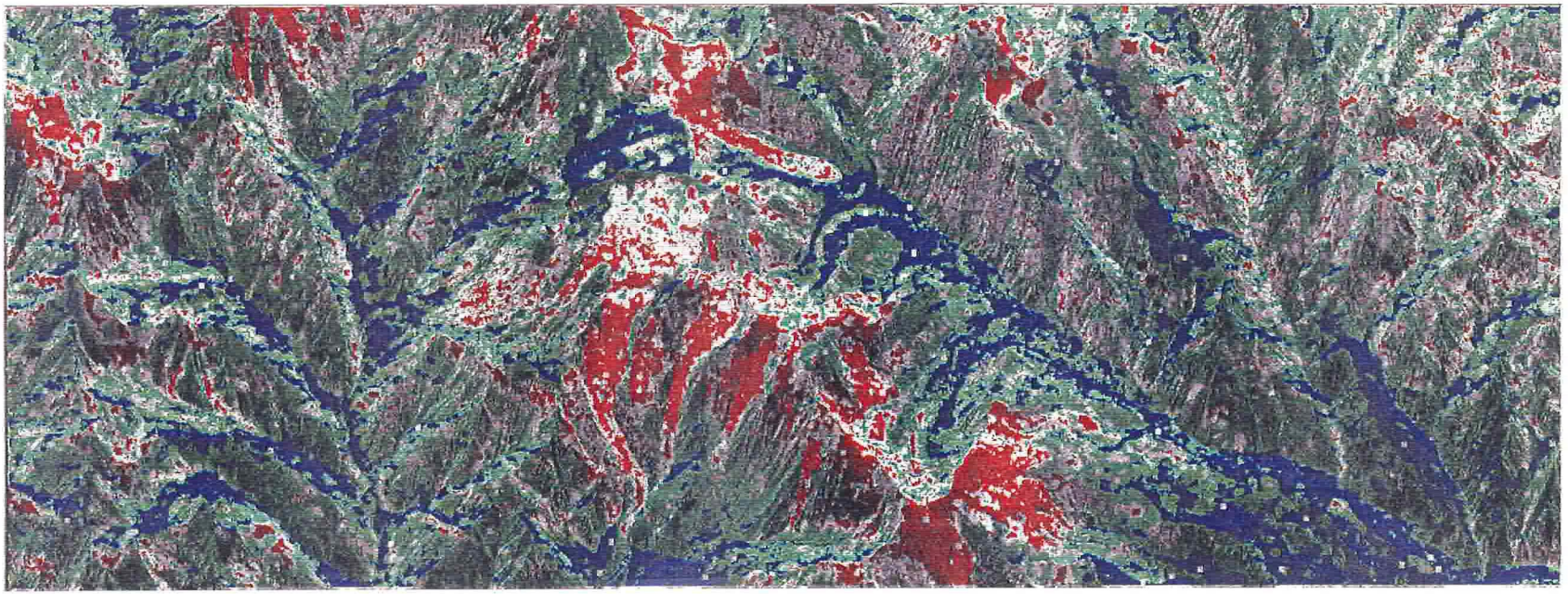

Figure 4.35 Tupungatito region L-band linear polarization ratios. Color assignments as in Fig. 4.32. Note that the L-band μ_l behavior is similar to the L-band μ_c behavior.

This is not surprising given the radar trasparency of cold firn, and the scattering possibilities offered by icy inclusions.

Other features appear from a comparison of the L-band polarization ratio maps to the C-band ratio maps. On the north flank of the lower slope of Tupungatito there is a site, 3km from the summit, where $\mu_c(L)>\mu_c(C)$, and $\mu_l(L)>\mu_l(C)$. In the visible photograph (Fig 4.31) the location also appears unremarquable. The polarization behavior is suggesting that some portion of the L-band scattering is due to volume scattering while C-band is being scattered to a greater degree right at the surface. A hint at the process at work may be offered by a similar trend at the much smaller region in the middle of the debris glacier flowing down from between the Tupungatito icefield and Cerro Alto. In Fig. 4.31 there appears to be a central portion of this glacier with high albedo, suggesting some ice at the end of summer. A thin layer of rock on the ice would affect the L-band less than the C-band, and allow the L-band to scatter from the deeper icy layers. If this were borne out, it suggests an application of multiple-polarization radar monitoring of debris-covered glaciers.

The general scattering behavior of the permanent ice regions outlined in Figs 4.31 through 4.35 can be addressed as it was for the Kunlun Shan by sampling sites within the scene with different incidence angles. The slopes in this Central Andes scene are somewhat steeper than those in the Western Kunlun. Thus there are more overlain (folded-over) features here. Note for example the mountain on the left edge of Fig. 4.30 that overlies the border. Also, several dark

regions on backslopes are quite likely due to shadowing. Determination of the scattering law requires careful assessment of the topography.

Sampling sites were picked in the image within regions of $\mu_c>1$. The locations were constrained to areas with coverage on the Chilean topographic map sheets. The sites picked are plotted on Fig. 4.36. Of all the sites selected, only the NP6 site was clearly shown to be shadowed after plotting on the topographic maps. Average scattering properties for all the sites shown in Fig. 4.36, with the exception of N06, are plotted in Fig. 4.37 for circular polarization behavior, and in Fig. 4.38 for linear polarization behavior.

First, the scattering behavior of the Tupungatito volcano flank sites (labelled TV1-TV4 in Fig. 4.36 and shown by filled symbols in Figs. 4.37 and 4.38) does appear to support the idea of L-band volume scattering. The C-band values are more reminiscent of scattering from the nearby rock surfaces, while the L-band values are more like that for the other icy sites examined in the plots. Given that debris-covered glaciers do occur in the Central Andes environment, the observations at the base of Tupungatito suggest that some component of the L-band σ° is from sub-surface volume scattering by ice.

In Fig 4.37 we again observe that the μ_c behavior seems to track what Rignot et al. (1993) observed in Greenland. The match is poorer here in the Central Andes that it was in the Western Kunlun. In particular the low incidence angle behavior appears to maintain the circular polarization inversion below 20°. As was the case in the Kunlun Shan however, the σ°(RR) behavior almost

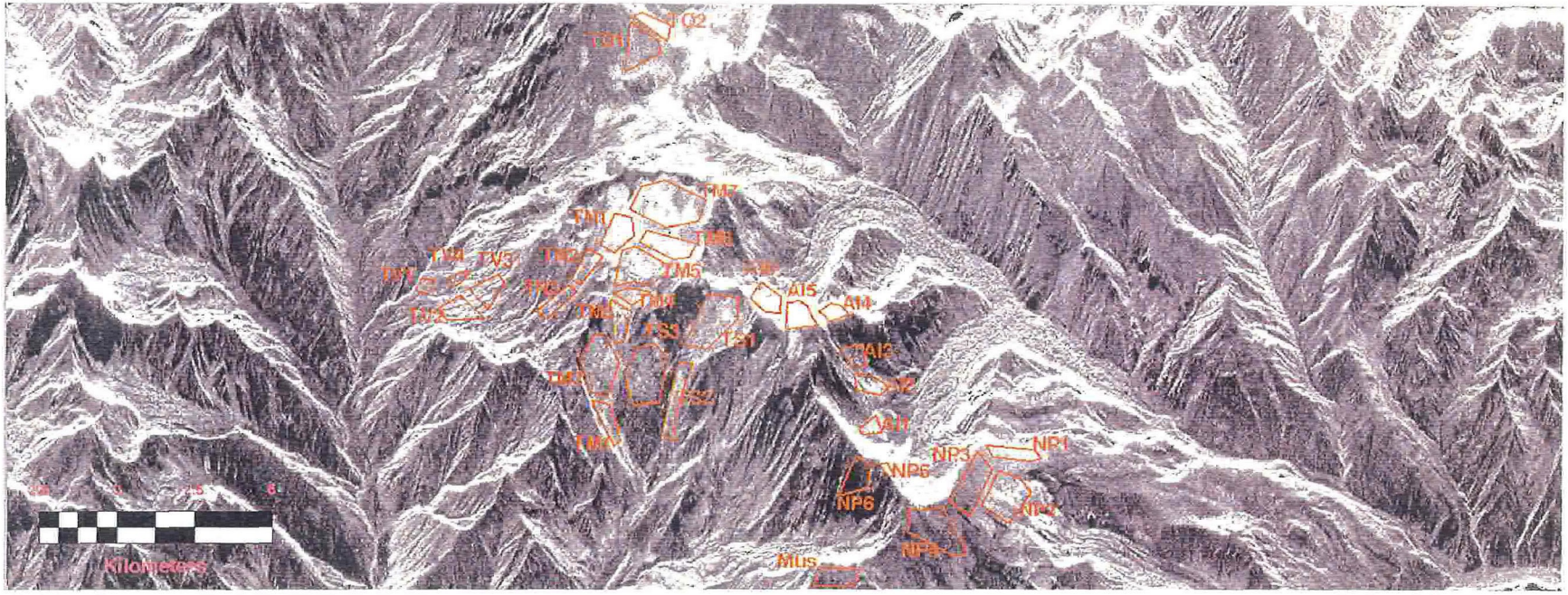

Figure 4.36 Distribution of statistical sampling regions for determination of enhanced μ scattering behavior. The site name abbreviation prefixes refer to nearby geographic features: Mus=Museo Gl., NP=Nevado de los Piuquenes, Al=Cerro Alto, TS=southern Tupungatito Gl., TM=Tupungatito II (middle), TN=Tupungatito I (north), TV=Tupungatito volcanic flank, TO=Tupungato.

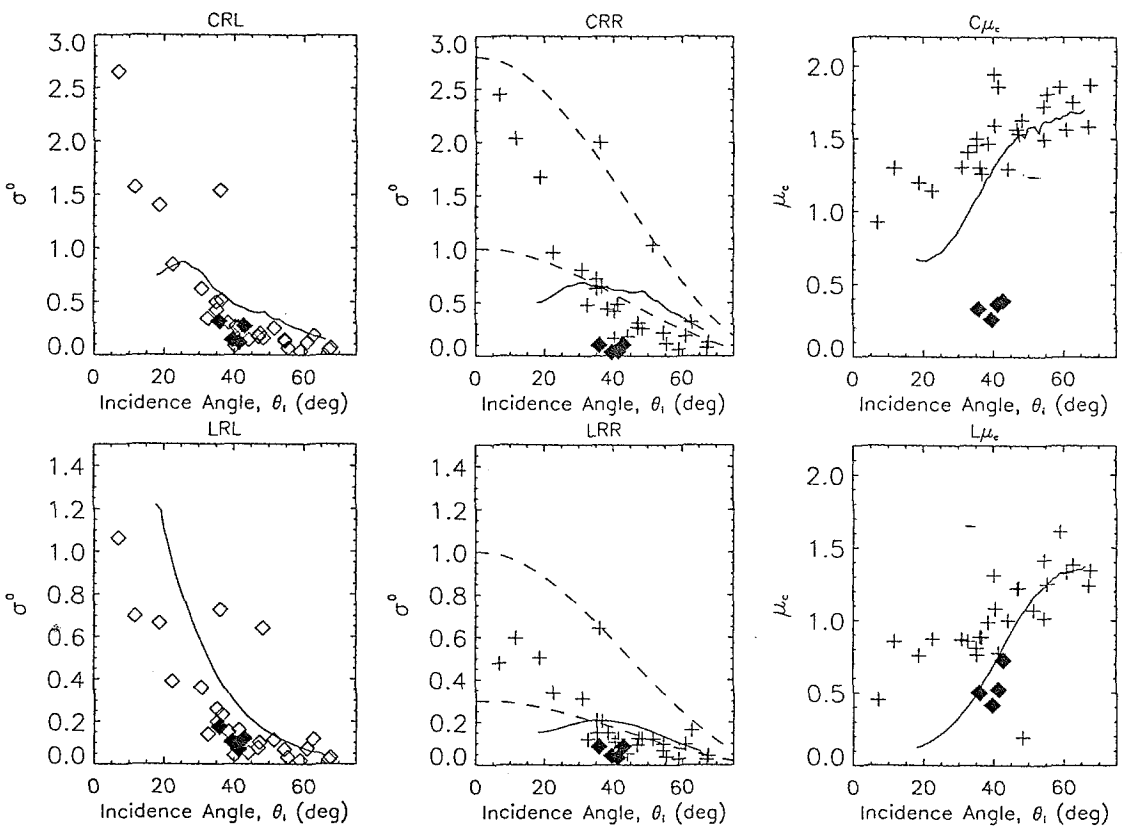

Figure 4.37 Circular polarization angular scattering behavior for thirty-one sites in DT 2/40.60 Tupungatito volcaon scenes. The solid line in the σ°(RL) and μ_c plots is the average behavior observed in Greenland by Rignot et al. (1993) The solid line in the σ°(RR) plot is deduced from the other two lines. The filled symbols correspond to the TV1-4 sites where $\mu_c(L) > \mu_c(C)$ suggesting L-band penetration to an enhanced volume-scattering region. The dashed lines in the σ°(RR) plot represent $A\cos^2(\theta_i)$ scattering behavior for A-values that bracket the data.

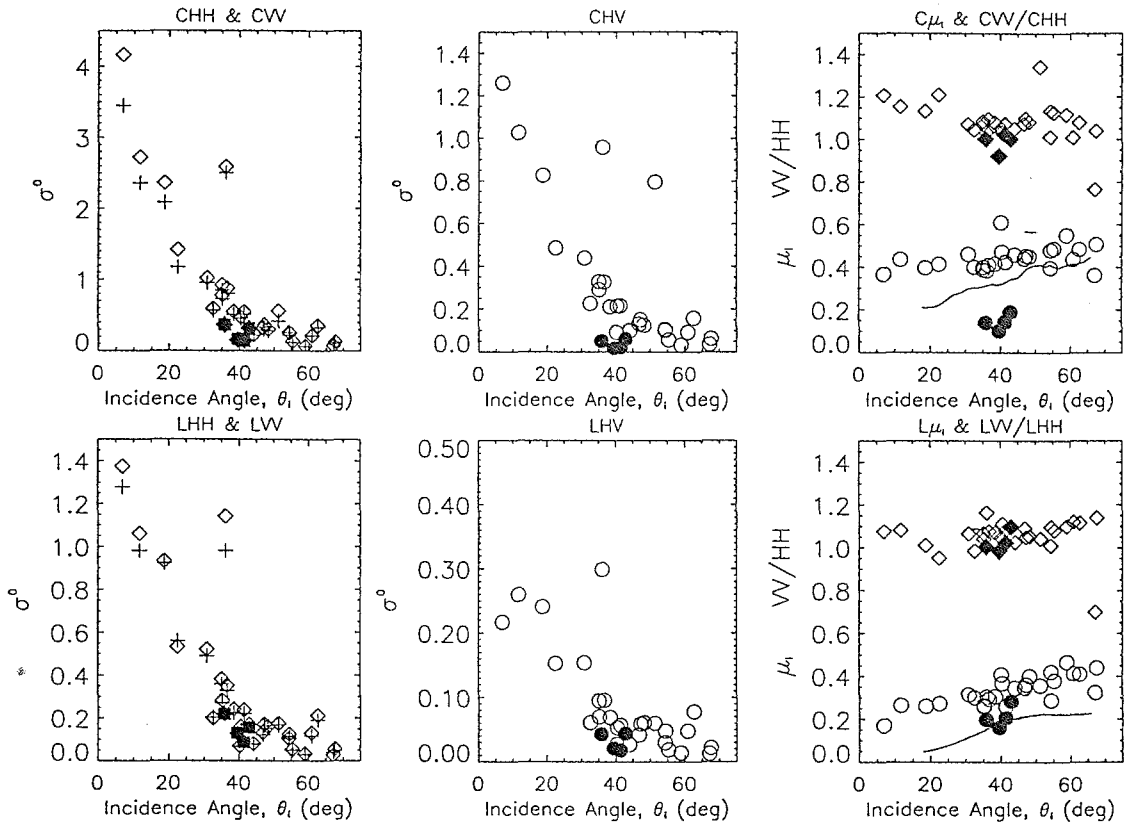

Figure 4.38 Linear polarization angular scattering behavior for the same sites as Fig. 4.37. Here the solid line in the μ_1 plots is the average μ_1 behavior that Rignot et al. (1993) observed. Symbols: HH-cross; VV-diamond; HV-circle, and the symbols for ratios correspond to the symbol of the numerator. The filled symbols represent the TV sites as in Fig. 4.37.

appears as if it were displaying a "specular" signature. This is rather perplexing, and remains unexplained. Possibilities include fold-over within all the selected regions enhancing the σ°, incorrect reconstruction of the σ°(RR), some geometric calibration effect not taken into account, or, perhaps, a unique scattering behavior that hints at the EGC behavior. While fold-over may be an explanation for a few of the high σ° points, it seems improbable that so many site determinations were in error. Certainly the L-band σ°(RL) trends in both the Kunlun (Fig 4.17) and here appear to resemble what was measured in Greenland, and if fold-over affects one polarization and wavelength channel, it affects them all. The possibility of an incorrect reconstruction of RR can apparently be discounted by both the Death Valley calibration and by the fact that the μ_c behavior in the Kunlun (where the scattering structures are known to resemble Greenland's) is comparable to Rignot's (1995) work. A similar argument stating that since the Kunlun L-band σ°(RL) and μ_c are reasonable fits to Greenland, there can't be any geometric calibration effects.

We are left with the idea that some mechanism is enhancing same-sense circular polarization scattering at small incidence angles. Now, this is in some sense the behavior exhibited by EGC. However, by inspection, of Figs. 4.37 and 4.17 we note that if we were to apply a cosine scattering dependence to the observations, the exponent would be greater than 2. This may be a new unique scattering behavior that can be attributed to ice.

4.5 Conclusions

We have applied a common planetary radar astronomy technique to produced the first mapping of terrestrial snow μ_c with images in the Western Kunlun Shan and the Central Andes. The images of these regions are startling in that, like images of the polar regions of Mercury and the RSPIC of Mars, μ_c values in excess of unity coupled with high radar cross-sections cover large areas.

The scattering behavior of the regions in both the Kunlun Shan and the Central Andes with $\mu_c>1$ is similar to the behavior observed over the percolation zone of the Greenland ice cap (Rignot *et al.*, 1993). The field information for the Kunlun Shan appears sufficient to confirm the importance of the percolation facies for at least part of the observed scattering behavior. Thus, the significance of radar scattering by the percolation zone on icefields beyond Greenland has been demonstrated. The implication is that similar behavior could be observed at any high altitude or high latitude site where the percolation facies is expressed.

A significant difference with Rignot et al. (1993) is found at smaller incidence angles ($\theta_i<30^\circ$). Our observed cross-sections increase where those in Greenland were observed to decrease. In particular the same-sense circular polarization channel, if fit to a cosine scattering model, would have an exponent of the cosine greater than 2. The small θ_i behavior for EGC is fit by a cosine scattering law with an exponent between 1.5 and 2. The possibility of unique snow formations in the Andes in particular being responsible for the observed behavior suggests avenues of future study. If it can be determined whether

penetentes were present either on the surface or buried in the firn in the Tupungatito region in October of 1994, then they may form a new model for snow/ice volume scattering signatures.

A buried tectonic structure is suggested by the Kunlun Shan SIR-C imaging. The variations in ice radar properties at the surface and near-surface can be determined by underlying structure in the glacier bed. This allows detection of buried regional structural features, such as the SSW-NNE Chongce fault line. The technique might well be applied more methodically than its serendipitous use here, to examine tectonic structure in ice-covered regions. This would of course require careful study of the local ice-scattering structure. A multiple-wavelength, multiple- if not full-polarization radar-remote sensing of mountain ice-cover tens of meters deep could yield valuable structural information in Antarctic regions for example. The technique also suggests that future radar mapping missions to icy planetary bodies would profit from multiple-polarization and multiple-wavelength capabilities.

The scattering response for the crevassed region at the top of the Chongce glacier in the Kunlun Shan demonstrates that fractured and rough ice can produce the unique radar response associated with the Galilean satellites. This fact suggests that the effects of subsurface cracks on ice scattering should not be discarded.

Chapter 5

5 Summary

5.1 Understanding Circular-polarization Radar

This thesis is a body of work that wrestles with the interpretation of radar scattering. There is ample evidence from all three planets observed that radar can serve well in a relative, qualitative sense. The more difficult task, which was addressed, yet remains to be pursued further, is to approach a fuller quantitative understanding of radar remote sensing. The discussions in this thesis have for the most part centered around quantitative analyses of the circular-polarization ratio μ_c In particular, how μ_c acts as a measure of scattering behavior "normalness." Progress remains to be made on some technical aspects of acquiring the quantitative information necessary to improve our understanding of radar scattering from natural targets.

5.1.1 Mars

Radar techniques were used to address three important issues for the selection of a landing site on Mars for the Pathfinder spacecraft.

Radar ranging described in Chapter 2 determined the elevations of the target sites. Elevation on Mars determines whether or not a sufficient atmospheric column is available to brake the interplanetary spacecraft's fall.

The radar echo strength at each of the sites indicates that the radar altimeter on the lander should have no problems detecting the planet's surface to gauge Pathfinder's progress through the descent and landing sequence.

Finally, the analyses of the radar scattering properties with both Doppler-only radar (CW) and delay-Doppler radar determined surface roughnesses at each of the sites considered. The roughness, which was assumed to be surface roughness or rockyness as a "worst case scenario", is an important factor for both Pathinder's airbag landing mechanism, and for the Sojourner rover which Pathfinder carries. The roughness results were quantified using a Hagfors approach. They provided a measure of comparison between the sites examined.

Table 5.1
Hagfors roughness determinations for VL1 and Ares Vallis

Site	Reference	λ (cm)	θ_i (deg.)	Remarks
VL1	Tyler et al. 1976	12.6	6	
	Harmon 1997	12.6	6.0±0.4	delay only
Ares Vallis	Harmon 1997	12.6	7.2±0.5	delay only, 36.7W
	Haldemann et al. 1997a	3.5	6.4±0.6	CW
	Haldemann et al. 1997a	3.5	4.8±1.1	delay-Doppler

The analyses were also compared to earlier radar observations of the Viking Lander 1 (VL1) site (Tyler *et al.* 1976), and compare favorably with other regional analyses made in aid of Pathfinder (Harmon 1997). Since some measure of ground-truth was obtained at VL1, the recent radar measurements are used to predict that Pathfinder's selected landing site at Ares Vallis should resemble VL1 in a "radar sense."

A more general result from Chapter 2 is that the evidence from the radar tracks distinguishes between different areomorphic environments, as determined from Viking imagery. The complete radar tracks should therefore be used more fully in any future detailed geologic and geomorphic mapping of Mars.

While polarization ratio was not measured in the delay-Doppler portion of the experiment a large preponderance of the OS channel had to be assumed to make a proper scattering model fit for parameter extraction. The Doppler-only measurements corroborated this approach, though future work with Mars delay-Doppler will focus on the power level that is reflected into the leading edge range-frequency channels (Slade 1997, personal communication).

5.1.2 Venus

With the Goldstone-VLA Venus experiment detailed in Chapter 3 it was hoped that the nature of the unique radar behavior in the highlands might be elucidated. Since almost all observations of Venus' surface have been carried out with radar the nature of the controversy is two-fold.

First is the question of how the observed radar behavior can arise, which can be summarized as being a controversy between enhanced surface scattering due to enhanced reflectivity, and volume scattering from more "normal" scatterers (rocks) buried in a relatively transparent matrix.

Second, the radar controversy is mirrored by the controversy over the environmental process producing the terrain with the unique radar signature. The general distinction is between an endogenic process and an exogenic process. Endogenic processes involve some properties of volcanic rocks as they are generated in the highlands, or some structural modification they undergo in being raised up on a highland. Exogenic processes are those that involve some external influence. In the Venus environment, where the highlands can behave as "cold traps" (Brackett *et al.* 1995), minerals may freeze out of the atmosphere at higher elevations, coating the rocks and producing the radar properties. Thus the "coatings" process is related to the enhanced surface reflectivity radar behavior arguments. However, materials delivered to higher elevations may not only coat the surface but interact with the rocks to some depth, and thus the altitude-related exogenic geochemical processes may also enhance radar volume scattering behavior.

The work described in Chapter 3 is unfortunately insufficient to fully distinguish between the two sides of the radar controversy. The evidence collected reconfirms that the anomalous radar behavior occurs in the cross-polarized (Tryka and Muhleman 1992 Alpha Regio SS images) channel as well as the co-polarized

(Pioneer Venus, Magellan in addition to earlier Earth-based observations data). The contribution presented demonstrates the relationship between the OS and SS polarization channels. The result is that SS and OS cross-sections rise in concert with increasing elevation on Venus, though σ°(SS) rises more steeply such that μ_c rises with altitude. The results of $\mu_c<1$ with elevated σ° are consistent with volume scattering, but also with areas of blocky dihedral backscatter ($\mu_c>1$) over areas smaller than the resolution of the experiment.

Future work to measure the complete Stokes matrix with the Goldstone-VLA technique may offer some further insight to the polarization behavior of these radar anomalous locales. Better spatial resolution on Venus cannot be expected from the Goldstone-VLA technique. However, the latter technique may be used in conjunction with delay-Doppler imaging by Goldstone alone, or by the upgraded Arecibo Observatory to calibrate cross-sections measured in RL and RR with those instruments. While these experiments may lay to rest the radar controversy, the true nature of the physical process producing them on Venus will probably have to wait for a landed or balloon-borne mission to the planet.

More generally, the Venus observations clearly confirm what radar has long shown: the geography is clearly visible in our images due not only to the highland anomalous reflectivity, but also to real variations in surface roughness in the lower regions as well.

5.1.3 Earth

In both the Kunlun Shan and the Central Andes with the excellent resolution provided by SIR-C, geographic location in the images is only limited by the resolution of the other available mapping instruments. This result has been well-known for many years and is in fact largely responsible for the development of imaging radar system like ERS-1 and SIR-C.

The discovery by Rignot *et al.* (1993) of $\mu_c>1$ behavior of the percolation facies in the accumulation zone of the Greenland icesheet suggested that terrestrial analogies could be made to the radar behavior of the icy Galilean satellites. This prompted a search for other unique radar behaviors of terrestrial ices at high altitudes. The initial hope was that high elevations might provide an environment where cold ice could demonstrate other unusual radar behaviors. If different ice structures could be found then perhaps different models for the behavior of Europa, Ganymede and Callisto (EGC) could be found.

The outcome of the search search was positive. Icefields in the Western Kunlun Shan in the Central Andes display $\mu_c>1$. However, the structures producing the observed behavior appear, in Tibet at least, to be the same as in Greenland: sub-surface ice pipes and layers internally reflect the radar producing elevated backscatter cross-sections with the observed polarization behavior. The case in the Tupungatito region of the Central Andes near Santiago is less clear. The unique radar behavior there is directly related to the permanent snow deposits, that are probably covered by fresh snow at the time the SIR-C data were collected.

The firn transition in the Central Andes is reported as taking only 4 months by Lliboutry (1965), so percolation zone refrozen ice structures may be responsible for the observed radar signature. However, more unique firn structures in the form of buried penetentes are also a possibility suggested here.

In either case, while the terrestrial ice structures produce unique radar behaviors, they do not truly mimic the behaviors displayed by EGC. Rignot (1995) suggested that internal reflections from buried ice fragments produced by cratering may have a similar behavior to buried ice pipes. This seems reasonable, thought the high nadir cross-sections of EGC need to be explained. It may be that a randomly oriented, appropriate size-distribution of ice blocks could do the trick. However, arguments about fractured ice on EGC need to be consistent with recent and future results from the Galileo spacecraft which is demonstrating that the three icy satellites are not all alike. There is clearly room for further study of both actual terrestrial ice scattering, and its theoretical framework, in view of resolving the mystery of the radar behavior of EGC.

5.1.4 What is "Normal" ?

The Earth's biospheric carpet complicates terrestrial quantitative radar work, while the comparatively static planets mostly behave as "normal". Following traditional radar astronomy, normal radar targets in this work are all of Mars, the low-lying areas of Venus, and the unvegetated rocky surfaces in Death Valley. Certainly, the "normalness" of Mars' radar properties were relied on to carry out applied planetary science in aid of the Pathfinder Lander mission.

Death Valley was used as a test site for SIR-C image processing techniques. As a site familiar to the author, the Stovepipe Wells area of Death Valley served reasonably well to confirm SIR-C image processing procedures. As it happens though, even in a dry desert environment on Earth there is $\mu_c > 1$ radar behavior. This may in places be explained by a vegetation canopy, or root structures, or by buildings. There may still be other mechanisms at play, in particular in the area of star-dunes at Stovepipe Wells: the cross-sections are low, so all the echo in both RL and RR polarizations may in fact be due to diffuse volume scattering.

5.1.5 What is "Unique" ?

Throughout this thesis "unique" has been used to describe high reflectivities or circular polarization ratios greater than unity. In fact only on the Earth were locales clearly discerned with $\mu_c > 1$. Venus' highlands may be guarding their secrets by displaying $\mu_c \leq 0.9$. Among the "unique," Venus is not as strikingly unique as Mercury's polar regions or the icy Galilean moons. Thus, by the measure adopted here, Venus is unique, but terrestrial icefields are more unique.

5.2 Applying Circular-polarization Radar: Outlook

5.2.1 Snows of Venus

The term "snow line" has been applied to the abrupt change in radar behavior with altitude observed in the highlands of Venus. As it happens, this is perhaps less of a misnomer in the hot Venus environment that it seems at first glance.

At high elevations on Venus, like on Earth, the thermal gradient may be expected to play an important role in determining the surficial processes. The onset of the observed radar behavior at a particular level on the gentle slopes of Beta Regio is reminiscent of the gradation of ice properties on the long and relatively gently sloping glaciers of the Western Kunlun.

While this is far from implying that the high elevation radar-anomalous regions on Venus experience some strange type of "snowfall," the conceptual framework of the altitude-radar-scattering relationship evidenced by terrestrial snow is nevertheless compelling. The analogy does underline the volume scattering side of the controversy over the scattering mechanism on Venus. The fact that $\mu_c < 1$ was observed argues against dihedral scattering from a blocky surface like the the SP flow in Arizona (Campbell *et al.* 1993). Above all, the snow analogy reinforces the fact that high backscatter cross-sections can arise from volume scattering.

5.2.2 *Snows of Earth*

It is worth pointing out that without the field information that was available for the Himalayas, the final analysis of the ice scattering might be in a similar state to the debate about Venus' highlands. Without a smoking-gun scattering population, confirmed by Jezek et al. (1994) for Rignot et al.'s (1993) observations, an argument might also surround discussion of processes that roughen the surface of the icecap preferentially at higher altitude.

A further advantage for the terrestrial snow observations is the opportunity to explore the full polarization response. In Chapter 4 the relationship between circular-polarization backscatter measurements and linear-polarization backscatter measurements was explored and exploited. The variety of information that radar polarimetry provides would be a boon for mapping Venus or applied to planetary ice deposits. Certainly the extension of the terrestrial ice observations to truly cold clear ice in the Antarctic winter would benefit from a complete polarization characterization.

The unique radar behavior of terrestrial ices poses a challenge and offers an opportunity for the future exploration of planetary ice deposits. The relative transparancy of ice suggests that we will be able to probe deeper into icy bodies by remote means that has been the case for rocky Solar System bodies. However, interpretation of the results would certainly benefit from advances in understanding the radar volume scattering behavior of cold terrestrial ice deposits.

5.3 Normal and Unique Radar Planetology

The modern body of knowledge about radar scattering is enormous, with many specialized aspects. Certainly, specialization is required by the technical complexity of radar. Still, there is a place for the global perspective which a planetary scientist is perhaps afforded.

Planetary radar astronomy developed following the logic imposed by the distance-to-the-fourth-power dependence of the radar equation. Thus, large, nearby celestial targets were targeted before more distant ones were examined. It is then perhaps simply an historical perspective that chooses the radar behavior of terrestrial/rocky planetary bodies as the norm, while any other radar behavior is considered anomalous. If our Moon had been an icy body, perhaps we would be further along in understanding the mechanism of radar scattering from cold ices. We would probably also be further along in understanding the behavior of cold ices on the Earth. Alternatively, if there had been life on Mars, we would have probably observed low reflectivity μ_c anomalies that might have spurred the understanding of terrestrial vegetation radar scattering by radar astronomers. As it is, we comfort ourselves in our rocky corner of the solar system in looking for unique rock-like environments, when the non-rock environments on the Earth offer a great variety of radar properties, whose characteristic may still teach us something about other worlds.

Appendix A

A. Venus Radar Glossary

A.1. Radar Terminology

AIPS : Astronomical Image Processing System software.

Circular polarization ratio : The ratio of the SS echo power to the OS echo power represented by the symbol μ_c.

CLEAN : Deconvolution algorithm. See Cornwell and Braun 1989.

Cosine model (Lambertian) : The best analytic form of the dependence of σ_{SS} on incidence angle has been found to be some power of the cosine of the angle times a constant.

Hagfors model : A form of analytic expression for the angular dependence of σ_{OS} for planets. This one depends on the parameters ρ_0, akin to the Fresnel reflectivity, and C which represents the wavelength-dependent inverse of the rms slope. This model assumes that height variations are small and gaussianly distributed, and that the surface correlation function is exponential. This model only fits data for incidence angles less than about 30 degrees.

Muhleman model : An analytic form of the dependence of σ_{OS} on incidence angle for planets. This particular expression depends on two parameters α and β.

α is related to the mean slope, and β is a constant. This model assumes that height variations are distributed exponentially, and assumes an exponential surface correlation function. The surface correlation function is a statistical representation of the surface roughness. The model fits data over the whole planetary disk.

OS, SS : When circularly polarized radio waves are reflected at a flat dielectric interface (*i.e.* specular reflection at infinite half space) the reflected wave has the opposite sense of circular polarization as the incident wave. We term this the OS echo (Opposite Sense). Elsewhere in the literature it is referred to synonymously as the OC echo (Opposite-sense Circular), polarized echo, or even expected echo. Natural surfaces are not perfect mirrors, and reflect some of the incident energy in the same sense of circular polarization as incident, which we call the SS echo. Elsewhere it is referred to as the SC echo or the depolarized echo.

Polarization isolation : Describes the circular polarization purity of the transmitter or receiver; 30 dB polarization isolation for the RCP transmitter means there is less than one per mil LCP in the transmitted signal.

Radar albedo / Radar cross-section : The terms as used in this paper are synonymous, and are represented by the symbols σ_{OS} and σ_{SS}. The normalized radar cross-section of an object refers to the relative cross-sectional area of a perfectly conducting sphere that would have the same echo power as the object. It includes both the effects of the true Fresnel surface reflectivity and of the dependence of the echo on incidence angle (radar backscatter phase function).

RCP, LCP : Right Circular Polarization and Left Circular Polarization; describes the helicity of the electromagnetic wave electric field vector as viewed in the direction of propagation.

Specular spike : In a similar way that a metal sphere viewed in the direction of illumination is brightest at the sub-viewing point, a terrestrial planet illuminated by radio waves will have a very bright spot or spike in the OS echo at the center of the apparent disk of the planet. This is an enhancement of σ_{OS} produced by the increased surface area of facets oriented toward the receiver at or near the sub-radar position.

A.2 Geologic Terminology

A'a : A rubbly, rough-looking lava flow morphology on Earth.

Accommodation zone : A region of rift axis lateral off-set. Term used for Earth continental rifting, and related to "transform fault zone".

Chasma / Rift : A trench-like structure bounded by parallel normal faults. Smaller features of this type are generally called graben.

Coeval : Occurring at the same geologic time.

Extension : Is used in the geologic sense here to refer to the evidence of deformation due to extension, *i.e.* rifting, and to the implied existence of extensional stress.

Pahoehoe : A relatively smooth ropy-surfaced lava flow morphology on Earth.

Tectonic : Refers to movement and deformation of the lithosphere.

Tessera: Term given to areas of regional deformation on Venus producing ridge-and-groove terrain. The term is Latin for tiles, referring to the tile-like, or rhombical and orthogonal parquet-like pattern of these regions, produced by at least two sets of intersecting ridges and grooves.

Appendix B

B. Experimental Data Reduction and Processing

B.1 Goldstone-VLA experiment

The basic datum obtained by an interferometer like the VLA is called a visibility. Each antenna-pair baseline of the array samples the complex visibility function, which is a component of the two-dimensional Fourier transform of the sky brightness function. Thus, a two-dimensional inverse Fourier transformation of the data gives an estimate of the sky brightness.

The VLA can observe a spectrum of frequencies as well as all polarizations. For our radar experiment we collect the radar information in a single channel with two polarizations. To do this, the DSN RCP transmission frequency was adjusted to maintain a constant receiver center frequency at the VLA. The DSN transmitter has a polarization isolation of 30 dB. At the VLA we collected visibilities in 256 channels centered on 8.510 GHz (3.51 cm) with channel widths of 763 Hz in both LCP and RCP. These data form the "line" data set. The Doppler spreading due to Venus' apparent rotation is so slight that the radar echo signal is in only the central channel. The other 255 channels "see" the Venusian thermal emission background, which we do not otherwise discuss in this paper. A so-called "channel 0" data set is also produced by averaging the inner 75 % of the

line channels, and its usefulness will be explained below. Three radio sources other than Venus were also observed at intervals during the experiment for instrument and data calibration purposes; these were the flux calibrator radio source 3C48, the array phase calibrator source 0042+233 and the frequency bandpass calibrator---a strong radio source for our small bandwidth---3C84.

The total observation time is important for image reconstruction with the VLA; the rotation of the Earth moves the baseline fringe patterns on the sky, synthesizing the small beam of a wide-aperture radio-telescope. On Feb. 28 it snowed heavily, so only 1 hr. 26 min. of Venus visibilities were obtained. On March 4 we got 5 hr. 14 min. of Venus visibilities. The size of the beam also depends on the separation of the antennas in the array. During the first quarter of 1993, the VLA was in its B configuration, with maximum baseline of 11 km, yielding resolution of approximately 0.6 arcsec or 160 km at the sub-Earth point.

B.2 Initial Data Reduction

The calibration and processing of the raw data was accomplished with the Astronomical Image Processing System (AIPS) software. The initial work was carried out on the channel 0 calibration data. The absolute flux was set from 3C48, and was taken to be 1.635 Jy. Next, 0042+233 was used to make antenna complex gain solutions across the run. Self-calibration on 0042+233 provides phase calibration. These calibrations from the channel 0 data were then applied to the line data. The bandpass across the 256 line data channels was calibrated from

the strong source 3C84, and applied to the line data for Venus. Following this, a file with the radar information from the central channel was separated out. Venus' position angle was "removed" by rotating the visibility data for subsequent processing, this is for convenience as it puts Venus' north pole at the top of all our images.

Self-calibration (Cornwell and Fomalont 1989) is a phase closure process which reduces phase noise due to atmospheric and antenna-based variations on timescales shorter than the intervals between phase calibrator scans, which have been included in the calibration process as described above. In our case the self-calibration is carried out on the OS radar signal . This signal contains the very large specular spike which is very near the phase center. This allows AIPS to pick high signal-to-noise visibilities which are used to calculate the antenna complex gain corrections. These were then applied to the data in both polarizations.

After self-calibration, the synthetic antenna response was deconvolved using the CLEAN algorithm to produce images. The calibrated visibilities are delta-functions sampled in Fourier-space. CLEANing interpolates through the gaps in the beam coverage. This was aided by specified initial models for the average response in each polarization: a Muhleman model for the OS echo, and a cosine model for the SS echo. The CLEAN algorithm (*i*) picks the maximum delta-function in the image field and notes its coordinates, (*ii*) calculates the antenna beam effects, (*iii*) subtracts those, and then iterates down to the noise level. For a more complete explanation see Cornwell and Braun (1989).

B.3 CLEAN Uncertainties

Unfortunately, "to date no one has succeeded in producing a noise analysis of CLEAN itself" (Cornwell and Braun 1989 p.173). CLEAN's deconvolution process can produce non-unique solutions. The net effect is to produce an uncertainty in the final image. This can be somewhat reduced by using *a priori* models as we do, and also by experimenting with the process. The quality of the images depends on both the image resolution and on the noise level in the final images. We take the noise level in an image of given polarization, N_{pol} (pol = OS or SS), to be the rms flux in the image away from the planetary disk. We carried out multiple CLEANs of our data with different reasonable initiating parameters and found that the flux at a given position in the images varies by less than 10%. The various parameters affecting image quality are summarized in Table II. It should be noted that $N_{OS} > N_{SS}$. This is due to self-noise from the source (Kulkarni 1989), which in our case was the large specular spike in the OS channel, and is unavoidable. Further, while the data for March 4 has lower N_{SS} and better spatial resolution, the stronger specular spike on that day hampers CLEANing by adversely affecting dynamic range, producing a "moat" around the spike, effectively restricting the geographic extent of acceptable data. We believe that our 10% uncertainty estimate also encompases these effects of CLEANing.

Appendix C

C. Venus Atmospheric Correction and Radar Cross-Sections

It is necessary to correct for the atmospheric attenuation in order to make maps of 3.5 cm radar cross-sections from the processed images. An average correction factor, $\alpha(x,y)$, was calculated for each 0.2 asec sky-pixel. We used the Venus model atmosphere of Muhleman *et al.* (1979) to obtain profiles of refractive index and of opacity. We used the refractive index profile to trace refracted rays down to the planet surface, as determined by Magellan altimetry. A 25-by-25 grid of sub-pixels (0.04 asec) centered on (x,y) was used for ray-tracing. This alleviated effects due to variation of projected area on the planet. With a ray path and opacity profile, we found multiplicative correction factors for each ray. For averaging, the correction factor for each sub-pixel was weighted by the attenuation (e.g. higher altitude features dominate a pixel's response) and by the gaussian beam weight.

Near the Venus limb the correction factors we obtain are huge, and it is clear that such factors would only serve to amplify noise. Two methods were considered to address this problem: (*i*) mapping the disk could be restricted to a

smaller radius where the correction factor is not so large or (*ii*) the images could be limited to some value above the noise level. The first method is somewhat artificial: how big a correction factor is unreasonable given our detection system? So the second method was chosen: only the pixels in the images that had value greater than three times the off-disk rms noise, N_{pol}, were retained. Another advantage of restricting the images is that it removes negative-valued pixels produced by CLEANing, and which are part of the noise. This procedure eliminates the possibility of identifying "stealthy" (low cross-section) features on Venus. We resign ourselves to this in favor of isolating significant reflective features. The correction factors have a numerical uncertainty, which is calculated. It is assumed independant of the noise and CLEAN uncertainties, and all three contribute to the cross-section error bars.

Appendix D

D. SIR-C High Altitude Full-polarization Data Takes

SRL-1:

track no.	orbit	site	pol.	start time	theta_i	lk dir	CD-ROM
13.6	a	Cerro Laukaru, Chile	16x	00/18:55:21	38.6	s	1_51
21.1	d	Nelson House, Manitoba	16x	01/05:52:07	24.96	s	1_12
25.3	d	Cerro Laukaru, Chile	16x	01/12:26:09	49.48	s	1_50
37.1	d	Nelson House, Manitoba	16x	02/05:32:39	23.18	s	1_41
41.5	d	Cerro Laukaru, Chile	16x	02/12:08:12	43.86	s	1_55
46.5	a	Charana, Bolivia	16x	02/19:56:35	29.14	n	1_20
57.5	d	Cerro Laukaru, Chile	16x	03/11:49:43	38.15	s	1_08
58.1	a	Hotien East, China	16x	03/12:30:09	28	s	1_34
61.7	a	Cerro Cumbrera, Chile	16x	03/17:59:36	47.38	s	1_10
69.1	d	Nelson House, Manitoba	16x	04/04:54:41	19.62	s	1_21
73.3	d	Cerro Laukaru, Chile	16x	04/11:30:04	31.91	s	1_09
74.1	a	Hotien East, China	16x	04/12:08:46	29	s	1_53
85.1	d	Nelson House, Manitoba	16x	05/04:35:05	17.98	s	1_08
110.5	a	Manaus Cabaliana, Brazil	16x	06/18:37:05	26.18	s	1_18
120.5	d	Cerro Aconcagua, Argent.	16x	07/08:54:39	23.44	n	1_57
122.11	a	Hotien East, China	16x	07/11:09:29	42	s	0
122.12	a	Tien Shan, China	16x	07/11:11:57	22.92	s	1_53
126.4	a	Charana, Bolivia	16x	07/18:16:17	43.71	s	1_25
143.52	d	Khumba, Himalaya	16x	08/18:35:43	45.22	s	0

SRL-2:

track no.	orbit	site	pol.	start time	theta_i	lk dir	CD-ROM
13.6	a	Cerro Laukaru, Chile	16x	00/18:55:17	38.27	s	2_25
21.1	d	Nelson House, Manitoba	16x	01/05:52:09	25.35	s	2_18
25.3	d	Cerro Laukaru, Chile	16x	01/12:26:11	47.33	s	2_31
26	a	Tien Shan, China	16x	01/13:08:54	38.48	n	2_32
37.1	d	Nelson House, Manitoba	16x	02/05:32:33	23.68	s	2_20
40.6	d	Cerro Aconcagua, Argent.	16x	02/10:33:47	34.6	s	2_30
41.5	d	Cerro Laukaru, Chile	16x	02/12:08:06	44.05	s	2_65
42.1	a	Tien Shan, China	16x	02/12:50:20	27.93	n	2_30
46.5	a	Charana, Bolivia	16x	02/19:56:22	30.26	n	2_03
57.5	d	Cerro Laukaru, Chile	16x	03/11:49:35	38.12	s	2_21
58.11	a	Haryana, India	16x	03/12:27:24	41.86	s	2_21
58.12	a	Hotien East, China	16x	03/12:31:22	35.22	s	2_65
61.7	a	Cerro Cumbrera, Chile	16x	03/17:59:31	48.12	s	2_21
69.1	d	Nelson House, Manitoba	16x	04/04:54:41	19.69	s	2_66
73.3	d	Cerro Laukaru, Chile	16x	04/11:30:23	31.92	s	2_37
74.1	a	Hotien East, China	16x	04/12:09:07	29	s	2_37
84.11	a	Juan de Fuca Straight	16x	05/03:02:45	27	s	2_40
84.12	a	Prince Albert, Saskat.	16x	05/03:06:05	41.77	s	2_40
85.1	d	Nelson House, Manitoba	16x	05/04:35:24	17.84	s	2_66
100.12	a	Prince Albert, Saskat.	16x	06/02:45:06	43.63	s	2_04
116.21	a	Juan de Fuca Straight	16x	07/02:22:22	27	s	2_55
116.22	a	Prince Albert, Saskat.	16x	07/02:25:12	45.17	s	2_55
122.2	a	Tien Shan, China	16x	07/11:06:29	24.86	s	2_15
138.2	a	Tien Shan, China	16x	08/10:43:30	24.86	s	2_11
154.2	a	Tien Shan, China	16x	09/10:20:37	24.86	s	2_28
167.9	d	Iturralde Crater, Boliv.	16x	10/06:10:59	53.38	s	2_14
170.2	a	Tien Shan, China	16x	10/09:57:42	24.86	s	2_11
174.97	a	Charana, Bolivia	16	10/17:07:29	44.19	s	2_34

Appendix E

E. Death Valley and SIR-C Circular-polarization Processing

E.1 Death Valley Data as Processing Check

Death Valley was designated a "geology supersite" for the two SRL missions. The supersite designation resulted in intensive coverage during the missions (JPL, 1993). Although not designated a calibration supersite, corner reflectors were distributed in Death Valley to check channel imbalance over wide areas within scenes. The coverage requirement for Death Valley prescribed at least on quad-pol data take (DT) on each SRL mission. In fact, there were 2 quad-pol DT's during SRL-1 and 2 during SRL-2. All four of these tracks were Stovepipe Wells DT's, and are listed in Table E.1.

Results of investigations in the Stovepipe Wells area already exist in the literature (Greeley 1995, Weeks 1996, 1997). Also, the region is somewhat familiar to the author, and contains mountainous topography. Therefore, Stovepipe Wells data were processed in the same manner as the Himalaya and Andes data for the high altitude ice investigation, as a means of checking the validity of the radar image processing that was used.

Several of the previously processed quad-pol scenes for DT 1/120.30 were obtained. The compressed Stokes scattering operator data is delivered on 8 mm Exabyte tape from the USGS EROS Data Center (EDC). Full resolution data for a given interval on a particular radar track is processed and calibrated at EDC and

Table E.1
SIR-C Death Valley quad-pol data takes

DT	Name	Orbit direction*	Illumi-nation**	θ_i
SRL1:				
35.1	Stovepipe Wells, CA	A	S	44.99°
120.30	Stovepipe Wells, CA	D	N	43.25°
SRL2:				
8.3	Stovepipe Wells, CA	D	S	40.85°
35.11	Stovepipe Wells, CA	A	S	44.90°

* A, ascending orbit; D, descending orbit
** S, illumination toward south; N, illumination toward north.

given a sequential processing scene number that begins with "1" for SRL-1 data and with "4" for SRL-2 data[¶¶¶]. For Stovepipe Wells DT 1/120.30, scenes pr12060 (L-band) and pr12061 (C-band) were ordered and decompressed. The scene preparation sequence for SIR-C data in this thesis is outlined in Figure E.1. JPL software is used to read and decompress the data from the tape (JPL D-11427, April 1995). A typical decompressed full-polarization slant-range (SLC) scene

[¶¶¶]Far from all SIR-C data has been processed at full resolution!

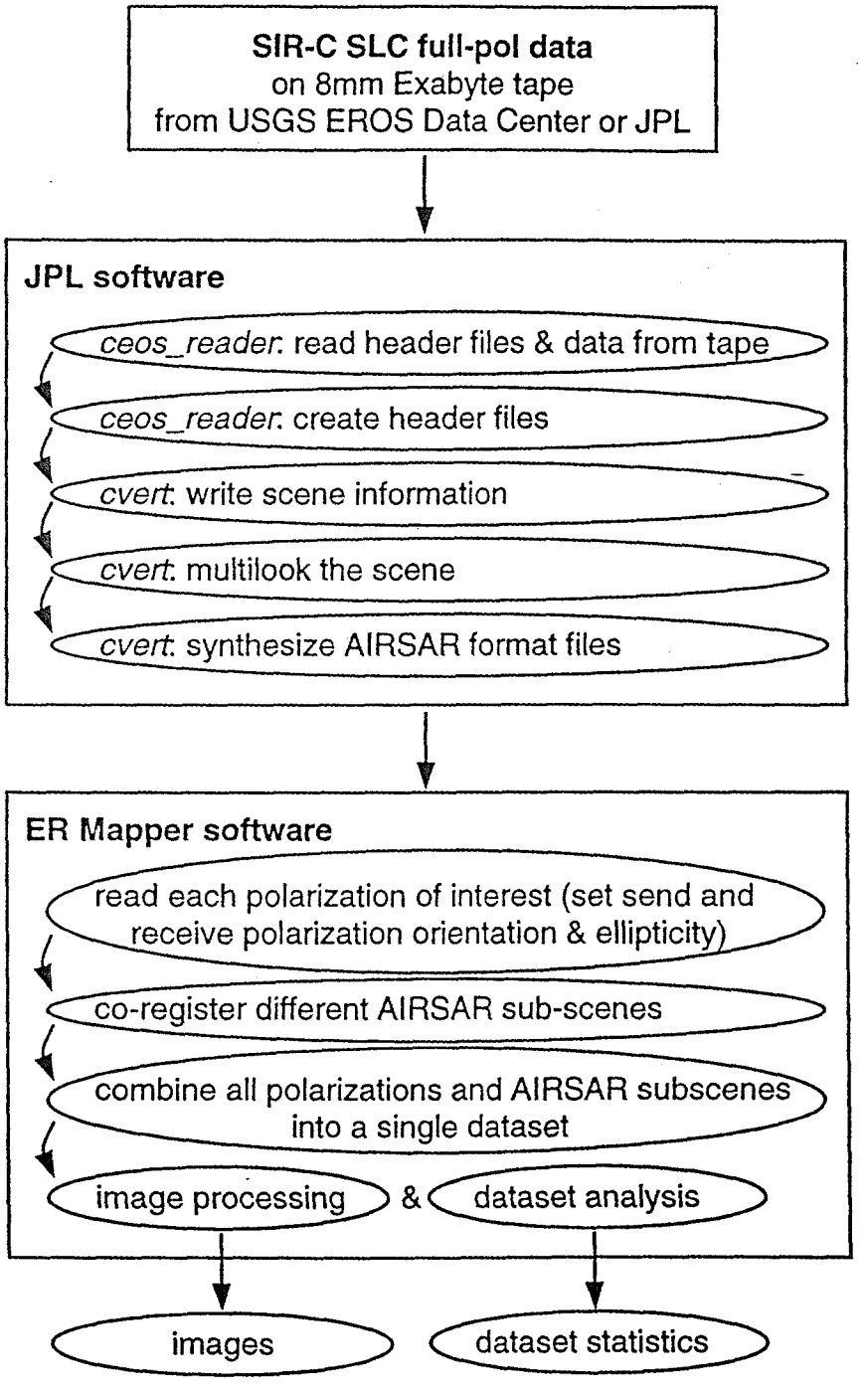

Figure E.1 SIR-C quad-pol image preparation and processing scheme

produces a single-wavelength file that takes up around 150 MBytes. To make the data volume more manageable, and also to reduce SAR speckle, the data is multi-looked with the same software package. Multi-looking averages the scattering operator over some number of pixels in each of the range and azimuth directions. Range and azimuth multi-look multipliers are chosen to make the SLC scene approximate ground-range projection. In this manner, all SIR-C images in this thesis have very similar range and azimuth distance scales, facilitating comparison with maps. The processing specifics for the two 1/120.30 scenes are listed in Table E.2. After multi-looking, the data must be converted to AIRSAR format in order to be read into the ER Mapper package as radar polarimetry data. AIRSAR scenes require, but are also limited to, 1024 pixels in the azimuth direction. SIR-C scenes are subdivided into overlapping AIRSAR sub-scenes that are then re-aligned with ER Mapper. Within ER Mapper, scene cross-section data was imported in five transmit/receive polarization combinations: HH, HV, VV, RL, and RR. Co-registering the two scenes produces a data set with ten layers, one for each of these polarizations in both L- and C-band. The L-band and C-band RL polarization images produced from the Stovepipe Wells data are shown in Figure E.2 and E.3 respectively. The overlapping of sub-scenes does not appear to affect the image processing either qualitatively or quantitatively.

Greeley and Blumberg (1995) analyzed Stovepipe Wells data from early in SRL-1 (DT 1/8.3) to investigate the radar behavior of aeolian features. They published SIR-C and AIRSAR average values of HH, HV, and VVσ°s at C- and

Table E.2
SIR-C Death Valley quad-pol scene processing parameters.

DT:		1/120.30	
Name:		Stovepipe Wells, CA	
Track angle:		141.52°	
Image center:		36.583°N, 117.008°W	
Time:	GMT	1994/106:19:40:37.5	
	Local	11:40:37.5, April 16th, 1994	
Scenes:	L-band (23.9 cm)	pr12060	
	C-band (5.65 cm)	pr12061	
θ_i:	near range	42.853°	
	image center	45.572°	
	far range	46.948°	
Shuttle roll angle*:		205.901°	
Near slant range:		295.4802 km	
Scales:		range	azimuth
	Slant range scene:	21.253 km	50.005 km
	Slant range pixels:	1595	9599
	Slant range pixel size:	13.325 m	5.209 m
	Ground range scene:	29.761 km	50.005 km
	Ground range pixel size:	18.659 m	5.209 m
	Multilook multiplier	2	7
	Multilook pixels:	797	1371
	Multilook pixel size:	37.32 m	36.47 m

* roll angle > 180° implies right illuminating/looking scene.

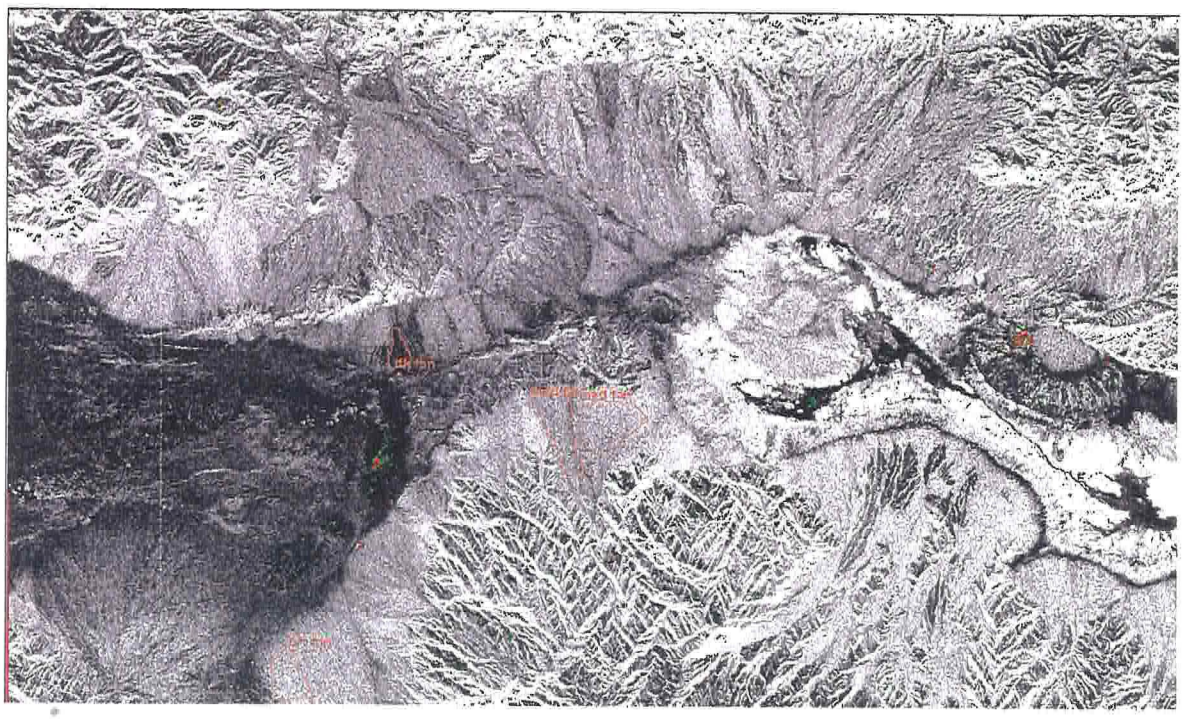

Figure E.2 SIR-C RL polarization radar image of Stovepipe Wells (DT 1/120.30) L-band (scene pr12060). The areas outlined in orange are alluvial fan surfaces that are compared to Greeley and Blumberg's (1995) results. The colored regions indicate locations with elevated μ_c; green for μ_c>1, red for μ_c>1.25. Illumination is from the bottom of the image.

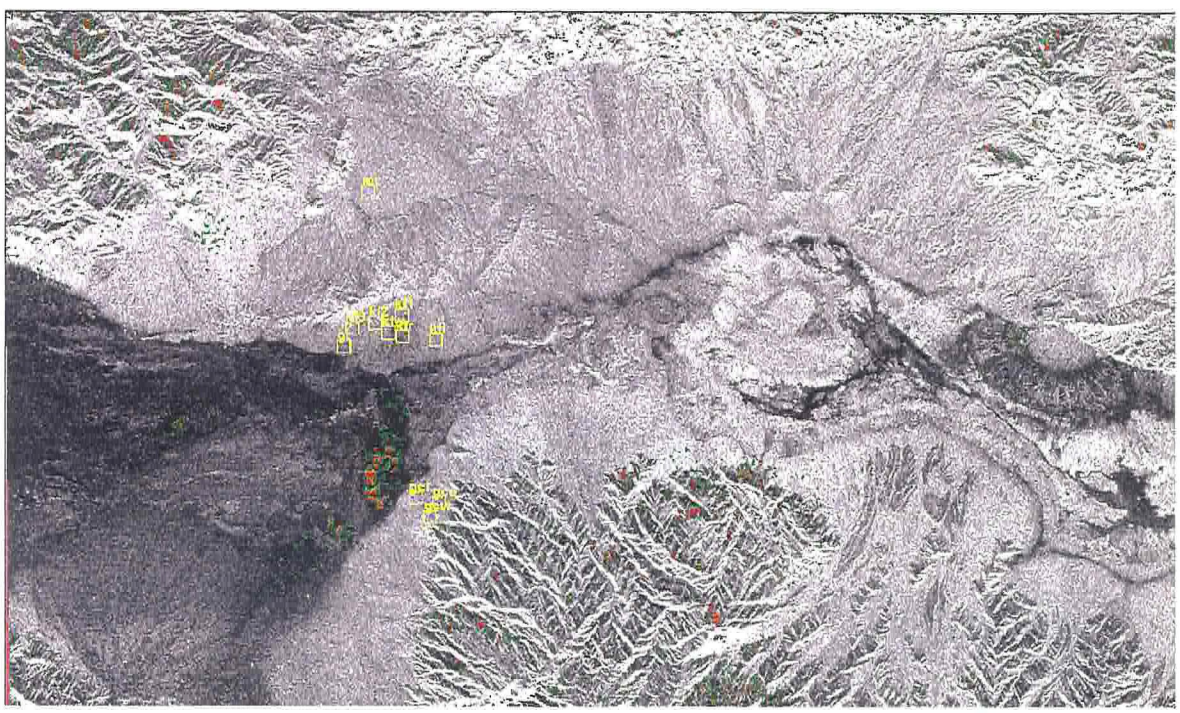

Figure E.3 SIR-C RL polarization radar image of Stovepipe Wells (DT 1/120.30) C-band (scene pr12061). The yellow boxes represent sites examined by Weeks et al. (1996; 1997) where the present data can be compared for processing correctness. The colored regions indicate locations with elevated μ_c as in Fig.E.2. Illumination is from the bottom of the image.

L-band for alluvial fan surfaces. Since they did not publish the exact locations where measurements were taken, some different alluvial fans are selected in the data processed here, and compared in Figure E.4 to the range of values given by Greeley and Blumberg (1995). In general, the average σ°'s measured with the image processing methods used here fall within the range of Greeley and Blumberg's (1995) alluvial fan σ° values. Since it is also unclear what the

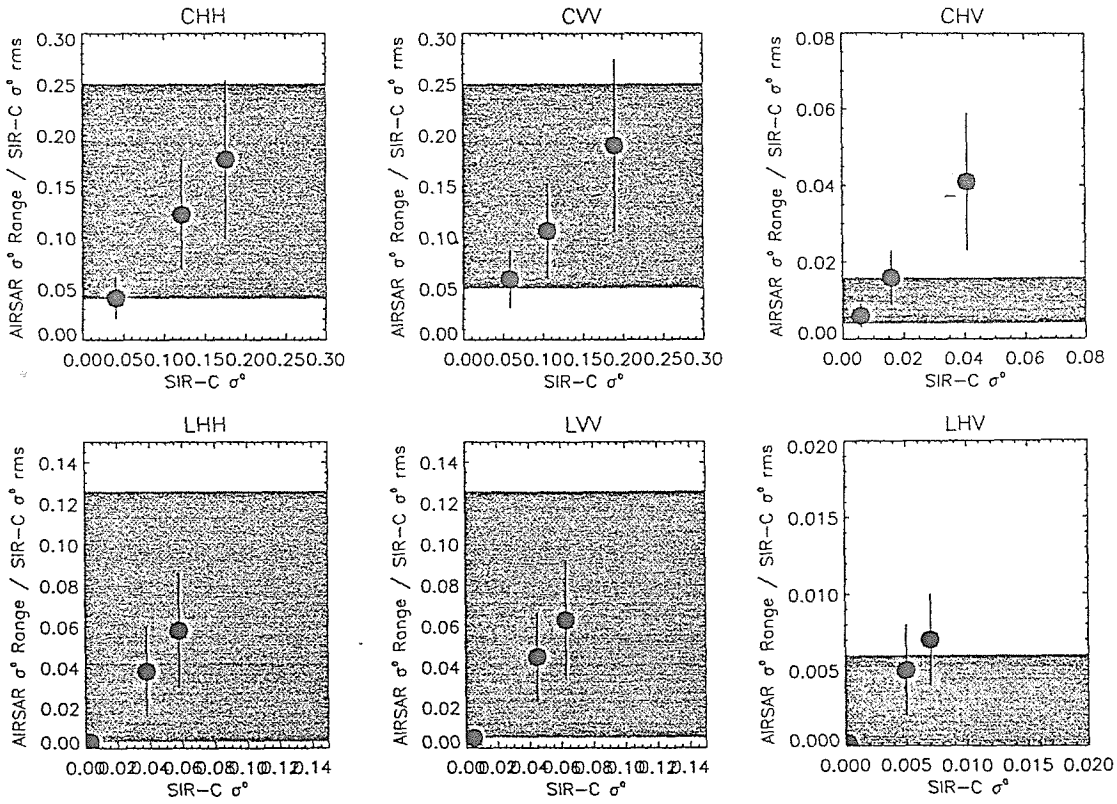

Figure E.4 Comparison of SIR-C σ° statistics from track 1/120.30 scenes pr12060 and pr12061 (points with rms standard deviation error bars), with (grey) ranges of AIRSAR σ° values from Greeley and Blumberg (1995). A one-to-one correspondence is imposed on the SIR-C points for graphical clarity.

illumination direction was for their calibrated AIRSAR data, it is not unreasonable that one point lie outside of their range in the C-band cross-polarization channel.

A more precise quantitative comparison can be made with the published results of Weeks et al. (1997). They studied the effect of surface roughness on the radar echoes at sites near the Kitt Fox Hills, and on Grotto Canyon Wash. Weeks et al. (1996; 1997) locate their sites on a Landsat image, although the clarity of their site labeling required some added information (Weeks, personal communication, 1997). They calculated statistics for 60x60.m^2 regions at those locales. Sites visually located in the Landsat view are plotted in Fig. E.3. The boxes encompass about 200 multilooked pixels each, in comparison to Weeks et

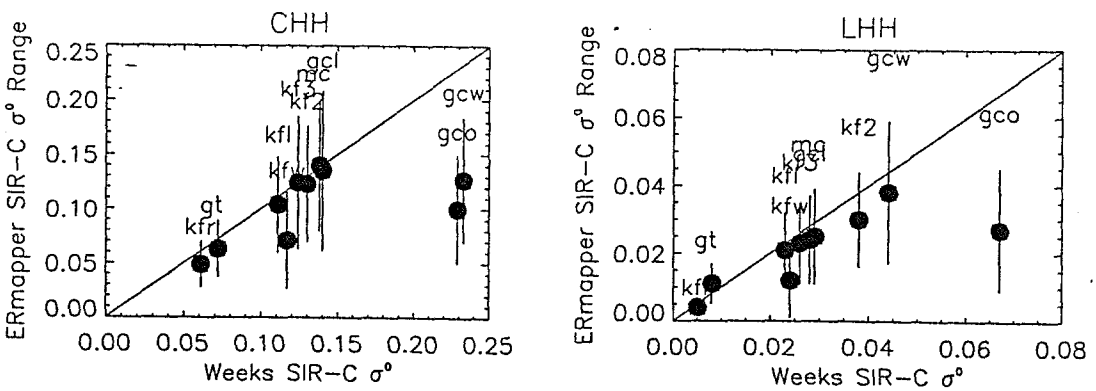

Figure E.5 Comparison of ER Mapper processed SIR-C CHH and LHH σ° statistics from Stovepipe Wells with published results of Weeks et al. (1997)

al.'s (1997). Still, the quantitative comparison of our values with theirs, shown in Fig. E.5, is very good. The discrepancies from the one-to-one correspondence occur at the Grotto Canyon sites gcw and gco, where the box averages may be low due to enforced avoidance of nearby σ° variations due to topography. It should also be noted that Weeks et al. (1996, 1997) relied on data from a different SIR-C track. DT 35.10 has an illumination direction almost perpendicular to that of DT 120.30, which might also explain the discrepancies observed. Overall, the consistency of the results is heartening.

E.2 Death Valley Polarization Ratios

Encouraged that the radar image preparation and processing sequence described in Fig.E.1 is sound, and produces sensible and reproducible outcomes, polarization ratios were also examined in Death Valley. Over most of the images, at both L- and C-bands, $\mu_c<0.25$. The surfaces with this "normal" behavior include the (old) fan surfaces, playas and valley floors, as well as possibly wet central portions of the salt flats and the salt plain edges. Other, possibly younger, fans, and rough salt areas as well as the dunes and sandy areas have $0.25<\mu_c<0.75$. The linear polarization ratio behavior mirrors the circular: $\mu_l<0.1$ where $\mu_c<0.25$, and $0.1<\mu_l<0.25$ where $0.25<\mu_c<0.75$. However, as shown by the green and red region classifications in Figs. E.2 and E.3, there are locations that display $\mu_c>1.0$.

The sites exhibiting C-band μ_c inversion in the mountain valleys could be associated with vegetation (top left and lower middle of Fig. E.3). At these sites

μ_c(L) is elevated, though not inverted, consistent with volume or multiple scattering from trees or bushes. Values of μ_l(C) are near 0.3 at these sites, consistent with the vegetation canopy explanation, and argues against a corner reflector-type behavior.

More intriguing is the μ_c behavior of the dune fields near Stovepipe Wells itself. The C-band μ_c behavior is somewhat astonishing; most of the surface of the Stovepipe Wells dune field exhibits μ_c(C)>1, and a not-insignificant portion displays μ_c>1.25. At L-band the μ_c behavior is somewhat subdued. The μ (C) values are around 0.3 when μ_c(C) > 1.0. Greeley and Blumberg (1995) mention the dune fields, and suggest that the σ° behavior of the linear dunes, to the west of those with μ_c inversion in this study, is due to vegetation. Specifically they point out that "the linear dunes were best seen on L-band HV images" moderately visible on L-band HH polarizations, but barely visible on C-band (Greeley and Blumberg 1995). They further remark that the dunes are sparsely vegetated, and that L-band penetrating deeper into the dry sand would scatter as if from a vegetated canopy, while C-band would not if it did not penetrate as deep.

The linear dunes Greeley and Blumberg (1995) describe do not exhibit μ_c inversion. Still, if the main Stovepipe Wells star dunes field is somewhat vegetated on the surface, one might well imagine that the plants require a well-developed root system, which would volume scatter C-band as we observe, as well as if a vegetation canopy were responsible. The fact that the μ_c values do not greatly exceed unity and that μ_l ~0.3 is consistent with this volume scattering

explanation. Certainly the overall behavior is nothing like EGC; the cross-sections of the dunes are by no means elevated. We might imagine that the plants responsible are not too deeply rooted, nor too large, or else the L-band μ_c signature would be more important.

E.3 Remarks on SIR-C Calibration

Each pixel in an image corresponds to a σ° or some function of σ°'s at several wavelengths and polarizations. The interpretation of σ°'s and polarization ratios does depend on the uncertainties on those values as delivered by the SIR-C instrument. The reported calibration uncertainties from both SIR-C missions were reported by Freeman et al. (1995), and are reproduced in Table E.3 in the published dB form, and converted to percentage uncertainties as well.

The most important uncertainty in Table E.3 is the noise level in any given image. The SAR processing and data storage choices for SIR-C are such that the noise level is in fact not a trivial quantity to determine, and it is different for each "block" of data (Freeman et al. 1995). In general though, the noise level is taken to lie 18 dB below the average level of a (sub-portion of a) scene. The other figure of merit which is most applicable to the image interpretation in this thesis is the cross-swath calibration uncertainty, reported as 1 dB. This suggests that across a swath measured cross-sections may differ from the true scattering

Table E.3

SIR-C calibration errors (Freeman et al. 1995)

Calibration errors	SRL-1		SRL-2	
	L	C	L	C
Absolute calibration	±2.3 dB (+70/-41 %)	±2.2 dB (+66/-40 %)	±2.0 dB (+58/-37 %)	±3.2 dB (+109/-52%)
Cross-swath calibration	±1.0 dB (+26/-21 %)	±1.0 dB (+26/-21 %)	±1.0 dB (+26/-21 %)	±1.0 dB (+26/-21 %)
Pass-to-pass calibration	±1.3 dB (+35/-26 %)	±1.2 dB (+32/-24 %)	±1.0 dB (+26/-21 %)	±2.2 dB (+66/-40 %)
HH/VV amplitude imbalance	±0.7 dB (+17/-15 %)	±0.6 dB (+15/-13 %)	±0.7 dB (+17/-15 %)	±0.6 dB (+15/-13 %)
HV/VH amplitude imbalance	±0.2 dB (+5/-5 %)	±0.2 dB (+5/-5 %)	±0.3 dB (+7/-7 %)	±0.5 dB (+12/-11 %)
HH/VV phase imbalance	±5°	±4°	±9°	±5°
HV/VH phase imbalance	±2°	±6°	±3°	±4°
Cross-talk	< -33 dB (0.05 %)	< -35 dB (0.03 %)	< -33 dB (0.05 %)	< -35 dB (0.03 %)

SIR-C noise equivalent backscatter cross-section is: $\sigma_{N.E.} \sim <\sigma^\circ> - 18 \text{ dB} = 0.016<\sigma^\circ>$

behavior as a function of θ_i by +26%/-21%. The cross-swath uncertainty arises from uncertainties in Endeavor's roll angle of the order 0.1°-0.2°, and its effect on elevation antenna pattern in the calibration. Fang and Moore (1997) point out that the JPL pre-flight elevation antenna pattern used to calibrate the data at EDC is more uncertain than Freeman et al. (1995) allow. Fang and Moore (1997) suggest that the calibration used is in error by about 0.5 dB at angles 3° from the center of the beam. This cross-swath uncertainty will be additive to the cross-swath uncertainty from Table E.3, so that the final cross-swath uncertainty is ±1.5 dB (+41/-29 %). This uncertainty is reduced if the antenna opening angle for a scene is reduced.

The pass-to-pass calibration errors also need to be factored into our comparisons with Weeks et al. (1996) and Greeley and Blomberg (1995), and make our comparison even better with the 50% uncertainty. Basically though, SIR-C is the best that can be accomplished at present with multifrequency multi-polarization SAR, and 50% uncertainty in radar cross-section reproducibility is quite good. So long as σ° values are above the noise level, it seems that the uncertainties should affect both polarizations in μ_c or μ_l equally, and cancel out in some sense. The propagation of the published phase uncertainties has not been pursued.

References

Ageta, Y., W. Zhang, and M. Nakawo, Mass Balance Studies on Chongce Ice Cap in the West Kunlun Mountains, *Bulletin of Glacier Research*, **7**, 37-45, 1989.

Anantharamaiah, K.R., R.D. Ekers, V. Radhakrishnan, T.J. Cornwell, and W.M. Gross, Noise in Images of Very Bright Sources, in *Synthesis Imaging in Radio Astronomy*, edited by F.R.Schwab, R. A. Perley, and A. H. Bridle, pp. 431-442, Astronomical Society of the Pacific, San Francisco, 1989.

Argent., C.T.R., Cerro Tupungato Sheet, Hoja 3369-26, Ejercito Argentino, Intstituto Geographico Militar, Buenos Aires, 1946.

Arvidson, R.E., R. Greeley, M.C. Malin, R.S. Saunders, N. Izenberg, J.J. Plaut, E.R. Stofan, and M.K. Shepard, Surface Modification of Venus as Inferred From Magellan Observations of Plains, *Journal of Geophysical Research Planets*, **97** (E8), 13303-13317, 1992.

Avouac, J.P., and G. Peltzer, Active Tectonics In Southern-Xinjiang, China - Analysis of Terrace Riser and Normal-Fault Scarp Degradation Along the Hotan-Qira Fault System, *Journal of Geophysical Research Solid Earth*, **98** (B12), 21773-21807, 1993.

Basilevsky, A.T., O.V. Nikolaeva, and C.M. Weitz, Geology of the Venera 8 Landing Site Region From Magellan Data: Morphological and Geochemical Considerations, *Journal of Geophysical Research*, **97** (E10), 16315--16335, 1992.

Benson, C.S., *Stratigraphic Studies in the Snow and Firn of the Greenland Ice Sheet,* U. S. Army Snow Ice and Permafrost Research Establishment 10, , 1962.

Bindschadler, R., K.C. Jezek, and J. Crawford, SEASAT Observations of Greenland, *Ann. Glaciol.*, **9**, 11-19, 1987.

Bindschadler, R., and P. Vornberger, Interpretation of SAR Imagery of the Greenland Ice-Sheet Using Coregistered TM Imagery, *Remote Sensing of Environment*, **42** (3), 167-175, 1992.

Brackett, R.A., B. Fegley, and R.E. Arvidson, Volatile Transport on Venus and Implications for Surface Geochemistry and Geology, *Journal of Geophysical Research Planets*, **100** (E1), 1553-1563, 1995.

Bredow, J., S.P. Gogineni, A.J. Gow, P.F. Blanchard, and R.K. Moore, Radar Backscattering From Artificially Grown Sea Ice, *IEEE Journal of Oceanic Engineering*, **14** (3), 259-264, 1989.

Bruggen, J., *Grundzüge der Geologie und Lagerstattenkunde Chiles*, Tubinger handelsdruckerei muller & bass, Tubingen, 1934.

Butler, B.J., *3.5-cm Radar Investigation of Mars and Mercury: Planetological Implications*, Ph.D. thesis, California Institute of Technology (Caltech), Pasadena, 1994.

Butler, B.J., D.O. Muhleman, and M.A. Slade, Mercury Full-Disk Radar Images and the Detection and Stability of Ice at the North-Pole, *Journal of Geophysical Research Planets*, **98** (E8), 15003-15023, 1993.

Butrica, A.J., *To See the Unseen: A History of Planetarty Radar Astronomy*, NASA, Washington, DC, 1996.

Campbell, B.A., Merging Magellan Emissivity and SAR Data for Analysis of Venus Surface Dielectric-Properties, *Icarus*, **112** (1), 187-203, 1994.

Campbell, B.A., R.E. Arvidson, and M.K. Shepard, Radar Polarization Properties of Volcanic and Playa Surfaces - Applications to Terrestrial Remote-Sensing and Venus Data Interpretation, *Journal of Geophysical Research Planets*, **98** (E9), 17099-17113, 1993.

Campbell, B.A., and D.B. Campbell, Analysis of Volcanic Surface-Morphology on Venus From Comparison of Arecibo, Magellan, and Terrestrial Airborne Radar Data, *Journal of Geophysical Research Planets*, **97** (E10), 16293-16314, 1992.

Campbell, B.A., and D.B. Campbell, Venus Highland Surface Characteristics, in *EOS, Transactions of the AGU*, AGU Spring Meeting, Baltimore, 1995.

Campbell, D.B., and B.A. Burns, Earth-Based Radar Imagery of Venus, *Journal of Geophysical Research*, **85**, 8271-8281, 1980.

Campbell, D.B., J.W. Head, J.K. Harmon, and A.A. Hine, Venus - Volcanism and Rift Formation in Beta Regio, *Science*, **226** (4671), 167-170, 1984.

Campbell, M.J., and J. Ulrichs, Electrical Properties of Rocks and Their Significance for Lunar Radar Observations, *Journal of Geophysical Research*, **74** (25), 5867--5881, 1969.

Carr, J.R., *Numerical Analysis for the Geological Sciences*, 592 pp., Prentice-Hall, Englewood Cliffs, NJ, 1995.

Chandrasekhar, S., *Radiative Transfer*, 393 pp., Dover, New York, 1950, 1960.

Chapman, Bruce, SIR-C Data Compression Software User Guide, ver. 3.1, JPL D-11427, April 1995.

Chen, J., Y. Wang, L. Liu, and P. Gu, Surveying and Mapping on the Chongce Ice Cap in the West Kunlun Mountains, *Bulletin of Glacier Research*, **7**, 1-7, 1989.

Clapperton, C.M., The Glaciation of the Andes, *Quaternary Science Reviews*, **2**, 83-155, 1983.

Clark, B.B., Coherence in Radio Astronomy, in *Synthesis Imaging in Radio Astronomy*, edited by F.R. Schwab, R. A. Perley, and A. H. Bridle, pp. 1-10, Astronomical Society of the Pacific, San Francisco, 1989.

Cohen, M.H., *Radar Echo from a Rough rRtating Planet,* Cornell Univercity EE 428, Ithaca, 1959.

Cornwell, T.J., and R. Braun, Deconvolution, in *Synthesis Imaging in Radio Astronomy*, edited by F.R. Schwab, R. A. Perley, and A. H. Bridle, pp. 167-184, Astronomical Society of the Pacific, San Francisco, 1989.

Corte, A.E., Glaciers and Glaciolithic Systems of the Central Andes, *World Glacier Inventory*, IAHS-AISH pub # 126, 11-23, 1980.

Corte, A.E., Central Andes Rock Glaciers: Applied Aspects, in *Rock Glaciers*, edited by J.R. Giardino, J.F.J. Shroder, and J.D. Vitek, Allen & Unwin, Boston, 1987.

Downs, G.S., R.R. Green, and P.E. Reichley, Radar Studies of the Martian Surface at Centimeter Wavelengths: The 1975 Opposition, *Icarus*, **33**, 441-453, 1978.

Downs, G.S., P.E. Reichley, and R.R. Green, Radar Measurements of Martian Topography and Surface Properties: The 1971 and 1973 Oppositions, *Icarus*, **26**, 273-312, 1975.

Drinkwater, M.R., LIMEX 87 Ice Surface Characteristics - Implications For C-Band SAR Backscatter Signatures, *IEEE Transactions on Geoscience and Remote Sensing*, **27** (5), 501-513, 1989.

Drinkwater, M.R., R. Kwok, D.P. Winebrenner, and E. Rignot, Multifrequency Polarimetric Synthetic Aperture Radar Observations of Sea Ice, *Journal of Geophysical Research Oceans*, **96** (C11), 20679-20698, 1991.

Elachi, C., *Introduction to the Physics and Techniques of Remote Sensing*, 430 pp., Wiley, New York, 1987.

Elachi, C., *Spaceborne Radar Remote Sensing: Applications and Techniques.*, IEEE press, New York, 1988.

Eshleman, Radar Glory from Buried Craters on Icy Moons, *Science*, **234**, 587-590, 1986.

Evans, J.V., and T. Hagfors, *Radar Astronomy*, 620 pp., McGraw-Hill, New York, 1968.

Fahnestock, M.A., and R.A. Bindschadler, Description of a Program for SAR Investigation of the Greenland Ice Sheet and an Example of Margin Change Detection Using SAR, *Annals of Glaciology*, **17**, 332-337, 1993.

Fang, and Moore, *Remote Sensing of Environment*, **59**, 407-414, 1997.

Fily, M., J.P. Dedieu, and S. Surdyk, A SAR Image Study of a Snow-Covered Area In the French Alps, *Remote Sensing of Environment*, **51** (2), 253-262, 1995.

Ford, P.G., David A. Senske, The Radar Scattering Characteristics of Venus Landforms, *Geophysical Research Letters*, **17** (9), 1361-1364, 1990.

Ford, P.G., and G.H. Pettengill, Venus - Global Surface Radio Emissivity, *Science*, **220** (4604), 1379-1381, 1983.

Forster, R.R., B.L. Isacks, and S.B. Das, Shuttle Imaging Radar (SIR-C/X-SAR) Reveals Near-Surface Properties of the South Patagonian Icefield, *Journal of Geophysical Research Planets*, **101** (E10), 23169-23180, 1996.

Freeman, A., M. Alves, B. Chapman, J. Cruz, Y. Kim, S. Shaffer, J. Sun, E. Turner, and K. Sarabandi, SIR-C Data Quality and Calibration Results, *IEEE Transactions on Geoscience and Remote Sensing*, **33** (4), 848-857, 1995.

Fung, A.K., and H.J. Eom, Application of Combined Rough Surface and Volume Scattering Theory to Sea Ice and Snow Backscatter, *IEEE Transactions on Geoscience and Remote Sensing*, **GE-20**, 528-536, 1982.

Garvin, J.B., J.W. Head, G.H. Pettengill, and S.H. Zisk, Venus Global Radar Reflectivity and Correlations with Elevation, *Journal of Geophysical Research Solid Earth and Planets*, **90** (B8), 6859-6871, 1985.

Gerth, H., *Der Geologische Bau der Sudamerikanischen Kordillere*, Gerbruder Borntraeger, Berlin, 1955.

Goldspiel, J.M., S.W. Squyres, M.A. Slade, R.F. Jurgens, and S.H. Zisk, Radar-Derived Topography of Low Southern Latitudes of Mars, *Icarus*, **106** (2), 346-364, 1993.

Goldstein, R.M., *Radar exploration of Venus*, California institute of technolgy, Pasadena, 1962.

Goldstein, R.M., and R.R. Green, Ganymede: Radar Surface Characteristics, *Science*, **207**, 179-180, 1980.

Goldstein, R.M., and Morris, Ganymede: Observations by Radar, *Science*, **188**, 1211-1212, 1975.

Golombek, M.P., R.A. Cook, H.J. Moore, and T.J. Parker, Selection of the Mars Pathfinder Landing Site, *Journal of Geophysical Research Planets*, **102** (E2), 3967-3988, 1997.

Greeley, R., R.E. Arvidson, C. Elachi, M.A. Geringer, J.J. Plaut, R.S. Saunders, G. Schubert, E.R. Stofan, E.J.P. Thouvenot, S.D. Wall, and C.M. Weitz, Aeolian Features on Venus - Preliminary Magellan Results, *Journal of Geophysical Research Planets*, **97** (E8), 13319-13345, 1992.

Greeley, R., and D.G. Blumberg, Preliminary-Analysis of Shuttle-Radar-Laboratory (Srl-1) Data to Study Aeolian Features and Processes, *IEEE Transactions on Geoscience and Remote Sensing*, **33** (4), 927-933, 1995.

Greeley, R., and J.E. Guest, Geologic Map of the Eastern Equatorial Region of Mars, U.S. Geological Survey, 1987.

Gurrola, E.M., *Interpretation of Radar Data from Icy Galilean Satellites and Triton*, Ph.D. thesis, Stanford, Stanford, 1995.

Hagfors, T., Backscattering from an Undulating Surface with Applications to Radar Returns from the Moon, *Journal of Geophysical Research Planets*, **69**, 3779-3784, 1964.

Hagfors, T., Relationship of Geometric Optics and Autocorrelation Approaches to the Analysis of Lunar and Planetary Radar, *J. Geophys. Res.*, **71** (2), 379-383, 1966a.

Hagfors, T., Relationship of Geometric Optics and Autocorrelation Approaches to the Analysis of Lunar and Planetary Radar, *Journal of Geophysical Research Planets*, **71**, 379-383, 1966b.

Hagfors, T., Refraction Scattering as Origin of the Anomalous Radar Returns of Jupiter's Satellites, *Nature*, **315**, 637-640, 1985.

Haldemann, A.F.C., D.L. Mitchell, R.F. Jurgens, M.A. Slade, and D.O. Muhleman, Mars Pathfinder Landing Site Assessement with Goldstone Delay-Doppler and CW Radar Experiments, *Journal of Geophysical Research*, **102** (E2), 4097-4106, 1997a.

Haldemann, A.F.C., D.O. Muhleman, B.J. Butler, and M.A. Slade, Beta Regio 3.5 cm Circular-Polarization Ratio, in *EOS, Transactions of the AGU*, AGU Fall Meeting, San Francisco, 1994.

Haldemann, A.F.C., D.O. Muhleman, B.J. Butler, and M.A. Slade, The Western Hemisphere of Venus: 3.5 cm Dual Circular-Polarization Radar Images, *Icarus*, (in press), 1997b.

Hall, D.K., and J.P. Ormsby, Use of Seasat Synthetic Aperture Radar and Landsat Multispectral Scanner Subsystem Data For Alaskan Glaciology Studies, *Journal of Geophysical Research Oceans and Atmospheres*, **88** (C3), 1597-1607, 1983.

Han, J., T. Zhou, and M. Nakawo, Stratigraphic and Structural Features of Ice Cores from Chongce Ice Cap, West Kunlun Mountains, *Bulletin of Glacier Research*, **7**, 21-29, 1989.

Hapke, B., Coherent Backscatter and the Radar Characteristics of Outer Planet Satellites, *Icarus*, **88** (2), 407-417, 1990.

Hapke, B., and Blewitt, Coherent Backscatter Model for the Unusual Radar Reflectivity of Icy Satellites, *Nature*, **352** (2), 46-47, 1991.

Harmon, J.K., D.B. Campbell, and S.J. Ostro, Dual-Polarization Radar Observations of Mars - Tharsis and Environs, *Icarus*, **52** (1), 171-187, 1982.

Harmon, J.K., and S.J. Ostro, Mars: Dual-Polarization Radar Observations with Extended Coverage, *Icarus*, **62** (1), 110-128, 1985.

Harmon, J.K., and M.A. Slade, Radar Mapping of Mercury - Full-Disk Images and Polar Anomalies, *Science*, **258** (5082), 640-643, 1992.

Harmon, J.K., M.A. Slade, and R.S. Hudson, Mars Radar Scattering - Arecibo Goldstone Results at 12.6-cm and 3.5-cm Wavelengths, *Icarus*, **98** (2), 240-253, 1992.

Harmon, J.K., M.A. Slade, R.A. Velez, A. Crespo, M.J. Dryer, and J.M. Johnson, Radar Mapping of Mercury's Polar Anomalies, *Nature*, **369** (6477), 213-215, 1994.

Harmon, J.K., A Radar Study of the Chryse Region, Mars, *Journal of Geophysical Research Planets*, **102** (E2), 4081-4095, 1997.

Head, J.W., A.R. Peterfreund, J.B. Garvin, and S.H. Zisk, Surface Characteristics of Venus Derived From Pioneer Venus Altimetry, Roughness, and Reflectivity Measurements, *Journal of Geophysical Research Solid Earth and Planets*, **90** (B8), 6873-6885, 1985.

Hoekstra, P., and D. Spanogle, Backscatter from Snow and Ice Surfaces at Near Incident Angles, *IEEE Trans. Ant. Propag.*, **AP-20**, 788-790, 1972.

Holton, J., R., *An Introduction to Dynamic Meteorolgy*, Acdemic Press, Inc., San Diego, 1992.

IGM, sheet "E" 69, 3330-6945, Rio Yeso, Instituto Geographico Militar, Santiago, 1985.

IGM, sheet "E" 61, 3315-6945, Tupungato, Instituto Geographico Militar, Santiago, 1994.

Jackson, J.D., *Classical Electrodynamics*, Wiley, New York, 1975.

Jezek, K.C., M.R. Drinkwater, J.P. Crawford, R. Bindschadler, and R. Kwok, Analysis of Synthetic Aperture Radar Data Collected Over the Southwestern Greenland Ice-Sheet, *Journal of Glaciology*, **39** (131), 119-132, 1993.

Jezek, K.C., P. Gogineni, and M. Shanableh, Radar Measurements of Melt Zones on the Greenland Ice-Sheet, *Geophysical Research Letters*, **21** (1), 33-36, 1994.

JPL, *SIR-C/X-SAR Mission Overview*, JPL Pub. 93-29, Pasadena, 1993.

Klose, K.B., J.A. Wood, and A. Hashimoto, Mineral Equilibria and the High Radar Reflectivity of Venus Mountaintops, *Journal of Geophysical Research Planets*, **97** (E10), 16353-16369, 1992.

Kulkarni, S.R., Self-Noise in Interferometers - Radio and Infrared, *Astronomical Journal*, **98** (3), 1112-1130, 1989.

Li, and Cheng, Recent Research on Glaciers on the Chinghai-Tibet Plateau, *World Glacier Inventory*, IAHS-AISH Publ. no. 126, 1980.

Li, B., and J. Li, Quaternary Glacial Distribution Map of the Qinghai-Xizang (Tibet) Plateau, Science Press, Beijing, 1991.

Livingstone, C.E., and M.R. Drinkwater, Springtime C-Band SAR Backscatter Signatures of Labrador Sea Marginal Ice - Measurements Versus Modeling Predictions, *IEEE Transactions on Geoscience and Remote Sensing*, **29** (1), 29-41, 1991.

Lliboutry, *Nieves y Glaciares de Chile*, Univ. de Chile, Santiago, 1956.

Lliboutry, L., The Origin of Penitents, *Journal of glaciology*, **2**, 331-338, 1954.

Lliboutry, L., *Traité de Glaciologie, Glace, Neige, Hydrologie Nivale*, Masson & Cie, Paris, 1965a.

Lliboutry, L., *Traité de Glaciologie, Glaciers, Variations du Climat, Sols Gelés*, Masson & Cie, Paris, 1965b.

Long, D.G., and M.R. Drinkwater, Greenland Ice-Sheet Surface-Properties Observed by the Seasat-A Scatterometer at Enhanced Resolution, *Journal of Glaciology*, **40** (135), 213-230, 1994.

Long, M.W., On the polarization and the Wavelength Dependence of Sea Echo, *IEEE Transaction on Antennas and Propagation*, **AP-13**, 749-754, 1965.

Lopez, B., *Arctic Dreams*, Harper, New York, 1980.

Lunine, J.I., D.J. Stevenson, and Y.L. Yung, Ethane Ocean on Titan, *Science*, **222**, 1229-1230, 1983.

Malin, M.C., Mass Movements on Venus - Preliminary-Results From Magellan Cycle-1 Observations, *Journal of Geophysical Research Planets*, **97** (E10), 16337-16352, 1992.

Masursky, H., and N.L. Crabill, The Viking Landing Sites: Selection and Certification, *Science*, **193** (4255), 809-812, 1976.

Mätzler, C., Microwave Permittivity of Dry Snow, *IEEE Transactions on Geoscience and Remote Sensing*, **34** (2), 573-581, 1996.

Mätzler, C., H. Aebischer, and E. Schanda, Microwave Dielectric-Properties of Surface Snow, *IEEE Journal of Oceanic Engineering*, **9** (5), 366-371, 1984.

Mätzler, C., E. Schanda, and W. Good, Towards the Definition of Optimum Sensor Specifications For Microwave Remote-Sensing of Snow, *IEEE Transactions on Geoscience and Remote Sensing*, **20** (1), 57-66, 1982.

Mätzler, C., and U. Wegmuller, Dielectric-Properties of Fresh-Water Ice At Microwave-Frequencies, *Journal of Physics D Applied Physics*, **20** (12), 1623-1630, 1987.

McCollom, T.M., and B.M. Jakosky, Interpretation of Planetary Radar Observations - the Relationship Between Actual and Inferred Slope Distributions, *Journal of Geophysical Research Planets*, **98** (E1), 1173-1184, 1993.

Moore, H.J., and T.W. Thompson, A Radar-Echo Model for Mars, *Proceedings of Lunar and Planetary Science*, **21**, 457-472, 1991.

Muhleman, D.O., D. Holeridge, and N. Block, The Astronomical Unit Determined by Radar Reflections from Venus, *Astronomical Journal*, **67**, 191, 1962.

Muhleman, D.O., Radar Scattering from Venus and the Moon, *Astronomical Journal*, **69** (1), 34--41, 1964.

Muhleman, D.O., B.J. Butler, A.W. Grossman, and M.A. Slade, Radar Images of Mars, *Science*, **253** (5027), 1508-1513, 1991.

Muhleman, D.O., A.W. Grossman, and B.J. Butler, Radar Investigation of Mars, Mercury and Titan, in *Annual Review of Earth and Planetary Science*, pp. 337-374, 1995.

Muhleman, D.O., A.W. Grossman, B.J. Butler, and M.A. Slade, Radar reflectivity of Titan, *Science*, **248**, 975-980, 1990.

Muhleman, D.O., G.S. Orton, and G.L. Berge, A Model of the Venus Atmosphere from Radio, Radar, and Occultation Observations, *Astronomical Journal*, **234**, 733--745, 1979.

Nakawo, M., Y. Nakayama, T. Kohshima, T. Nishimura, J. Han, and T. Zhou, Ice Coring Operation at High Altitudes in West Kunlun Mountains, China, *Bulletin of Glacier Research*, **7**, 15-21, 1989.

Ohata, T., and X. Kang, Full Year Surface Meterological Data on Northwestern Tibetian Plateau Using an Automatic Meteorological System, *Bulletin of Glacier Research*, **8**, 87-93, 1990.

Ohata, T., S. Takahashi, and X. Kang, Meteorological Conditions of the West Kunlun Mountains in the Summer of 1987, *Bulletin of Glacier Research*, **7**, 67-77, 1989.

Ostro, S.J., Radar Properties of Europa, Ganymede, and Callisto, in *Satellites of Jupiter*, D. Morrison, ed., pp. 213-236, Univ. Arizona Press, Tucson, 1982.

Ostro, S.J., Europa, Ganymede, and Callisto: New Radar Results From Arecibo and Goldstone, *Journal of Geophysical Research*, **97**, 18227-18244, 1992.

Ostro, S.J., Planetary Radar Astronomy, *Reviews of Modern Physics*, **65** (4), 1235-1279, 1993.

Ostro, S.J., and Pettengill, Icy Craters on the Galilean Satellites, *Icarus*, **34**, 268-279, 1978.

Ostro, S.J., and E.M. Shoemaker, The Extraordinary Radar Echoes From Europa, Ganymede, and Callisto - a Geological Perspective, *Icarus*, **85** (2), 335-345, 1990.

Paige, D.A., S.E. Wood, and A.R. Vasavada, The Thermal-Stability of Water Ice at the Poles of Mercury, *Science*, **258** (5082), 643-646, 1992.

Paterson, W.S.B., *The Physics of Glaciers*, Pergamon, London, 1994.

Peixoto, J.P., and A.H. Oort, *Physics of Climate*, AIP, New York, 1992.

Peltzer, G., P. Tapponnier, and R. Armijo, Magnitude of Late Quaternary Left-Lateral Displacements Along the North Edge of Tibet, *Science*, **246** (4935), 1285-1289, 1989.

Pettengill, G.H., E. Eliason, P.G. Ford, G.B. Loriot, H. Masursky, and G.E. McGill, Pioneer Venus Radar Results: Altimetry and Surface Properties, *Journal of Geophysical Research*, **85**, 8261-8270, 1980.

Pettengill, G.H., P.G. Ford, and B.D. Chapman, Venus - Surface Electromagnetic Properties, *Journal of Geophysical Research Solid Earth and Planets*, **93** (B12), 14881-Continues, 1988.

Pettengill, G.H., P.G. Ford, W.T.K. Johnson, R.K. Raney, and L.A. Soderblom, Magellan - Radar Performance and Data Products, *Science*, **252** (5003), 260-265, 1991.

Pettengill, G.H., P.G. Ford, and S. Nozette, Venus - Global Surface Radar Reflectivity, *Science*, **217** (4560), 640-642, 1982.

Pettengill, G.H., P.G. Ford, and R.A. Simpson, Electrical-Properties of the Venus Surface From Bistatic Radar Observations, *Science*, **272** (5268), 1628-1631, 1996.

Pettengill, G.H., P.G. Ford, and R.J. Wilt, Venus Surface Radiothermal Emission as Observed by Magellan, *Journal of Geophysical Research Planets*, **97** (E8), 13091-13102, 1992.

Piddington, J.D., *Radio Astronomy*, Hutchinson, London, 1961.

Press, W.H., S.A. Teukolsky, W.T. Vetterling, and B.P. Flannery, *Numerical Recipes in C: the Art of Scientific Computing*, Cambridge Univ. Press, Cambridge, 1992.

Ray, T.W., *Remote Monitoring of Land Degradation in Arid/Semiarid Regions*, California Institute of Technology, Pasadena, 1995.

Reichert, F., Das Gletschergebiet Zwischen Aconcagua und Tupungato, *Zeitsch. f. Gletschscherk.*, **4**, 193, 1910.

Rignot, E., Backscatter Model for the Unusual Radar Properties of the Greenland Ice-Sheet, *Journal of Geophysical Research Planets*, **100** (E5), 9389-9400, 1995.

Rignot, E.J., S.J. Ostro, J.J. Vanzyl, and K.C. Jezek, Unusual Radar Echoes from the Greenland Ice-Sheet, *Science*, **261** (5129), 1710-1713, 1993.

Rott, H., and C. Matzler, Possibilties and Limits of Synthetic Aperature Radar for Snow and Glacier Surveying, *Annals of Glaciology*, **9**, 195-200, 1987.

Rotto, S., and K.L. Tanaka, Geologic/Geomorphologic Map of the Chryse Planitia Region of Mars, U.S. Geol. Surv., Denver, Colo., 1995.

Saunders, R.S., R.E. Arvidson, J.W. Head, G.G. Schaber, E.R. Stofan, and S.C. Solomon, An Overview of Venus Geology, *Science*, **252** (5003), 249-252, 1991.

Saunders, R.S., G.H. Pettengill, R.E. Arvidson, W.L. Sjogren, W.T.K. Johnson, and L. Pieri, The Magellan Venus Radar Mapping Mission, *Journal of Geophysical Research Solid Earth and Planets*, **95** (B6), 8339-8355, 1990.

Senske, D.A., D.B. Campbell, J.W. Head, P.C. Fisher, A.A. Hine, A. Decharon, S.L. Frank, S.T. Keddie, K.M. Roberts, E.R. Stofan, J.C. Aubele, L.S. Crumpler, and N. Stacy, Geology and Tectonics of the Themis Regio-Lavinia Planitia-Alpha Regio-Lada Terra Area, Venus - Results From Arecibo Image Data, *Earth Moon and Planets*, **55** (2), 97-161, 1991a.

Senske, D.A., D.B. Campbell, E.R. Stofan, P.C. Fisher, J.W. Head, N. Stacy, J.C. Aubele, A.A. Hine, and J.K. Harmon, Geology and Tectonics of Beta-Regio, Guinevere Planitia, Sedna Planitia, and Western Eistla Regio, Venus - Results From Arecibo Image Data, *Earth Moon and Planets*, **55** (2), 163-214, 1991b.

Senske, D.A., J.W. Head, E.R. Stofan, and D.B. Campbell, Geology and Structure of Beta Regio, Venus - Results From Arecibo Radar Imaging, *Geophysical Research Letters*, **18** (6), 1159-1162, 1991c.

Senske, D.A., G.G. Schaber, and E.R. Stofan, Regional Topographic Rises on Venus - Geology of Western Eistla Regio and Comparison to Beta-Regio and Atla-Regio, *Journal of Geophysical Research Planets*, **97** (E8), 13395-13420, 1992.

Sharp, R.P., *Glaciers*, Oregon State System of Higher Education, Eugene, 1960.

Sharp, R.P., *Living Ice*, Cambridge University Press, New York, 1988.

Shepard, M.K., R.E. Arvidson, R.A. Brackett, and B. Fegley, A Ferroelectric Model for the Low Emissivity Highlands on Venus, *Geophysical Research Letters*, **21** (6), 469-472, 1994.

Shi, J., and J. Dozier, Mapping Seasonal Snow with SIR-/X-SAR in Mountainous Areas, *Remote Sensing and Enviroment*, **59**, 294-307, 1997.

Shih, Y., T. Hsieh, P. Cheng, and C. Li, Distribution, Features and Variations of Glaciers in China, *World Glacier Inventory*, IAHS-AISH Publ. no. 126, 1980.

Simons, M., B.H. Hager, and S.C. Solomon, Global Variations In the Geoid/Topography Admittance of Venus, *Science*, **264** (5160), 798-803, 1994.

Simpson, R.A., J.K. Harmon, S.H. Zisk, T.W. Thompson, and D.O. Muhleman, Radar Determination of Mars Surface Properties, in *Mars*, edited by H.H. Kieffer, B.M. Jakosky, C.W. Snyder, and M.S. Matthews, pp. 652-685, University of Arizona Press, Tucson, AZ, 1992.

Simpson, R.A., G.L. Tyler, and D.B. Campbell, Arecibo Radar Observations of Mars Surface Characteristics in the Northern Hemisphere, *Icarus*, **36**, 153-173, 1978a.

Simpson, R.A., G.L. Tyler, and D.B. Campbell, Arecibo Radar Observations of Martian Surface Characteristics Near the Equator, *Icarus*, **33**, 102-115, 1978b.

Slade, M.A., B.J. Butler, and D.O. Muhleman, Mercury Radar Imaging - Evidence for Polar Ice, *Science*, **258** (5082), 635-640, 1992.

Smith, A.G., and T.D. Carr, *Radio Exploration of the Planetary System*, Van Nostrand, Princeton, NJ, 1964.

Smith, D.E., and M.T. Zuber, The Shape of Mars and the Topographic Signature of the Hemispheric Dichotomy, *Science*, **271** (5246), 184-188, 1996.

Solomon, S.C., S.E. Smrekar, D.L. Bindschadler, R.E. Grimm, W.M. Kaula, G.E. McGill, R.J. Phillips, R.S. Saunders, G. Schubert, S.W. Squyres, and E.R. Stofan, Venus Tectonics - an Overview of Magellan Observations, *Journal of Geophysical Research Planets*, **97** (E8), 13199-13255, 1992.

Sramek, R.A., and F.R. Schwab, Imaging, in *Synthesis Imaging in Radio Astronomy*, edited by F.R. Schwab, R. A. Perley, and A. H. Bridle, pp. 117-138, Astronomical Society of the Pacific, San Francisco, 1989.

Stiles, W.H., and F.T. Ulaby, The Active and Passive Microwave Responce to Snow Parameters 1. Wetness, *Journal of Geophysical Research*, **85**, 1037-1044, 1980.

Stofan, E.R., D.L. Evans, C. Schmullius, B. Holt, J.J. Plaut, J. Vanzyl, S.D. Wall, and J. Way, Overview of Results of Spaceborne Imaging Radar-C, X-Band Synthetic-Aperture Radar (SIR-C/X-SAR), *IEEE Transactions on Geoscience and Remote Sensing*, **33** (4), 817-828, 1995a.

Stofan, E.R., J.W. Head, D.B. Campbell, S.H. Zisk, A.F. Bogomolov, O.N. Rzhiga, A.T. Basilevsky, and N. Armand, Geology of a Rift-Zone on Venus - Beta-Regio and Devana Chasma, *Geological Society of America Bulletin*, **101** (1), 143-156, 1989.

Stofan, E.R., S.E. Smrekar, D.L. Bindschadler, and D.A. Senske, Large Topographic Rises on Venus - Implications For Mantle Upwelling, *Journal of Geophysical Research Planets*, **100** (E11), 23317-23327, 1995b.

Streiff-Becker, R., Zur Entstehung der Penitentes, *Zietschrift fur Gletscherkunde und Glaziologie*, **111**, 245-248, 1954.

Svitek, T., *Martian Water Frost: Control of Global Distribution by Small-Scale Processes*, California Institute of Technolgy, Pasadena, 1992.

Swan, A.R.H., M. Sandilands, *Introduction to Geological Data Analysis*, Blackwell Science Ltd., Oxford, GB, 1995.

Takahashi, S., T. Ohata, and Y. Xie, Characteristics of Heat and Water Fluxes on Glacier and Ground Surfaces in the West Kunlun Mountains., *Bulletin of Glacier Research*, **7**, 89-99, 1989.

Thompson, L.G., Climatic Changes for the Last 2000 years from Ice-Core Evidence in Tropical Ice Cores, in *Climatic Varaitions and Forcing*

Mechanisms of the Last 2000 years, edited by P.D. Jones, pp. 281-295, Springer-Verlag, Berlin, 1996.

Thompson, L.G., E. Mosley-Thompson, M.E. Davis, P.N. Lin, J. Dai, J.F. Bolzan, and T. Yao, A 1000 Year Ice Core Record from the Guliya Ice Cap, China: its Relationship to Global Climate Variabilty, *Annals of Glaciology*, **21**, 175-181, 1995.

Tryka, K.A., and D.O. Muhleman, Reflection and Emission Properties on Venus - Alpha-Regio, *Journal of Geophysical Research Planets*, **97** (E8), 13379-13394, 1992.

Tyler, G.L., D.B. Campbell, G.S. Downs, R.R. Green, and H.J. Moore, Radar Characteristics of the Viking 1 Landing Sites, *Science*, **193** (4255), 812-815, 1976.

Tyler, G.L., P.G. Ford, D.B. Campbell, C. Elachi, G.H. Pettengill, and R.A. Simpson, Magellan - Electrical and Physical-Properties of Venus Surface, *Science*, **252** (5003), 265-270, 1991.

Tyler, G.L., R.A. Simpson, M.J. Maurer, and E. Holmann, Scattering Properties of the Venusian Surface - Preliminary-Results From Magellan, *Journal of Geophysical Research Planets*, **97** (E8), 13115-13139, 1992.

Ulaby, F.T., Radar Signatures of Terrain - Useful Monitors of Renewable Resources, *Proceedings of the IEEE*, **70** (12), 1410-1428, 1982.

Ulaby, F.T., R.K. Moore, and A.K. Fung, *Microwave Remote Sensing : Active and Passive*, 2162 pp., Addison-Wesley, Reading, Mass., 1986.

Ulaby, F.T., W.H. Stiles, and M. Abdelrazik, Snowcover Influence on Backscattering From Terrain, *IEEE Transactions on Geoscience and Remote Sensing*, **22** (2), 126-133, 1984.

USGS, U.S.G.S., Mars Digital Topographic Map, Version 2, 1993.

Van Zyl, J.J., B.D. Chapman, P. Dubois, and J.C. Shi, The Effect of Topography on SAR Calibration, *IEEE Transactions on Geoscience and Remote Sensing*, **31** (5), 1036-1043, 1993.

Van Zyl, J.J., and F.T. Ulaby, Scattering Matrix Representation for Simple Targets, in *Radar Polarimetry for Geoscience Applications*, edited by F.T. Ulaby, and C. Elachi, pp.1-16, Artech House, Inc., Norwood, 1990.

Van Zyl, J.J., H.A. Zebker, and C. Elachi, Polarimetric SAR Applications, in *Radar Polarimetry for Geoscience Applications*, edited by F.T. Ulaby, and C. Elachi, pp. pp.315-359, Artech House, Inc., Norwood, 1990.

Vitek, J.D., and J.R. Giardino, Rock Glaciers: A Review, in *Rock Glaciers*, J.R. Giardino, J.F.J. Shroder, and J.D. Vitek eds., Allen&Unwin, Boston, 1987.

Voronovich, A.G., *Wave Scattering from Rough Surfaces*, 229 pp., Springer-Verlag, Berlin, 1994.

Watanabe, and B. Zheng, First Glaciological Expedition to West Kunlun Mountains 1985, *Bulletin of Glacier Research*, **5**, 77-84, 1987.

Weeks, R., M. Smith, K. Pak, and A. Gillespie, Inversions of SIR-C and AIRSAR Data For the Roughness of Geological Surfaces, *Remote Sensing of Environment*, **59** (2), 383-396, 1997.

Weeks, R.J., M. Smith, K. Pak, W.H. Li, A. Gillespie, and B. Gustafson, Surface-Roughness, Radar Backscatter, and Visible and Near-Infrared Reflectance in Death-Valley, California, *Journal of Geophysical Research Planets*, **101** (E10), 23077-23090, 1996.

Weitz, C.M., and A.T. Basilevsky, Magellan Observations of the Venera and Vega Landing Site Regions, *Journal of Geophysical Research Planets*, **98** (E9), 17069-17097, 1993.

Xie, Z., and W. Zhang, Characteristics of Ice Formation in the West Kunlun Mountains, *Bulletin of Glacier Research*, **7**, 29-37, 1989.

Yoshino, Radar Transmission in the Icecap, *IEEE Trans. Ant. Propag.*, **AP-15** (4), 542-551, 1967.

Zeil, W., *Geologie von Chile*, Gerbruder Borntraeger, Berlin, 1964.

Zhang, W., R. An, H. Yang, and K. Jiao, Conditions of Glacier Development and Some Glacial Features in the West Kunlun Mountains, *Bulletin of Glacier Research*, **7**, 49-59, 1989.

Zhang, W., and K. Jiao, Modern Glaciers on the South Slope of West Kunlun Mountains (in Aksayqin Lake and Guozha Co Lake Drainage Areas), *Bulletin of Glacier Research*, **5**, 85-91, 1987.

Zheng, B., Preliminary Studies of Quaternary Glaciation and Palaeogeography on the South Slope of West Kunlun, *Bulletin of Glacier Research*, **5**, 93-102, 1987.

Zuhui, S., *Terrain Map of the Qinghai-Xizang plateau*, Science Press, Shanghai, 1990.

Zwally, Microwave Emissivity and Accumulation Rate of Polar Firn, *Journal of Glaciology*, **18**, 195-215, 1977.